Constant- and frequency-dependent seismic quality factors measured from surface and borehole seismic surveys.

James Alexander Beckwith

School of Earth and Environment

University of Leeds

Submitted in accordance with the requirements of the degree of

Doctor of Philosophy

6th January 2017

The candidate confirms that the work submitted is his own, except where work which has formed part of jointly authored publications has been included. The contribution of the candidate and the other authors to this work has been explicitly indicated below. The candidate confirms that appropriate credit has been given within the thesis where reference has been made to the work of others.

The work in Chapter 2 of the thesis has appeared in publication as follows: **Beckwith, J.A.**, R.A.Clark and L.Hodgson (2016), *The estimation of spectra from time-frequency transforms for use in attenuation studies*, Geophysical Prospecting, doi:10.1111/1365-2478.12407.

The work is predominantly that of James Beckwith with input and guidance from Roger Clark and Linda Hodgson.

The work in Chapter 3 of the thesis has appeared in publication as follows: **Beckwith, J.A.**, R.A.Clark and L.Hodgson (2016), *Estimating frequency-dependent attenuation quality factor values from pre-stack surface seismic data*, Geophysics, accepted for publication.

The work is predominantly that of James Beckwith with input and guidance from Roger Clark and Linda Hodgson.

Acknowledgements

I would like to thank Roger Clark, Linda Hodgson, David Cornwell, Greg Houseman and Andy Hooper for their supervision through my PhD. Their support and useful ideas and comments have led to many interesting discoveries and avenues of research that I would not have thought of by myself. I would also to like to thank all of the participants in the applied geophysics research group for allowing me to present my work at various stages of completion in order to receive feedback and guidance.

I would like to thank BP exploration for providing the funding for my research and an abundance of data upon which to work. I would also like to thank BP for accommodating me in Aberdeen from time to time and making me feel very welcomed in their office. My thanks go out to all at BP exploration Aberdeen that provided useful input on various aspects of processing and the background geology of the central North Sea. I would also like to thank the Norwegian Petroleum Directorate, and especially Svein Finnestad, for providing data for research at no expense.

I would like to thank the IT staff in the School of Earth and Environment who have managed to solve all my technical and computer related problems with blistering speed.

My thanks go to all those who have helped me blow off steam throughout my PhD through various sports and activities, unfortunately you are too many to name individually, but you have my sincerest thanks.

Finally, I would like to thank my family, friends and flat mates who have made the past few years highly enjoyable and the best years of my life.

Abstract

In this thesis, I have introduced and presented a new time-frequency distribution, termed the Signal-Dependent Distribution (SDD), which can by-pass the Gabor Uncertainty Principle, with a trade-off instead between joint time-frequency transform and suppression of transform artefacts. In two different synthetic seismic data sets, the SDD provided estimates of attenuation in closer agreement to the input attenuation than those from a fixed- (short-time-Fourier-transform) and a variable-window (Stockwell transform) time-frequency transform. The SDD also provided spectral ratio surfaces from a pre-stack gathers, using the pre-stack Q inversion (PSQI) method, more consistent with a frequency-independent attenuation model than the fixed- and variable-window transforms.

Frequency-dependent Q can be estimated in the PSQI method if the seismic attenuation quality factor, Q, is assumed to follow a power-law frequency-dependence, $Q=af^b$. Utilising the SDD to form spectra, the modified PSQI method found a frequency exponent, b, of only 0.074 ± 0.001 (median 0.06) for the Kinnoull field in the North Sea, implying that an approximation of frequency-independent Q is valid for the Kinnoull dataset. Higher b values were found to coincide with sudden, localised, drops in centroid frequency beneath amplitude anomalies: they were inferred not to be due to a genuine frequency-dependence of Q, but to interference on the spectral ratio surface.

The SDD was then used to estimate spectra in the PSQI method applied to: the Kinnoull pre-stack surface seismic dataset; a spectral ratio method applied to a stacked surface seismic survey;

and VSP data for well 16/23-7. The three sets of attenuation estimates were compared to each other, and also to average energy and average centroid frequency maps derived from the stacked seismic dataset. Only the attenuation values estimated from the stacked seismic data and the VSP data correlated well with each other (median 1000/Q of 9.2±0.1 and 10.4±2.0 respectively). 1/Q attenuation maps from stacked and pre-stack seismic data did not correlate coherently with the centroid frequency or energy maps, nor did the pre-stack attenuation values correlate with the VSP data. This inconsistency remains unexplained.

This method of estimating frequency-dependent seismic attenuation quality factor was then applied to 6 VSP datasets located in the Barents Sea. Although the formation-averaged frequency exponent b varied between -0.1 and 0.2, the median value was 0.02, again supporting an assumption of frequency-independent attenuation within the seismic bandwidth. Using coincident well logs, statistically significant correlations were found between intrinsic attenuation and bulk, shear, and Young's moduli, and Poisson's ratio. In contrast, no robust relationship was found between petrophysical parameters and attenuation in the seismic bandwidth. However, a squirt flow model fitted to the estimated power-law curves of frequency-dependent 1/Q implied crack aspect of between 1 and 6 x 10^{-3}, similar to the crack aspect ratio of 0.1-1.0 x 10^{-3} expected to be responsible for the majority of squirt flow induced attenuation.

Abbreviations

a	coefficient of frequency dependence of Q
b	exponent of frequency dependence of Q
BI	Brittleness index
CMP	Common midpoint gather
CWT	Continuous wavelet transform
G	Geometric spreading term
K	Bulk modulus
M	P-wave modulus
OBC	Ocean bottom cable
p	Slowness
P	Energy partitioning function
Q	Seismic attenuation quality factor
SDD	Signal-dependent-distribution
STFT	Short-time-Fourier-transform
S_x	Horizontal slowness
VSP	Vertical seismic profile
Yo	Young's modulus
α	attenuation rate
η	Alkhalifah anisotropy parameter
θ	angle
λ	lameé's parameter
μ	Shear-wave modulus
ν	Poisson's ratio
ρ	Density
τ	Intercept time
ϕ	porosity

Contents

List of Figures

List of Tables

Chapter 1

Background

1.1 Why study seismic attenuation?

Attenuation of a seismic wave is the loss of amplitude of a wave with propagation distance. This can be caused by a redistribution of the wave energy as in scattering attenuation or by geometric spreading. Loss of amplitude can also be caused by the conversion of wave energy into heat by intrinsic attenuation/inelastic dissipation. Some processes, such as geometric spreading, are not of much interest in the regards to estimating intrinsic attenuation, given that it has been corrected for in the data, and thus will not be focused on.

Energy of a propagating wave can also be redistributed at acoustic impedance contrasts as, for example, reflections. When a compressional wave impacts an acoustic impedance contrast at an angle other than normal then mode conversion will take place in which part of the compressional wave energy is converted to shear wave energy. Shear waves travel at lower speeds than compressional waves and so the energy of the wave will also be redistributed via mode conversion.

The processes that affect the amplitude of a propagating wave outlined so far are physical phenomenon. However, it is also important to note that the way in which the seismic data is processed after acquisition can artificially change the amplitude and shape of recorded waveform.

When mentioning seismic attenuation, unless otherwise stated, I will be referring to intrinsic attenuation or effective seismic attenuation (a combination of

intrinsic and scattering attenuation) rather than any of the other process outlined that affect the amplitude of a propagating wave.

Knowledge of the interval seismic attenuation quality factor value, Q, which is used to quantify attenuation, is of great interest in seismic data processing and for the analysis of seismic data for hydrocarbon exploration. Interval Q values vary much more than interval velocities with a change in lithology or pore fluid and can therefore be used as lithological and petrological discriminators (Tonn (1991)). It is hoped that high resolution estimates of interval seismic attenuation can be used for interpretation purposes much the same that velocity models estimated from full waveform inversion (FWI) is interpretable.

Seismic attenuation preferentially attenuates higher frequencies which will lower the apparent resolution in seismic data and thus accurate knowledge of the quality factor, Q, is important for restoring not only amplitude but higher frequencies to deeper reflectors in seismic data through the use of inverse-Q filters (Wang (2008)). Attenuation can also cause phase changes in the seismic signal which can lead to misties between well and seismic data. Accurate Q values can then be used in phase only inverse-Q deconvolution to improve seismic-to-well misties (Ziolkowski et al. (1998)).

Pride et al. (2003) and Pride and Berryman (2003) discuss and show evidence for a relationship between the frequency dependence of the seismic quality factor, Q, and permeability. If permeability of specific intervals is to be estimated from seismic data, whether that be surface seismic surveys or vertical seismic profiles, it is necessary to estimate the frequency dependence of the seismic attenuation.

To answer the question in the title of this section, seismic attenuation should be studied in order to better constrain lithological boundaries and changes in pore fluid fill within specific intervals in the subsurface, correct recorded seismic data for the phase change and amplitude decay imparted by seismic attenuation and, to be able to estimate petrophysical rock properties such as permeability directly from seismic data.

In this chapter I will start by giving a review of some processes which give rise to intrinsic attenuation and an overview of scattering attenuation. I will then overview how attenuation can affect a propagating wave and outline some methods which can be used to estimate attenuation.

1.2 What causes seismic intrinsic attenuation?

Intrinsic attenuation occurs when pores in rocks are saturated with fluids (Murphy (1982a)). Figure 1.1 gives a schematic overview of a few attenuation mechanisms that can occur in fluid saturated rocks (after Johnston et al. (1979)). Dry rock samples in a vacuum have been measured to have very low attenuation values (Tittmann et al. (1972) and Pandit and Tozer (1970)). The mechanism whereby saturating fluids move relative to the rock frame due to the passage of a seismic wave is generally referred to as wave-induced-fluid-flow (WIFF). Wave induced fluid flow can occur on various different scales from the pore scale to the macro scale. Here I define the pore scale as the spatial scale up to the size of the largest pore, the meso-scale as any spatial scale from the largest pore to the smallest seismic wavelength and the macro-scale as the spatial scale which is equal to or larger than the smallest wavelength of the propagating wave (following Mller et al. (2010), figure 1.2).

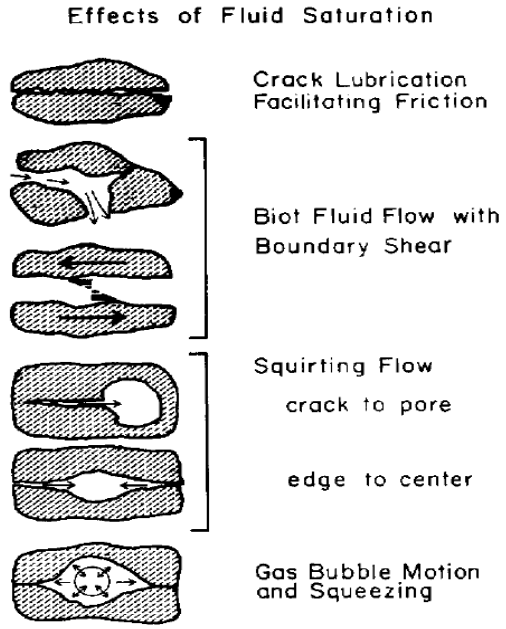

Figure 1.1: Schematic illustration of a few attenuation mechanisms that can occur in fluid saturated rocks. (image courtesy of Johnston et al. (1979)).

On the macro-scale, the propagation of a seismic wave through a permeable,

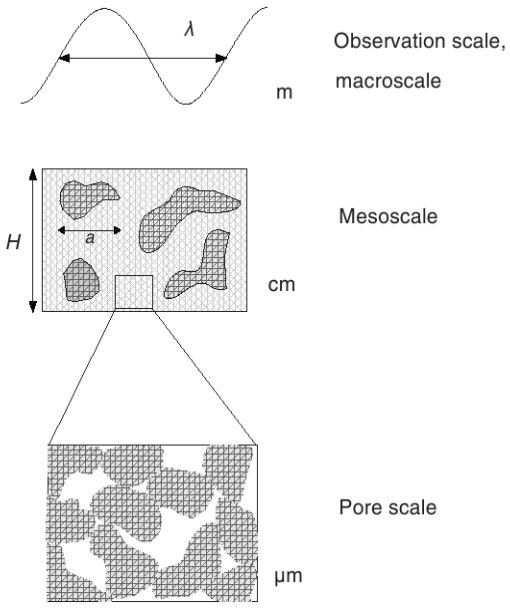

Figure 1.2: representation of different scales of observation for attenuation studies. The dominant attenuation mechanism will depend upon the scale of heterogeneity which depends upon the frequency of the seismic wave. For wave induced fluid flow to occur at typical surface seismic survey frequencies (5Hz-100Hz), the relevant scale of heterogeneity is typically the mesoscopic scale (image taken from Mller et al. (2010)).

fluid-saturated rock will cause displacements on the rock frame and pore fluid is then moved by viscous friction. Pressure gradients of scale equivalent to the wavelength of the propagating wave are then created between the peaks and troughs of the seismic wave. This process is also described as Biot flow, named after Maurice Anthony Biot who formalized the mechanism (Biot (1956a), Biot (1956b)). The Biot theory predicts that attenuation caused by this macro scale process is only significant at frequencies of over 100kHz, well outside the typical exploration seismic bandwidth of 5Hz-100Hz.

On the meso-scale (i.e. larger then the pore scale and smaller than the seismic wavelength) heterogeneities in the pore fluid, sometimes called patchy saturation, can result in pressure gradients formed within the fluid. As the seismic wave passes, in the compression phase, fluid flows from elastically softer regions and vice versa in the rarefaction phase of the propagating wave. Significant levels of attenuation can only occur if the difference between the elastic properties of the

different regions which make up the rock are significant (Pride et al. (2004)). A similar scenario giving rise to meso-scale attenuation promoted by Pride et al. (2004) is that of a double-porosity system in which rocks with different elastic properties reside within the same geology, for instance interlaced sands and clays.

Squirt flow can be thought of as both a meso-scale and a pore-scale mechanisms. As a meso-scale mechanism attenuation can arise due to squirt flow between compressible fractures and the rock frame (O'Connell and Budiansky (1977), Gurevich et al. (2009)), which occurs on a scale greater than the pore scale but less than the seismic scale. The alignment of these fractures can lead to frequency dependent anisotropy (Chapman (2003)). On the pore scale, pores can have different compliances, and thus the passage of a seismic wave can cause an increase in the fluid pressure in one pore relative to another, thus setting up a pressure gradient which causes fluid flow and subsequently attenuation and dissipation (Johnston et al. (1979)). Mavko and Nur (1979) show that the attenuation values predicted by squirt flow is much closer to that measured in seismic surveys than those predicted the Biot flow and squirt flow has been shown to be responsible for attenuation measured in sedimentary rocks by William F. Murphy et al. (1986) and Wang and Nur (1990).

The squirt flow model was later extended to treat both Biot flow and squirt flow as a coupled process to produce a new combined Biot/squirt (BISQ) model (Dvorkin and Nur (1993), Dvorkin et al. (1994), figure 1.3).

1.3 Scattering attenuation

The redistribution of direct wave energy by very short path multiples (time lag much less than the duration of the propagating wave) is known as scattering attenuation, distinct from intrinsic attenuation as it is not associated with a conversion of seismic energy to heat but is rather a redistribution of seismic energy. The redistribution of energy by the multitude of very short path multiples existing in the subsurface means that the energy in the direct wave at depth will be minimal and the observed wavefront constitutes the direct wave, but mainly energy from very short path multiples which have both constructively and destructively interfered with the direct wave (Odoherty and Anstey (2006)). The

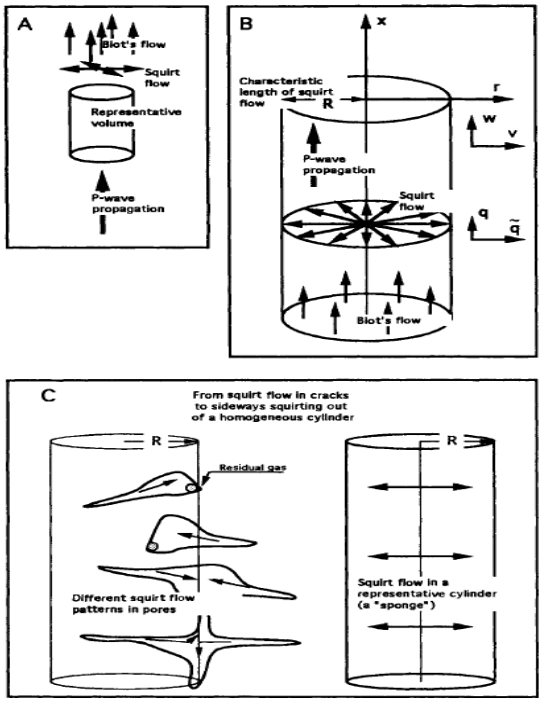

Figure 1.3: Graphical representation of the BISQ model as given by Dvorkin and Nur (1993). a/b.) representation of the BISQ model in a cylindrical representative volume of a rock showing the fluid motion due to both Biot and squirt flow. c.) A model of squirt flow in cracks of different geometries and the representative cylinder used to approximate this squirt flow as a sponge model.

nature of the reflectivity series which gives rise to short path multiples determines the effect of the interference by very path multiples on the direct wave. Odoherty and Anstey (2006) illustrates how a reflectivity series corresponding to a transitional layering in acoustic properties acts as a low-cut frequency filter and a reflectivity series corresponding to a cyclic change in acoustic properties acts as a high-cut frequency filter for a propagating wave train and can have a significant effect on the amplitude spectrum.

The high-cut filter effect of Earth's reflectivity can mimic the effect of intrinsic attenuation and is often referred to as scattering attenuation.

Odoherty and Anstey (2006) outlined the following relationship between the amplitude spectrum of the transmissivity of a medium, —T(ω)—, and the power

spectrum of the reflectivity series of that medium, R(ω).

$$|T(\omega)| = e^{-R(\omega)t} \tag{1.1}$$

Here $R(\omega)$ is has previously been normalised by the traveltime through the medium, t, where $t = \tau N$, N is the number of layers and τ is the traveltime through each layer.

This result was later derived by Banik et al. (1985) and Shapiro and Zien (1993) using stochastic averaging and localization theory respectively. Shapiro and Zien (1993) derived $1/Q_{sc}$, the inverse-Q value associated with scattering attenuation, for a medium whose squared slowness profile can be described by a constant part, c_0^{-2}, plus a normalised variation with depth, $\mu(z)$, (equation 1.2) which has an exponential shape to it's auto-correlation function. Shapiro et al. (1994) extended this to include density fluctuations (equation 1.2) and Van Der Baan (2001) investigated media where auto-correlation of the normalised variations of the incompressibility with depth have Gaussian or Von Karman distributions as well as exponential distributions.

$$\begin{aligned} \frac{1}{c_{true}^2} &= \frac{1}{c_0^2}(1 + \mu(z)) \\ \rho_{true} &= \rho_0(1 + \delta\rho(z)) \end{aligned} \tag{1.2}$$

Here $\frac{1}{c_{true}^2}$ is the measured squared slowness, c_0 is a background velocity and $\mu(z)$ is deviation on the background squared slowness, similarly for the density ρ the deviation on the background, ρ_0 is given by $\delta\rho(z)$.

The equation for the inverse quality factor given by Shapiro et al. (1994) for a medium whose normalised variations in density and squared slowness have an exponential auto-correlation function is

$$Q_{sc}^{-1}(\omega, \theta) = C(0)\frac{ka\cos^2(\theta)}{2(1 + (2k_0a)^2\cos^2(\theta))} \tag{1.3}$$

Here k is the wavenumber, k_0 is the wavenumber at vertical incidence, a is the scale length of the medium, θ is the angle of incidence and $C(0)$ value of the combined auto-correlation function at zero lag. The combined auto-correlation

function is given by

$$C = 4C_{\rho\rho} - \frac{4C_{\rho\mu}}{\cos^2(\theta)} + \frac{C_{\mu\mu}}{\cos^4(\theta)} \tag{1.4}$$

Here $C_{\rho\mu}$ is the cross-correlation of the normalised variation in density with that of the squared slowness and the other variables follow the same rule.

The scale length describes the characteristic scale length for variations in the density and squared-slowness profiles.

This method for estimating scattering attenuation independent of intrinsic attenuation requires well log data, therefore many experiments estimate scattering attenuation and then subtract those values from effective attenuation estimated from a coincident vertical seismic profile (VSP) (Portsmouth et al. (1993) and Pevzner et al. (2014)).

1.4 What effect does seismic attenuation have on a propagating wave?

The decay of seismic amplitudes with traveltime leads to the incontrovertible fact that some seismic energy is converted into other forms of energy. Knopoff and MacDonald (1958) borrows from electrical circuit theory to describe the loss of energy in the system per cycle by a constant, Q.

$$\frac{1}{Q} = \frac{T\Delta S_{irr}}{2\pi E} \tag{1.5}$$

Here $T\Delta S_{irr}$ is a measure of the energy dissipated from the stress wave system per cycle and E is elastic energy per unit volume at maximum strain. The system can be modeled by a damped harmonic oscillator where the attenuation coefficient α denotes the degree of attenuation.

$$u(x,t) = u_0 e^{-\alpha(\omega)x} e^{i(\omega t - kx)} \tag{1.6}$$

Here u denotes a displacement, k is a wavenumber and ω is an angular frequency. The dissipation of energy in the system can be approximated by the

squared amplitudes at subsequent peaks and if the dissipation is small this leads to the a relation between the attenuation coefficient α and the quality factor, Q.

$$\frac{1}{Q} = \frac{2c\alpha}{\omega} \tag{1.7}$$

Here c is the wave speed of the stress wave. This leads to the expression for the amplitude of a wave at time, t, after traveling through a medium of attenuation, Q, given in equation 1.8 for a large number of cycles, n, where the number of cycles is given by $\omega t/2\pi$ and a linear stress-strain relationship.

$$S = S_0 e^{-\frac{\omega t}{2Q}} \tag{1.8}$$

Here S_0 is the amplitude at time $t = 0$. Equation 1.8, which describes the amplitude decay of a signal, does not incorporate the processes of apparent attenuation, the source wavelet or the possible anisotropic effects of different take off angles (Zhu et al. (2007)). A more detailed form of the equation for the decay of the amplitude of a wave is given by (equation 1.9).

$$S^{\theta}(f) = D^{\theta}(f) P^{\theta} G^{\theta} S_0(f) e^{-\frac{\omega t^{\theta}}{2Q(f)^{\theta}}} \tag{1.9}$$

Here P is the energy partitioning term (which is equal to 1 if no impedance boundary is crossed by the wave), G is the geometric spreading term, S_0 is the source wavelet and $D(f)$ accounts for both source-receiver array directivity effects (Hustedt and Clark (1999)). A θ superscript denotes angle dependence.

Equation 1.9 highlights that, for a frequency independent Q, higher frequencies are more attenuated than lower frequencies and so the dominant frequency of a wave will decrease as it travels through an attenuative media. This leads to a loss of apparent resolution for deeper reflectors.

A wave traveling through a horizontally stratified media will also experience a loss of energy due to energy partitioning at interfaces. Energy partitioning processes at interfaces, such as mode conversion and reflection/transmission, redistribute the energy of the primary wavefield. Intrinsic attenuation can also be dependent upon the angle at which the wave propagates and thus can be anisotropic (Zhu et al. (2007)).

An example of a use for derived quality factor values is to correct for the effect of intrinsic attenuation on AVO results (Avseth et al. (2010), Luh (1993)). Luh (1993) demonstrated an approach for correcting these AVO measurements for the effects of attenuation. This method involves decomposing the attenuation into horizontal and vertical attenuation whereby the vertical attenuation is the zero-offset, vertical incidence attenuation. Horizontal attenuation is the extra attenuation suffered by a wave as it traverses laterally through the ground. Luh (1993) suggests a correction, δG, for the AVO gradient, G, of $\delta G = f_1 t_0 / Q_e$ where t_0 is the zero-offset traveltime, f_1 is the peak frequency of the seismic wavelet and Q_e is the effective attenuation. Effects of attenuation on the amplitude versus offset (AVO) gradient can be as great as 20% of the AVO gradient for a reflection at 1 second with a source of peak frequency 30Hz and an overburden of $Q_e = 150$ (Luh (1993)).

1.5 Frequency-dependence of seismic quality factor

Intrinsic attenuation of a material can be measured in laboratory experiments at kilohertz frequencies and the frequency-dependence of the attenuation quality factor measured. A typical laboratory measurement might involve drying the rock sample and then saturating with water to ensure full water saturation followed by using a kHz or MHz transducer to send a pulse through the sample surrounded by a control medium. The reflections from the interface of the top and base of the sample with the control medium can then be used to estimate attenuation in a similar manner to that used for exploration scale seismic surveys. An illustration of this kind of set up is shown in figure 1.4. Other experimental methods exist for measuring attenuation, for example the resonant bar technique which can be used to measure extensional attenuation down to below 100Hz (Murphy (1982b), Bruckshaw and Mahanta (1961)).

Laboratory experiments by Collins and Lee (1956), Bruckshaw and Mahanta (1961), Birch and Bancroft (1938) and Gemant and Jackson (1937) have shown that the intrinsic attenuation quality factor (referred to as specific dissipation

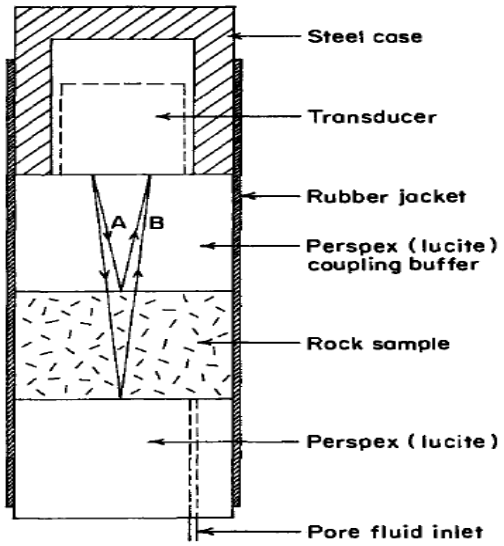

Figure 1.4: Example of a laboratory experimental setup to investigate seismic velocity and attenuation in a rock sample by way of analysis of reflections from the top and base of the rock sample with the control medium (in this example perspex) after Klimentos and McCann (1990).

in many of the papers) is frequency-independent for a range of materials. The study of Bruckshaw and Mahanta (1961) is of special interest in exploration seismics, because they found that the specific dissipation in sandstones over the frequency range of 40Hz to 120Hz, similar to the surface seismic exploration bandwidth, is independent of frequency. The study of Gemant and Jackson (1937) was performed on a range of materials including wood and glass at frequencies lower than that encountered in exploration seismics, Birch and Bancroft (1938) performed their study on granite and Bruckshaw and Mahanta (1961) worked with dry rocks, in all cases different from what might be expected in exploration seismics.

Sams et al. (1997) demonstrate with VSP, crosshole, sonic and core attenuation measurements over 5 orders of magnitude of frequency (and a factor of 3 in seismic quality factor values) how Q is frequency-dependent over a wide frequency scale by modeling the observed attenuation with a squirt-flow model (using the methods of Jones (1986) and Mavko and Jizba (1991)). This and other recent work (Adam et al. (2009)) suggest a frequency-dependence of attenuation within

the seismic bandwidth of 5Hz-100Hz.

Figure 3.1 is a reproduction of the results given by Sams et al. (1997) within the bandwidth of 0Hz to 200Hz. All 3 models, which are derived from the squirt flow model of Jones (1986) (we direct the reader to the papers of Sams et al. (1997) and Jones (1986) for further details), are well fit by a power-law frequency-dependent Q, $Q = f^{-b}/a$, within this bandwidth with exponents, b, in the range of -0.39 to -0.66 and coefficients, a, between 204 and 1500.

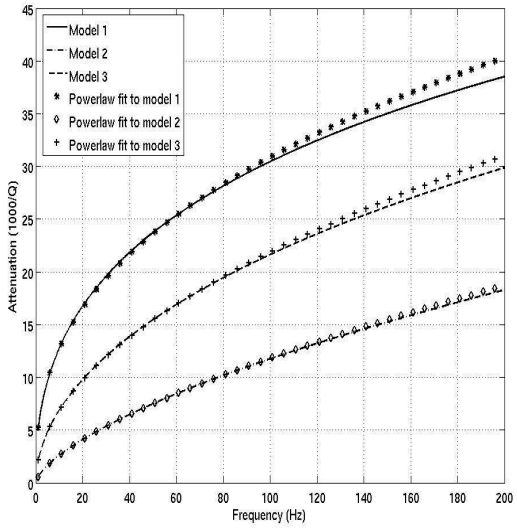

Figure 1.5: Reproduction of the results of Sams et al. (1997) within the bandwidth 0Hz to 200Hz with powerlaw frequency-dependent Q (equation 3.2) fitted.

Whether intrinsic attenuation is frequency-dependent within the seismic bandwidth or not, the aforementioned scattering attenuation can be highly frequency dependent and significant within the seismic bandwidth.

1.6 How can we measure seismic attenuation?

Q values are most accurately determined from laboratory experiments, VSP data or well logging. The drawback of these approaches to determining Q values is the need for a borehole to exist prior to the determination of Q values and that any derived Q values are only valid for the borehole location. As it has been stated

that attenuation can be used as an exploration tool it would be useful to derive Q values from surface seismic data and hence without the need of a borehole. A method to derive Q from surface seismic data would also have a much larger spatial coverage of the derived Q values.

Extrapolation of this frequency back to the seismic bandwidth, roughly 5Hz to 100Hz, would suggest a small, almost frequency-independent Q value (Liner (2012)). However, many authors have previously found evidence for an almost linear dependence of the compressional (P) wave quality factor, Qp, with frequency within the seismic bandwidth. This is generally modeled by a power law frequency dependence of Q with an exponent close to 1 (Bowles (1997), Yoshimoto et al. (1993), Sams et al. (1997)).

One method of deriving attenuation estimates is by comparison of the frequency spectrum of the seismic wave before and after passing through a target medium. A simple example of comparison is the spectral ratio method (Bath (1974), Tonn (1991)). In the spectral ratio method the ratio of the spectra of a reference signal at depth z_1 and at a target depth z_2 are taken. The slope of the natural logarithm of the spectral ratio against frequency plot (m in equation 1.10) can then be used to determine the quality factor, Q.

$$\ln\left(\frac{|S(\omega)_2|}{|S(\omega)_1|}\right) = \ln\left(\frac{|A_0(\omega)_2|}{|A_0(\omega)_1|}\right) - m\omega$$
$$m = \frac{\Delta z}{2Qc} = \frac{\Delta t}{2Q} \tag{1.10}$$

The spectral ratio method has been adapted by various authors to work on pre-stack seismic data (Dewangan and Tsvankin (2006), Dasgupta and Clark (1998) and Reine et al. (2012)). The Pre-Stack Q Inversion (PSQI) (Reine et al. (2012)) algorithm estimates interval apparent attenuation via inversion of a log spectral ratio surface (figure 1.6). The log spectral ratio surface is a number of natural log spectral ratios derived for common horizontal slowness traces of the reflectors bounding the region of interest. When matching common horizontal slowness values the spectral ratio surface equation is given by equation 1.11.

$$\ln\left[\frac{S_2(f)}{S_1(f)}\right] = -\frac{\pi}{Q}\Delta t f + \ln(PG) \tag{1.11}$$

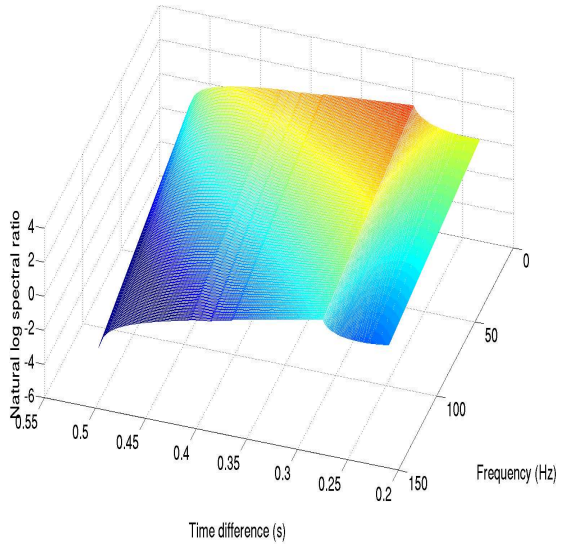

Figure 1.6: Theoretical natural log spectral ratio surface used in the PSQI algorithm.

Here common horizontal slowness values are replaced by the TWT difference between the reflectors bounding the region of interest at common horizontal slowness values. Here P denotes the energy partitioning function, a ratio of reflection amplitudes at common horizontal slowness values multiplied by the transmission coefficients into and out of the region of interest, and G denotes geometric spreading. To retain linearity in the inversion process, frequency-independent Q is assumed.

Matching common horizontal slowness values on the reflectors bounding a region of interest negates angle dependent effects in the overburden in equation 1.9 as the ray path for reflectors with the same horizontal slowness are the same through the overburden. Reine et al. (2012) found that matching common horizontal slowness values in the $\tau - p$ domain provide more accurate results than matching common horizontal slowness values in the time-offset domain.

A main problem in deriving spectra from $\tau - p$ domain data, as in the PSQI algorithm, is contamination of reflector energy by spatially aliased energy of shallower reflectors (Stoffa et al. (1981)). Stoffa et al. (1981) describe a method which will remove any aliased energy which does not occupy the same $\tau - p$ location as reflector energy but if a reflector lies within the aliased energy of a shallower reflector then the interference effect of the aliased energy with the reflector energy

is not accounted for and removed.

Here I will describe extensions to the PSQI algorithm including a process in which aliased energy can be mitigated in τ-p domain data for the sole use of deriving spectra as well as introducing power law dependent Q determination into the PSQI algorithm. The performance of the reduced interference distribution (RID, Bradford et al. (2006)), Wigner-Ville distribution (WVD, Ville (1958)) and matching pursuit decomposition (Wang (2007)) will also be tested in lieu of the Stockwell transform as a means of deriving spectra via time-frequency distributions.

Reine et al. (2012) also showed the potential for the PSQI algorithm to derive the quality factor-free energy partitioning ratio between the two reflectors bounding the interval of interest, in the absence of geometric spreading. This report will finish with an analysis of energy partitioning ratios derived via PSQI for their accuracy to theoretical curves and an investigation into whether it is possible to derive p- and s-wave interval velocities as well as densities for the seismic units which create the energy partitioning ratio curves. If the ambitious target of decomposing inversion intercepts into underlying p-wave, s-wave and density functions is found to be too difficult then the focus could be changed to instead attempt to derive the coefficients to the A, B and C to the Shuey (Shuey (1985)) approximation of the Aki and Richards approximation of the Zoeppritz equations (equation 1.12).

$$R_{pp}(\theta) = A + B\sin^2\theta + C(\tan^2\theta - \sin^2\theta) \tag{1.12}$$

Here θ denotes the angle (measured from the vertical) at which the propagating wave strikes a subsurface interface.

1.6.1 Spectral ratio derived methods

In the spectral ratio method the ratio of the spectra of a reference signal at depth z_1 and a target interval at z_2 is taken. The slope of a natural logarithm against frequency plot (m, equations 1.10 and 1.13) can then be used to determine the

quality factor, Q.

$$m = \frac{\Delta z}{2Qc} = \frac{\Delta t}{2Q} \tag{1.13}$$

QVO

The Q-versus-offset (QVO) method developed by Dasgupta and Clark (1998) was developed due to a lack of studies which had, up until that point, successfully produced Q estimates (Raikes and White (1984)). The QVO method was designed to provide accurate measurements quality factor, Q, and hence attenuation, from surface seismic data, which would be of use in improving AVO analysis and well ties as well as increasing the apparent resolution of seismic data at depth through the use of inverse Q deconvolution using accurate Q values.

The amount of intrinsic attenuation a signal is subject to is dependent upon the path length travelled through the attenuative media and the degree of attenuation within the medium. For a CMP gather generated from a wave travelling through a single attenuative layer, the amount to which the signal at each source-receiver offset is attenuated will increase with increasing path length travelled through the attenuative layer. Therefore if the CMP gather is NMO corrected and stacked, the different attenuation effects present at each source-receiver offset will also be stacked making accurate attenuation estimations from a stacked section more difficult.

The QVO method, covered in detail in Dasgupta and Clark (1998) but summarised here, allows the determination of attenuation from prestack data. The first step in the QVO process is to preprocess the CMP data, taking care to preserve true relative amplitudes, and then apply normal move-out (NMO) corrections. The spectra of a window of data around the reflection of interest is taken for each offset in the gather and then the complex spectra is corrected for the effects of NMO stretch. The source wavelet is then removed from the spectra of the reflection of interest, forming a spectral ratio. The spectral ratios are stacked over a few traces to increase stability of the measured Q value and a least squares regression of spectral ratios against frequency taken to form the spectral ratio slopes for each trace. If the traveltime variations are given by the classic

NMO correction equation then the spectral ratio slopes should vary as a function of the offset squared. A second regression of the spectral ratio slopes against offset squared is then taken to determine the zero-offset spectral ratio slope and hence the average source to receiver Q value. Tonn (1991) provides a method of determining interval Q, a much more useful parameter for interpretation, from average source to receiver Q values (equation 1.14).

$$Q_i = \frac{t_n - t_{n-1}}{\frac{t_n}{Q_n} - \frac{t_{n-1}}{Q_{n-1}}} \tag{1.14}$$

Due to negative Q values being obtained from the QVO method, Carter (2003) undertook a critical assessment of the QVO method. It must be noted that negative Q values are possible if interbed multiples interfere to reinforce the downgoing wavefield and partially reverse the effects of apparent attenuation (Odoherty and Anstey (2006)). Carter (2003) found that QVO results can be largely affected by AVO effects and the effects caused by moveout and its subsequent correction. It was also found that the colouring of reflectivity, due to the inclusion of primary events not related to the reflector of interest in the window of data taken to be Fourier transformed, can have potentially large effects on the QVO results. It was also found that QVO results show sudden changes which are correlatable with faults crossing the seismic data. The QVO method was found to be applicable to analysis of saturation and pressure changes in time-lapse data and fracture orientation identification using multi-azimuth data through the analysis of data from the Osberg field and offshore Africa, respectively.

Layer-stripping approach

Behura and Tsvankin (2009) noted that the QVO method required knowledge of the source signature, which is typically unknown. They then offered an alternative method for analysing the attenuation of an interval of arbitrary isotropy and homogeneity, assuming that for a 2D data set that a plane of symmetry in the target layer is the vertical incidence plane and the overburden is laterally homogeneous with a horizontal symmetry plane. The method relies on the layer stripping approach derived in Dewangan and Tsvankin (2006) which involves matching the horizontal slowness measured at the shot point x_1 (figure 1.7) in

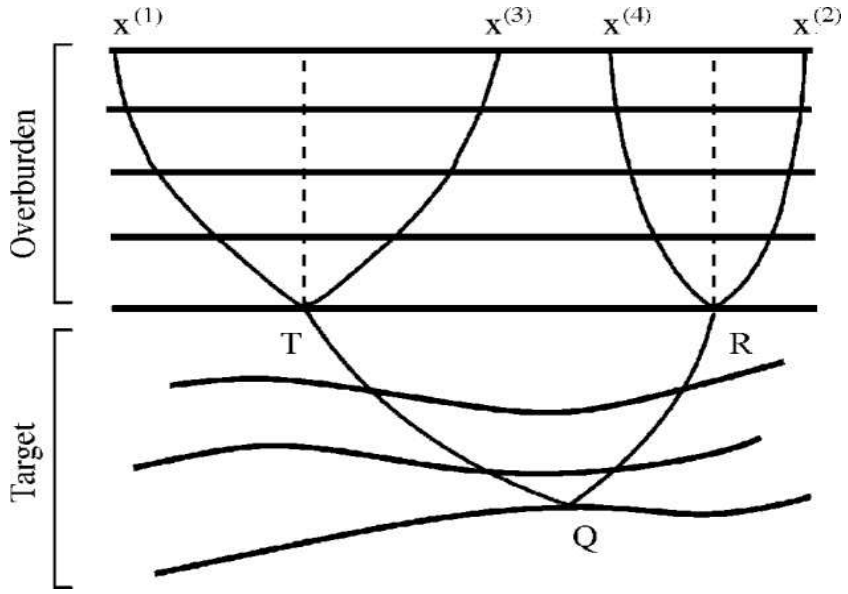

Figure 1.7: 2D diagram of the layer stripping algorithm. Reproduced from Dewangan and Tsvankin (2006).

a common receiver gather at receiver location x_2 to a point in a common shot gather at shot point x_1 which will be found at receiver point x_3. The ray path $x_1 - T - x_3$ shares the same downgoing leg as the target reflection event.

After applying a similar methodology for matching the upgoing leg of the target reflection event, it is then possible to determine the time the raypath has spent within the target interval via equation 1.15.

$$t_{TQR} = t_{x_1TQRx_2} - \frac{1}{2}(t_{x_1Tx_3} + t_{x_4Rx_2}) \tag{1.15}$$

t_{TQR} is the traveltime between points T, Q and R and all other symbols follow a similar logic.

The spectral ratio is then formed from the square of the target reflection event spectra divided by the product of the spectra of the overburden reflections found to share either an upgoing or downgoing leg with the target reflection event (equation 1.16).

$$\ln\left(\frac{|U_{x_1TQRx_2}(\omega)|^2}{|U_{x_1Tx_3}(\omega)||U_{x_4Rx_2}(\omega)|}\right) = \ln(\mathcal{G}) - 2\omega\mathcal{A}t_{TQR} \tag{1.16}$$

Here $\mathcal{G}$ takes account of reflection/transmission coefficients, geometric spreading and source-reciever radiation patterns for all three raypaths and $\mathcal{A}$ is the normalised phase attenuation coefficient.

Along with knowledge of the phase angle for each source-receiver offset it is possible to invert the normalised phase attenuation coefficient for the normalized symmetry-direction attenuation coefficient (which is relatable to the quality factor Q) as well as the attenuation anisotropy parameters introduced in Zhu and Tsvankin (2006).

PSQI

Pre-Stack Q Inversion (PSQI, Reine et al. (2012)) is another spectral ratio derived method of determining attenuation. Similarly to the layer stripping approach of Behura and Tsvankin (2009) and the QVO method of Dasgupta and Clark (1998), the PSQI method can work in the pre-stack domain which is not only useful for deriving attenuation magnitudes but also for analysing how the attenuation changes with propagation angle.

To remove the effects of attenuation in the overburden present in reflections from the top and bottom of the interval of interest, the PSQI method matches events with common horizontal slowness, similar to the layer stripping approach of Behura and Tsvankin (2009). The method described for analysing common horizontal slowness events in Reine et al. (2012) differs from that of the layer stripping approach by working in the $\tau - p$ domain. Integration of amplitudes inherent in the slant-stack operation make $\tau - p$ domain data less sensitive to local noise and static shifts occurring in the data.

Following the method given by van der Baan and Kendall (2002), any point in $\tau - p$ space, for an anisotropic media with transverse isotropy, can be mapped to a point in $t - x$ space if the interval vertical traveltime (τ_{0i}), the interval stacking velocity (v_i) and the anisotropy parameters (ν_i, Alkhalifah and Tsvankin (1995)) are known. Equations 1.18 and 1.19 give the time and offset of any point in $\tau - p$ space given that the $\tau - p$ moveout within an interval (τ_i) is derived via equation

1.17.

$$\tau_i = \tau_{0i}\left(1 - \frac{p^2 v_i^2}{1 - 2\eta_i p^2 v_i^2}\right)^{1/2} \tag{1.17}$$

$$x = \sum \frac{\tau_{0i} p v_i^2}{(1 - 2\eta_i p^2 v_i^2)^2 [1 - p^2 v_i^2 (1 - 2\eta_i p^2 v_i^2)^{-1}]^{1/2}} \tag{1.18}$$

$$t = \tau + \sum \frac{\tau_i p^2 v_i^2}{(1 - 2\eta_i p^2 v_i^2)^2 [1 - p^2 v_i^2 (1 - 2\eta_i p^2 v_i^2)^{-1}]} \tag{1.19}$$

In determining the attenuation factor the PSQI method utilizes a single simultaneous inversion scheme, as opposed to the two back to back inversions used in the QVO method. The natural log of the spectral ratio of the reflections from the top and bottom of the interval of interest (equation 1.20) is a function of the product of the quality factor within the interval, the traveltime within the attenuative media and frequency.

$$\ln\left[\frac{S_2(f)}{S_1(f)}\right] = -\frac{\pi}{Q}\Delta t f + \ln(PG) \tag{1.20}$$

Here P denotes the energy partitioning function, a ratio of reflection amplitudes at common horizontal slowness values multiplied by the transmission coefficients into and out of the region of interest (equation 3.5), and G denotes geometric spreading.

$$P_{ij} = \frac{T_{d,i} T_{u,j} R_j}{R_i} \tag{1.21}$$

Here R_j is the reflection coefficient at the j^{th} relfection interface and $T_{d,j}$ is the transmission coefficient down from the i^{th} interface whilst $T_{u,j}$ is the transmission coefficient upwards from the j^{th} interface. This is shown in figure 1.8.

The linear system of equations given by equation 1.20 can be solved as one inverse problem if the information contained within the data vector and kernel

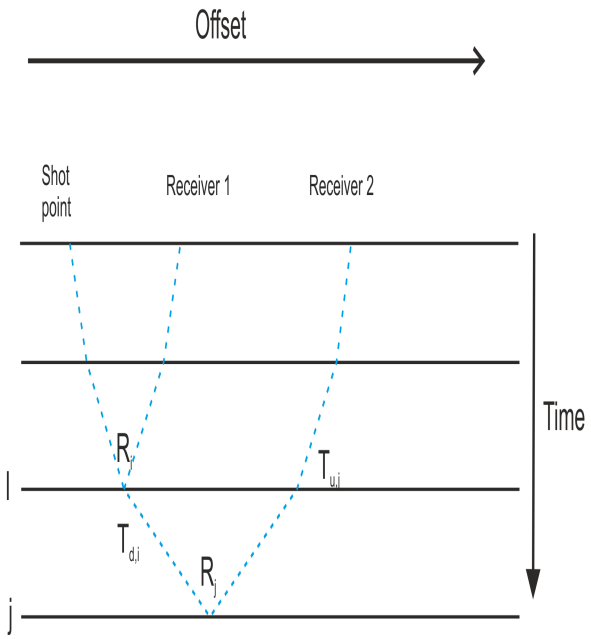

Figure 1.8: Schematic illustration of the transmission coefficients downards (T_d) and upwards (T_u) from an interval and the reflection coefficients at an interface, as described used in equation 3.5 to give the inversion intercepts of the PSQI algorithm.

matrix are ordered in the manner shown in equation 1.22.

$$\begin{pmatrix} d_{11} \\ d_{21} \\ \vdots \\ d_{N1} \\ d_{12} \\ d_{22} \\ d_{N2} \\ \vdots \\ d_{NM} \end{pmatrix} = \begin{pmatrix} \Delta t_1 f_1 & 1 & 0 & \dots & 0 \\ \Delta t_2 f_1 & 0 & 1 & \dots & 0 \\ \vdots & \vdots & \vdots & \ddots & \vdots \\ \Delta t_N f_1 & 0 & 0 & \dots & 1 \\ \Delta t_1 f_2 & 1 & 0 & \dots & 0 \\ \Delta t_2 f_2 & 0 & 1 & \dots & 0 \\ \vdots & \vdots & \vdots & \ddots & \vdots \\ \Delta t_N f_2 & 0 & 0 & \dots & 1 \\ \vdots & \vdots & \vdots & \ddots & \vdots \\ \Delta t_N f_M & 0 & 0 & \dots & 1 \end{pmatrix} \begin{pmatrix} A \\ B_1 \\ B_2 \\ \vdots \\ B_N \end{pmatrix} \tag{1.22}$$

The advantage of this inversion scheme is not only the determination of the

attenuation factor from

$$A = -\frac{\pi}{Q} \tag{1.23}$$

but also, in the absence of geometric spreading, attenuation free energy partitioning information as a function of time difference, and hence angle, is given by

$$B_n = \ln(P_n G_n) \tag{1.24}$$

In the PSQI method the attenuation within the target layer is assumed to be homogeneous and isotropic in the vertical plane and, along with energy partitioning and geometric spreading, is assumed to be frequency independent.

1.7 Structure of this thesis

In this PhD thesis I will first develop a novel time-frequency distribution, called the signal-dependent distribution (SDD), which will be shown, using synthetic, zero-offset and, pre-stack seismic data, to provide more accurate estimates of the spectrum of seismic reflections than a Fourier transform, short-time-Fourier-transform (STFT) or a Stockwell transform. These spectra are then used to estimate attenuation from pre-stack data using the PSQI method.

The PSQI method is then adapted to be able to estimate frequency-dependent $1/Q$ values rather than constant Q values. The frequency-dependence of $1/Q$ within the seismic bandwidth is assumed to have a power-law form but the method for estimating the necessary parameters is simple and could be adapted to any other form of frequency-dependence. This adapted PSQI method is then tested using synthetic data sets before being applied to pre-stack from the Kinnoull field, North Sea.

Attenuation, both frequency-dependent and frequency-independent $1/Q$ and scattering attenuation, is then estimated and analysed for stacked, pre-stack and, vertical seismic profile (VSP) data from the Kinnoull field. The estimated $1/Q$ values from the different data sources are compared with each other as well as centroid frequency maps and average energy maps estimated from the stacked

seismic volume.

Finally, a simplified version of the SDD, the Wigner-Ville distribution (WVD), is used to estimate both frequency-dependent and frequency-independent $1/Q$ (via applying the same modification for the PSQI method to a simple spectral ratio method) from VSP data from 6 wells in the Barents Sea. Scattering attenuation and petrophysical parameters are estimated from wells logs coincident with the VSP data such that intrinsic attenuation can be estimated. The frequency-dependent $1/Q$ values are then fitted with a squirt-flow model in order to assess crack aspect ratio, assuming squirt-flow is the dominant attenuation process.

References

Adam, L., M. Batzle, K. T. Lewallen, and K. van Wijk, 2009, Seismic wave attenuation in carbonates: Journal of Geophysical Research: Solid Earth, **114**, B06208. 11

Alkhalifah, T., and I. Tsvankin, 1995, Velocity analysis for transversely isotropic media: Geophysics, **60**, 1550–1566. 19

Avseth, P., T. Mukerji, and G. Mavko, 2010, Quantitative seismic interpretation: Applying rock physics tools to reduce interpretation risk: Cambridge University Press. 10

Banik, N. C., l. Lerche, and R. T. Shuey, 1985, Stratigraphic filtering, part i: Derivation of the odohertyanstey formula: Geophysics, **50**, 2768–2774. 7

Bath, M., 1974, Spectral analysis in geophysics: Elsevier Scientific Publishing Company, Amsterdam, volume **7** *of* Developments in Solid Earth Geophysic. 13

Behura, J., and I. Tsvankin, 2009, Estimation of interval anisotropic attenuation from reflection data: Geophysics, **74**, A69–A74. 17, 19

Biot, M. A., 1956a, Theory of propagation of elastic waves in a fluid-saturated porous solid. i. low-frequency range: The Journal of the Acoustical Society of America, **28**, 168–178. 4

———, 1956b, Theory of propagation of elastic waves in a fluidsaturated porous solid. ii. higher frequency range: The Journal of the Acoustical Society of America, **28**, 179–191. 4

Birch, F., and D. Bancroft, 1938, Elasticity and internal friction in a long column of granite: Bulletin of the Seismological Society of America, **28**, 243–254. 10, 11

Bowles, F. A., 1997, Observations on attenuation and shear-wave velocity in fine-grained, marine sediments: The Journal of the Acoustical Society of America, **101**, 3385–3397. 13

Bradford, S., J. Yang, and T. Heaton, 2006, Variations in the dynamic properties of structures: The wigner-ville distribution: Presented at the Proceedings of the 8th US National Conference on Earthquake Engineering. 15

Bruckshaw, J. M., and P. C. Mahanta, 1961, The Variation of the Elastic Con-

stants of Rocks with FREQUENCY*: Geophysical Prospecting, **9**, 65–76. 10, 11

Carter, A., 2003, Seismic wave attenuation from surface seismic reflection surveys - an exploration tool?: PhD thesis, University of Leeds. 17

Chapman, M., 2003, Frequency-dependent anisotropy due to meso-scale fractures in the presence of equant porosity: Geophysical Prospecting, **51**, 369–379. 5

Collins, F., and C. C. Lee, 1956, Seismic wave attenuation characteristics from pulse experiments: Geophysics, **21**, 16–40. 10

Dasgupta, R., and R. Clark, 1998, Estimation of q from surface seismic reflection data: Geophysics, **63**, 2120–2128. 13, 16, 19

Dewangan, P., and I. Tsvankin, 2006, Velocity-independent layer stripping of pp and ps reflection traveltimes: Geophysics, **71**, U59–U65. 13, 17

Dvorkin, J., R. NolenHoeksema, and A. Nur, 1994, The squirtflow mechanism: Macroscopic description: Geophysics, **59**, 428–438. 5

Dvorkin, J., and A. Nur, 1993, Dynamic poroelasticity: A unified model with the squirt and the biot mechanisms: Geophysics, **58**, 524–533. 10, 5, 6

Gemant, A., and W. Jackson, 1937, Xciii. the measurement of internal friction in some solid dielectric materials: The London, Edinburgh, and Dublin Philosophical Magazine and Journal of Science, **23**, 960–983. 10, 11

Gurevich, B., M. Brajanovski, R. J. Galvin, T. M. Muller, and J. Toms-Stewart, 2009, P-wave dispersion and attenuation in fractured and porous reservoirs poroelasticity approach: Geophysical Prospecting, **57**, 225–237. 5

Hustedt, B., and R. A. Clark, 1999, Source/receiver array directivity effects on marine seismic attenuation measurements: Geophysical Prospecting, **47**, 1105–1119. 9

Johnston, D. H., M. N. Toksoz, and A. Timur, 1979, Attenuation of seismic waves in dry and saturated rocks: Ii. mechanisms: Geophysics, **44**, 691–711. 10, 3, 5

Jones, T. D., 1986, Pore fluids and frequency-dependent wave propagation in rocks: Geophysics, **51**, 1939–1953. 11, 12

Klimentos, T., and C. McCann, 1990, Relationships among compressional wave attenuation, porosity, clay content, and permeability in sandstones: Geophysics, **55**, 998–1014. 10, 11

Knopoff, L., and G. J. F. MacDonald, 1958, Attenuation of small amplitude stress

waves in solids: Rev. Mod. Phys., **30**, no. 4, 1178–1192. 8

Liner, C. L., 2012, Elements of seismic dispersion: A somewhat practical guide to frequency-dependent phenomena: Society of Exploration Geophysicists. 13

Luh, P., 1993, Wavelet attenuation and bright-spot detection: Offset-Dependent Reflectivity: Theory and Practice of AVO Analysis, 190–198. 10

Mavko, G., and D. Jizba, 1991, Estimating grain-scale fluid effects on velocity dispersion in rocks: Geophysics, **56**, 1940–1949. 11

Mavko, G. M., and A. Nur, 1979, Wave attenuation in partially saturated rocks: Geophysics, **44**, 161–178. 5

Murphy, W. F., 1982a, Effects of partial water saturation on attenuation in massilon sandstone and vycor porous glass: The Journal of the Acoustical Society of America, **71**, 1458–1468. 3

———, 1982b, Effects of partial water saturation on attenuation in massilon sandstone and vycor porous glass: The Journal of the Acoustical Society of America, **71**, 1458–1468. 10

Mller, T. M., B. Gurevich, and M. Lebedev, 2010, Seismic wave attenuation and dispersion resulting from wave-induced flow in porous rocks, a review: Geophysics, **75**, 75A147–75A164. 10, 3, 4

O'Connell, R. J., and B. Budiansky, 1977, Viscoelastic properties of fluid-saturated cracked solids: Journal of Geophysical Research, **82**, 5719–5735. 5

Odoherty, R., and N. Anstey, 2006, Reflections on amplitudes: Geophysical Prospecting, **19**, 430–458. 5, 6, 17

Pandit, B., and D. Tozer, 1970, Anomalous propagation of elastic energy within the moon: Nature, **226**, 335–335. 3

Pevzner, R., T. Mueller, A. Alasbali, R. Galvin, and B. Gurevich, 2014, Seismic attenuation from vsp and well log data - nw shelf australia case study: EAGE Technical Program Extended Abstracts 2014, Th P06 01. 8

Portsmouth, I. R., M. H. Worthington, and C. C. Kerner, 1993, A field study of seismic attenuation in layered sedimentary rocks i. vsp data: Geophysical Journal International, **113**, 124–134. 8

Pride, S. R., and J. G. Berryman, 2003, Linear dynamics of double-porosity dual-permeability materials. i. governing equations and acoustic attenuation: Phys. Rev. E, **68**, no. 3, 036603. 2

Pride, S. R., J. G. Berryman, and J. M. Harris, 2004, Seismic attenuation due to wave-induced flow: Journal of Geophysical Research: Solid Earth, **109**, n/a–n/a. (B01201). 5

Pride, S. R., J. M. Harris, D. L. Johnson, A. Mateeva, K. T. Nihel, R. L. Nowack, J. W. Rector, H. Spetzler, R. Wu, T. Yamomoto, J. G. Berryman, and M. Fehler, 2003, Permeability dependence of seismic amplitudes: The Leading Edge, **22**, 518–525. 2

Raikes, S., and R. White, 1984, Measurements of earth attenuation from downhole and surface seismic recordings*: Geophysical Prospecting, **32**, 892–919. 16

Reine, C., R. Clark, and M. van der Baan, 2012, Robust prestack Q-determination using surface seismic data: Part 1-Method and synthetic examples: Geophysics, **77**, R45–R56. 13, 14, 15, 19

Sams, M., J. Neep, M. Worthington, and M. King, 1997, The measurement of velocity dispersion and frequency-dependent intrinsic attenuation in sedimentary rocks: Geophysics, **62**, 1456–1464. 10, 11, 12, 13

Shapiro, S. A., and H. Zien, 1993, The o'doherty-anstey formula and localization of seismic waves: Geophysics, **58**, 736–740. 7

Shapiro, S. A., H. Zien, and P. Hubral, 1994, A generalized o'doherty-anstey formula for waves in finely layered media: Geophysics, **59**, 1750–1762. 7

Shuey, R., 1985, A simplification of the zoeppritz equations: Geophysics, **50**, 609–614. 15

Stoffa, P., P. Buhl, J. Diebold, and F. Wenzel, 1981, Direct mapping of seismic data to the domain of intercept time and ray parameter2̆014a plane2̆010wave decomposition: Geophysics, **46**, 255–267. 14

Tittmann, B. R., M. Abdel-Gawad, and R. M. Housley, 1972, Elastic velocity and Q factor measurements on Apollo 12, 14, and 15 rocks: Lunar and Planetary Science Conference Proceedings, 2565. 3

Tonn, R., 1991, The determination of the seismic quality factor q from vsp data: A comparison of different computational methods.: Geophysical Prospecting, **39**, 1–27. 2, 13, 17

Van Der Baan, M., 2001, Acoustic wave propagation in one dimensional random media: the wave localization approach: Geophysical Journal International, **145**, 631–646. 7

van der Baan, M., and J. Kendall, 2002, Estimating anisotropy parameters and traveltimes in the τp domain: Geophysics, **67**, 1076–1086. 19

Ville, J., 1958, Theory and application of the notion of complex signal: Technical report, DTIC Document. 15

Wang, Y., 2007, Seismic time-frequency spectral decomposition by matching pursuit: Geophysics, **72**, V13–V20. 15

———, 2008, Seismic inverse q filtering: Wiley-Blackwell. 2

Wang, Z., and A. Nur, 1990, Dispersion analysis of acoustic velocities in rocks: The Journal of the Acoustical Society of America, **87**, 2384–2395. 5

William F. Murphy, I., K. W. Winkler, and R. L. Kleinberg, 1986, Acoustic relaxation in sedimentary rocks: Dependence on grain contacts and fluid saturation: Geophysics, **51**, 757–766. 5

Yoshimoto, K., H. Sato, and M. Ohtake, 1993, Frequency-dependent attenuation of p and s waves in the kanto area, japan, based on the coda-normalization method: Geophysical Journal International, **114**, 165–174. 13

Zhu, Y., and I. Tsvankin, 2006, Plane-wave propagation in attenuative transversely isotropic media: Geophysics, **71**, T17–T30. 19

Zhu, Y., I. Tsvankin, P. Dewangan, and K. Wijk, 2007, Physical modeling and analysis of p-wave attenuation anisotropy in transversely isotropic media: Geophysics, **72**, D1–D7. 9

Ziolkowski, A., J. Underhill, and R. Johnston, 1998, Wavelets, well ties, and the search for subtle stratigraphic traps: Geophysics, **63**, 297–313. 2

Chapter 2

Time-frequency transforms and the Signal-Dependent Distribution (SDD)

2.1 Abstract

We introduce the signal dependent time-frequency distribution (SDD), a time-frequency distribution which allows the user to optimize the trade off between joint time-frequency resolution and suppression of transform artefacts. The SDD, as well as the short-time-Fourier transform (STFT), Stockwell transform and the Fourier transform are analyzed for their ability to estimate the spectrum of a known wavelet used in a tuning wedge model. Next, the SDD as well as a fixed- and, variable-window transform are used to estimate spectra from a zero-offset synthetic seismogram. Attenuation is estimated from the associated spectral ratio curves, and the accuracy of the results is compared. The synthetic consisted of six pairs of strong reflections, based on real well log data, with a modeled intrinsic attenuation value of $1000/Q = 20$. The SDD was the only time-frequency transform found to produce spectra which estimated consistent attenuation values, with an average of $1000/Q$=26$\pm$2; results from the fixed and variable window transforms were 24$\pm$17 and 39$\pm$10, respectively. Finally, all three time-frequency transforms were used in a pre-stack attenuation estimation method (the PSQI

algorithm) applied to a gather from a North Sea seismic data set, to estimate attenuation between 9 different strong reflections. In this case the SDD produced spectra more consistent with the constant-Q model of attenuation assumed in the pre-stack attenuation estimation algorithm: the average L1 residual of the spectral ratio surfaces from the theoretical constant-Q expectation for the SDD, STFT and Stockwell transform were 0.12, 0.21 and 0.33 respectively. Based on the results shown, the SDD is a time-frequency distribution which can provide more accurate and precise estimations of the amplitude spectrum of a reflection, due to a higher attainable time-frequency resolution.

2.2 Introduction

Time-frequency transforms show the time-varying nature of the frequency content of a time-series, and have been used as a seismic attribute that can add further knowledge and value to the interpretation of seismic data (Castagna et al. (2003) and Hall (2006a)). Zhang et al. (2009) and Zhao et al. (2006) have shown the various applications that time-frequency transforms can have in analyzing various seismic dataset types for various different attributes. Time-frequency transforms have also been used for spectral based attenuation estimation schemes (Reine et al. (2009)).

Although time-frequency transforms are used in a qualitative sense, for example, to detect low frequency shadows associated with hydrocarbons (Castagna et al. (2003)), using time-frequency transforms to estimate spectra in the spectral ratio method (Tonn (1991), Bath (1974)) of attenuation estimation is necessarily quantitative. Any spectra estimated from a time-frequency gather must therefore be as accurate as possible, because any bias in estimating the spectrum of a signal will be propagated through to the estimated attenuation quality factor value, Q.

Methods to form a time-frequency representation of a signal include but are not limited to: fixed window transformations such as the short-time Fourier transform (STFT) (Koenig et al. (1946)), variable window transforms such as the Stockwell transform (Stockwell et al. (1996)), decomposition of seismic traces using a dictionary of wavelets such as the matching pursuit method (Wang (2007)), and quadratic time-frequency transforms which analyze the instantaneous auto-

correlation function of the signal (Boashash (2003)).

Reine et al. (2012) show an example of using time-frequency distributions to estimate the spectra of reflections which they then used in a modified spectral ratio method, the pre-stack Q inversion (PSQI) method. The PSQI method uses gathers to produce spectral ratio surfaces which are a function of frequency and time spent within an interval of interest (Δt) rather than just frequency and shall be used in this study.

The purpose of this study is to estimate the accuracy and precision in spectra estimated through three qualitatively different time-frequency transform methods, and determine which of them provides the best estimate of the true spectrum of individual reflections, that will then be used in a spectral ratio based attenuation estimation scheme similar to that of Reine et al. (2012). To this end, a new time-frequency transform is introduced which is proposed to give better estimates of the time-frequency content of individual reflections which will then lead to more accurate spectra and more stable estimates of attenuation.

We have limited ourselves to studying only the short-time-Fourier transform (or its square modulus, the spectrogram), the Stockwell transform, and the new time-frequency distribution, which is a quadratic time-frequency transform whose window function is built based on the dynamics of the signal and will be referred to as the signal-dependent distribution (SDD).

First, we will briefly review the fixed- and variable-window transforms. Quadratic time-frequency distributions will then be introduced, the proposed signal-dependent distribution (SDD) outlined and an example of how to implement the SDD given. We will then briefly cover estimating spectra from time-frequency panels. The performance of the newly proposed SDD in estimating the spectrum of a Ricker wavelet in a wedge model will be assessed as well as the ability of the SDD to recover the input attenuation in a 1-D synthetic, zero-offset seismic reflection trace. Finally, the SDD, STFT and Stockwell transform will be applied in the process of estimating attenuation in a pre-stack seismic gather over a North Sea oil field. The estimated spectral ratio surfaces will then be compared to best fit models and the residuals analysed in order to ascertain which time-frequency transform provided the most accurate spectra.

2.3 Time-frequency transforms

2.3.1 Short-time Fourier transform

The Short-time Fourier transform (STFT) is a method of estimating the time-frequency distribution of a signal by Fourier transforming a series of small windows of data, each of which have set durations in time but are centered at consecutively increasing times. Through the application of a window function to the time series, the amount of information to be Fourier transformed is reduced and therefore the spectral resolution will decrease.

Gabor (1946) outlined the consequences of analyzing the spectrum of small windows of data in terms of a trade-off between time resolution and frequency resolution. If a small window is applied to a time series prior to a Fourier transform then time resolution is good, as the estimated spectrum must be due to data within the window, but the frequency resolution suffers due to the reduced amount of information. Conversely if a large window is applied to a time series then the spectral resolution is good but the time resolution suffers. This is known as the Gabor uncertainty principle (Gabor (1946)) and takes the form

$$\Delta t \Delta f \geq \frac{1}{4\pi} \tag{2.1}$$

Where Δt and Δf are defined by Gabor (1946) as "$\sqrt{2\pi}$ times the r.m.s. deviation of the signal from the mean epoch time" and "$\sqrt{2\pi}$ times the r.m.s. deviation from f [the mean frequency]".

2.3.2 Variable window transforms

Variable window transforms, such as the Stockwell transform (Stockwell et al. (1996)), attempt to optimise the trade-off between good time resolution and good frequency resolution imposed by the Gabor transform. To do so, variable window transforms analyse different lengths of a time series for different frequencies. This is most readily understood in terms of *logons* (Gabor (1946), Hall (2006b)).

Logons (figure 2.1) describe the smallest region that is resolvable in the time-frequency domain due to the size of window applied to a time series prior to

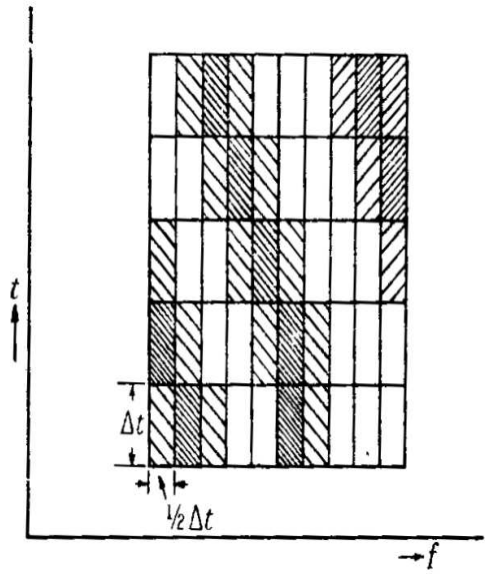

Figure 2.1: Representation of a signal in terms of logons. Taken from Gabor (1946).

transformation into the time-frequency domain. Hall (2006b) shows that the logons of a STFT are constant, due to the application of a window of fixed length to the time series, and that the logons of a variable window transform are of different sizes for different frequencies. In general, variable window transforms will apply larger windows to the time series to analyse lower frequencies; this results in good frequency resolution and poor time resolution at low frequencies and poor frequency resolution with good time resolution at high frequencies.

In terms of attenuation estimation, the larger the bandwidth of usable frequencies, the more stable the inversion for attenuation due to a larger set of data points. Low frequencies can also be helpful in estimating frequency-dependent seismic attenuation quality factors, $Q(f)$, due to a greater change in Q at lower frequencies (for instance Q will change more from 5Hz to 10Hz than it will for 10Hz to 15Hz) for Q modelled as a powerlaw with exponent less than 1.

A main advantage of the Stockwell transform over other variable window time-frequency transforms, such as the continuous wavelet transform (CWT, Daubechies (1990)) is its simplicity. The CWT provides a time-scale images rather than a time-frequency image and the scale parameter axis has to then be transformed into a frequency axis, whereas the Stockwell transform provides a

time-frequency image. Nevertheless, the Stockwell transform and CWT are very similar, as outlined by Ventosa et al. (2008).

Although the Stockwell transform is more closely related to the CWT than the STFT, it can be thought of as a STFT with a Gaussian window whose width is frequency-dependent.

$$S(\tau, f) = \int_{-\infty}^{\infty} h(t) \frac{|f|}{\sqrt{2\pi}} e^{-\frac{(t-\tau)^2 f^2}{2}} e^{-i2\pi f t} dt \tag{2.2}$$

Here, $h(t)$ is a signal and all other symbols have their usual meanings.

2.3.3 Quadratic time-frequency transforms and the SDD

Introduction to Quadratic time-frequency transforms

For a signal, $s(t)$, the quadratic time-frequency transform of $s(t)$ can be fully described by the equation

$$\rho(t, f) = \mathcal{F}_{\tau \to f}\{J(t, \tau) *_t K_z(t, \tau)\} \tag{2.3}$$

Here $\rho(t, f)$ is the time-frequency energy distribution, $\mathcal{F}_{\tau \to f}$ denotes the Fourier transform over the time lag variable, τ, to frequency, f. $*_t$ denotes a convolution over the time variable, $J(t, \tau)$ is the time-lag kernel and $K_z(t, \tau)$ is the instantaneous autocorrelation function (hereafter IAF) defined by

$$K_z(t, \tau) = z(t + \frac{\tau}{2}) z^*(t - \frac{\tau}{2}) \tag{2.4}$$

Here $z(t)$ is the complex signal (Taner et al. (1979)) and $z^*(t)$ is the complex conjugate of $z(t)$ which is calculated from the signal, $s(t)$.

$$z(t) = s(t) + i\mathcal{H}(s(t)) \tag{2.5}$$

Here, $\mathcal{H}$ denotes a Hilbert transform. In equation 2.3, only the IAF contains information about the signal and $J(t, \tau)$ is any filter function applied to the IAF. Any quadratic time-frequency transform can be defined by its time lag kernel, $J(t, \tau)$, which describes the filter applied to the IAF.

In equation 2.3, the time-lag kernel is convolved in time with the IAF, which

is equivalent to a multiplication in the frequency domain. The subject of the Fourier transform in equation 2.3 can also be Fourier transformed along the time axis to convert the convolution operation into a multiplication.

$$\rho(t, f) = \mathcal{F}_{\tau \to f} \mathcal{F}^{-1}_{\nu \to t} \{ j(\nu, \tau) A_z(\nu, \tau) \} \tag{2.6}$$

Here, $A_z(\nu, \tau)$ is the ambiguity function (the representation of the IAF in the Doppler-frequency (ν)/time-lag domain, hereafter the ambiguity plane), so named as it has dimensions of frequency and time but is not a time-frequency representation of the signal (Boashash (2003)). $j(\nu, \tau)$ is the representation of the time-lag kernel in the ambiguity plane. ν is the Fourier transform of the time variable and is referred to as the Doppler frequency, in analogy with time-lag.

The time-lag kernel, $J(t, \tau)$, is a filter to be applied to the IAF which is represented by a windowing function in the ambiguity plane. In the ambiguity plane, autocorrelation terms will lie in a region around the origin defined by the time extent and frequency bandwidth of the wavelet. The window function $j(\nu, \tau)$ should therefore be centered on the origin. The extent of the window in the time-lag and Doppler frequency axes should be as large as possible to retain as much energy localization as possible.

The IAF will contain all autocorrelation terms (hereafter auto-terms) but will also contain cross-correlation terms (hereafter cross-terms), which are the cross-correlation of one component of the signal with another. All auto-terms will lie along the zero time-lag axis whereas cross-terms lie off the zero time-lag axis. The inclusion of cross-terms in the Fourier transform in equation 2.3 generates energy located at a time half-way between every pair of interfering wavelets in the time-frequency gather. It is these cross terms which produce transform artefacts. The time-lag kernel is a filter applied to the IAF to remove cross-term energy and keep auto-term energy.

The Wigner-Ville distribution (Ville (1958), hereafter WVD) is the prototypical quadratic time-frequency transform and can be defined by a time-lag kernel, $G(t, \tau)$, equal to unity. The WVD is formed by using equation 2.3 with $G(t, \tau)$ set equal to 1, and thus in forming the WVD, no windowing function is used. This means that the WVD can have the time resolution equal to twice the original

time sampling as well as the spectral resolution expected from a Fourier transform across the entire original time series. The WVD has exceptional time-frequency resolution, but the cost of this resolution is the presence of transform artefacts in the WVD. Quadratic time-frequency representations of the signal therefore do not suffer from the time-resolution/frequency-resolution trade-off of the Gabor uncertainty principle, but instead suffer from a trade-off between a joint time-frequency resolution and the presence of transform artefacts (Boashash (2003)). They accomplish this by transforming the instantaneous autocorrelation function, which must obey the Gabor uncertainty principle, but itself is a transform of the signal and not the signal itself.

The signal-dependent distribution (SDD)

To remove cross-term energy it is necessary to apply a filter to the IAF in the form of the time-lag kernel, $G(t, \tau)$. This filter is defined and applied in the ambiguity plane (equation 2.6) by selecting a window function that only keeps energy centered around the origin of the ambiguity plane.

As wavelets in a seismic trace become closer to one another in time it is necessary to apply greater smoothing to the IAF through the time-lag kernel, via a smaller window in the ambiguity plane, to reduce cross-term artefacts in the subsequent time-frequency gather. This reduces the localization of the energy content of the signal in the time-frequency domain and would also occur with fixed- and variable-window transforms in order to reduce spectral perturbations.

There exist many different time-frequency transforms which vary only in the mathematical form of the time-lag kernel. Rather than using a fixed definition of the windowing function, we propose that it is advantageous to determine a window function in the ambiguity plane based on the form of the ambiguity function of the signal. Although requiring more user input, in this way the trade-off between joint time-frequency resolution and suppression of cross-term energy can be optimized. Here, the method of interactively selecting a window function based on the ambiguity plane response of a time series is termed the signal-dependent distribution or SDD for short.

The following is a step-by-step guide to applying the SDD

1. Calculate the complex seismic trace, $z(t)$, from the seismic trace, $s(t)$, using equation 2.5.

2. Form the Instantaneous auto-correlation function (IAF), $K_z(t, \tau)$, from the complex signal via equation 2.4.

3. Transform the IAF into the ambiguity plane response, $A_z(\nu, \tau)$, by Fourier transforming over the time dimension.

4. Design a window, $g(\nu, \tau)$, to keep coherent energy seen around the origin of the ambiguity plane response of the IAF.

5. Form the SDD time-frequency panel via equation 2.6, the calculated ambiguity plane response of the IAF, $A_z(\nu, \tau)$, and your designed window function, $g(\nu, \tau)$.

Example application of SDD

Figure 2.2b shows the IAF of a seismic trace containing two zero-phase 50Hz Ricker wavelets centered at 0.512s and 1.536s and a windowed 250Hz sine wave windowed between 0.4s and 0.7s, shown in figure 2.2a. Figure 2.2b is produced from figure 2.2a via steps 1 and 2 in the SDD workflow. As expected, two high amplitude events exist at 0s time lag and 0.512s and 1.536s respectively, which correspond to the auto-terms, i.e the instantaneous autocorrelation of one wavelet with itself. Two other events exist at 1.024s time and $\pm$1.024s time-lag which correspond to the cross-terms, i.e. the instantaneous auto-correlation of one wavelet with a separate wavelet. The time lag of the cross-terms is 1.024s, as this is the time separation between the two wavelets, and they are at 1.024s along the time axis as this corresponds to the mid-point between the two events in time.

The IAF is next transformed into the ambiguity plane by a Fourier transform along the time axis, step 3 in the SDD workflow. This ambiguity plane response of the signal is shown in figure 2.2c. The cross-terms can then be muted out from the ambiguity plane representation of the signal by selection of an appropriate window (black box in figure 2.2c) centered on the origin of the ambiguity plane, step 4 in the SDD workflow. The muted ambiguity plane response is then transformed

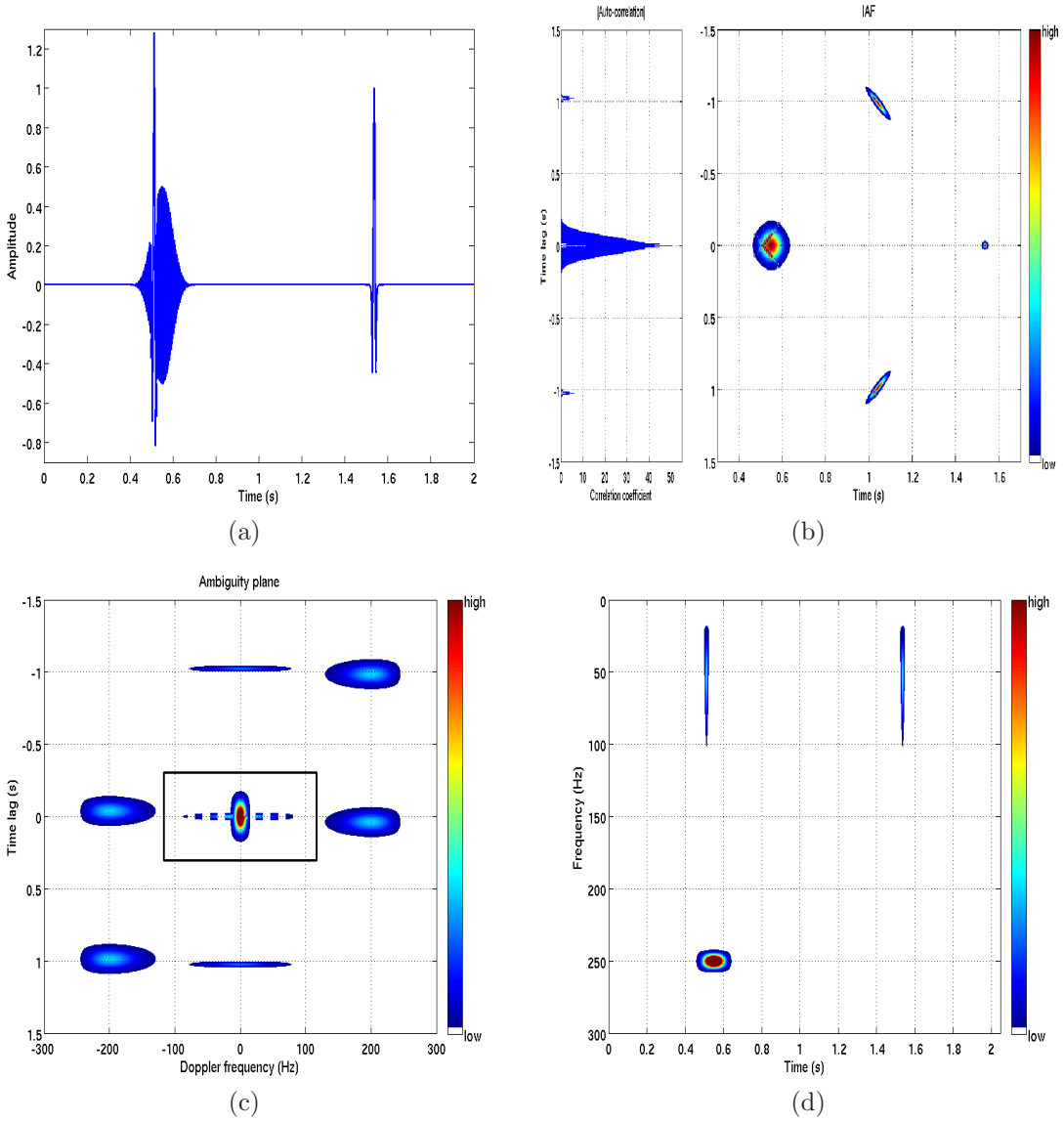

Figure 2.2: a.) A synthetic trace with 2x50Hz Ricker wavelets located at 512ms and 1536ms along with a 250Hz sine windowed sine wave between 0.4s and 0.7s. b.) The corresponding absolute value of the IAF and auto-correlation. c.) The ambiguity plane response along with the outline of the window (black box) then applied to it. d.) The SDD time-frequency representation of the signal.

back into the time-frequency domain (figure 2.2d) via equation 2.6, step 5 in the SDD workflow. Further examples of ambiguity plane window functions are given in figures 2.13 and 2.15.

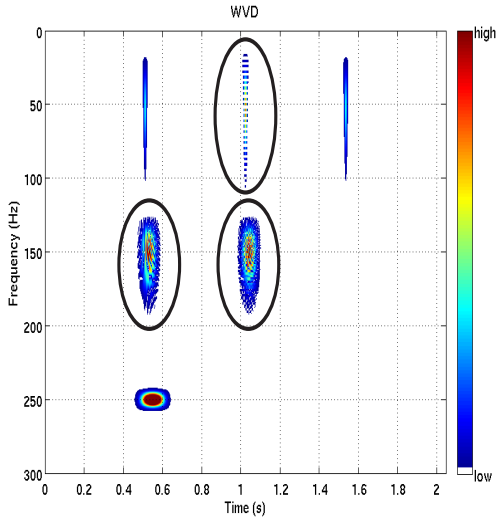

Figure 2.3: Wigner-Ville distribution of the signal given in figure 2.2a. Interference between different time and frequency components are highlighted with black ellipses.

The cross-terms present in the IAF of the signal at 1.024s and -1.024s time lag appear at the same time, 1.024s. If a transformation of the IAF directly into the time-frequency domain (figure 2.3), via a Fourier transform along the time-lag axis, was taken, then the energy at $\pm$1.024s would create a notched frequency response at 1.024s in the time-frequency panel, where there is no energy in the signal. In this case, we could have easily muted the IAF rather than transforming into the ambiguity plane and applying a window function there, but this would not have removed the interference occurring half way between the Ricker wavelet at 0.512s and the 250Hz sine wave (highlighted by a black ellipse at 150Hz, 0.5s), i.e. interference between different frequency components. This interference would not be visible in the IAF but would be visible in the ambiguity plane. This is why windowing is performed in the ambiguity plane rather than applying a window function directly onto the IAF.

The integration of a quadratic time-frequency distribution along each dimension must obey Gabor's uncertainty principle (equation 2.1), but Gabor's un-

certainty principle does not apply to any region of a quadratic time-frequency distribution.

Whereas logons can be used to describe the time-frequency resolution of fixed- and variable-window transforms, it is non-trivial to define a time-frequency resolution for quadratic time-frequency transforms. de Bruijn (1973) and Flandrin (1999) propose time-frequency resolution measures which only apply to the Wigner-Ville distribution (WVD) and other specific Cohen class distributions, but does not apply to the SDD that will be described here.

Linear FM signals (chirps) - A further example of the SDD in action.

As has been previously mentioned, the goal of a time-frequency transform is to assess the time varying frequency content of a signal. It is therefore prudent, when investigating time-frequency transforms, to assess the performance of each time-frequency transform on a signal whose frequency content changes over time. An example of such a signal is the linear FM, or chirp, signal. The linear FM signal is a sinusoidal wave whose frequency changes linearly as a function of time. An example of the linear FM signal in exploration seismology is linear vibrator sweep from a vibroseis source. In the case of a vibroseis source, the autocorrelation of the vibroseis sweep is taken to collapse the sweep to a wavelet, known as a Klauder wavelet (Ryan (1994)).

In order to test the joint time-frequency resolution of the time-frequency transforms, a test signal consisting of three superimposed linear chirps is created. The test signal (figure 2.4) contains three linear FM signals whose central frequency changes from 10Hz, 20Hz and 30Hz respectively at a rate of 50Hz/s over 2.047s. By superimposing three linear FM signals, I can test the ability of each transform to not only accurately localise the energy in both time and frequency, but to also handle multiple frequency components at a signal time instant.

Figure 2.5 contains the time-frequency transforms of the test signal (figure 2.4) using the SDD, spectrogram, Stockwell transform and reassigned spectrogram. The reassigned spectrogram is included in this analysis as it can provide a much higher time-frequency resolution than the standard spectrogram. The reassigned spectrogram differs from the spectrogram in that once a Fourier transform of a

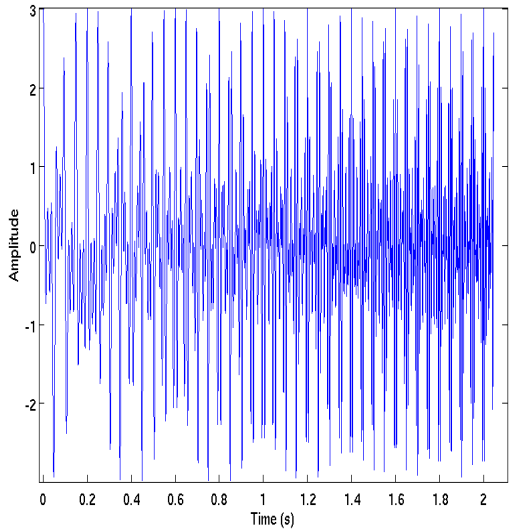

Figure 2.4: Test linear FM signal comprising of three linear FM signals defined by a frequnecy at time 0 of 10Hz, 20Hz and 30Hz respectively and each having a change of frequency of 50Hz/s.

window of data is taken, the resulting spectrum is placed at the centre of gravity of the window of data rather than the geometrical centre of the window.

The three linear FM signals have been recovered in each of the time-frequency transforms in figure 2.5. The amplitude of each component of the signal is equal and constant through time, which is represented in the SDD and spectrogram. The amplitude of the components of the test signal in the Stockwell transform increase with increasing frequency of the signal (a proxy for time in this signal). The variation in amplitude of the signal with time given by the Stockwell transform is a result of the variable windows used in estimating different frequencies in the signal, this lends more weight to high frequencies which are analysed with smaller windows.

The three linear FM signals which comprise the test signal are, at a given time instant, monochromatic (i.e. of a set frequency). Similarly, at a given frequency, there should only exist energy at discrete time instants. To asses the resolution in time and in frequency, a slice down the frequency axis is taken at 499ms and a slice along the time axis is taken at 80Hz, the corresponding plots are shown in figure 2.6. Ideally, with continuous data, the only energy present should exist at

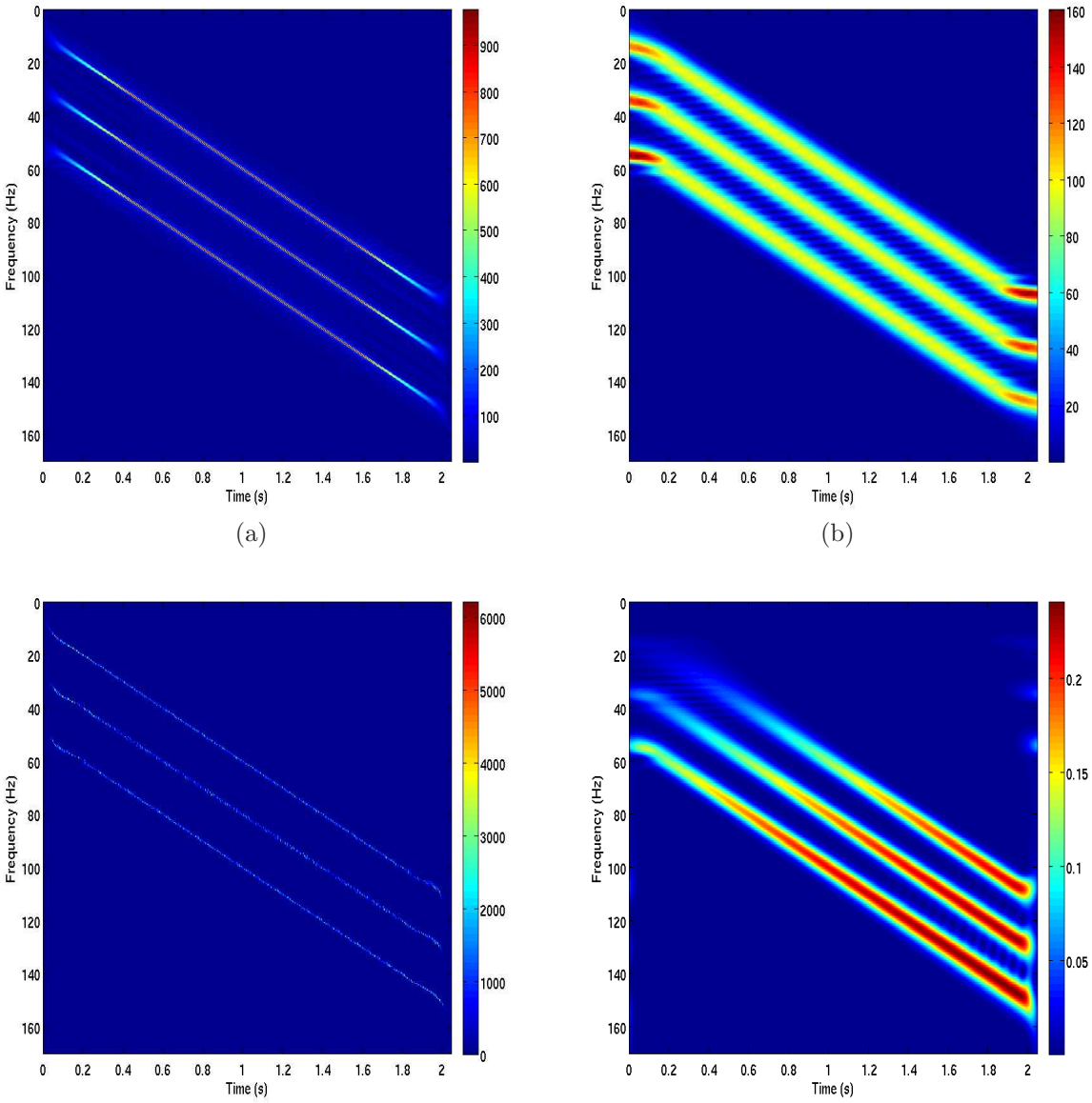

Figure 2.5: Time-frequency transforms of the test signal in figure 2.4 by the SDD (a), spectrogram (b), reassigned spectrogram (c) and Stockwell transform (d).

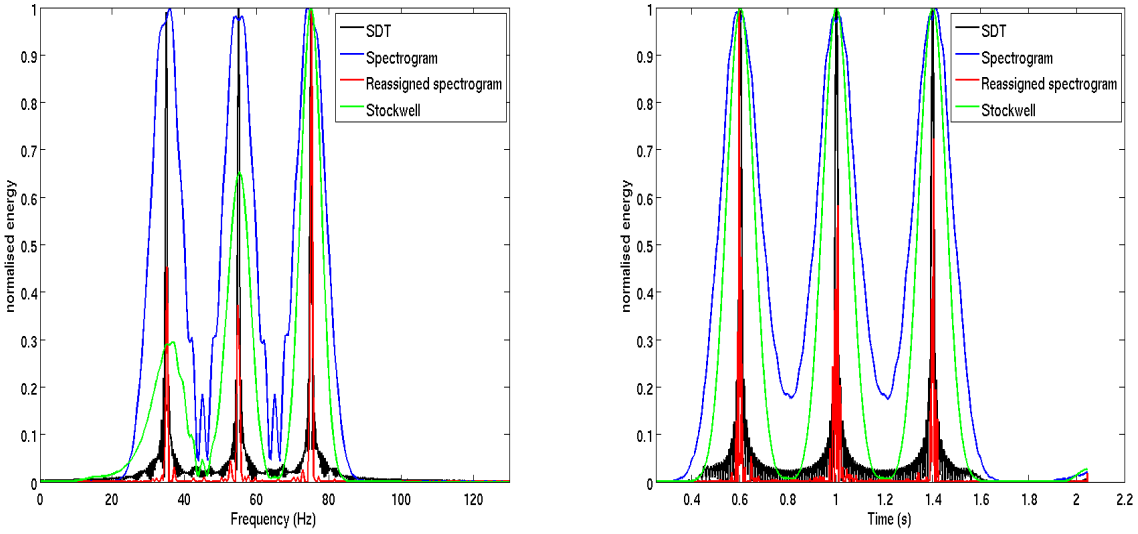

(a) (b)

Figure 2.6: Amplitude spectrum at 499ms (a) along with the amplitude at each time instant at 80Hz (b) of each time-frequency transform shown in figure 2.4.

34.95Hz, 54.95Hz and 74.95Hz in the amplitude spectrum and energy should only exist at 06.s, 1s and 1.4s in the frequency slice at 80Hz. Realistically, each time-frequency transform is subject to limitations on the time-frequency resolution in can attain, this limited resolution will determine how narrow a peak, and hence closer to the theoretical result, each time-frequency transform will estimate. The half-width of the peak is measured at 1/e of the peak amplitude and results are summarised in table 2.1, where smaller widths denote more localised energy in time of frequency.

Table 2.1 highlights the increase in both time and frequency resolution of the SDD over fixed and variable window time-frequency transforms. The large range of frequency peak widths for the Stockwell transform can be attributed tp the variable window sizes used, for example, at low frequencies the half-width of the peak is 6Hz, whereas at high frequencies this half-width reduces to 4Hz, due to a smaller analysis window used at high frequencies.

The reassigned spectrogram also shows an improvement in both time and frequency resolution when compared to the standard spectrogram. However, by

Table 2.1: Table of half-widths of frequency and time slices at 499ms adn 80Hz respectively. The half-wdith is defined as half the width of the peak, including any side lobe energy present, at 1/e of the maximum amplitude of the peak. The avergage for all three peaks shown in figure 2.6 is shown as well as the range in widths.

Transform method	half-width in frequency (Hz)	range in frequency (Hz)	half-width in time (s)	range in time (s)
Stockwell	4.85	2.05	0.078	0
spectrogram	5.69	0.16	0.124	0.011
SDD	0.37	0.05	0.008	0
reassigned spectrogram	0.42	0.2	0.08	0.01

placing the energy estimated in the sliding window function at the centre of gravity, this causes the spectrum of the signal at different times to be superimposed and interfere. This interference can be seen as a lack of coherency in the time-frequency transform of the test signal (figure 2.5) and also in figure 2.7, which is the estimated spectrum of Ricker wavelet from a reassigned spectrogram time-frequency transform (analogous to figure 2.10).

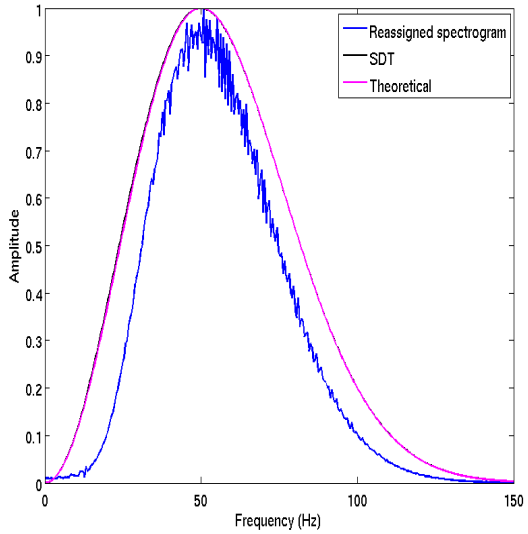

Figure 2.7: Amplitude spectrum of a Ricker wavelet estimated from a reassigned spectrogram time-frequency transform, analogous to figure 2.10.

Although the SDD out performs the other time-frequency transforms tested,

in terms of both time and frequency resolution as well as coherency of the signal in the time-frequency domain, it still suffers from cross-term artefacts. To avoid cross-term interference, the ambiguity plane response of the signal is windowed (figure 2.8) to keep all coherent energy around 0Hz Doppler frequency and 0s time-lag. The windowing problem is such that either remnant cross-term energy is left in the ambiguity plane or a small enough window is applied such that Gibb's phenomenon is introduced into the time-frequency transform. It is hard to distinguish between these two forms of "noise" as the cross-term interference occurs at a rate dependent upon the time- (or frequency-) separation of the different components in a signal, and will appear as ringing energy, similar to that of the Gibb's phenomenon. The effect of this is to essentially add a 20dB noise floor to the spectrum estimated in figure 2.6.

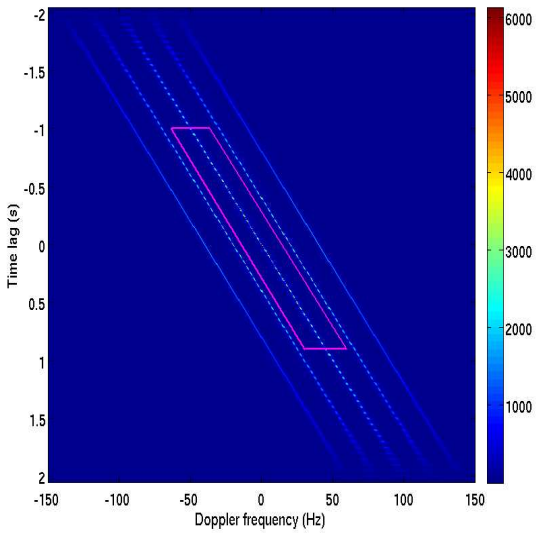

Figure 2.8: Ambiguity plane response of the test signal in figure 2.4. Also shown is the outline of the window function applied to the ambiguity function in the SDD.

2.4 Estimating spectra from time-frequency transforms

It is perhaps enticing to try to extract amplitude spectra from a time-frequency representation of a signal, as it may be possible to increase frequency resolution over a standard Fourier transform when analyzing small data segments. There are two main ways to do so: the first is to integrate over the time axis in a small region encompassing the energy of the signal which is of interest. The second method is to take the amplitude at a single discrete time instant for each discrete frequency. The latter approach would only provide a good estimate of the true spectrum of a wavelet if the wavelet has a time-frequency response that does not vary in time over the length of the wavelet. Figure 2.9 is the time-frequency response of a 50Hz Ricker wavelet at 0.5s and highlights the fact that the Ricker wavelet does not fulfill this criterion. The maximum envelope of the wavelet is used as the centre of the integration window, and is also used the time instant at which to extract amplitudes to form a spectrum.

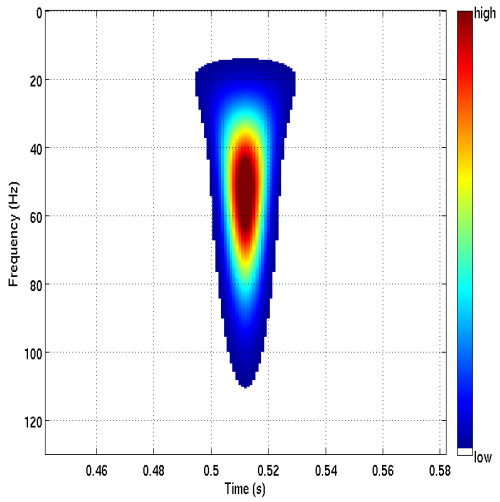

Figure 2.9: Time-frequency response of a trace containing only a single 50Hz Ricker wavelet at 0.5s. Note the asymmetry in the time-frequency response.

Figure 2.10a shows the spectrum estimated by integrating over a 600ms window, centered at 512ms, of the time-frequency response of a 50Hz Ricker wavelet

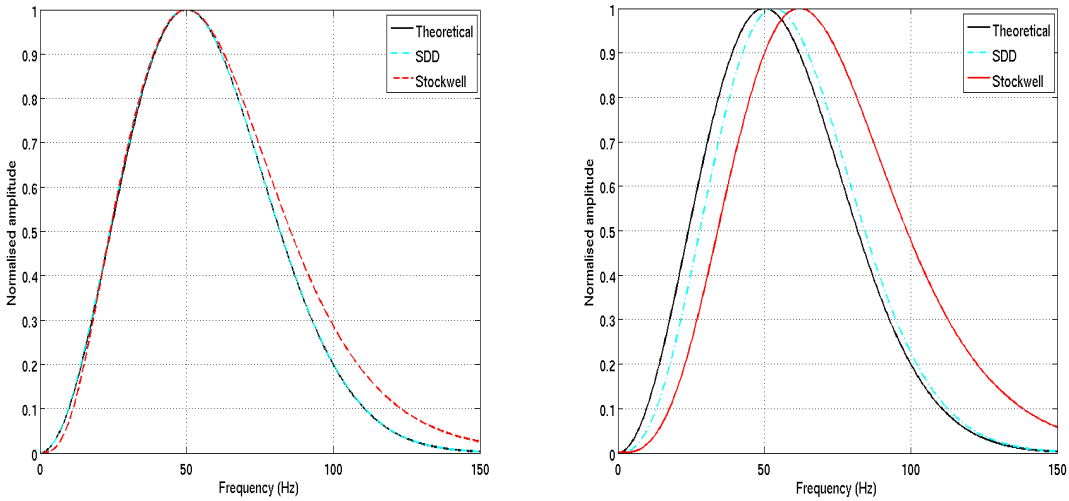

(a) (b)

Figure 2.10: Spectrum of a Ricker wavelet estimated by integration of a 600ms time window (a) (note that the estimated spectrum from SDD lies on top of the expected spectrum and the two cannot be visually separated) and the spectrum of a Ricker wavelet estimated by taking a slice along the time-frequency representation of the signal (b).

formed via the SDD and the Stockwell transform (note that the estimated spectrum from the SDD is visually indiscernible from the expected spectrum). Figure 2.10b gives the spectrum estimated by taking the amplitudes at each discrete frequency at the discrete time instant 512ms. By taking a slice of the time-frequency domain response of the signal, the amplitude of high frequency components has been overestimated, because the energy at higher frequencies is more concentrated towards the centre of a Ricker wavelet compared to amplitudes at lower frequencies (figure 2.9). A Ricker wavelet has a time-frequency response which is only symmetric in time and not in frequency.

2.5 Wedge model

Although the spectral interference caused by closely spaced reflectors has been the subject of much study (Liner (2012)), and used to highlight thin bed tuning

(Sinha et al. (2003)), it is the aim of this paper to outline a method for accurately estimating the spectrum of a wave for use in seismic attenuation studies. In seismic data, it is often the case that strong reflectors may be closely spaced and thus an analysis of how to estimate the spectrum of a reflection accurately in this scenario is of interest. The SDD described in section 2.3.3, as well as the STFT, Stockwell transform and a Fourier transform, are applied to a wedge model consisting of two 50Hz Ricker wavelets which are centered between 0s and 0.1s apart on seismic traces with a 1ms time sample.

The spectrum of the wavelet at 100ms is estimated for each trace for each of the time-frequency transforms and the Fourier transform. The length of the integration window in the time-frequency domain is set to 31ms and is centered at 0.1s. An integration window of 31ms is used as this is equivalent to twice the wavelet breadth of a 50Hz Ricker wavelet (Ryan (1994)). The Fourier transform is carried out on the data segment 100ms±1 wavelet breadth. A wavelet breadth is defined as $\sqrt{6}/\pi f$ where f is the dominant frequency of the wavelet.

Figure 2.11 shows the wedge model used in this test (created with a 1ms sample interval), along with a measure of the accuracy of the estimated spectra: the normalized L1-norm between the estimated spectrum at each trace in the wedge model and the known spectrum of a 50Hz Ricker wavelet. In Figure 2.11, the spectrum of the wavelet extracted from the time-frequency representation of the signal formed via the SDD has a lower residual, over more time separation values, than wavelets formed from the other methods.

For all methods, there is a peak in the normalized L1 residual values at 0.01s time separation, and to a lesser extent a peak near 0.03s time separation. For every method in figure 2.11 the highest residual values occur in the range 0.003s to 0.05s time separation. Both of those characteristics can be explained by notch theory (Liner (2012)), which states that a trace containing two spikes at time, Δt, apart will cause notches at frequencies f_n in the spectrum on that trace according to

$$\begin{aligned} f_n &= \frac{1+2n}{2\Delta t} \\ n &= 0, 1, 2... \end{aligned} \tag{2.7}$$

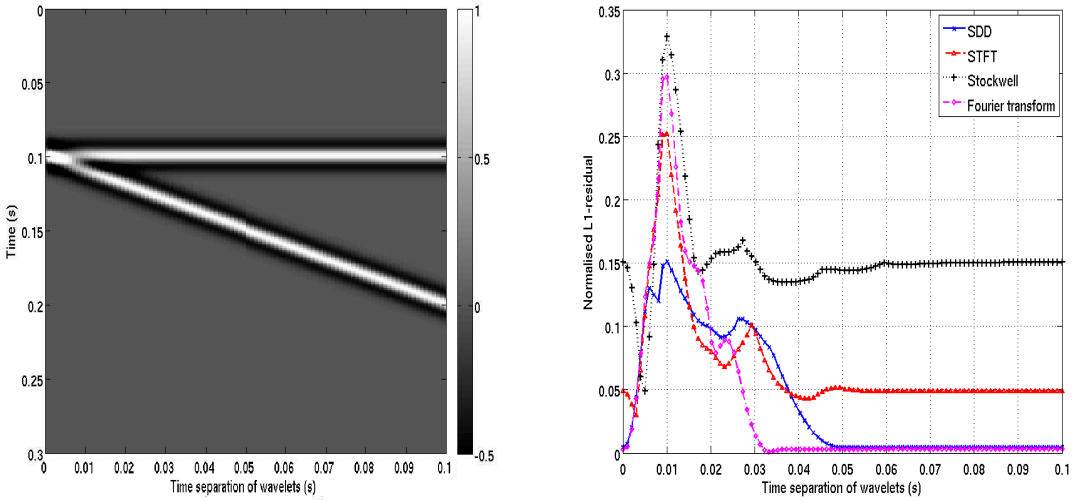

(a) (b)

Figure 2.11: a.) Wedge model of 2 converging 50Hz Ricker wavelets. b.) normalised L1-norm between the estimated spectrum of the wavelet at 100ms in (a) and the known spectrum of the input wavelet.

To cause notches in the spectrum at frequencies used to form the residual seen in figure 2.11b, between 10Hz to 150Hz, the time separation of the two wavelets would be between 0.0033s and 0.05s, according to equation 2.7 with $n = 0$, which explains the general rise in residual values in this time separation range. The frequency notch should have the largest impact on the residual when it occurs at the same frequency as the peak energy of the wavelet, 50Hz, as the notch will remove the largest amount of energy from the spectrum. This occurs when the time separation between the two wavelets is 0.1s. Similarly, the second notch (n=1) occurs at 50Hz when the time separation between the wavelets is 0.03s. The frequency notching coinciding with the peak energy of the estimated wavelet explains the peaks in the distribution of residual values with time separation. The values calculated here for the location of frequency notches assumes two spikes rather than two wavelets, so some spread around the peaks is to be expected.

Although the aim of using small windows of data is to separate out different wavelets, this is not possible when the wavelets in question are less than 2 wavelet breadths apart. In this example, the STFT, Stockwell transform and Fourier

transform all contain a Fourier transform of a window of data which contains at least parts of both wavelets and therefore notches in the amplitude spectrum will form. Similarly, the SDD cannot completely remove the cross term energy: this is located half way between the wavelets, with periodic notching defined by notch theory, so the cross terms in the SDD are included in the integration window which is used to form the spectra.

Figure 2.12 shows the resultant effective attenuation measured when taking a spectral ratio between the amplitude spectrum at the top and bottom of the wedge model. It is clear to see that the variations in effective attenuation measured via a Fourier transform are significant, with $1/Q$ values of between -0.03 (Q=-33) and 0.02 (Q=50), a wide range of values. The effective attenuation measured from all other time-frequency transforms show, on average, an order of magnitude less effective attenuation, typically between -0.0015 (Q=-600) and 0.001 (Q=1000), which, in the seismic bandwidth, is not a significant level of attenuation. Ideally, the measured effective attenuation, at all time separation of the wavelets, would be zero.

It is speculated that the SDD method may be adapted for use in tuning studies by reversing the action of the window functions seen so far, such that all energy around the origin of the ambiguity plane is removed rather than kept. The resultant time-frequency panel should only contain cross-term energy which will have periodic notching defined by the time-separation of the two constituents of the cross-correlation. By Fourier transforming the time-frequency panel it will be possible to highlight the time separation causing tuning at each time instant.

2.6 Zero offset reflection experiment

To test how the Stockwell transform, SDD and STFT perform in a more realistic experiment, a zero-offset reflection synthetic trace has been created using blocked well logs from a North Sea well, shown in figure 2.13 top left, which also shows the resultant seismic trace to the right. A 70Hz, zero-phase Ricker wavelet is used in the generation of the synthetic seismogram with 1ms sampling; note that a Ricker wavelet is not representative of wavelets encountered in production seismic surveys but is nevertheless regularly used due to the simplicity of the wavelet. A

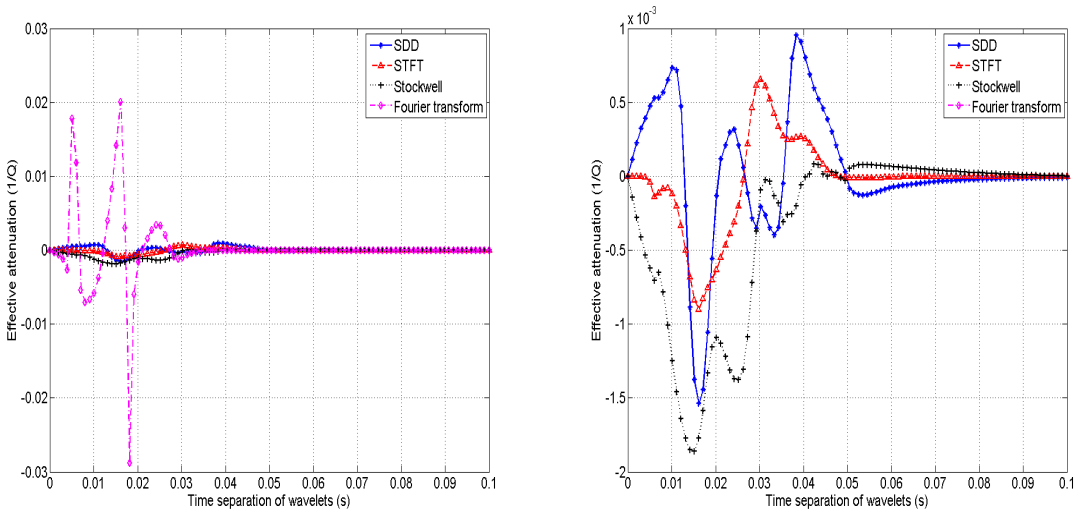

(a) (b)

Figure 2.12: a.) Estimated effecitve attenuation using the spectrum of the top and bottom reflections in the wedge model (figure 2.11a) formed by the SDD, STFT, Sotckwell transform and a Fourier transform. b.) The same image as in (a) with the exclusion of the results for the Fourier transform (and a subsequent rescaling of the y-axis).

zero-phase source wavelet may produce better results owing to a larger available bandwidth which will help in constraining the seismic attenuation quality factor, Q. The bandwidth used to estimate $1/Q$ in this experiment is 20Hz-120Hz. The model used in generating the synthetic trace contains a constant compressional seismic attenuation quality factor value of $1000/Q_{intrinsic} = 20$ ($Q_{intrinsic} = 50$). The attenuation is then estimated from the signal by use of the spectral ratio method. For use in the spectral ratio method, four different strong reflections are selected, the depth and timing of which are denoted by dashed red lines in figure 2.13. To form the spectra of the aforementioned reflections, a time-frequency integration window of 10ms is used.

Figure 2.14 shows the natural log spectral ratio curves formed from the spectra estimated by each method over the frequency range 20Hz to 120Hz, the bandwidth used to estimate Q; these are then used to estimate the attenuation within the trace. Table 2.2 gives the estimated Q^{-1} values determined from a straight line fit of the natural log spectral ratio surfaces. Figure 2.14 also shows the natural log

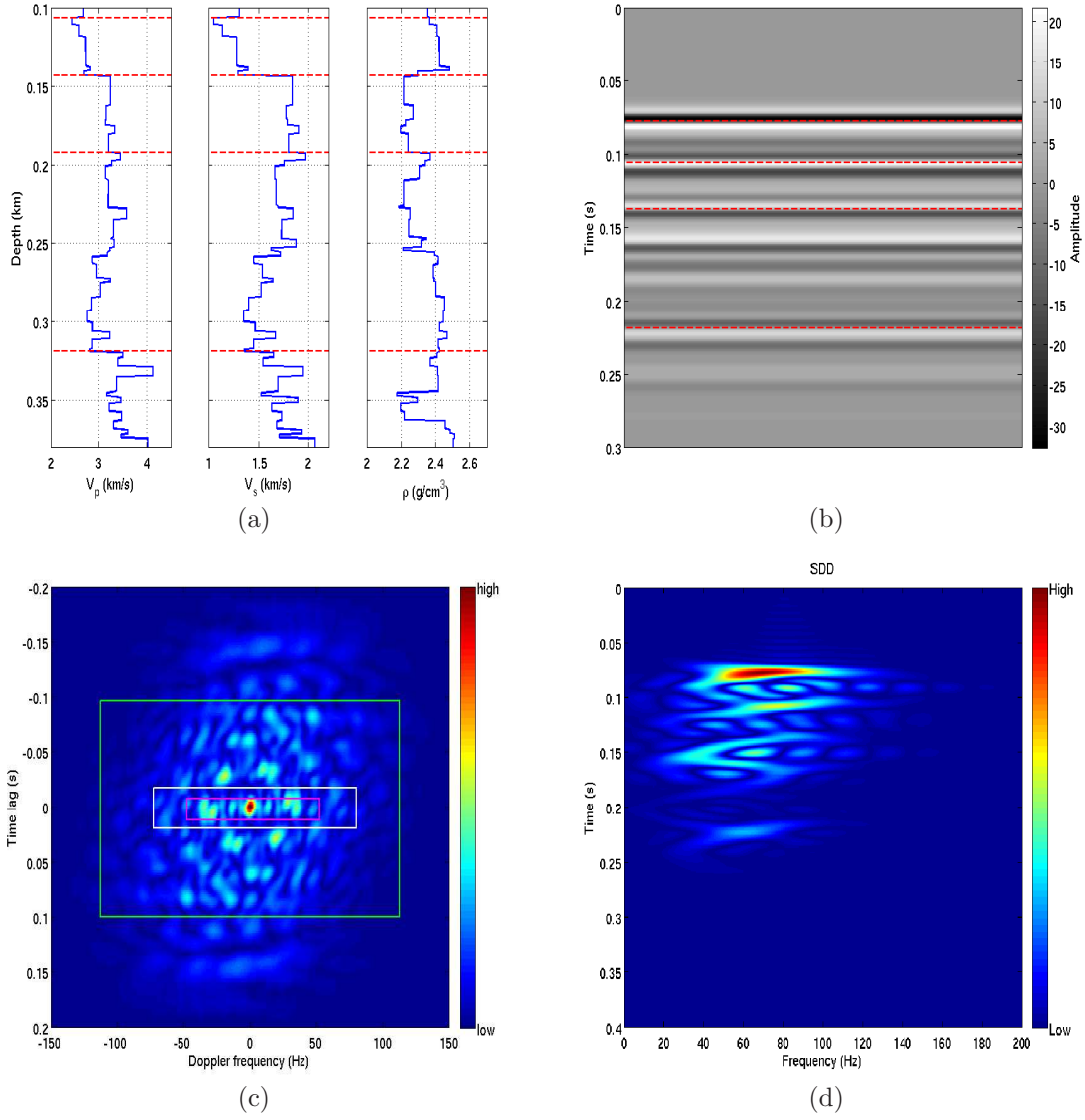

Figure 2.13: Blocked well logs (a) used to create a zero offset synthetic seismic trace (b). The attenuation within the model is set to a constant value of intrinsic Q^{-1}=0.02. Dashed red lines denote the reflections that will be used in the spectral ratio method. The reflections will be referred to as 1-4 where reflection 1 is the shallowest. Also shown is the ambiguity plane representation of the synthetic seismogram (c) on which is plotted three different sizes of ambiguity window which were used to assess the impact of the ambiguity window design. The resultant time-frequency gather (d) generated from windowing the ambiguity plane response with the window outlined in white (c) is also shown.

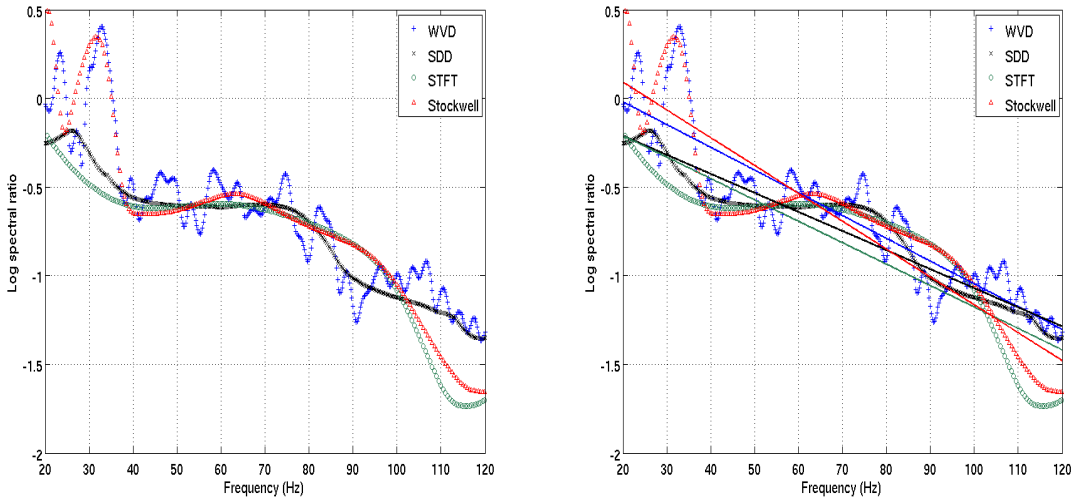

(a) (b)

Figure 2.14: An example of the natural log spectral ratio curves for the pair of reflections 1 and 4 in figure 2.13 formed by spectra which are extracted from the time-frequency gather of the seismic trace using the Stockwell transform, SDD, WVD and STFT (a) and their corresponding best least squares linear fit (b).

spectral ratio curve formed from the spectra extracted from the WVD of the zero offset reflection signal. The interference in the WVD, which is caused by cross terms in the IAF, is included within the integration window and is also located at the same time as the reflections. The inclusion of this interference causes the natural log spectral ratio curve of the WVD derived spectra not to vary smoothly with frequency. The overall trend of the WVD curve in figure 2.14 is in agreement with the curves formed from the other methods so the estimated attenuation quality factor value will be similar, as can be seen in table 2.2. However the WVD is adding unnecessary noise to the spectral ratio curve, which is why smoothed WVDs such as the SDD are preferred for estimating spectra.

Table 2.2 summarizes the $1000/Q$ values derived for different reflection pairs in figure 2.13 and different time-frequency transform methods. The mean of the estimated $1000/Q_{app}$ values is an indication of the overall accuracy of each method, and the standard deviation σ is related to the precision. The standard deviations are biased as not all the data points are independent. Only the mean

Table 2.2: Table of estimated apparent attenuation quality factor values for each possible pair of the four reflections shown in figure 2.13. The mean and standard deviation, σ, of the six $1000/Q$ values determined from the six possible permutations of reflection pairs is also given. The values denoted $x - y$ correspond to the $1000/Q$ value derived using reflection pair x and y. The expected value of $1000/Q$ is 20 for every receiver pair.

Transform method	$1000/Q_{app}$							
	1-2	1-3	1-4	2-3	2-4	3-4	mean	σ
Stockwell	4±6	43±5	35±1	78±9	43±2	30±4	39	24
STFT	-51±4	14±3	27±1	70±5	47±2	37±3	24	41
SDD	26±3	28±2	24±1	31±1	24±1	21±1	26	4
WVD	76±5	46±2	29±1	21±4	17±1	16±2	34	23

Table 2.3: Table of the average estimated apparent attenuation quality factor values for each method given in table 2.2 for a 20ms, 10ms (used in table 2.2) and 1ms integration window.

Integration window (ms)	20ms	10ms	1ms
	mean $1000/Q_{app}$	mean $1000/Q_{app}$	mean $1000/Q_{app}$
Stockwell	37±7	39±10	40±11
STFT	28±10	24±17	22±31
SDD	28±3	26±2	33±13
WVD	36±2	34±9	68±20

from the SDD method has an error less than the actual value and hence is the only value that contains any credible information. The large standard deviation of the $1000/Q$ attenuation values derived using the Stockwell transform, STFT and WVD as the time-frequency transform mean that the $1000/Q$ values estimated are highly imprecise, whereas the standard deviation of the $1000/Q$ derived using the SDD as the time-frequency transform is approximately 15% of the mean $1000/Q$ value. It is clear that the $1000/Q$ values estimated using the SDD as the time-frequency transform are much more precise than those derived from any other time-frequency transform tested and are in general also more accurate (although there are some exceptions, for example reflection pair 2-3).

The effect of varying the integration window in the time-frequency gather was investigated to determine how sensitive the estimated $1000/Q_{app}$ values given in

Table 2.4: Table of the average estimated apparent attenuation quality factor value for the SDD method for a 10ms integration using three ambiguity plane windows of different sizes (seen in figure 2.13. The color in brackets denotes the color of the outline of the window in figure 2.13).

Ambiguity plane window size	mean $1000/Q_{app}$
small (magenta)	18±8
normal (white)	26±2
large (green)	35±9

table 2.2 are to the integration window used. Table 2.3 summarizes the mean estimated $1000/Q_{app}$ values estimated for each transform method given in table 2.2 for a 20ms and 1ms (which equals the sampling rate in the seismogram) integration window. When the scattering attenuation present within the model of $1000/Q$=4 is taken into account then the SDD method with a 10ms and 1ms window and all STFT results agree with the input model value of $1000/Q$=20. However, in the case of the STFT and the SDD with 1ms integration window, the error on the estimated $1000/Q$ value is large, due to the large variation in values for different reflection pairs (seen in table 2.2).

It can be argued that little difference can be seen between the results for the 20ms and 10ms integration windows, although the SDD method with a 20ms window falls just outside the input model value with an estimated $1000/Q_{intrinsic}$ of 24±3. The SDD result for the 10ms integration window is the most precise of those that agree with the input attenuation whereas the STFT method a 1ms integration window is the most accurate.

All methods have a tendency to over-estimate the attenuation, due to notches in the higher frequencies incurred from arrivals that are closely packed in time. An integration window of larger than 20ms is not analyzed as the time separation between the first and second reflections of interest in the seismogram is 25ms. The variation in estimated attenuation values with varying integration window shows the difficulty in parameterizing any transform, including the SDD.

The effect of varying the size of the window function in the ambiguity plane on the $1000/Q_{app}$ values estimated by the SDD method is summarized in table 2.4. The outline of the different window functions used are shown in figure 2.13.

Table 2.4 highlights the fact that a large ambiguity plane window will make the time-frequency gather and thus the estimated $1000/Q_{app}$ values of the SDD tend towards those of the WVD, in which the ambiguity plane response is not windowed. The mean estimated attenuation values for the large window in table 2.4 is very similar to that of the WVD result seen in table 2.2. The mean estimated attenuation value for the small ambiguity plane window has a larger error (approximately 44%). This is due to the small ambiguity plane window cutting out signal energy in the ambiguity plane response of the signal.

Tables 2.3 and 2.4 show that the length of the integration window used in the time-frequency gather as well as the size of the ambiguity plane window used in the SDD are important parameters that can have serious impacts on estimated spectra. As long as a sensible integration window (larger than the sampling rate) is used, then length of the integration window is not as important. In this example, it is found to be advantageous to keep the integration window as large as possible, as the attenuation values estimated for the 20ms integration window are generally more precise than those estimated for a 10ms integration window. The size of the ambiguity plane window should be large enough to contain all coherent energy around the origin of the ambiguity plane window, but no more. The larger the window in the ambiguity plane, the more the SDD tends towards being a WVD.

The mean attenuation value of the six reflection pairs, when using the SDD, is not in agreement with the intrinsic attenuation within the model (1/Q=0.02). However, the estimated attenuation values are apparent attenuation and do not take into account the scattering attenuation that may be present within the model. Scattering attenuation has been measured for the entire log interval shown in figure 2.13 (Beckwith and Clark (2014)) using the wave localization approach of Van Der Baan (2001), finding a maximum $1000/Q$ value of 4 within the bandwidth used here to estimate $1000/Q$ values. If this scattering attenuation is taken into account, then, for both the small and normal sized ambiguity plane windows (table 2.4), the estimated intrinsic attenuation is in agreement with the input model value, although the error for the small window derived $1000/Q$ value is still large.

2.7 Attenuation estimation on a pre-stack receiver gather using the PSQI method

Figure 2.15 shows a $\tau - p$ domain gather of a CDP supergather over a North Sea oil field. The pre-stack Q inversion method (hereafter PSQI, Reine et al. (2012)) is used to estimate apparent attenuation from the CDP supergather. The PSQI method works within the $\tau - p$ domain by comparing the spectrum of two reflections at the same common horizontal slowness. Note that the PSQI algorithm assumes that the attenuation quality factor is frequency-independent and homogeneous within the spatial range covered by the CDP superbin and that it is isotropic within the interval to be analysed. Figure 2.15 highlights the reflections which are used in the PSQI algorithm: all possible pairs of reflections are used in the attenuation analysis. The Stockwell transform, SDD and STFT are used to transform each horizontal slowness trace into the time-frequency domain, from which the spectrum of each reflection is extracted. A spectral ratio surface is then formed, the slope of which can be inverted for the attenuation quality factor, Q.

The true attenuation quality factor value in the intervals between the reflections shown in figure 2.15 is clearly not known, so it not possible to assess which time-frequency transform provides the most accurate estimate of the attenuation quality factor. However, the quality factor values estimated by each time-frequency transform can be assessed in terms of whether they are realistic or not. Attenuation quality factors values in the range of $1000/Q$ equal to 1.2 and 77 have previously been estimated from pre-stack gathers from the North Sea (Dasgupta and Clark (1998)). Taking this into account, only the negative attenuation quality factor values estimated in figure 2.18 are deemed unrealistic.

It is possible to estimate a negative $1000/Q$ value, which means that there appears to be relatively more high frequency content in the signal with depth. This can be due to several processes which affect the spectrum of the wavelet, such as thin bed tuning, or interference of primary reflections with multiples of shallower events. However, in the context of measuring spectra for use in the spectral ratio method, a negative Q value is most likely due to inconveniently placed notches in the frequency spectra used to form the spectral ratio.

Equally, it is possible that the estimated attenuation values (figure 2.18) are

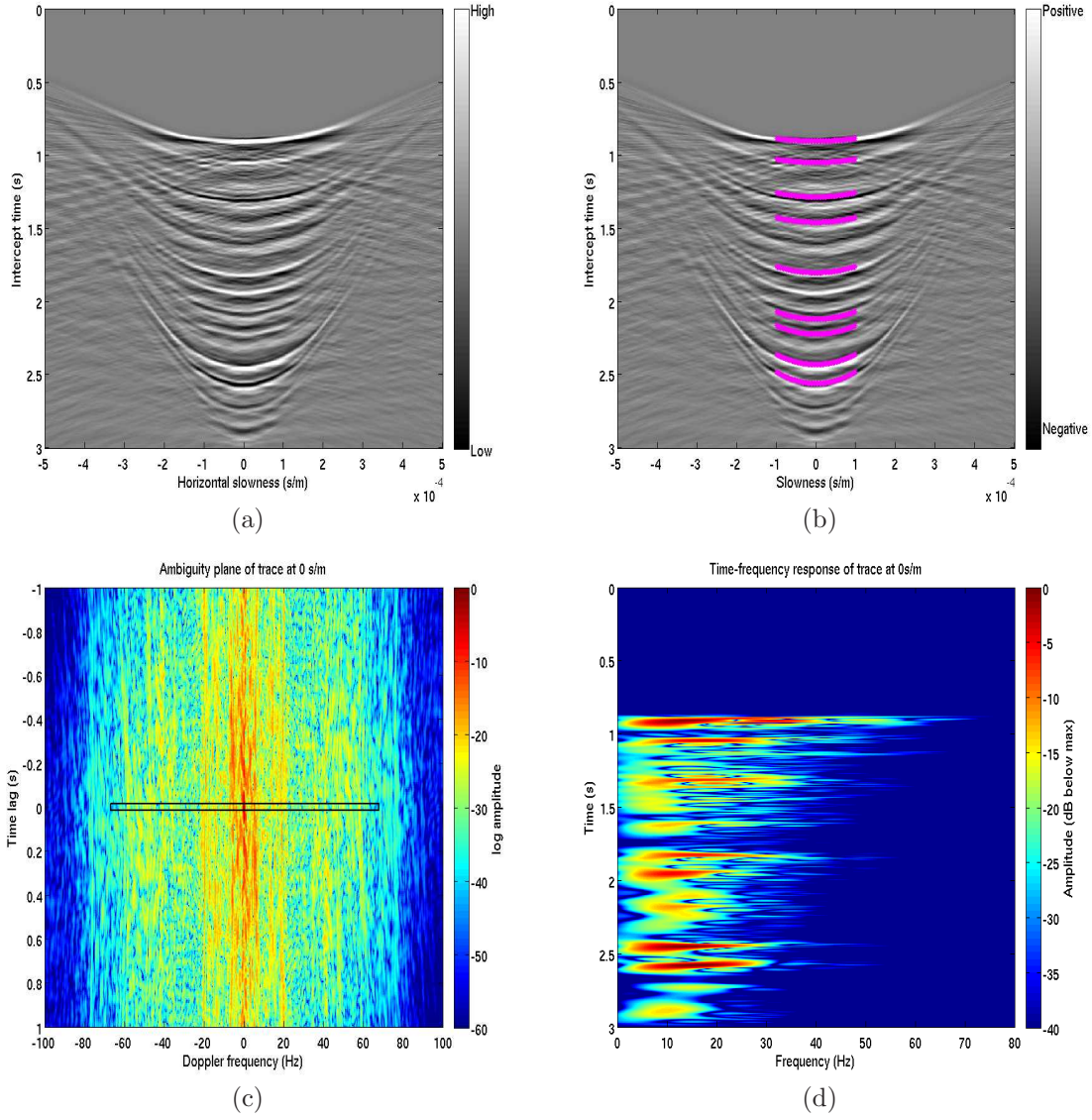

Figure 2.15: $\tau - p$ domain gather of a CDP supergather over a North Sea oil field (a), also with the reflections to be analyzed highlighted (b). The ambiguity plane response of the 0 s/m horizontal slowness trace seen in the $\tau - p$ gather (c) and the corresponding time-frequency response formed from via the SDD (d) in a decibel scale.

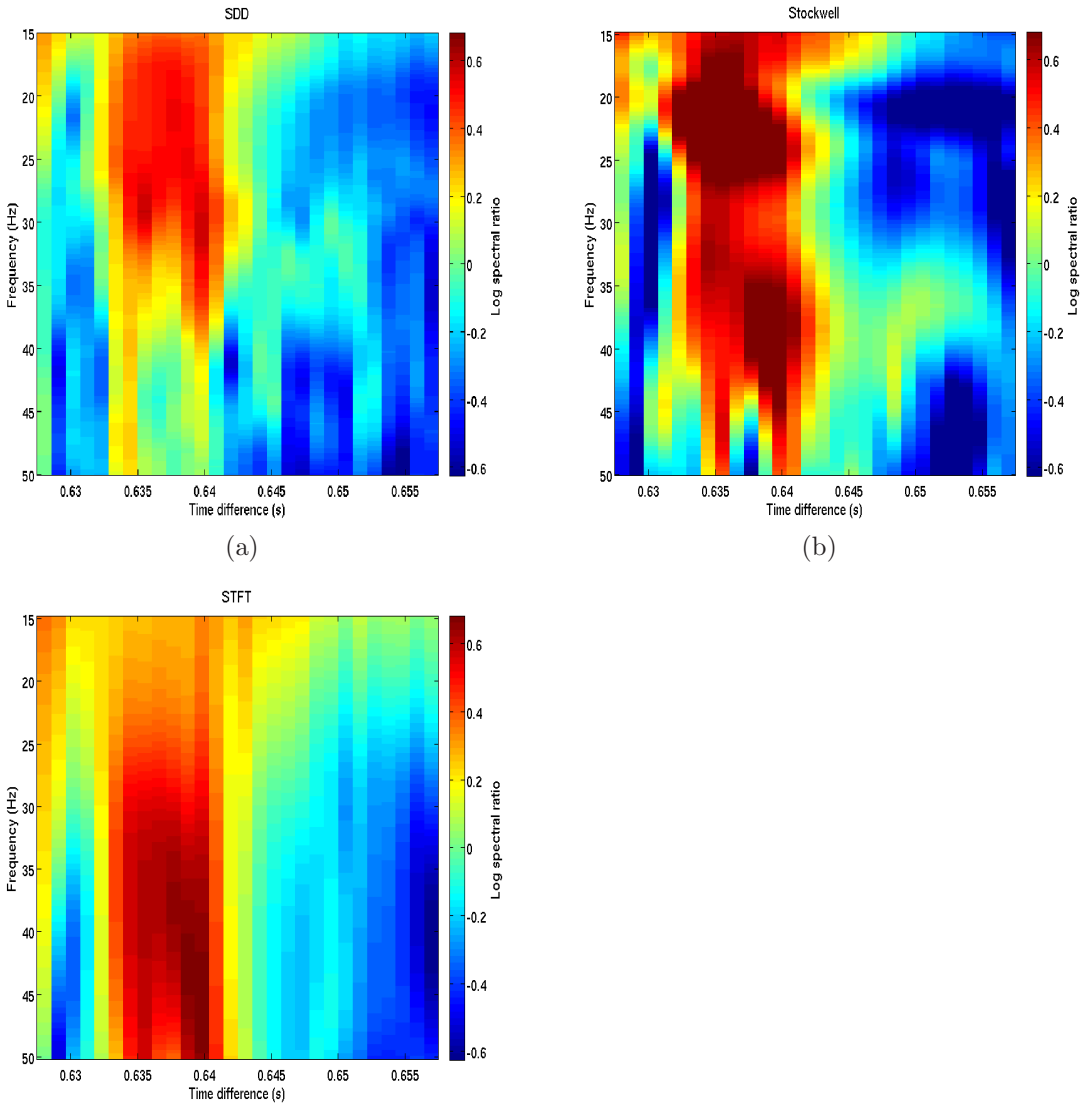

Figure 2.16: Natural log spectral ratio surfaces generated by the PSQI algorithm for the shallowest and deepest reflections highlighted in figure 2.15 for each of the time-frequency transforms: SDD (a), Stockwell transform (b) and STFT (c).

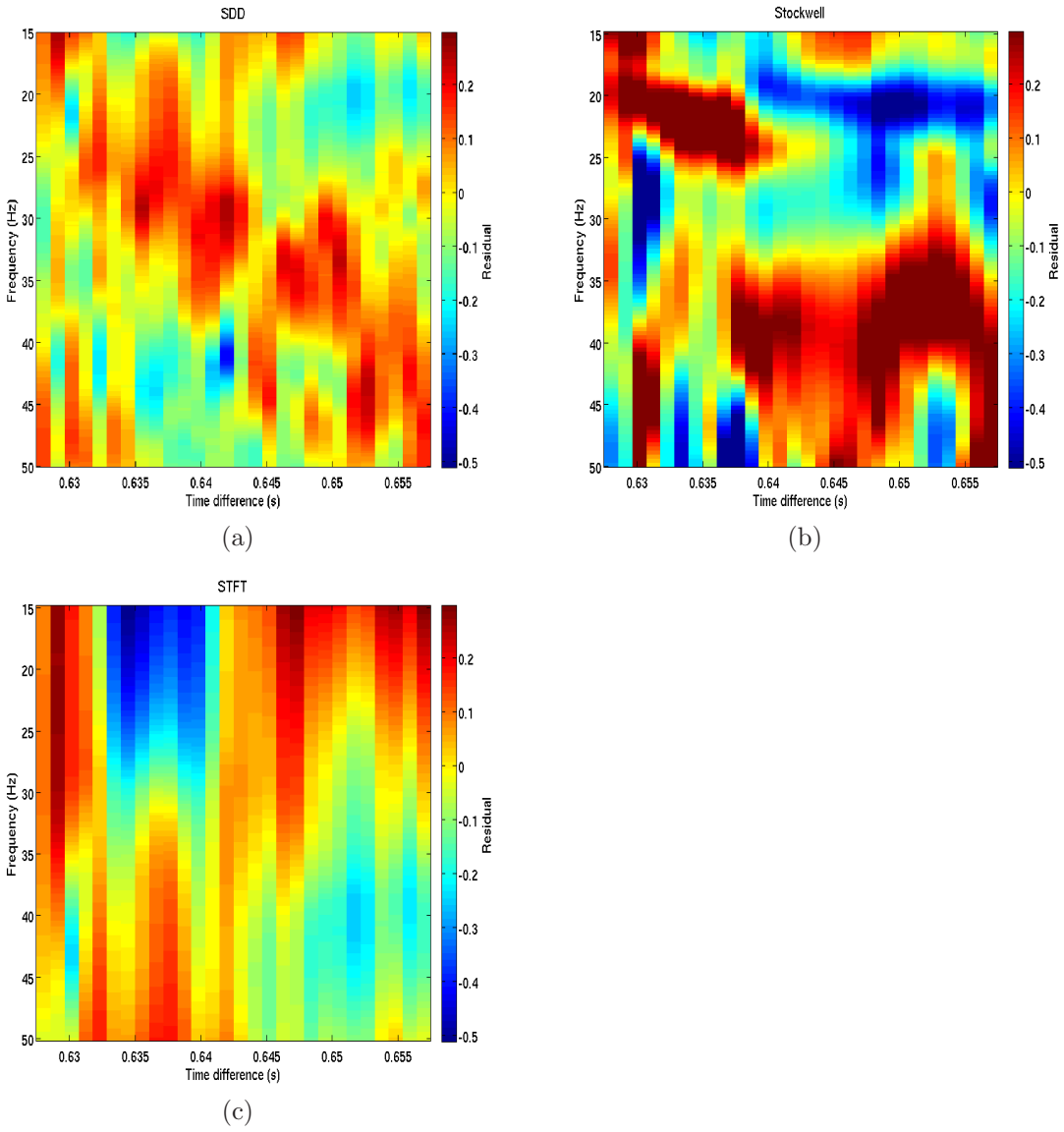

Figure 2.17: Residual surfaces formed by removal of a best fit surface to the natural log spectral ratio surfaces given in figure 2.16 from those surfaces: SDD (a), Stockwell transform (b) and STFT (c).

Table 2.5: Table of the mean normalized L1-residual across the 36 PSQI surfaces for every pair of reflections in figure 2.15. The mean residual in every transform across every surface is 0 to 4 decimal places. The mean standard deviation across the 36 surfaces (along with the standard deviation of the distribution of standard deviations) is also given.

Transform method	mean normalized L1 residual	mean standard deviation
Stockwell	0.33±0.06	0.40±0.07
STFT	0.21±0.08	0.22±0.07
SDD	0.12±0.03	0.16±0.04

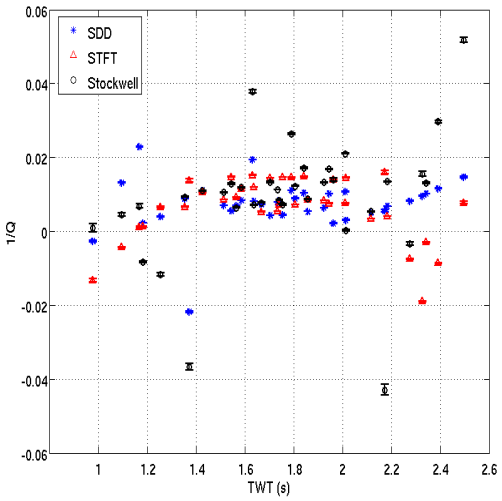

Figure 2.18: Attenuation quality factor value estimated for each reflection pair in figure 2.15 for each of the three time-frequency transform methods; SDD, STFT and Stockwell transform

simply a product of conveniently placed peaks and notches in the frequency spectrum of each common horizontal slowness trace (which is a proxy for the time difference axis). If a peak is located at the low end of the frequency band used to fit the spectral surface and a notch lies at higher frequencies then this could simulate an attenuation signal.

The $1/Q$ profile estimated using the SDD method (figure 2.18) shows the lowest number of negative $1/Q$ values and the smallest variation over the profile depth, which is to be expected given a background $1/Q$ trend with possible seismic attenuation anomalies.

A useful QC of the method is therefore to see how closely the estimated spectral ratio surface for each time-frequency transform matches the fitted surface from the PSQI algorithm, i.e a model of interference-free, frequency-independent Q, attenuation. This assumes that the peaks and notches, if they exist, do not create a spectral ratio surface which replicates the same trend as attenuation.

Table 2.5 shows the mean and standard deviation of the normalized sum of the absolute deviation of each point from the best fit surface estimated by the PSQI method (the normalized L1-residual) across all 36 spectral ratio surfaces. Figure 2.16 shows the spectral ratio surfaces used to measure Q, for the interval between the shallowest and deepest reflections highlighted in figure 2.15b. The constituent spectra for these surfaces were extracted from time-frequency gathers created by the SDD (a), STFT (b) and Stockwell transform (c). This is used as a goodness of fit measure. An L1-residual is used as it weighs each point equally and does not put undue emphasis on outliers. In all cases the mean deviation is 0 to 4 decimal places. A normalized L1 residual value of 0 denotes a perfect fit between the spectral ratio surface and the best fit surface estimated via PSQI. The larger the value of the normalized L1 residual, the worse the fit between the estimated spectral ratio surface and the PSQI fit.

The residual spectral ratio surfaces shown in figure 2.17 are created by subtracting the best fit spectral ratio surface estimated from the PSQI algorithm from the spectral ratio surfaces given in figure 2.16. The normalised histograms of these residuals are given in figure 2.19, in which each distribution was binned over the same interval. These residual surfaces, and the normalized L1 residual values given in table 2.5, are used to assess which of the time-frequency trans-

forms provides the most stable spectral ratio surfaces and hence an attenuation quality factor estimate. The time-frequency transform associated with the residual surface which is closest to zero over the widest range of frequency and time difference values therefore provides a spectral ratio surface which is closest to that which is expected (within the assumptions of the PSQI algorithm).

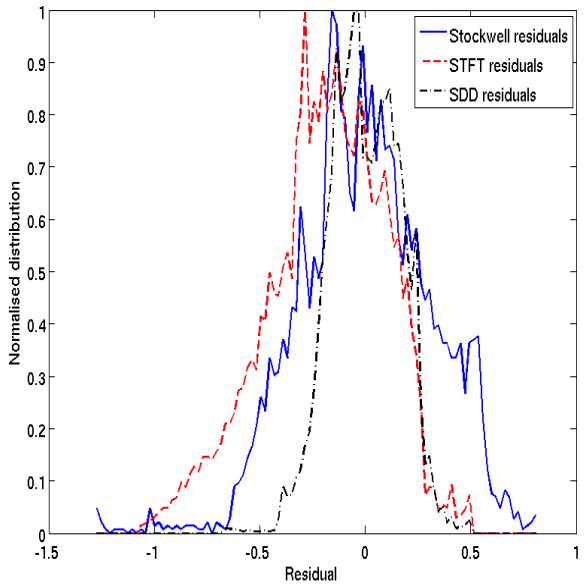

Figure 2.19: Normalised histograms of the residual values seen in the residual surfaces in figure 2.17.

In table 2.5 and figure 2.17, the SDD provides the lowest normalized L1 residual, and furthermore provides the residual surface which is closest to zero over the largest range of time-difference and frequency values, as is highlighted by the histogram of the residuals for the surfaces in figure 2.19. The SDD method also provides fewer negative attenuation estimates than other methods. The spectral ratio surface estimated by the SDD is therefore the most representative of a spectral ratio surface corresponding to an attenuation signal. The Stockwell transform has the highest residual value and thus provides the poorest estimate of the spectra which constitute the spectral ratio surfaces, based on the assumptions of the PSQI algorithm.

2.8 Conclusions

A new quadratic time-frequency transform, which requires the creation of a window within the ambiguity plane, based on the dynamics of the signal, has been introduced and termed the Signal Dependent Distribution method (SDD). The SDD is a quadratic time-frequency transform, and, as such, does not suffer from the same uncertainty principle as fixed- and variable-window transforms, but instead is subject to a trade-off between joint time-frequency resolution and suppression of cross-terms.

We have outlined why it is always best to integrate the time-frequency domain representation of a signal over the entire time extent of the wavelet. A spectrum should only be extracted from a time-frequency domain via a slice (i.e taking the amplitude of only 1 time instant per discrete frequency) if the wavelets contained within the seismic trace have a time-frequency response which is symmetric in both time and frequency, and conservation of the total energy of the signal is not important.

Estimates of the spectrum of a wavelet have been formed from the SDD, Stockwell transform, STFT and Fourier transform for a wedge model. The estimates of the spectrum of the wavelet formed from the SDD were found to match more accurately the known wavelet in the model. The distribution of residual spectral amplitude values with respect to the time separation of the wavelets in the wedge model has been explained as being due to notches in the frequency spectrum caused when two wavelets are close enough to interfere.

The SDD has been tested against a fixed and a variable window transform, in the STFT and Stockwell transform respectively, for its ability to estimate seismic attenuation accurately from a synthetic zero-offset reflection experiment based on well log data. We found that the SDD was the only time-frequency transform for which the standard deviation of the estimated attenuation values did not exceed the mean of the attenuation value estimated from the 6 reflection pairs, and is therefore the only apparently credible result. The mean $1000/Q$ value estimated from the SDD method is, within errors, in agreement with the attenuation built into the input model, when using a 20ms integration window. The effect of the time-frequency domain integration window on the resultant attenuation values

was investigated, concluding that the time-frequency integration window should be kept as large as possible. Whilst a larger integration window made the resultant attenuation values more meaningful, the values did not change much in their absolute value. The shape of the window function used in the SDD time-frequency transform method was found to have a large impact on the estimated attenuation values; additionally, a larger ambiguity plane window function produces results very similar to that of the WVD, as expected.

The SDD, Stockwell transform and STFT have been applied to a $\tau - p$ transform of a common receiver gather from a real data set, in order to estimate spectra for use in the PSQI method of attenuation estimation. The attenuation within the survey area is not known, so the log spectral ratio surfaces that are produced from the spectra estimated by each method have been compared to the best fit surface estimated by PSQI. The surface corresponding to the SDD has the lowest residual over the largest range of time difference (a pseudo slowness axis) and frequency values, meaning that the surface produced from the SDD is closer to that expected by the constant-Q assumption of the PSQI method. The SDD also provides fewer negative Q estimates, which are likely due to poorly estimated spectra, than the STFT or Stockwell transform.

The SDD was found to produce more plausible estimates of the spectrum of reflections in a $\tau - p$ gather over a from a seismic dataset covering a North Sea oil field, if the residual spectral ratio surface is taken as a reasonable metric of accuracy.

References

Bath, M., 1974, Spectral analysis in geophysics: Elsevier Scientific Publishing Company, Amsterdam, volume **7** *of* Developments in Solid Earth Geophysic. 30

Beckwith, J., and R. Clark, 2014, Improved spectral estimates for attenuation studies: EAGE Technical Program Extended Abstract. 56

Boashash, B., 2003, Time frequency signal analysis and processing: a comprehensive reference: Elsevier Science Limited. 31, 35, 36

Castagna, J., S. Sun, and R. Siegfried, 2003, Instantaneous spectral analysis: Detection of low-frequency shadows associated with hydrocarbons: The Leading Edge, **22**, 120–127. 30

Dasgupta, R., and R. Clark, 1998, Estimation of q from surface seismic reflection data: Geophysics, **63**, 2120–2128. 57

Daubechies, I., 1990, The wavelet transform, time-frequency localization and signal analysis: Information Theory, IEEE Transactions on, **36**, 961–1005. 33

de Bruijn, N., 1973, A theory of generalized functions, with applications to wigner distributions and weyl correspondence: Nieuw Archief voor Wiskunde, **21**, no. 3, 205–280. 40

Flandrin, P., 1999, Time-frequency/time-scale analysis: Academic Press. 40

Gabor, D., 1946, Theory of communication. part 1: The analysis of information: Electrical Engineers - Part III: Radio and Communication Engineering, Journal of the Institution of, **93**, 429–441. 11, 32, 33

Hall, M., 2006a, Predicting bed thickness with cepstral decomposition: The Leading Edge, **25**, 199–204. 30

———, 2006b, Resolution and uncertainty in spectral decomposition.: First Break, **24**, 43–47. 32, 33

Koenig, W., H. K. Dunn, and L. Y. Lacy, 1946, The sound spectrograph: The Journal of the Acoustical Society of America, **18**, 19–49. 30

Liner, C. L., 2012, Elements of seismic dispersion: A somewhat practical guide to frequency-dependent phenomena: Society of Exploration Geophysicists. 47, 48

Reine, C., R. Clark, and M. van der Baan, 2012, Robust prestack Q-determination

using surface seismic data: Part 1-Method and synthetic examples: Geophysics, **77**, R45–R56. 31, 57

Reine, C., M. van der Baan, and R. Clark, 2009, The robustness of seismic attenuation measurements using fixed- and variable-window time-frequency transforms: Geophysics, **74**, WA123–WA135. 30

Ryan, H., 1994, Ricker, ormsby, klauder, butterworth - a choice of wavelets: CSEG Recorder, **19**. 40, 48

Sinha, S. K., P. S. Routh, P. D. Anno, and J. P. Castagna, 2003, Time-frequency attribute of seismic data using continuous wavelet transform: SEG Technical Program Expanded Abstracts 2003, 1481–1484. 48

Stockwell, R., L. Mansinha, and R. Lowe, 1996, Localization of the complex spectrum: The s transform: Signal Processing, IEEE Transactions on, **44**, 998–1001. 30, 32

Taner, M. T., F. Koehler, and R. E. Sheriff, 1979, Complex seismic trace analysis: Geophysics, **44**, 1041–1063. 34

Tonn, R., 1991, The determination of the seismic quality factor q from vsp data: A comparison of different computational methods.: Geophysical Prospecting, **39**, 1–27. 30

Van Der Baan, M., 2001, Acoustic wave propagation in one dimensional random media: the wave localization approach: Geophysical Journal International, **145**, 631–646. 56

Ventosa, S., C. Simon, M. Schimmel, J. Danobeitia, and A. Manuel, 2008, The s -transform from a wavelet point of view: Signal Processing, IEEE Transactions on, **56**, 2771–2780. 34

Ville, J., 1958, Theory and application of the notion of complex signal: Technical report, DTIC Document. 35

Wang, Y., 2007, Seismic time-frequency spectral decomposition by matching pursuit: Geophysics, **72**, V13–V20. 30

Zhang, K., K. J. Marfurt, R. M. Slatt, and Y. Guo, 2009, Spectral decomposition illumination of reservoir facies: SEG Technical Program Expanded Abstracts, 3515–3519. 30

Zhao, B., D. Johnston, and W. Gouveia, 2006, Spectral decomposition of 4d seismic data: SEG Technical Program Expanded Abstracts, 3235–3239. 30

Chapter 3

Adaptations to the PSQI algorithm

3.1 Frequency-dependent attenuation quality factor

3.1.1 Abstract

The intrinsic attenuation is known from poro-elastic rock physics theory to be frequency-dependent, even within typical bandwidths of individual surface- and borehole-based surveys - where measurement methods usually deliver frequency-*independent* Q. Thus, measuring frequency-dependent Q instead offers better characterization of seismic properties and a potential step towards estimating permeability directly from seismic data. Therefore, we introduce a method to measure frequency-dependent Q from pairs of reflections in pre-stack τ-p domain surface seismic data - a data type that, unlike a VSP, offers useful areal coverage. Whilst, in principle, any analytic form with a manageable number of parameters could be prescribed, frequency-dependence of Q is modeled here as a power-law, $Q(f) = af^b$. Inversion is done with a simple grid-search over coefficient $(1/a)$ and exponent b, seeking a minimum L1-norm: we show, using a numerical experiment and a synthetic dataset that it is robust and also accurate down to a signal-to-noise ratio of approximately 0.65. Q is then estimated for some 955 250mx250m

superbins of a 3D pre-stack OBC dataset over the Kinnoull Field, central North Sea. All combinations of 8 prominent reflections between Top Miocene and Base Cretaceous were treated together, to give some 21,000 frequency-dependent and (for comparison) constant-Q results. The median coefficient $(1/a)$ and exponent b are 0.0074 and 0.06 respectively, with sharply-peaked distributions (excess kurtosis >10). Outlier, strongly frequency-dependent results, given by b >0.2, coincide with low-frequency 'shadows' under amplitude anomalies, adversely affecting the spectra of reflections. The inferred frequency-dependent Q at 32.5Hz, the center of the available bandwidth, is not statistically different from the frequency-independent Q, 181 with a standard error from the distribution of 1, derived from the same data. Hence for this dataset, a constant-Q assumption would in fact be adequate. Nevertheless, our method has the ability to measure stable estimates of $Q(f)$.

3.1.2 Introduction

It is generally assumed in most seismic attenuation estimation schemes that attenuation rate, α, varies linearly with frequency, or equivalently, the seismic quality factor value, Q, is independent of frequency over the measurement bandwidth (as a common assumption is that $\alpha = \pi f/Qc$, Aki and Richards (2002)), despite decades of awareness that Q should be frequency-dependent (Tonn (1991)). Indeed, Pride et al. (2003) provide an overview of whether or not permeability can be estimated from seismic data. One conclusion drawn is that inversion of seismic data for frequency-dependent Q is necessary and examples of models whereby Q is dependent upon both frequency and permeability are provided (Pride and Berryman (2003)). The measurement of frequency-dependent Q within the exploration surface seismic reflection bandwidth of roughly 5Hz to 100Hz therefore provides a very useful step towards estimating permeability directly from surface seismic reflection data.

Laboratory experiments by Collins and Lee (1956), Bruckshaw and Mahanta (1961), Birch and Bancroft (1938) and Gemant and Jackson (1937) have shown that the intrinsic attenuation quality factor (referred to as specific dissipation in many of the papers) is frequency-independent for a range of materials. The

study of Bruckshaw and Mahanta (1961) is of special interest in exploration seismics, because they found that the specific dissipation in sandstones over the frequency range of 40Hz to 120Hz, similar to the surface seismic exploration bandwidth, is independent of frequency. The study of Gemant and Jackson (1937) was performed on a range of materials including wood and glass at frequencies lower than that encountered in exploration seismics, Birch and Bancroft (1938) performed their study on granite and Bruckshaw and Mahanta (1961) worked with dry rocks, in all cases different from what might be expected in exploration seismics.

Sams et al. (1997) demonstrate with VSP, crosshole, sonic and core attenuation measurements over 5 orders of magnitude of frequency (and a factor of 3 in seismic quality factor values) how Q is frequency-dependent over a wide frequency scale by modeling the observed attenuation with a squirt-flow model (using the methods of Jones (1986) and Mavko and Jizba (1991)). This and other recent work (Adam et al. (2009)) suggest a frequency-dependence of attenuation within the seismic bandwidth of 5Hz-100Hz.

Many models exist that aim to understand the fundamental physical cause of attenuation and are more or less relevant at different frequencies. O'Connell and Budiansky (1977) present a microscopic flow mechanism in which pores and cracks perpendicular to the direction of propagation of seismic energy are compressed, setting up pressure gradients that cause fluid flow (sometime referred to as squirt flow). Biot (1956) outlines a macroscopic flow mechanism in which friction and inertial coupling can cause pore fluid to move with the solid frame as a seismic wave propagates through the rock. These two methods were later combined into the BISQ method by Dvorkin and Nur (1993). The squirt flow, and subsequently BISQ, method gives a characteristic frequency at which attenuation peaks, this attenuation being inversely proportional to fluid viscosity. Pride et al. (2004) outline a mesoscopic model where in attenuation is caused by wave induced fluid flow in which peak attenuation can be described by a characteristic frequency that is proportional to permeability. It is important to note that many of the models currently present in literature predict a frequency dependent attenuation.

However, frequency-dependent Q has far less often been measured from single survey types. Reid et al. (2001) found seismic quality factor values proportional

to $f^{-1.53}$ in a North Sea vertical seismic profile (VSP) dataset in the bandwidth 10Hz to 95Hz. Jeng et al. (1999) proposed a technique that makes no assumption about the analytical form of the frequency dependence and found that attenuation quality factor values in the near surface can be dependent upon frequency in the seismic bandwidth. Gusmeroli et al. (0000) also found a frequency-dependent Q value which varies by a factor of approximately 3 over the frequency range 50Hz to 200Hz in glacial valley ice. Carey et al. (2008) used a powerlaw frequency-dependence of Q to measure a frequency exponent of Q of between 0.6 and 0.87 through analysis of transmission losses in sandy/silty shallow water bottoms, although their investigation took place over the frequency range 50Hz to 1kHz, mainly outside the frequency bandwidth of standard exploration surface seismic data.

Whether intrinsic attenuation is assumed to be frequency-independent or not, it is important to remember that attenuation quality factor values estimated from surface seismic data are generally effective attenuation values, and are thus a harmonic average of the intrinsic and scattering attenuation (see Odoherty and Anstey (2006) and Sato et al. (2012) for an overview of the mechanisms of which give rise to scattering attenuation). The methods of estimating scattering attenuation given by Van Der Baan (2001) and Mangriotis et al. (2013) highlight how scattering attenuation can have a non-trivial magnitude and be highly frequency dependent within the seismic frequency bandwidth. Therefore, the effective attenuation quality factor value estimated from surface seismic could be frequency-dependent due solely to the influence of scattering attenuation.

Therefore, attenuation estimation schemes should, ideally, measure frequency-dependent attenuation quality factor values, but often do not. If the attenuation quality factor is frequency-independent, then attenuation rate is a linear function of frequency and we need only estimate the rate of loss of amplitude with frequency of a propagating wave. However, if the attenuation quality factor is frequency-dependent, then the acceleration of the loss of amplitude with frequency on the propagating wave needs to be taken into account. This is more difficult, because second order changes to the amplitude spectrum of the wave now need to be quantified.

Jeng et al. (1999) found that, for unconsolidated sediments, the attenuation

quality factor value was almost linearly dependent upon frequency. Herein lies a trade-off: attenuation preferentially cuts out higher frequencies, but the frequency dependence of the attenuation quality factor is most readily observed at lower frequencies, where the change in the quality factor is greatest, i.e. the relative change of attenuation in the 5Hz to 10Hz band would be the same as that in the 30Hz to 60Hz band.

The estimation of frequency-dependent attenuation quality factor values will be introduced here through an adaptation of the pre-stack Q inversion (PSQI, Reine et al. (2012a)) method developed for surface seismic reflection surveys. The method is tested on synthetic data based upon blocked well log data in which scattering attenuation is minimal. Finally, the method is applied to a pre-stack CDP supergathers from a 3D ocean bottom cable (OBC) survey in the North Sea. The effect of altering the bandwidth used in estimating attenuation is investigated with a simple synthetic model.

3.1.3 Estimating frequency-dependent attenuation

The PSQI method is a modified spectral ratio method (an evolution of the QVO method of Dasgupta and Clark (1998)) designed to work on pre-stack data which has had a linear Radon transform applied, so that the data are in the intercept-time/horizontal-slowness ($\tau - p$) domain. For a locally 1D structure, each horizontal slowness trace corresponds to a common take-off and emergence angle in the overburden for two pairs of reflections. By matching the ray paths in the overburden, it is possible to suppress angle dependent effects (such as source-receiver directivity, overburden attenuation and anisotropy) on the spectra used in the spectral ratio method. By also considering different take-off angles, then the change in spectral content of an increased path length within an interval of interest can also be observed.

$$\ln\left(\frac{A_j(f,\Delta t)}{A_i(f,\Delta t)}\right) = \ln(PG) - \frac{\pi f \Delta t}{Q_{ij}} \tag{3.1}$$

Equation 3.1 shows the general form of the spectral ratio equation used in the PSQI method, where $A_i(f,\Delta t)$ is the amplitude spectrum of the i^{th} reflection at each horizontal slowness value analyzed (Δt is the travel time within the

interval of interest and a proxy for slowness). P is the energy partitioning term (corresponding to a ratio of attenuation-free amplitude versus slowness curves multiplied by transmission coefficients into and out of the interval of interest), G is a geometrical spreading term, and Q_{ij} is the estimated interval attenuation between reflections i and j.

If the geometrical spreading is corrected for, the energy partitioning terms are assumed to be independent of frequency, and the travel time within the interval (Δt) is known, then equation 3.1 can be solved through linear least squares inversion to obtain Q_{ij}. Here I modify the spectral ratio method, within the framework of the PSQI workflow, to include a frequency-dependent Q. If Q_{ij} is now frequency dependent, in the form given in equation 3.2, then equation 3.1 cannot be solved with a least-squares linear inversion.

$$\frac{1}{Q_{ij}} = \frac{1}{a_{ij} f^{b_{ij}}} \tag{3.2}$$

This power-law model of frequency-dependence of Q is the same as that proposed by Jeng et al. (1999). Here, a and b refer to the coefficient and exponent of the dependence of the attenuation quality factor on frequency. The difference between our model and that of Gurevich and Pevzner (2015) and Carey et al. (2008) is that their coefficient of frequency dependence (termed 'a' here, but 'Q_1' in Gurevich and Pevzner (2015) where $Q(f) = Q_1(\omega/\omega_1)^{-n}$) is scaled by a factor of ω_1^n where 'n' is the exponent in their paper. Their exponent, n, is the negative of our exponent, b, and ω_1 is a reference frequency at which the coefficient is measured, I use 1Hz in this study as a reference frequency so this normalization factor disappears in the equations.

Figure 3.1 is a reproduction of the results given by Sams et al. (1997) within the bandwidth of 0Hz to 200Hz. All 3 models, which are derived from the squirt flow model of Jones (1986) (we direct the reader to the papers of Sams et al. (1997) and Jones (1986) for further details), are well fit by a power-law frequency-dependent Q, as in equation 3.2, within this bandwidth with exponents, b, in the range of -0.39 to -0.66 and coefficients, a, between 204 and 1500.

$$\ln\left(\frac{A_j(f,\Delta t)}{A_i(f,\Delta t)}\right) = \ln(PG) - \frac{\pi f^{1-b_{ij}} \Delta t}{a_{ij}} \tag{3.3}$$

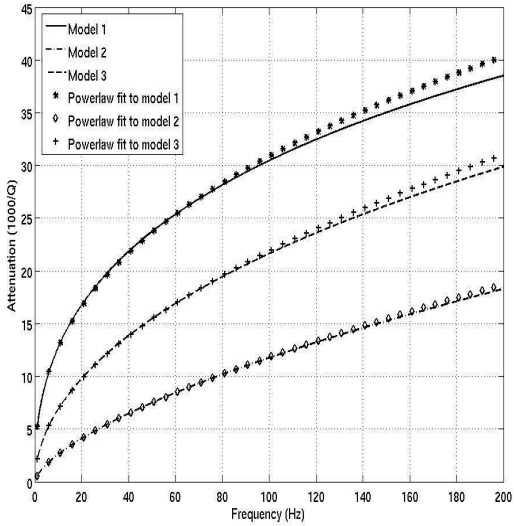

Figure 3.1: Reproduction of the results of Sams et al. (1997) within the bandwidth 0Hz to 200Hz with powerlaw frequency-dependent Q (equation 3.2) fitted.

Equation 3.3 can be solved by many different methods including but not limited to; non-linear inversion, Monte Carlo, directed Monte Carlo and grid search methods. I will assume that the energy partitioning terms are independent of frequency, and equal to the energy partitioning terms estimated via equation 3.1 and test the non-linear inversion, grid-search and directed Monte-Carlo methods in terms of their accuracy and computational time in estimating the attenuation present in synthetic shot gathers.

In order to carry out the non-linear inversion for frequency-dependent Q, the partial derivatives of the log spectral ratio equation (equation 3.3) are taken with respect to the coefficient, a, and the exponent, b. The partial derivatives are given in equation 3.4 and are used to invert the model misfit for updates to the model. The initial estimate of the coefficient, a, in equation 3.2 can be defined as the Q value estimated from a constant-Q PSQI inversion and the coefficient can be assumed to carry a value somewhere between -1 and 1, this range covers negative, positive and zero frequency-dependence of the attenuation quality factor. In the results quoted here I use an initial estimate for the exponent, b, of zero, the

frequency-independent case, unless otherwise stated.

$$\frac{\partial \ln\left(\frac{A_2}{A_1}\right)}{\partial b} = \frac{\pi \Delta t f^{1-b} \ln(f)}{a}$$
$$\frac{\partial \ln\left(\frac{A_2}{A_1}\right)}{\partial a} = \frac{\pi \Delta t f^{1-b}}{a^2} \tag{3.4}$$

Forward modelling can be carried out relatively simply by creating log spectral ratio surfaces, using equation 3.3, with a range of different values for the inverse coefficient, $1/a$, and exponent, b. The inverse coefficient will be estimated in the forward modelling approach as modelling in inverse coefficient space allows for a better distribution of attenuation values to be included in the modelling, with denser sampling in high attenuation regions and sparse sampling in low attenuation regions. The value of ln(PG) used is the same as those derived from a constant-Q PSQI and the misfit of the various different surfaces with the log spectral ratio surface is calculated. This assumes that body waves are not, or are negligibly, dispersive over the available frequency range and are thus not frequency-dependent.

The value of $\ln(PG)$ is set to be the same as those derived from a constant-Q PSQI and the misfit of the various different surfaces with the log spectral ratio surface is calculated: this assumes that body waves are not, or are negligibly, dispersive over the available frequency range.

3.1.4 Synthetic tests

First, a theoretical natural log spectral ratio surface will be created using equation 3.3 and then the input frequency-dependent Q parameters ($1/a$ and b) are estimated by forward modeling a range of possible values and finding the best fit surface. This will serve to test the validity of the proposed algorithm and to highlight any possible complications that may arise. To investigate more complex noise impacts, such as transform artifacts, two synthetic shot gathers will be made: first, a simple 1D model used to generate a synthetic shot gather and test the robustness of the algorithm to transform artifacts; and, second, a 1D model based on well log data will be used to create a synthetic shot gather which will test the accuracy of the forward modeling approach to estimating frequency-

Table 3.1: Table of parameters used to create theoretical natural log spectral ratio surface with frequency-dependent Q.

thickness	V_p (m/s)	V_s (m/s)	ρ (g/cm^3)	$1/a$	b
500m	2000	800	2.0	0.05	0.5
350m	3000	1200	2.5	0.05	0.5
∞	4500	1800	3.0	0.05	0.5

dependent Q in a more realistic shot gather.

Synthetic tests - theoretical surface

First, to test if it feasible to estimate frequency-dependent attenuation quality factor values from a natural log spectral ratio surface, such as that given by the PSQI method, a theoretical natural log spectral ratio surface is generated using equation 3.3. It uses the parameters given in table 3.1 to form the inversion intercepts through the Knott-Zoeppritz equations, and uses inverse coefficient and exponent values of 0.05 and 0.5 respectively. The theoretical surface is given in figure 3.2a, Gaussian noise with a standard deviation of 0.3 and mean 0 is then added to the surface (figure 3.2b).

Figure 3.3 shows the residual surface corresponding to a range of inverse coefficients of -0.1 to 0.1 and a range of exponents of -1 to 1, formed from forward modeling the theoretical log spectral ratio surface shown in figure 3.2b using an L1-residual. While the minimum L1-residual correctly identifies the input model values of $1/a$=0.05 and b=0.5, it is apparent (figure 3.3) that a range of coefficient and exponent values can still nevertheless provide a good fit to the theoretical surface. To estimate a coefficient and exponent with a more realistic approximation of the distribution of residual values, even though the distribution of residual values is not Gaussian in either the coefficient or exponent, the mean and standard deviation of the lowest 0.05% of the residual values are taken to estimate the coefficient, exponent pair and error upon them respectively for all tests. In this case then the results for the estimated inverse coefficient and exponent for the L1-residual are 0.053$\pm$0.009 and 0.51$\pm$0.04 respectively. The results obtained using an L1 forward model, L2 forward model, non-linear inversion and genetic algorithm directed Monte Carlo method are all summarised in table 3.2. On noise

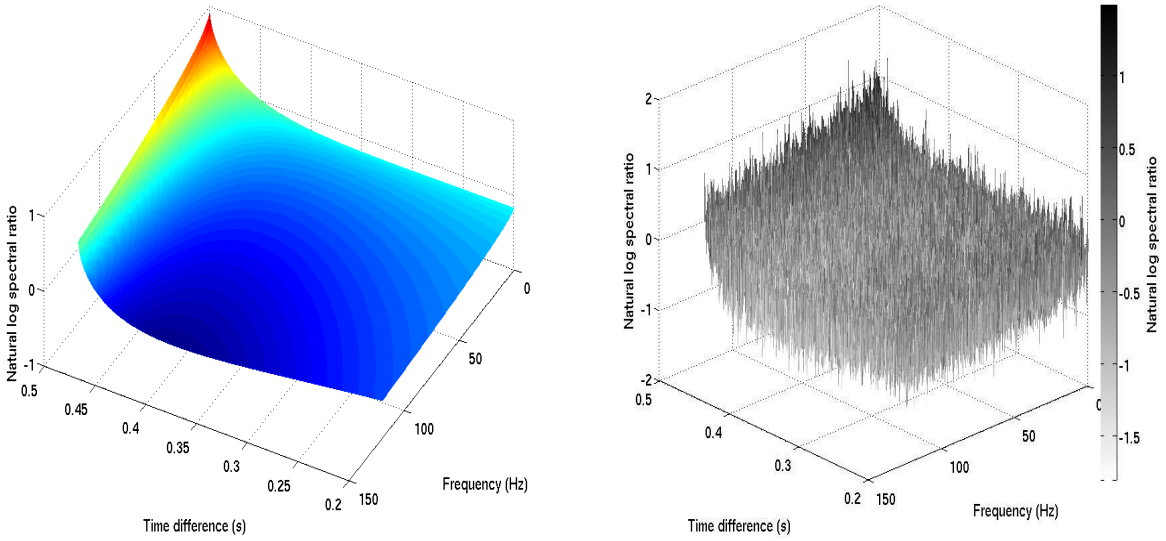

(a) (b)

Figure 3.2: a.) Noise-free theoretical natural log spectral ratio surface formed via equation 3.3 for the 350m interval given in table 3.1 with $1/a$=0.05, b=0.5 and inversion intercepts derived from the Knott-Zoeppritz equations. b.) Model surface in (a) with added Gaussian noise of standard deviation 0.3 and mean 0, it is assumed that geometric spreading has been corrected for in both surfaces.

free synthetic data, the lowest 0.05% of residual values for the forward modelling with an L1 residual still lay within the global minimum and do not extend far enough to adversely shift the centre point of the parameter pair.

The genetic algorithm (Mitchell (1998)) is a directed Monte-Carlo method which falls under the class of evolutionary computational method. The specific algorithm used works by first creating a random initial population, the size of this initial population can be set but was kept at 1000 in this example and was bounded such that the initial population must be within the range of coefficients 0 to 200 and exponents -1 to 1. Each member of the population is rated by its residual value and the lowest residual members are carried on to the next generation. Some low residual value members are selected as "parents" and "children" are formed from these "parents" which will carry on to the next generation. A "child" is generated by either altering a single "parent" by random processes or combining the vector components of two "parents". The process is then repeated

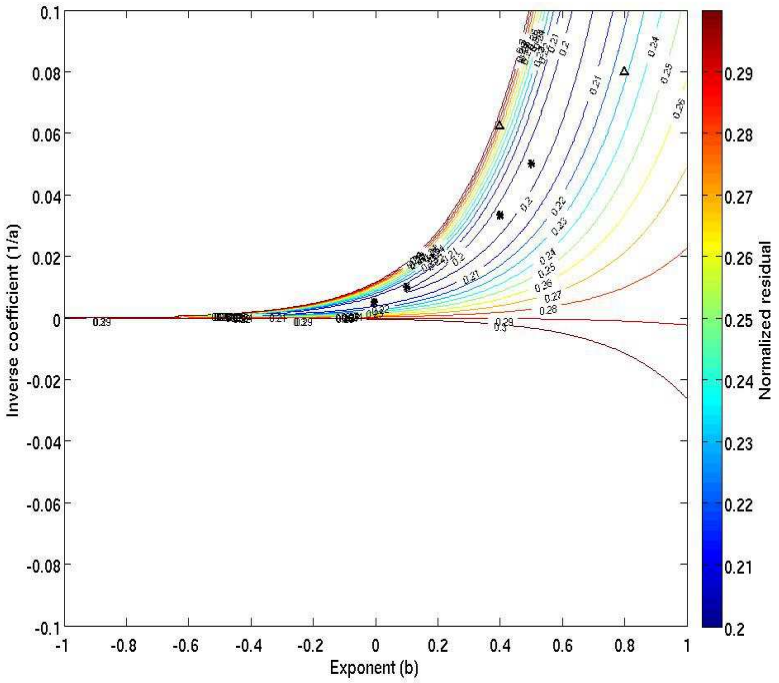

Figure 3.3: L1-Residual map of the modeled log spectral ratio surface with respect to the theoretical surface given in figure 3.2. Four low residual points are marked by white dots and two higher residual areas are marked by black dots, the trends of these are compared qualitatively in figure 3.4.

until a maximum number of generations is reached (this is set to 500 in the following examples), the lowest residual value becomes lower than a predefined value (this value is set such that it can never be reached) or the relative change in the lowest residual values becomes negligible. The results of running this genetic algorithm on the theoretical surface is given in table 3.2.

The results of both the genetic algorithm and the forward modelling utilising an L1 residual are the only methods to estimate the input coefficient and exponent, within errors, with the genetic algorithm being the least precise of the two methods. The non-linear inversion is the most precise method of all those tested, but is not accurate. These results (table 3.2) show how difficult it is to measure frequency-dependent attenuation quality factor values even on theoretical data with only a small amount of noise.

Table 3.2: Table of inverse coefficient and exponent values estimated from the theoretical natural log spectral ratio surface in figure 3.3 using non-linear inversion (NLI), forward modelling (FM) and a genetic algorithm (GA).

Method	Inverse Coefficient ($1/a$) (expected = 0.05)	Exponent (b) (expected = 0.5)
NLI	0.071±0.005	0.58±0.01
FM (L1)	0.053±0.009	0.51±0.04
FM (L2)	0.091±0.016	0.64±0.03
GA	0.059±0.017	0.54±0.07

The inverse coefficient, $1/a$, describes the overall slope of the natural log spectral ratio surface whereas the exponent, b, describes its curvature. In this way, a surface with a higher curvature and lower gradient can still be well fit by a surface with a higher gradient and a lower curvature as the two can trade off against one another. For example, as is seen in figure 3.4, a seismic quality factor described by an inverse coefficient of 0.005 and an exponent of -0.05 (Q=$200f^{0.05}$) has a similar trend to that of a seismic quality factor with an inverse coefficient of 0.05 and an exponent of 0.5 (Q=$20f^{0.5}$). Figure 3.4 highlights the trade-off between coefficient and exponent in fitting a spectral ratio surface (a spectral ratio line is shown in the example for ease of viewing). The plot shows spectral ratio curves for four different coefficient and exponent pairs, ranging from coefficients of 20 to 200 and exponent values of -0.05 to 0.5, taken from the low residual value regions (white dots in figure 3.3). For comparison, two spectral ratio curves are also shown for coefficient and exponent pairs (black dots in figure 3.3) which lie within higher residual value regions. The trend of all four lower residual value curves over the bandwidth of 0Hz to 80Hz are qualitatively similar, whereas the trend for the higher residual value curves are markedly different. The similarity of these trends explains the shape of the low residual region in the residual map in figure 3.3, which is a trade-off between coefficient (slope) and exponent (curvature).

The estimation of the parameters $1/a$ and b has been carried out on theoretical surfaces with a range of different Gaussian noise levels. The result of the estimated inverse coefficient and exponent as a function of the signal to noise ratio of the surface is given in figure 3.5. The estimated inverse coefficient and exponent

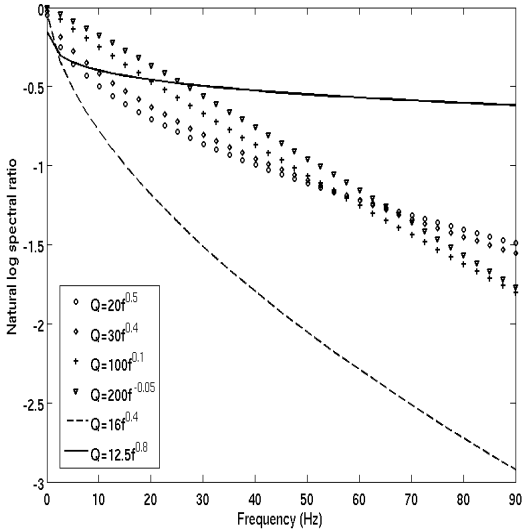

Figure 3.4: Four different numerical spectral ratio curves formed using coefficient and exponent pairs picked manually within the low residual zone in figure 3.3. Although the coefficient and exponent values vary significantly, the overall trend within the bandwidth of 0Hz to 80Hz is similar.

values are within 10% of the expected values down to a signal to noise ratio of 0.65. Whilst the same experiment with a different underlying $(1/a,\, b)$ pair would likely give a different threshold for the signal-to-noise ratio, this result suggests the proposed method is robust down to low signal-to-noise ratios.

Forward modeling the theoretical surface with random noise has shown that the inverse coefficient and exponent can be correctly estimated by forward modeling the natural log spectral ratio surface. However, random noise is not seen on such surfaces for real data (figures 3.15) and random noise tests do not simulate the coherent interference that may be present on surfaces derived from real data. Although the random noise test has proven successful, it is still prudent to test this method using synthetic shot gathers, in which artifacts from the $\tau - p$ transform and spectral estimation scheme may be present in the natural log spectral ratio surface.

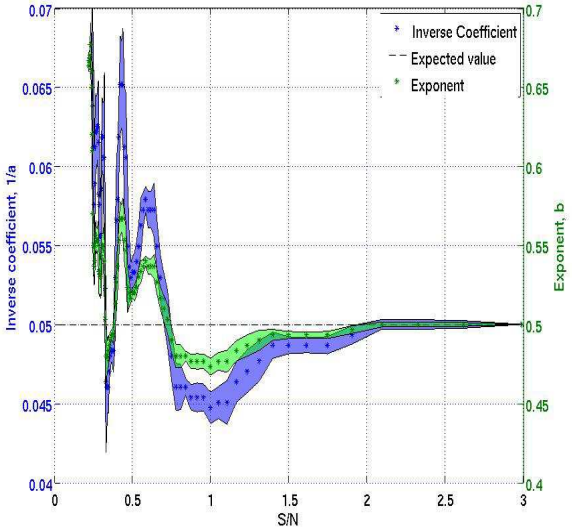

Figure 3.5: Exponent (green stars) and inverse coefficient values (blue stars) estimated from theoretical surfaces with variable levels of Gaussian noise. The estimated parameters are unreliable at a signal to noise ratio of less than 0.65.

The effect of the seismic bandwidth choice

We now generate synthetic gathers from the same model (figure 3.2) used for the previous test using the synthetic software package *OASES* (Schmidt (1987)). Figure 3.6 shows the resultant shot gather when using the model given in table 3.1 and using a homogeneous frequency-dependent attenuation quality factor with inverse coefficient and exponent of 0.05 and 0.5 respectively. The primary reflections occur at 0.5s and 0.73s two-way-time (TWT) and two multiples can also be seen at later TWTs of 1s and 1.23s. The interval that will be analyzed, corresponding to the two primary reflections, is the 350m thick unit in table 3.1.

The forward modelling approach to estimating frequency-dependent attenuation quality factors is applied to the synthetic shot gather in figure 3.6. The spectral ratio surface in figure 3.6b is formed from the $\tau - p$ gather of the time-offset data in figure 3.6a for slowness values up to 0.1m/ms, in order to avoid interference at high slowness values where reflections converge and to avoid post-critical reflections. The resultant estimated coefficient and exponent for the frequency-dependence of Q estimated from the three different methods are summarised in

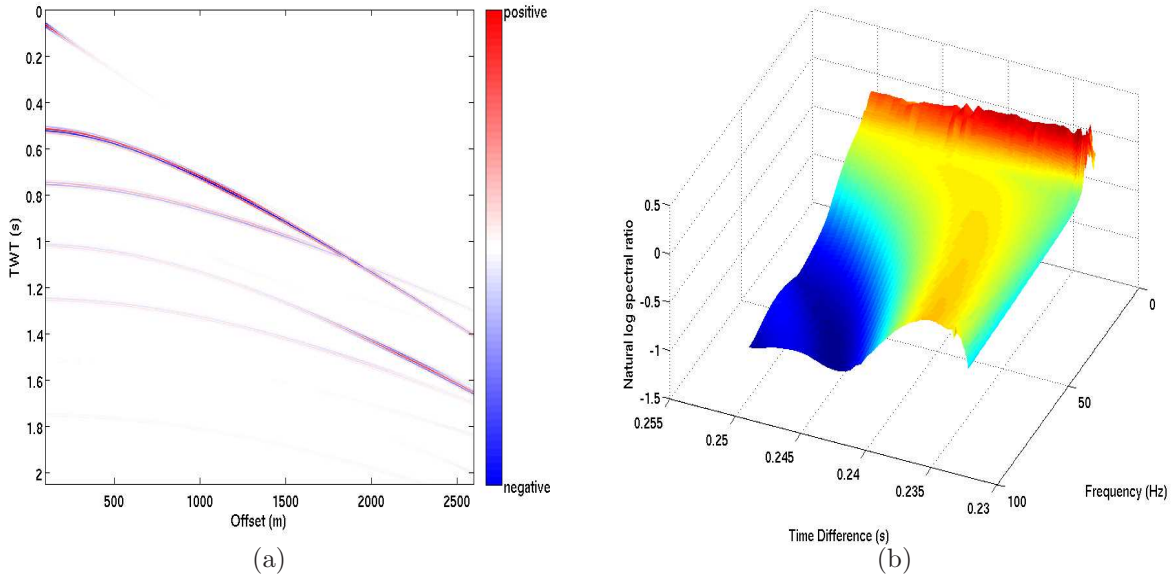

(a) (b)

Figure 3.6: Synthetic shot gather (a) generated using the OASES synthetic software package and using the model given in figure 3.2 with a homogeneous, frequency-dependent attenuation quality factor value described by equation 3.2 of $1/a$=0.05, b=0.5. The log spectral ratio surface estimated from the synthetic data for slownesses up to 0.1m/ms is also shown (b).

Table 3.3: Table of inverse coefficient and exponent values estimated from the synthetic shot gather in figure 3.6 using non-linear inversion (NLI), forward modelling (FM) and a genetic algorithm (GA).

Method	Coefficient ($1/a$) (expected = 0.05)	Exponent (b) (expected = 0.5)
NLI	0.021±0.004	0.25±0.05
FM (L1)	0.05±0.004	0.46±0.05
FM (L2)	0.021±0.002	0.25±0.03
GA	0.008±0.001	-0±0

table 3.3.

The genetic algorithm, non-linear inversion and forward modelling approach using an L2 residual have all failed to recover the input frequency-dependent attenuation coefficient and exponent. The forward modelling approach utilising an L1 residual has recovered the input frequency-dependent attenuation coefficient and exponent. Given these results, and those from the previous synthetic test, it is safe to conclude that the forward modelling approach using an L1 residual is the most accurate method of estimating the frequency-dependence of the attenuation quality factor tested so far.

The L2-residual forward modelling, non-linear inversion and genetic algorithm have failed to recover the input coefficient and exponent for different reasons. The use of an L2-residual in the forward modelling means that a greater weight is given to outliers and anomalous points. This means that any feature of the natural log spectral ratio surface will move the best fit frequency-dependent surface away from that of the true value more so than if using an L1-residual. The non-linear inversion and genetic algorithm converge into local minima in the residual plane which are very close in value to the global minimum and provide a good fit to the data. Figure 3.3 and 3.4 show that the residual map for the coefficient and exponent has a well defined but diverse range of values of the coefficient and exponent which provide a good fit to the natural log spectral ratio surface.

Given the power-law form of frequency dependence of the attenuation quality factor shown in equation 3.2, then lower frequencies in the spectral ratio surface, defined by equation 3, will provide the most information about the frequency dependence of the attenuation quality factor. Figure 3.7 shows a numerical spec-

tral ratio curve with a frequency-dependent Q defined by $1/a$=0.05 and b=0.5, $\ln(PG)$=1 and Δt=0.5s. The rate of change of the gradient provides information about the curvature of the surface, and figure 3.7 shows that the rate of change of the gradient of the spectral ratio curve is greatest at lower frequencies. However, seismic signals are band limited and only contain information within a certain frequency range. It is prudent to therefore investigate how the frequency band which is used to estimate attenuation will affect the derived value of attenuation itself.

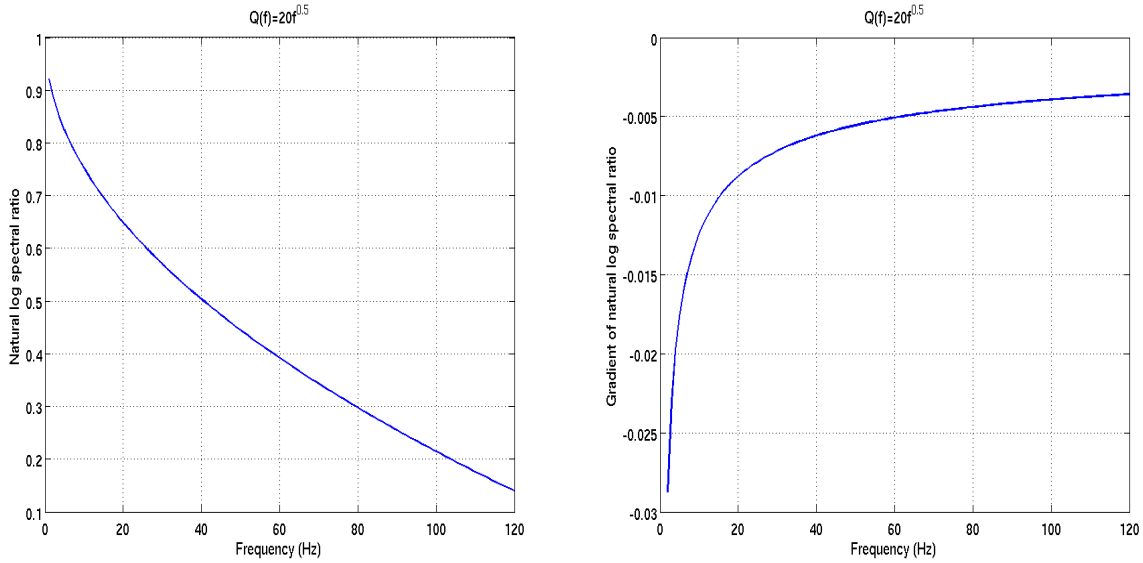

(a) (b)

Figure 3.7: a.) Numerical example of a natural log spectral ratio curve in which frequency-dependent Q is defined by the coefficient 20 and the exponent 0.5. b.) Gradient of the natural log spectral ratio curve in (a).

To assess this, the estimation of frequency-dependent attenuation quality factors is carried out on the synthetic data shown in figure 3.6 for the frequency bandwidths starting at 0Hz to 35Hz and ending at 40Hz to 80Hz and incrementing in 5Hz increments (figure 3.8).

Figure 3.8 shows that for frequency bandwidths starting at >10Hz, the estimated coefficient and exponent become increasingly less accurate. The exponent is slightly more sensitive to the loss of low frequencies within the regression bandwidth than the exponent, as a regression bandwidth starting at 15Hz and

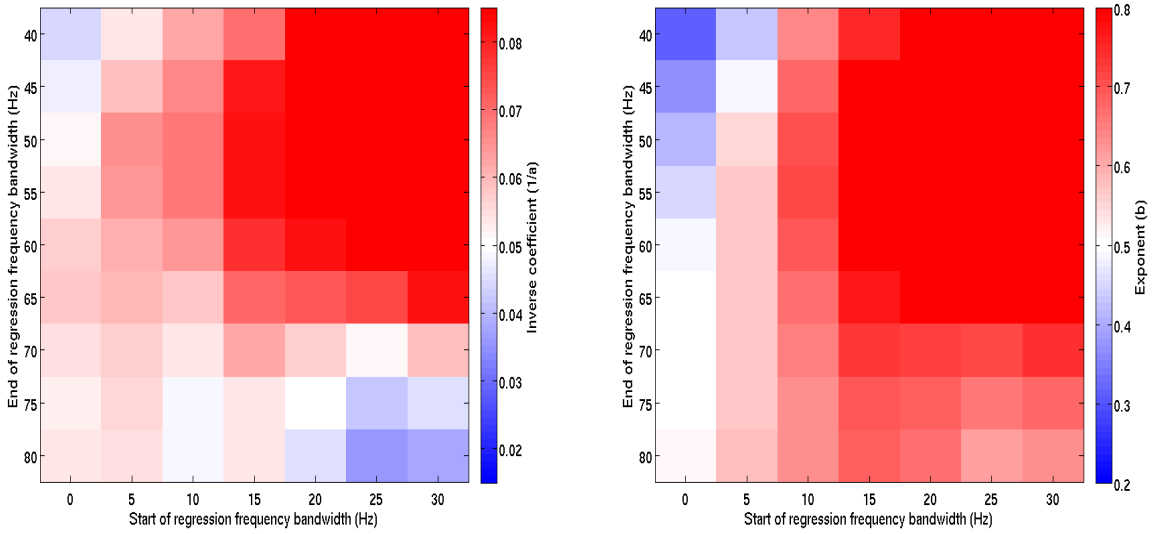

(a) (b)

Figure 3.8: The estimated coefficient (a) and exponent (b) value as a function of the different frequency bandwidths used for the surface fitting.

ending at 75Hz can estimate the expected coefficient, within errors, but cannot estimate the expected exponent. Figure 3.8a shows the importance of a large bandwidth when estimating Q (not just frequency-dependent Q) as the accuracy of the estimated coefficient decreases with decreasing bandwidth. Figure 3.8b shows the sensitivity of estimating frequency-dependent Q to low frequencies, without low frequency, <10Hz, information, it is difficult to estimate accurate frequency-dependent Q. However, low frequencies are also less sensitive to attenuation and, at frequencies of 0Hz-20Hz, it is difficult to accurately estimate the low frequency content of seismic signals with good time-localization. This is because the effective medium experienced by lower frequencies is larger than for the central frequency of the propagating seismic wave, meaning that any information derived primarily from lower frequencies is necessarily of lower temporal resolution.

Synthetic test - well log derived synthetic

Figure 3.9b shows a more complex synthetic shot gather which has been generated to test the accuracy of the adapted PSQI method in estimating a frequency-dependent attenuation quality factor using software which incorporates wavenumber integration in combination with the Direct Global Matrix solution technique and hence provides a full-wave solution (Schmidt (1987) and references within this paper). The synthetic gather is generated using blocked density, compressional and shear wave sonic logs from a North Sea well. The depth scale has been expanded and shifted such that the synthetic model has no water column (although this does not fully simulate a land acquisition owing to the lack of ground roll, a significant noise source in land seismic surveys). A homogeneous attenuation quality factor has been used in the synthetic model with an inverse coefficient and exponent ($1/a$ and b in equation 2) of 0.005 and 0.5 respectively.

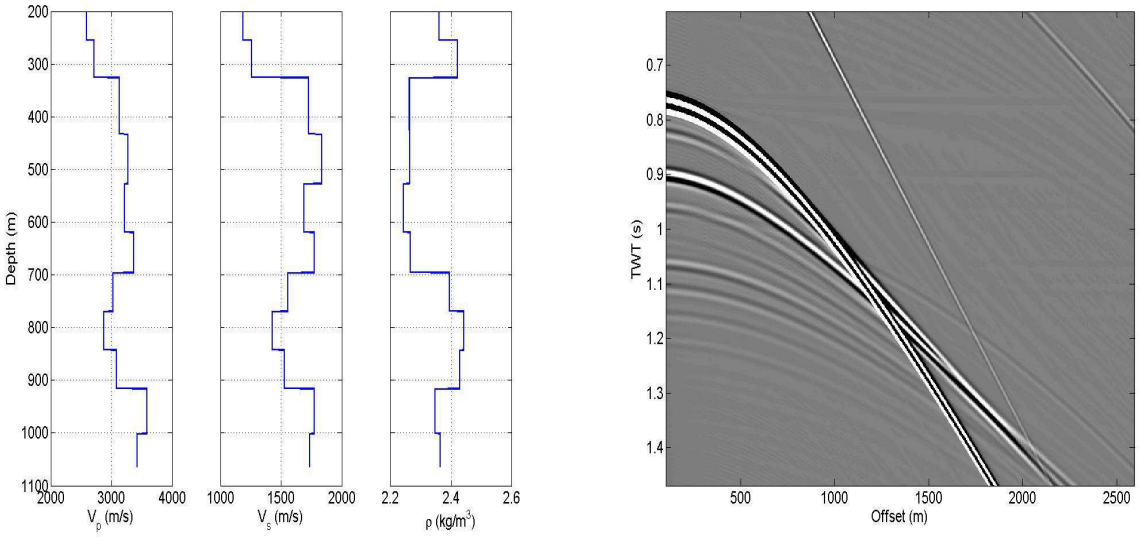

(a) (b)

Figure 3.9: Blocked, scaled and shifted density, compressional- and shear-velocity logs from a North Sea well (a) along with the synthetic shot gather (b) created from the well log data using the OASES synthetic software package and a homogeneous frequency-dependent attenuation described by equation 3.2 with a=20, b=0.5.

Figure 3.9b and 3.10 show the difficulty of isolating the reflections from one another. The synthetic gather uses a zero-phase, 50Hz Ricker wavelet and the

spectrum of each reflection is formed via integration of a 120ms window of the time-frequency gather of each slowness trace. A window length of 120ms will encompass some energy from neighbouring reflections, which is unavoidable if one wants to estimate the spectrum of each reflection as accurately as possible. A bandwidth of 5Hz to 65Hz was used as this constituted the usable bandwidth for all reflections.

The adapted PSQI method, outlined by equation 3.3, is applied to the 36 different intervals defined between acoustic impedance contrasts in the model in figure 3.9a. The mean inverse coefficient and exponent estimated from the various combinations of the 36 different intervals, using the L1-norm forward modelling method of estimating frequency-dependent attenuation, are 0.061±0.008 and 0.21±0.03 respectively. The errors, defined as the standard error of the estimated exponent and coefficient values, need to be viewed with caution as the intervals are not independent of one another. The average estimated values of the coefficient and exponent are not equal to the model values of 0.05 and 0.5 respectively. This experiment shows that when strong acoustic impedance contrasts are closely spaced then the estimated frequency coefficient and exponent value are influenced by interference between the different reflections. One could imagine that when this result for a few strong reflections is extrapolated to many closely spaced and high amplitude reflections then the scattering attenuation would be dominant (Odoherty and Anstey (2006)).

In summary, based on these numerical experiments and synthetic seismic tests, we conclude that the method outlined has been proven to estimate accurately the coefficient and exponent, which describe the frequency dependence of Q from synthetic data. It has also been shown that it is important to include low frequencies into the attenuation estimation scheme in order to estimate accurately the degree of frequency dependence. Soubaras and Dowle (2010) show evidence of modern broadband technology recovering signals down to 2.5Hz.

3.1.5 Application to a 3D Seismic Dataset

The forward modeling approach to estimating frequency-dependent attenuation quality factor values is now applied to a pre-stack 3D ocean bottom cable (OBC)

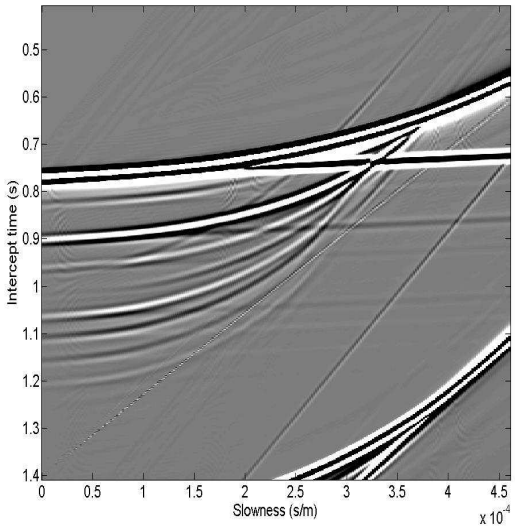

Figure 3.10: τ-p domain representation of the synthetic gather in figure 3.9b transformed into th τ-p domain by a slant stack of the gather mirrored around zero offset and a near-offset window applied to reduce transform artefacts.

data set over the Kinnoull oil and gas field, an Andrews area development project located in the central North Sea (Padmos et al. (2010)). In terms of preprocessing, the data have had a data signature filter, PZ summation and $\tau - p$ demultiple applied. The data are unmigrated.

To increase the signal to noise ratio, 955 supergathers have been created (Reine et al. (2012b))over a 20 inline by 20 crossline range. This limits the spatial resolution of the resultant seismic attenuation values but, given that the inline/crossline spacing of the survey is 12.5m, this smoothing is applied over an area smaller than the first Fresnel zone (Gisolf and Verschuur (2010)) at depth, which is 370m in diameter. The seismic attenuation quality factor values are estimated from spectral data over the bandwidth of 10Hz to 55Hz. The range of exponent values used is determined from those stated in previous literature, as given in the introduction, and the range of inverse coefficient values has been taken as the same as a reasonable range of 1/Q values, making sure to account for negative attenuation through a negative inverse coefficient. Here we will focus on the statistics of the attenuation values rather than use them as a seismic attribute.

The estimation of frequency-dependent 1/Q was carried out over 22 different

intervals defined by combinations of 8 different horizons within the seismic data (black lines in figure 3.11). This provides a total of over 21,000 data points, which constitutes a statistically significant sample, although the data points are not completely independent of one another as some of the intervals analyzed do overlap.

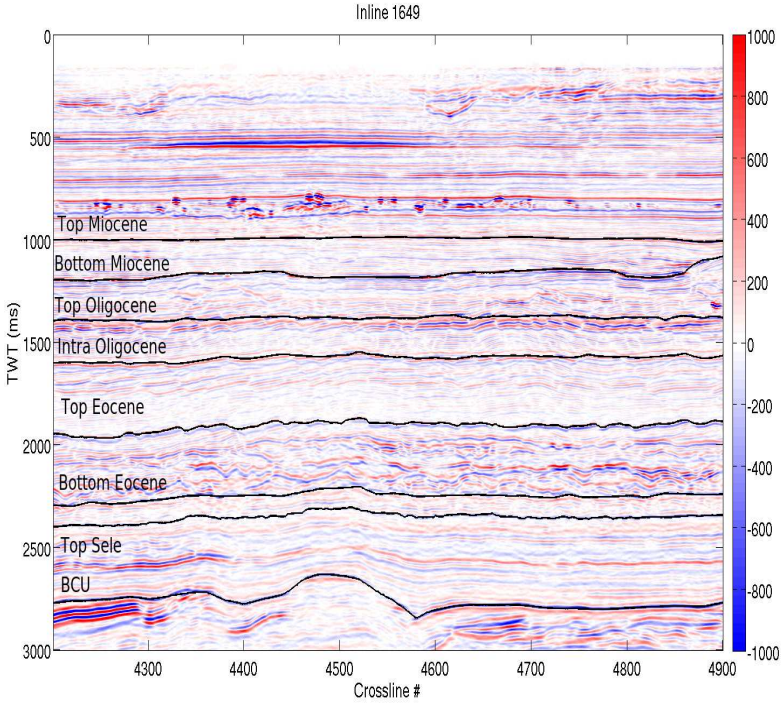

Figure 3.11: Stacked seismic data section of inline 1649. The 8 reflections used in this study are highlighted by black lines. Here, the acronym BCU stands for Base Cretaceous Unconformity.

Figures 3.12a and 3.12b show the histogram of the frequency exponent, b, and the inverse frequency coefficient, 1/a (equation 3.2) respectively. Histograms of the frequency-dependent parameters are shown because the aim of this study is to ascertain whether frequency-dependent Q can be measured, and not to analyse the interval frequency coefficient and exponent of frequency-dependence. There is a well defined probability distribution to both the coefficient and exponent values. The statistics of both distributions, up to the fourth statistical moment about the mean, are summarized in table 3.4. A 2D histogram of the coefficient/exponent

pairs is given in figure 3.13. The well-focused histograms of the measured 1/a and b values in figures 3.12a and 3.12b demonstrate the ability of this method to obtain stable estimates of frequency-dependence of Q in real data. For comparison the histogram of $1/Q$ values estimated assuming a frequency-independent $1/Q$ is given in figure 3.14.

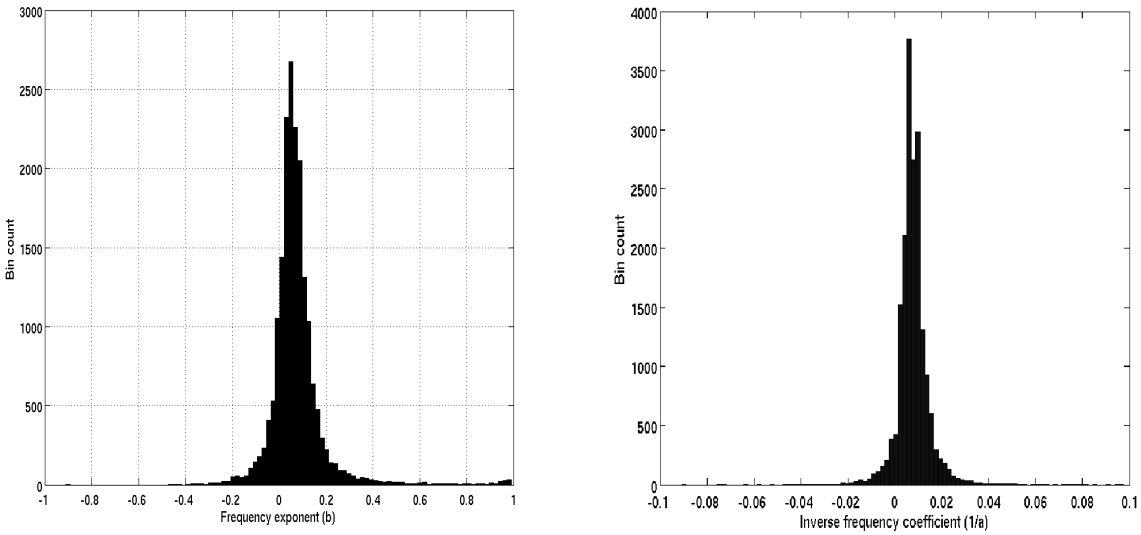

(a) (b)

Figure 3.12: Histograms of frequency exponent (a) and inverse frequency coefficient (b) estimated from pre-stack supergathers.

Although figure 3.12a shows that the distribution of frequency exponent values is well peaked around the mean value of 0.09, it also shows that some large exponent values ($|b|$ >0.2) are also found, but specifically associated with inverse frequency coefficients close to 0 (figure 3.13), for which the attenuation trend on the spectral surface is very weak. Consequently, the dominant feature of spectral ratio surface may easily be due to small peaks and notches caused by interference, which may be best fit by a curved surface, mimicking frequency-dependent attenuation. A small cluster of points with $|b|$ >0.2 exists around an inverse coefficient of 0.01 and these relatively high frequency exponent values can arise from a number of situations; the attenuation quality factor may, of course, actually be frequency-dependent. Alternatively, interference is the dominant feature on a spectral ratio surface (whether because the attenuation may be low and

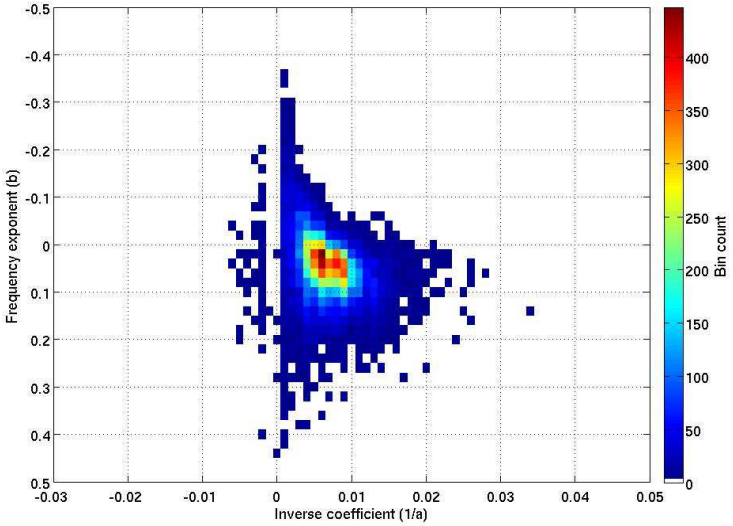

Figure 3.13: 2D histogram of the estimated coefficient/exponent pairs from the North Sea survey.

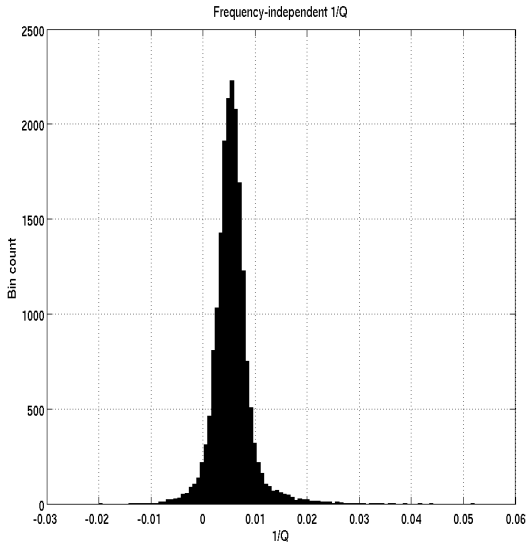

Figure 3.14: Histogram of frequency-independent $1/Q$ values estimated via PSQI for the same data and frequency bandwidth used to estimate the frequency-dependent attenuation coefficient and exponent.

therefore its expression in the spectral ratio is weak, or because the interference is itself strong, due to, for example, closely spaced strong, high amplitude reflec-

tions). Scattering attenuation can also have a strong, non-power-law frequency dependence in the seismic bandwidth (Mangriotis et al. (2013), Van Der Baan (2001)).

Scattering attenuation has been previously estimated from well logs using the wave localization method of Van Der Baan (2001), finding a maximum value of $1000/Q_{sc}$=3 within the 10Hz to 55Hz bandwidth (Beckwith and Clark (2014)) for the interval 2450m to 2800m measured depth. This would mean that scattering attenuation could be a significant contributor to the measured effective Q values. However, this value of scattering attenuation comes from measured depths of between 2450m and 2800m, and is an averaged estimate of scattering attenuation within that region. When using an analysis window of 45m, roughly equivalent to one seismic wavelength, scattering attenuation can be as high as $1000/Q_{sc}$=10, although only for a 50m interval. Other intervals may have substantially different values of scattering attenuation, dependent on their layering properties and thus a significant contribution to effective attenuation from scattering effects cannot be ruled out. The average scattering attenuation between 1400m measured depth and 2800m measured depth is $1000/Q_{sc}$ <1 though and thus probably not a significant contributor to the effective attenuation.

Figure 3.15a is a map of the estimated exponent values for the full interval between top Miocene and the Base Cretaceous Unconformity (BCU). The distribution of high exponent values is reasonably spatially coherent. Regions of high exponent values exist around inline 1630-1660, crossline 4450-4470: Figure 3.15c shows a spectral ratio surface from within it (inline 1649, crossline 4470) and in contrast figure 3.15d shows a spectral ratio surfaces from the low exponent zone around inline 1649, crossline 4650.

The spectral ratio surface in figure 3.15a, which corresponds to the high exponent zone, shows a clear break in the slope of the surface around 30Hz whereas the spectral ratio surface for the low exponent zone (figure 3.15d) does not. This abrupt change in trend of the surface means that a frequency-dependent Q value is unlikely to be the source of the high exponent value, as the surface would curve gradually rather than change abruptly. Again, it is necessary to take a step back and investigate the spectra which formed and the spectral ratio surface. A local, temporary drop in the relative high frequency content of the top Miocene

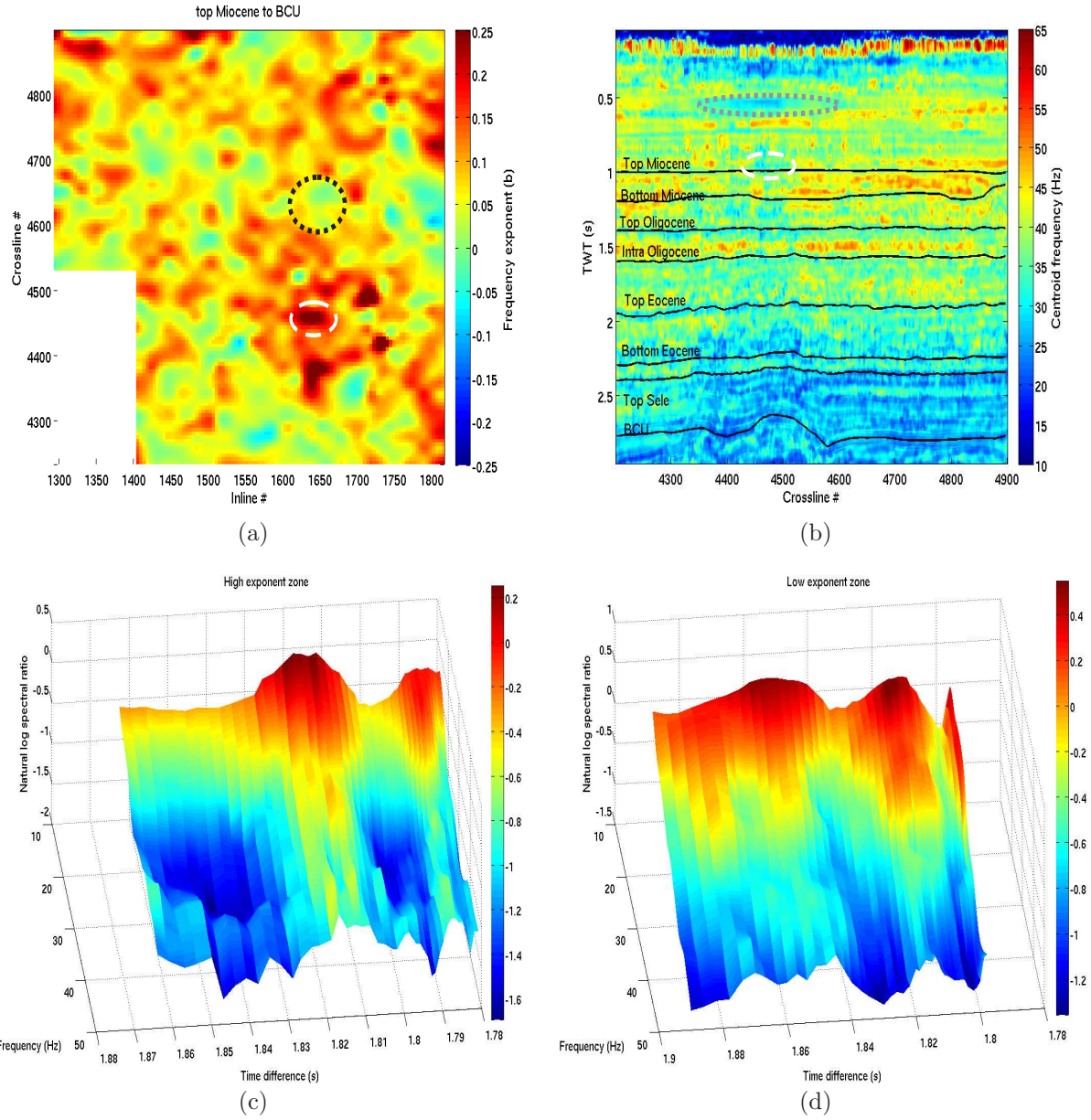

Figure 3.15: Estimated exponent values for the top Miocene to BCU interval with regions of low (black dotted line) and high (white dashed line) highlighted (a). b.) Centroid frequency section estimated via a short-time-Fourier-transform (STFT). White dashed and gray dotted ellipses correspond to low frequency shadows under amplitude anomalies. c.) Spectral ratio surfaces formed from the pre-stack data centered around inline 1649, crossline 4470 (white dashed ellipse in (a)). d.) Spectral ratio surface centered around inline 1649, crossline 4650 (blacked dotted ellipse in (a).

reflection can be seen in figure 3.16.

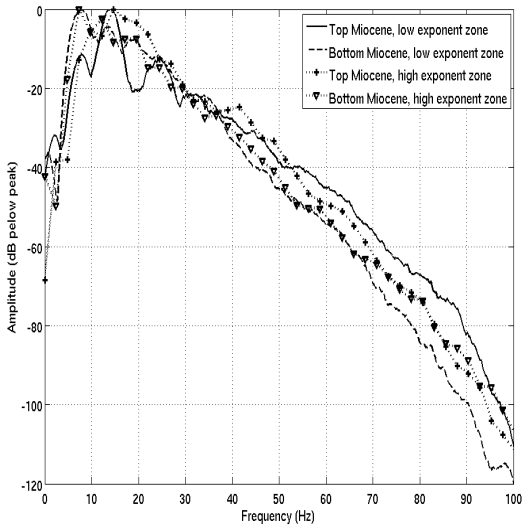

Figure 3.16: Amplitude spectrum of the top and bottom Miocene reflections for the high and low exponent zones in decibel.

To investigate this phenomenon further, the centroid frequency (Quan and Harris (1997)) was estimated as a function of time and crossline for the inline 1649 via a short-time-Fourier-transform (STFT) of each trace. This centroid frequency section (figure 3.15b) highlights that a low centroid frequency region exists 25ms above the top Miocene reflection at crosslines 4420-4500. The centroid frequency around the top Miocene is extracted, smoothed to the size of the supergathers used, and plotted in figure 3.17. High exponent regions are coincident with drops in the centroid frequency beyond that which is expected from the scatter around the background value. The exponent map given in figure 3.15a is for the top Miocene to BCU interval and is therefore estimated from reflections from the top Miocene and from the BCU. If the top Miocene reflection is compromised then the estimated inverse coefficient and exponent for that region will also be compromised.

It is worth noting that this drop in centroid frequency is below a high amplitude anomaly in the seismic data (figure 3.11): a similar feature can be seen in the centroid frequency section below the high amplitude anomaly at 500ms in

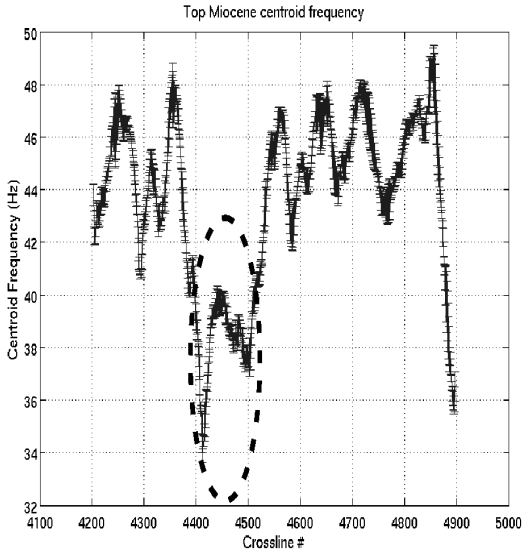

Figure 3.17: Centroid frequency around the top Miocene reflection smoothed to the size of a pre-stack supergather. The black dashed ellipse corresponds to the white dashed ellipses in figures 3.15b and 3.15a.

the seismic data. This localized lowering of frequency could be due to any of the mechanisms highlighted by Ebrom (2004) in explaining low frequency shadows in seismic data.

3.1.6 Discussion

While the overall aim is to encourage and facilitate measurement of frequency-dependent Q, we also now carry out a conventional constant-Q inversion using the same supergathers and the same regression bandwidth of 10Hz to 55Hz, to provide a 'benchmark' against which to review our case study results for frequency-dependent Q. The resultant histogram of 1/Q values is given in figure 3.14.

Table 3.4 lists some of the statistical properties of the distribution of estimated inverse coefficients and exponents for the frequency-dependent Q estimates as well as statistics for the $1/Q$ values estimated from constant-Q inversion. The distributions of exponent and inverse coefficient values are right-skewed, i.e. the distribution of coefficients is skewed towards high values, and the distribution of exponent values is skewed to more positive values. They are also leptokurtic

Table 3.4: Statistical properties of the distribution of frequency-independent 1/Q values as well as frequency-dependent inverse coefficient ($1/a$) and exponent (b) values. $\bar{\sigma}$ is a standard deviation, σ is the standard error and γ is the kurtosis excess.

	mean	median	$\bar{\sigma}$	σ	skewness	γ
1/Q	0.0055	0.0054	0.0036	0.0001	1.3	10
1/a	0.0074	0.0070	0.0055	0.0001	1.8	15
b	0.074	0.060	0.120	0.001	3.1	20

(more peaked than a Normal distribution) with narrow, well-defined peaks and a small range of values. The distribution of estimated frequency-independent 1/Q values also shows a right skewed distribution and is leptokurtic. No censoring of estimated exponent and inverse coefficient values (b, $1/a$) based on goodness of fit statistics was carried out in the statistical analysis.

It is expected that the distribution of $1/Q$ and $1/a$ values should be right skewed, as few, if any, negative values should exist whilst the distribution is generally assumed to peak at around $1/Q$=0.0067 (Q=150, a typical value used in seismic processing) but can extend to over $1/Q$=0.15. Although one would expect a right skewed distribution, positive skewness value, the absolute value of skewness is unknown prior to analysis of the results. The kurtosis excess value of the distribution of $1/Q$ is also hard to determine a priori. Although one could use prior knowledge to estimate what general order of magnitude of kurtosis to expect given prior knowledge of the study area. For example, a homogeneous medium would have a single valued distribution and essentially an infinite kurtosis value whereas a medium with equally distributed $1/Q$ values would have a kurtosis value of -6(n^2+1)/5(n^2-1), where n is the number of samples used.

The effective attenuation at 32.5Hz (corresponding to the center of the bandwidth used for spectral ratio surface fitting) is taken and compared, in Figure 3.18a, to estimated frequency-independent $1/Q$ values. The correlation between the estimated effective attenuation at 32.5Hz from the frequency-dependent $1/Q$ parameters and the estimated frequency-independent $1/Q$ values is shown in Figure 3.18b and shows a statistically significant correlation, with a correlation coefficient of 0.9993. This means that the hypothesis that the two distributions seen in Figure 3.18a are from the same underlying distribution cannot be rejected at

the 95% confidence interval.

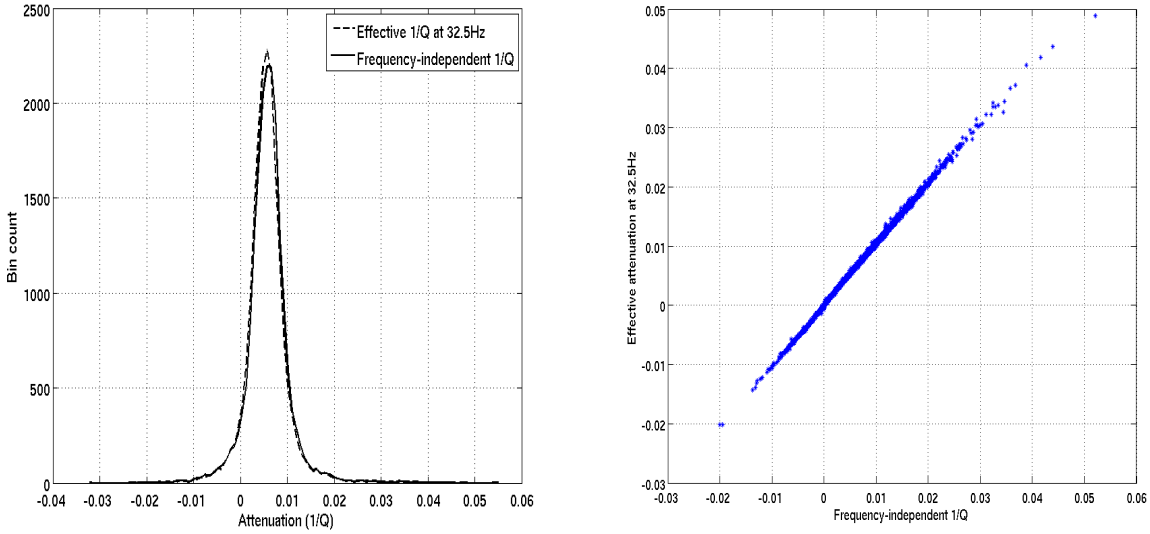

(a) (b)

Figure 3.18: Histograms comparing estimated frequency-independent Q to the effective frequency-independent Q estimated at 32.5Hz from the frequency-dependent coefficient and exponent (a) and a plot of effective attenuation at 32.5Hz against the frequency-independent 1/Q measured at the same location (b).

This agreement is pleasing, insofar as most actual Q estimates are made under constant-Q algorithms and assumptions: for many purposes, such values may well be perfectly adequate. We would *not*, though, want it to be taken as an argument against measuring frequency-dependent Q. Certainly, in this case, the variation across the bandwidth is modest - the frequency exponent is only 0.090±0.001, but this small value conceals a statistically significant Q change of approximately 12%, from 1/Q of 0.0062±0.0001 at 10 Hz down to 0.0055±0.0001 at 55 Hz (or Q=161±2 up to 182±2). Amplitude loss rates for the constant-Q ($1/Q$=0.0056, Q=179) and the frequency-dependent Q results are indeed negligibly different at the high frequency end of the bandwidth, but give amplitudes some 5-10% different, after travel times of approximately 3 seconds, at the low-frequency end. However, it is a very stable result, consistent across all reflector pairs and hence intervals (Figures 3.11 and 3.12a): hence, it may represent an intrinsic attenuation characteristic, rather than scattering attenuation whose expression is likely to be

far more erratic from one reflector/interval to another.

Our frequency-dependence is lower than that measured by Carey et al. (2008) who found a frequency-dependent Q with exponent of 0.6-0.87. It is larger in magnitude, but of opposite sign, to the exponent values between -0.39 to -0.66 estimated by fitting power-law curves to the results of Sams et al. (1997) in the bandwidth 0Hz-100Hz (figure 3.1) - a perfectly credible circumstance, given the range of exponent characteristics described by Gurevich and Pevzner (2015), but nevertheless suggesting (given that 1/Q must be 0 at 0Hz) an 'absorption peak' is present between 0Hz and 10Hz. However, both Sams et al. (1997) and Carey et al. (2008) analyzed data over a relatively small depth range covering unconsolidated strata, and propose that for deeper, more consolidated sediments, such as those encountered in the survey area at depths greater than 1km below the sea floor, the frequency-dependence Q may be lower than that of unconsolidated sediments.

Reid et al. (2001) find a frequency-dependent Q of exponent -1.53 in a North Sea VSP dataset. Although the value is only calculated for one interval in one VSP dataset, it is suggested that the frequency-dependence they find could be due to fracturing, which may be a local effect and, given, our greater range of depths and spatial locations, may be averaged out.

3.1.7 Conclusions

In this paper, measurement of frequency-dependence of the seismic attenuation quality factor values from surface seismic reflection surveys has been investigated. First, an adaptation of an existing attenuation estimation algorithm is proposed to measure the frequency-dependence of attenuation modelled as a power-law with frequency, a model prevalent in literature. Although a power-law form of frequency-dependence is used in this study, the methodology applied could be expanded to any analytically defined form of frequency-dependence of Q. For a frequency-dependence characterized by a larger number of parameters the forward-modelling approach may be too computationally expensive and a non-linear inversion approach will need to be adopted.

The adapted algorithm is tested using a theoretical surface and two synthetic shot gathers, one with a simple underlying model and one in which the under-

lying model is based on scaled and translated blocked well log data. Tests on the theoretical surface with differing levels of noise suggest that the method is accurate (results within 10% of expectations) down to signal to noise ratios of 0.65. The coefficient of exponent of frequency in the frequency-dependent attenuation estimation are solved through forward modelling with an L1-norm, and shown to estimate accurately the frequency-dependent attenuation coefficient and exponent parameters in each experiment.

However, there is a trade-off between the coefficient and exponent of the frequency dependence of the seismic quality factor such that, for example, in the seismic bandwidth, a seismic quality factor described by an inverse coefficient of 0.005 and an exponent of -0.05 (Q=$200f^{-0.05}$) has a similar trend to that of a seismic quality factor with an inverse coefficient of 0.05 and an exponent of 0.5 (Q=$20f^{0.5}$); this arises because the coefficient describes the gradient of the spectral ratio and the exponent describes the curvature of the spectral ratio.

Low frequencies can be useful in detecting frequency-dependent attenuation quality factor values. A synthetic test using a range of regression bandwidths starting at 0Hz to 35Hz and ending at 40Hz to 80Hz, in 5Hz increments, shows that at frequency bandwidths starting at >15Hz the estimated coefficient and exponent become increasingly erroneous. Low frequency content will be a great asset in estimating frequency-dependent seismic quality factors, however the effective medium seen by low frequencies is larger than for the central frequency of the propagating wave, meaning that any estimated frequency-dependence of attenuation will likely be of lower temporal resolution than estimated frequency-independent seismic attenuation.

Frequency-dependent attenuation has then been estimated for a pre-stack 3D OBC dataset in the central North Sea for 22 intervals corresponding to 8 seismic horizons. The distribution of estimated frequency-dependent attenuation at 32.5Hz, the centre of the frequency bandwidth used for the surface fitting, can not be proven to be statistically different from the distribution of frequency-independent $1/Q$ values estimated from the PSQI algorithm, with a correlation coefficient of 0.9993.

The distribution of frequency-dependent attenuation exponent values has a non-zero median value of 0.06 and is a sharply peaked distribution, with a kurtosis

excess of 20. Hence, for this study area, the low exponent values reveal that an assumption of frequency-independent Q may, in fact, be adequate.

Higher values of exponent, those with $|b|$ >0.2, are associated with spatially local drops in centroid frequency located less than a few tens of milliseconds below high amplitude anomalies, which suggests that the spectrum of the reflection in these regions is adversely affected by low frequency shadows, or mechanisms which can contribute to the formation of low frequency shadows.

Estimating frequency-dependent attenuation parameters of 1/a and b has provided more information than a constant-Q inversion. This extra information, in the form of the frequency exponent, has been shown to be useful in detecting interference on reflections and could be used as quality control check for constant-Q inversion.

Arguably the most significant result presented here is that the seismic attenuation quality factor, estimated from surface seismic reflection data within the bandwidth 10Hz to 55Hz, has a small but detectable and statistically significant frequency-dependence. Whilst, in this specific dataset, the frequency-dependence is modest, it has been quantified. As has been done for frequency-independent Q over the last few decades, making frequency-dependent Q estimation standard practice will result in much deeper understanding of the relationship between petrophysical parameters and attenuation and contribute towards efforts to estimate permeability directly from seismic data.

3.2 Energy partitioning term ratios

3.2.1 Introduction

Attenuation has been described as a process that preferentially degrades the amplitude of the high frequencies of a propagating wave but nevertheless degrades the amplitude of all frequency component (assuming a positive seismic quality factor). The degree to which the amplitude at a certain frequency is degraded depends not only on the seismic quality factor, which describes the attenuation within the medium, but also upon the time a wave spends propagating through an attenuative medium. The time spent within an attenuative medium will increase

with increasing take-off angle as the path length through the medium increases. It follows that the effect of the attenuative medium increase with increasing take-off angle and thus the amplitude-versus-angle (AVA) results will be affected by the attenuation of the medium (as well as contrasts in rock properties across the interface) (Samec and Blangy (1992)).

The PSQI method of estimating seismic quality factor values from pre-stack seismic gathers is described (Reine et al. (2012a)) as being able to simultaneously extract attenuation-free AVA results from spectral ratio surfaces. The PSQI method works within the τ-p domain which has been shown to be superior for AVA analysis than the time-offset ($t-x$) domain (van der Baan and Smit (2006)). However, What is estimated in the PSQI algorithm is not AVA but a ratio of AVA terms modified by transmission coefficients into and out of the interval of interest.

The inversion intercept term described by Reine et al. (2012a) is estimated as the exponential of the zero-frequency component, at each individual time-difference (a proxy for horizontal slowness), of the inversion of the natural log spectral ratio surface in the PSQI algorithm, in the absence of geometrical spreading. Essentially, the intercept terms provides a shift to the natural log spectral ratio values, at every frequency, that can change be different for each value of time-difference.

The inversion intercepts can be described as the product of all reflection and transmission terms down to the seismic horizon corresponding to the bottom reflection of interest divided by those to the top reflection of interest. Assuming that the medium through which the wave travels is the same for the upgoing and downgoing paths within the overburden, then all reflection and transmission terms within the overburden will cancel. What is left, and what constitutes the ratio of the energy partitioning terms, is the product of the downgoing transmission term into the interval of interest, the upgoing transmission term of the signal out of the interval of interest and the reflection term at the bottom reflection of interest divided by the reflection term at the reflection corresponding to the top of the interval of interest.

This is more readily understood in the form given in equation 3.5, where $T_{d,i}$ corresponds to a downwards transmission term across the i^{th} reflector and R_i corresponds to a reflection term at the i^{th} reflector. This assumes that the interval

between the top and bottom reflector of interest is homogeneous, otherwise extra transmission terms will need to be included in equation 3.5 to account for each individual layer. Only two transmission terms are included in equation 3.5 in order to make the problem as simple as possible, with more layers comes more transmission terms and extra variables that need to be taken account of. All reflection and transmission terms are for a propagating compressional wave to a propagating compressional wave, i.e. no mode conversion terms are included.

$$P_{ij} = \frac{T_{d,i} T_{u,j} R_j}{R_i} \tag{3.5}$$

The transmission and reflection terms are given by the Knott-Zoeppritz equations (Knott (1899), Zoeppritz (1919)). The Knott-Zoeppritz equations are large and complex and it can be more insightful to deal with approximate forms of the equations (Avseth et al. (2010)), such as the Aki and Richards approximation (Aki and Richards (2002)). The four terms in equation 3.5 can be easily written using the Aki and Richards approximation to the Knott-Zoeppritz equations.

$$\begin{aligned} T_{d,i} &= 1 - A_{0,i} + C_i \frac{p^2 V_{pi}^2}{1 - p^2 V_{pi}^2} \\ T_{u,j} &= 1 + A_{0,j} - C_j \frac{p^2 V_{pj}^2}{1 - p^2 V_{pj}^2} \\ R_k &= A_k + B_k p^2 V_{pk}^2 + C_k \frac{p^4 V_{pk}^4}{1 - p^2 V_{pk}^2}, \end{aligned} \tag{3.6}$$

Here, the sine functions have been swapped for the product of interval compression wave velocity (V_p) and horizontal slowness (p) via Snell's law (the cosine and tangent functions are also substituted in a similar manner). The variables A, B and C correspond to the AVO intercept, gradient and the far offset effects

of the amplitude versus angle (AVA) function and are detailed in equation 3.7.

$$\begin{aligned} A &= \frac{1}{2}\left(\frac{\Delta V_p}{\overline{V_p}} + \frac{\Delta\rho}{\overline{\rho}}\right) \\ B &= \frac{1}{2}\frac{\Delta V_p}{\overline{V_p}} - \frac{2\overline{V_s}^2}{\overline{V_p}}\left(\frac{2\Delta V_s}{\overline{V_s}} + \frac{\Delta\rho}{\overline{\rho}}\right) \\ C &= \frac{1}{2}\frac{\Delta\rho}{\overline{\rho}}, \end{aligned} \tag{3.7}$$

Here ΔV_p is the difference between the interval compressional velocity for successive layers and $\overline{V_p}$ is the average interval compressional velocity across an interface, similarly for shear wave interval velocity (V_s) and density (ρ).

3.2.2 Inverting the inversion intercepts

To test if it is possible to gain useful information, such as individual AVO intercept and gradient terms, from the inversion intercepts, an inversion scheme first needs to be set up for the variables A, B, and C in equation 3.7. The equation 3.5 is not linear in all of the variables A, B and C for both reflections. In this case a non-linear inversion is adopted which relies on the derivatives of equation 3.5 with respect to the variables A, B and C to form updates to some supplied initial guess which will then converge on a minimum residual value.

The rock properties given in the model in figure 3.2 will be used to form the inversion intercepts given by the two interfaces shown and will then by inverted for using an initial guess which is close to the true A, B, C variable values and then using an initial guess of the variables which may be assumed given no a priori information. The results are given in table 3.5.

The results of the first inversion test which use initial guess values for each variable which are on average 17% in error with the expected values has returned variables which more accurately match the expected variable values, with an average error of 12%. However, the second inversion, which has an initial guess not based on any a priori information, has returned variables values with an average error of 93%, it has not recovered the expected values. The average deviation of each point in the resultant inversion intercepts using the variable values in table 3.5 for the first and second inversion is $4\text{x}10^{-6}$% and $8\text{x}10^{-5}$% respectively, show-

Table 3.5: Table of expected AVA gradient, intercept and far offset effect given the model in figure 3.2. Also given is the initial guess of the variables used as input for the non-linear inversion and the resultant variables from the non-linear inversion.

		Inversion 1		Inversion 2	
Variable	Expected	Initial guess	Result	Initial guess	Result
A_1	0.311	0.300	0.316	0.100	0.089
B_1	0.036	0.030	0.052	0.000	-0.013
C_1	0.200	0.250	0.239	0.000	0.001
A_2	0.291	0.300	0.296	0.100	0.076
B_2	0.043	0.030	0.044	0.000	0.003
C_2	0.200	0.250	0.210	0.000	0.035

ing that both sets of variables accurately fit the expected inversion intercepts. For all intents and purposes, without a priori knowledge of the true values, both inversions are a success. Figure 3.19 shows a comparison of the individual amplitude versus slowness (AVp) curves for the compressional wave reflection coefficients given the values in table 3.5. Even though both sets of curves are different, and indeed even have a different sign of gradient for one of the AVp curves, they provide very similar inversion intercepts (given by equation 3.5).

3.2.3 Discussion

Logically, it is not surprising that different sets of the variables A,B and C can provide the same inversion intercepts. As a thought experiment, if we reduce the inversion intercepts down to a single number, x, and ask what two numbers when divided give x, then we have an infinite set of answers which are all correct. Similarly, it is not possible to find the individual AVp curves which constitute the inversion intercepts.

However, if good well control is available then a priori information about the amplitude versus slowness curves can be estimated form the well log data and used to provide a reasonable initial guess for the non-linear inversion of the inversion intercepts. Note that the inversion scheme used thus far has been tested on noise-free numerical data.

The main drawback of the inversion intercept model given in equations 3.5, 3.6 and 3.7 is that the medium is assumed to be non-dispersive, i.e. velocity

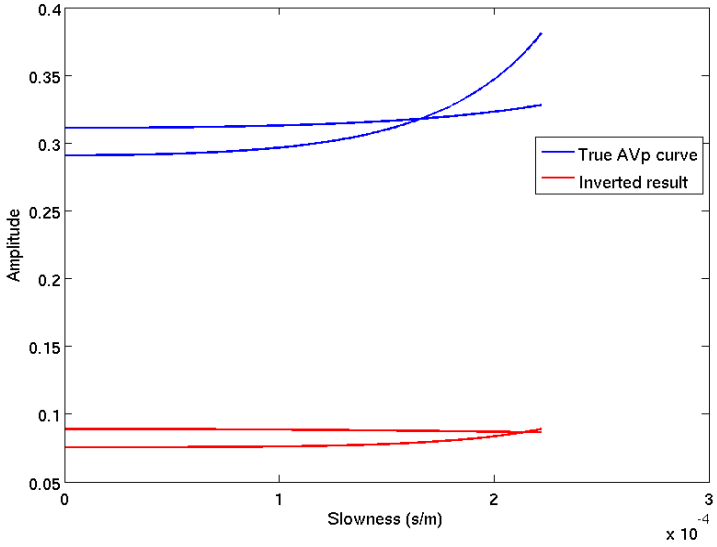

Figure 3.19: A comparison of the amplitude versus slowness curves of the reflection coefficients given by the two inversion tests given in table 3.5. Both sets of variables given in table 3.5 provide the same inversion intercepts described by equation 3.5.

is not a function of frequency. Velocity dispersion is a necessity for a wave to remain causal whilst being attenuated (see Aki and Richards (2002) chapter 5.5 for example). Chapman et al. (2006) use an equivalent medium theory based on a squirt flow concept in which fluid-saturated rock is replaced by a homogeneous, isotropic equivalent medium in which the velocity and attenuation is a function of frequency and find that the frequency dependence of velocity can be significant in AVO interpretation. Chapman et al. (2006) also find that, through a frequency-dependent reflection coefficient, highly attenuative media can actually boost the high frequency content of a signal.

To include the effect of dispersion in the PSQI algorithm, then it would be necessary to include velocity dispersion in equation 3.7 and then invert the natural log spectral ratio surface and the modified inversion intercepts jointly. Replacing each compressional wave velocity term in equation 3.7 by the velocity dispersion relation given by Kjartansson (1979) (equation 3.8) or Futterman (1962) (equation 3.9), following this through to the inversion intercepts in equation 3.5 and inverting a natural log spectral ratio surface for not only Q but all the AVp

parameters is a very complex task.

$$\begin{aligned} V_p(\omega) &= V_{p,0}\left(\frac{\omega}{\omega_0}\right)^{\gamma} \\ \gamma &= \frac{1}{\pi}\tan^{-1}\left(\frac{1}{Q}\right) \end{aligned} \tag{3.8}$$

$$V_p(\omega) = V_{p,0}\left(1 - \frac{1}{\pi Q_0}\ln\left(\frac{\omega}{\omega_0}\right)\right)^{-1} \tag{3.9}$$

References

Adam, L., M. Batzle, K. T. Lewallen, and K. van Wijk, 2009, Seismic wave attenuation in carbonates: Journal of Geophysical Research: Solid Earth, **114**, B06208. 70

Aki, K., and P. Richards, 2002, Quantitative seismology: Univ Science Books. 69, 102, 105

Avseth, P., T. Mukerji, and G. Mavko, 2010, Quantitative seismic interpretation: Applying rock physics tools to reduce interpretation risk: Cambridge University Press. 102

Beckwith, J., and R. Clark, 2014, Improved spectral estimates for attenuation studies: EAGE Technical Program Extended Abstract. 92

Biot, M. A., 1956, Theory of propagation of elastic waves in a fluid-saturated porous solid. i. low-frequency range: The Journal of the Acoustical Society of America, **28**, 168–178. 70

Birch, F., and D. Bancroft, 1938, Elasticity and internal friction in a long column of granite: Bulletin of the Seismological Society of America, **28**, 243–254. 69, 70

Bruckshaw, J. M., and P. C. Mahanta, 1961, The Variation of the Elastic Constants of Rocks with FREQUENCY*: Geophysical Prospecting, **9**, 65–76. 69, 70

Carey, W. M., A. D. Pierce, R. E. Evans, and J. D. Holmes, 2008, On the exponent in the power law for the attenuation at low frequencies in sandy sediments: The Journal of the Acoustical Society of America, **124**, EL271–EL277. 71, 73, 98

Chapman, M., E. Liu, and X.-Y. Li, 2006, The influence of fluid sensitive dispersion and attenuation on avo analysis: Geophysical Journal International, **167**, 89–105. 105

Collins, F., and C. C. Lee, 1956, Seismic wave attenuation characteristics from pulse experiments: Geophysics, **21**, 16–40. 69

Dasgupta, R., and R. Clark, 1998, Estimation of q from surface seismic reflection data: Geophysics, **63**, 2120–2128. 72

Dvorkin, J., and A. Nur, 1993, Dynamic poroelasticity: A unified model with the squirt and the biot mechanisms: Geophysics, **58**, 524–533. 70

Ebrom, D., 2004, The low-frequency gas shadow on seismic sections: The Leading Edge, **23**, 772–772. 95

Futterman, W. I., 1962, Dispersive body waves: Journal of Geophysical Research, **67**, 5279–5291. 105

Gemant, A., and W. Jackson, 1937, Xciii. the measurement of internal friction in some solid dielectric materials: The London, Edinburgh, and Dublin Philosophical Magazine and Journal of Science, **23**, 960–983. 69, 70

Gisolf, D., and E. Verschuur, 2010, The principles of quantitative acoustical imaging: EAGE Publications. 88

Gurevich, B., and R. Pevzner, 2015, How frequency dependency of q affects spectral ratio estimates: Geophysics, **80**, A39–A44. 73, 98

Gusmeroli, A., R. A. Clark, T. Murray, A. D. Booth, B. Kulessa, and B. E. Barrett, 2010-06-01T00:00:00, Seismic wave attenuation in the uppermost glacier ice of storglacaren, sweden: Journal of Glaciology, **56**, 249–256. 71

Jeng, Y., J.-Y. Tsai, and S.-H. Chen, 1999, An improved method of determining near-surface q: Geophysics, **64**, 1608–1617. 71, 73

Jones, T. D., 1986, Pore fluids and frequency-dependent wave propagation in rocks: Geophysics, **51**, 1939–1953. 70, 73

Kjartansson, E., 1979, Constant q-wave propagation and attenuation: Journal of Geophysical Research: Solid Earth, **84**, 4737–4748. 105

Knott, C., 1899, Iii. reflexion and refraction of elastic waves, with seismological applications: Philosophical Magazine Series 5, **48**, 64–97. 102

Mangriotis, M.-D., J. W. RectorIII, E. F. Herkenhoff, and J. C. Neu, 2013, Scattering versus intrinsic attenuation in the vadose zone: A vsp experiment: Geophysics, **78**, B49–B63. 71, 92

Mavko, G., and D. Jizba, 1991, Estimating grain-scale fluid effects on velocity dispersion in rocks: Geophysics, **56**, 1940–1949. 70

Mitchell, M., 1998, An introduction to genetic algorithms: MIT Press. 77

O'Connell, R. J., and B. Budiansky, 1977, Viscoelastic properties of fluid-saturated cracked solids: Journal of Geophysical Research, **82**, 5719–5735. 70

Odoherty, R., and N. Anstey, 2006, Reflections on amplitudes: Geophysical Prospecting, **19**, 430–458. 71, 87

Padmos, L., D. Davies, M. Davies, and J. McGarrity, 2010, Using high-density

obc seismic data to optimize the andrew satellites development.: First Break, **28**, 61–67. 88

Pride, S. R., and J. G. Berryman, 2003, Linear dynamics of double-porosity dual-permeability materials. i. governing equations and acoustic attenuation: Phys. Rev. E, **68**, no. 3, 036603. 69

Pride, S. R., J. G. Berryman, and J. M. Harris, 2004, Seismic attenuation due to wave-induced flow: Journal of Geophysical Research: Solid Earth, **109**, n/a–n/a. (B01201). 70

Pride, S. R., J. M. Harris, D. L. Johnson, A. Mateeva, K. T. Nihel, R. L. Nowack, J. W. Rector, H. Spetzler, R. Wu, T. Yamomoto, J. G. Berryman, and M. Fehler, 2003, Permeability dependence of seismic amplitudes: The Leading Edge, **22**, 518–525. 69

Quan, Y., and J. M. Harris, 1997, Seismic attenuation tomography using the frequency shift method: Geophysics, **62**, 895–905. 94

Reid, F. J. L., P. H. Nguyen, C. MacBeth, and R. A. Clark, 2001, Q estimates from north sea vsps: SEG Technical Program Expanded Abstracts, 440–443. 70, 98

Reine, C., R. Clark, and M. van der Baan, 2012a, Robust prestack Q-determination using surface seismic data: Part 1-Method and synthetic examples: Geophysics, **77**, R45–R56. 72, 101

———, 2012b, Robust prestack q-determination using surface seismic data: Part 2 - 3d case study: GEOPHYSICS, **77**, B1–B10. 88

Samec, P., and J. P. Blangy, 1992, Viscoelastic attenuation, anisotropy, and avo: Geophysics, **57**, 441–450. 101

Sams, M., J. Neep, M. Worthington, and M. King, 1997, The measurement of velocity dispersion and frequency-dependent intrinsic attenuation in sedimentary rocks: Geophysics, **62**, 1456–1464. 13, 70, 73, 74, 98

Sato, H., M. C. Fehler, and T. Maeda, 2012, Seismic wave propgataion and scattering in the heterogeneous earth : Second edition: Springer-Verlag. 71

Schmidt, H., 1987, Safari. seismo-acoustic fast field algorithm for range independent environments. user's guide: SACLANT ASW Research Centre, **SR113**. 81, 86

Soubaras, R., and R. Dowle, 2010, Variable-depth streamer - a broadband marine

solution: First Break, **28**, 89–96. 87

Tonn, R., 1991, The determination of the seismic quality factor q from vsp data: A comparison of different computational methods.: Geophysical Prospecting, **39**, 1–27. 69

Van Der Baan, M., 2001, Acoustic wave propagation in one dimensional random media: the wave localization approach: Geophysical Journal International, **145**, 631–646. 71, 92

van der Baan, M., and D. Smit, 2006, Amplitude analysis of isotropic p-wave reflections: Geophysics, **71**, C93–C103. 101

Zoeppritz, K., 1919, Erdbebenwellen viiib, on the reflection and propagation of seismic waves: Gottinger Nachrichten, **1**, 66–84. 102

Chapter 4

Estimation of frequency-dependent Q and application of the SDD to the Kinnoull area survey

4.1 Abstract

Attenuation is estimated over the Kinnoull discovery, central North Sea, via analysis of well log, vertical seismic profile, stacked seismic and pre-stack seismic data. Through analysis of well log data, the scattering attenuation in the vicinity of three wells in the Kinnoull region is found to be minimal, with an average $1000/Q_{sc}$ value of 0.36 and a mean characteristic scale length of 1.01m. The estimated scattering attenuation correspond to 4% of the attenuation value estimated from vertical seismic profile data ($1000/Q=10.4\pm2$) co-located with one of the three wells. This is likely an underestimate of the true scattering attenuation as it does not take into account any scattering due to subsurface structure (i.e. it is a 1D assumption). Due to interference, attenuation is only estimated accurately to a depth of 2300m but an attenuation peak was found to coincide with the interval between the intra-Oligocene and top Eocene reflections.

The median 1000/Q estimated from stacked seismic data, 9.2, is in agreement

with that estimated from the vertical seismic profile data of 10.4. Maps of attenuation as a function of inline and crossline are found to not correlate with average centroid frequency or average energy within the same interval on a consistent basis. Attenuation estimated from pre-stack seismic data shows an imprint of the acquisition geometry for shallower intervals and no correlation with average centroid frequency or average energy for any intervals analysed. The median 1000/Q estimated from the pre-stack seismic data, 4.5, is not in agreement with the stacked seismic data or the vertical seismic profile data.

The difference between the 1000/Q values estimated from the stacked and pre-stack seismic data is due to the extra processing required to produce a stack, such as normal-moveout-correction and stacking, and the increased signal-to-noise in the stacked data.

4.2 Introduction

As a seismic wave propagates in the subsurface it loses energy per cycle via a variety of mechanisms that are dominant at different frequencies (Pride et al. (2004), Mller et al. (2010)). This loss of energy per cycle leads to a preferential loss of high frequency content with propagation distance in the subsurface, which subsequently leads to a loss of temporal resolution. The preferential loss of high frequency content of a propagating seismic wave is termed seismic attenuation and is often defined by a unitless variable, Q, whereby $1/Q$ is proportional to loss of energy per cycle of a wave. The loss of temporal resolution with depth can be corrected for via inverse-Q filtering (Wang (2008)), though this requires an accurate estimate seismic attenuation quality factor (Q) with the subsurface. With an accurate model of seismic Q, phase only inverse-Q deconvolution can be applied to improve seismic-to-well misties by correcting for the phase rotation that accompanies dispersion (Ziolkowski et al. (1998)). Dispersion occurs when different frequencies of a wave travel at different velocities and seismic velocities almost always increase with frequency (Mavko et al. (2009))

The seismic wave energy can be redistributed through reflection and refraction, spread out by geometric spreading and lost through intrinsic attenuation due to fluid flow induced by the propagating wave (Chapman et al. (2002), Mller

and Gurevich (2005)). Seismic wave energy can also be redistributed by scattering due to finely layered lithology in the subsurface (Mangriotis et al. (2013), Van Der Baan (2001) and Odoherty and Anstey (2006)) and can also mimic the effect of intrinsic attenuation via preferentially lowering the amplitude of higher frequencies. It may not be possible to separate out the effects of scattering attenuation from intrinsic attenuation, and indeed even reflection and transmission coefficients are a problem if seismic Q was to be determined from the loss of amplitude alone.

Methods for estimating the scattering attenuation of a medium based on well log data (Van Der Baan (2001), Shapiro et al. (1994)) are available and can be used to separate out scattering from intrinsic attenuation at a well location, but are limited in their spatial extent. Scattering attenuation can also be estimated through analysis of full waveform synthetic seismograms (Pevzner et al. (2016)).

Seismic attenuation lowers the bandwidth of seismic data by preferentially cutting out higher frequencies, thus changing the shape of the wavelet. Estimates of attenuation can be made by analyzing the change in the shape of the wavelet or the changing spectrum of the wave as it propagates through the subsurface (Tonn (1991), Quan and Harris (1997)). The spectral ratio method (Bath (1974)) is a popular method by which to estimate attenuation. The spectral ratio method works by analyzing the change in the frequency content of a seismic wave as it propagates in the subsurface. It does this by comparing the spectrum of the seismic wave before and after it has propagated a known distance in the subsurface. The extra path length travelled by the deeper/later wave will have caused more attenuation to occur and higher frequencies to be lost to a greater extent. The spectral ratio method can be expressed in the equation

$$\ln\left(\frac{A_i(f)}{A_j(f)}\right) = \ln(PG) - \frac{\pi f \Delta t_{ij}}{Q_{ij}} \tag{4.1}$$

Here A_i is the amplitude spectrum of the wavelet after a propagation time t_i and A_j is the amplitude spectrum of the wavelet after a propagation time t_j, where $t_j < t_i$. P is the energy partitioning term and G is the geometric spreading factor, both are assumed to be independent of frequency. Δt_{ij} is the time difference between t_i and t_j and Q_{ij} is the attenuation in the interval between

i and j. The spectrum of the source wavelet (A_0), if known, can be set to be A_j and a cumulative attenuation estimated with propagation time, which can then be converted to an interval attenuation by the equation

$$\frac{1}{Q_{ij}} = \frac{1}{\Delta t_{ij}} \left(\frac{t_j}{Q_{0j}} - \frac{t_i}{Q_0 j} \right) \tag{4.2}$$

Here Q_{0j} is the cumulative attenuation between the source wavelet and the wavelet at a propagation time of t_j.

Attenuation, in particular Q, has been used in a wide range of geophysical scenarios. For instance, Dasgupta and Clark (1998) discriminate between prospective sediments and metamorphic/crystalline lithology based upon the estimated Q values. They also show a clear decrease in Q coincident with the maximum thickness of a reservoir known to contain gas, and derive an even lower Q for the reservoir interval itself. Reine et al. (2012b) also show Q values estimated via the PSQI method, which show correlation with the presence of top gas in a reservoir. Q variation with offset and azimuth (QVOA) has been used to characterize fractures (Behura and Tsvankin (2009)). Q has also been used as an aid for impedance inversion (Singleton (2008)).

In this paper we will first analyze well log data from three wells located in the region of the Kinnoull discovery, central North Sea, for scattering attenuation. Attenuation will then be estimated from the downgoing direct wave in a vertical seismic profile (VSP) dataset, shot in one of the wells used in the scattering attenuation analysis, and we will show that VSP data may not always be useful in estimating attenuation at every depth interval.

The spectral ratio method will then be applied to stacked surface seismic data and pre-stack surface seismic data over the Kinnoull field. To help estimate spectra for use in the spectral ratio method, the signal-dependent-distribution (SDD) will be used to estimate the frequency content of reflections. The attenuation values estimated from the stacked and pre-stack seismic data will be compared to average centroid frequency and average energy maps, as well as being compared to each other, for several intervals and compared to the average attenuation estimated from the VSP dataset.

Finally, Frequency-dependent attenuation will also be estimated for the sur-

face seismic data by modification of the PSQI algorithm to allow for a frequency-dependent Q.

4.3 The Kinnoull field

The Kinnoull field is a satellite field of the Andrew field in the central North Sea and is part of the Andrew area development project. The Kinnoull reservoir is in the Paleocene sandstones, which along with Cretaceous sandstones also form the reservoirs of the Andrew field. The Kinnoull area is overlain by a dense Eocene channel system in which anomalously fast sandstone channels (velocity≈3200m/s) sit amongst slower shales (velocity≈2400m/s). These fast sandstone channels have caused imaging problems below the Eocene interval, which includes the reservoir interval, in conventional towed streamer data. This imaging problem led to the acquisition of a high shot density, wide-azimuth ocean bottom cable (OBC) seismic data set (Padmos et al. (2010)). Three wells in the Kinnoull area, 16/23-7, 16/23-1 and 16/24a-1 along with pre-stack and stacked seismic data and vertical seismic profile (VSP) data will be used in analysing the attenuation signature over the Kinnoull field. Figure 4.1 shows the location of the Kinnoull field relative to the Andrew field (adapted from Padmos et al. (2010)) as well as the location of the three wells used in this study and an outline of the extent of the seismic data.

The pre-stack and stacked data used in this study are from the same acquired data set. The details of the acquisition parameters can be found in Padmos et al. (2010) and a few are summarised in table 4.1. The receiver and sail lines trend North/South.

As the acquisition system is OBC then the effect of receiver ghost notches is typically removed within the PZ summation process (Egan et al. (2007)). The PZ summation process discriminates between up-going and down-going waves but will also attenuate ghost notches as the reflection coefficient on the under side of the sea-surface is negative but the ghost wave will still be downward travelling. Source side receiver ghosts are still present but the second source ghost notch is at 62Hz, outside the bandwidth of analysis, at the near offsets and increasing with offset.

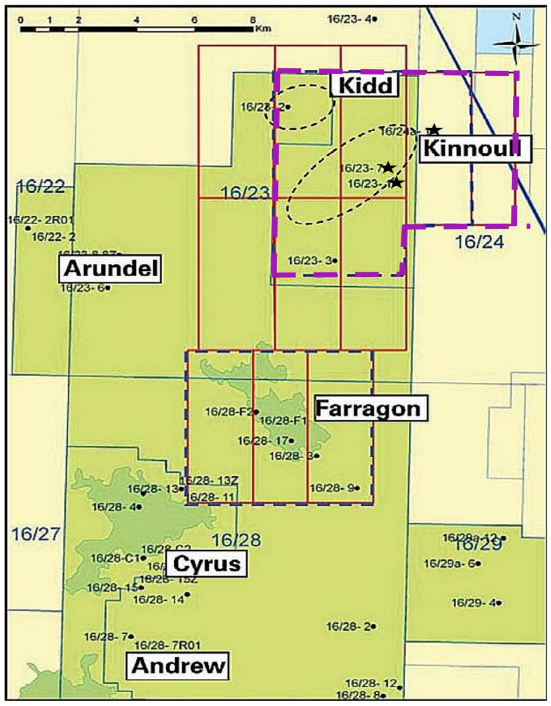

Figure 4.1: Location of the Kinnoull field relative to the Andrew field. The wells used in this study are highlighted by stars and the thick purple dashed line denotes the outline of the extent of the seismic data used in this study. Green boxes are acreage operated by BP, darker green shapes corresponded to reservoirs and the red dashed lines is the extent of the complete OBC survey shot in the Andrews area development.

4.4 Scattering attenuation

The well log data used to investigate scattering attenuation comes from wells 16/23-1, 16/23-7 and 16/24A-1, located over, or near, the Kinnoull discovery in the Andrew Area Development Project, North Sea (Padmos et al. (2010)). The compressional- and shear-wave logs as well as the density logs for the three wells are shown in figures 4.2 to 4.4. Where both density and compressional-velocity logs are available, the method of Mangriotis et al. (2013) and Shapiro et al. (1994) has been applied to estimate scattering attenuation. Where only velocity logs are available, the method of Van Der Baan (2001) (similar to that of Shapiro and Zien (1993)) has instead been used to estimate scattering attenuation, as it does

Table 4.1: Acquisition parameters for the Andrews areas OBC survey. Adapted from Padmos et al. (2010), some parameters vary slightly, such as record length, to adapt the data for the purposes of this study.

Receiver line length	6000m
Receiver line spacing	375m
Receiver group interval	25m
Sail line increment	100m
Shot point interval	25m (flip/flop)
Gun depth	6m
Record length	3s
Water depth	60m-70m
Maximum offset	5500m

not require density logs.

To estimate the depth dependence of scattering attenuation, the analysis method has been applied to 45m (equivalent to the wavelength of a wave which reflects at 1.2km depth) rolling windows of well log data (figures 4.2 to 4.4), the spacing of measurements in the log data is 0.153m. A maximum scattering attenuation estimated using the same methods, but for the entire depth range of the well log, is also given in table 4.2.

The scattering attenuation given by Van Der Baan (2001) and Shapiro et al. (1994) is frequency-dependent where the maximum attenuation occurs at a frequency dependent upon the scale length value, a, which is a measure of the wavelength of variability in the velocity and density logs about a background trend (a mean value usually or a linear fit to the velocity or density log data). For example, a high value of the scale length, a, denotes a low frequency variation on the background trend of the velocity or density well log data, where as a lower value of a denotes a higher frequency variation around the background trend. The degree of variation of the velocity and density logs around their background trends gives rise to the magnitude of the attenuation. White et al. (1990) report finding scale lengths (referred to as correlation lengths in their paper) of 1.5m to 3m in four sets of well log data. The method has been applied more recently in the CO2CRC Otway project, in which scattering attenuation was found to play only a minor role in the overall attenuation (Galvin et al. (2013)).

Figures 4.5 to 4.7 show the scattering $1/Q$ profiles from three wells located

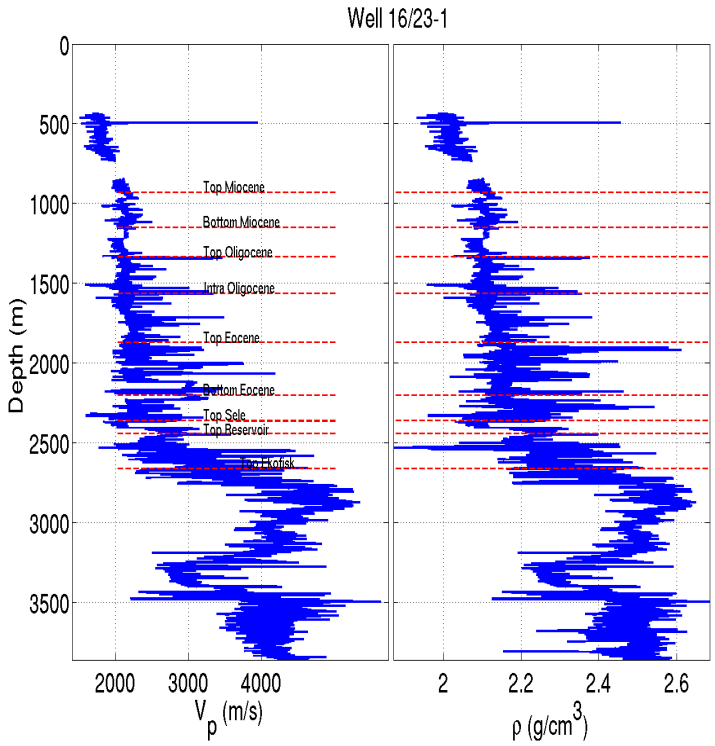

Figure 4.2: Compressional- and shear-wave sonic logs and density logs for wells 16/23-1.

estimated using a 45m rolling window. Different colours in figures 4.5 to 4.7 highlights the use of different methods, with the blue section of the scattering attenuation profile denoting scattering attenuation estimated by the method of Shapiro et al. (1994) whilst a red line uses the method of Van Der Baan (2001). To compare scattering attenuation, which is frequency-dependent, to constant-Q attenuation, estimated from VSP data, the maximum scattering attenuation within the 10Hz to 55Hz bandwidth will be used to give a maximum scattering attenuation that could be present within the analysis bandwidth used to estimate constant-Q.

The maximum scattering attenuation for all three scattering $1/Q$ profiles in figures 4.5 to 4.7 is 0.0135 (Q_{sc}=74). However, this only exists over a relatively short depth range of 100m. Well 16/23-1 shows a high variability in the scattering attenuation over the depth range 1300m to 3600m, whereas well 16/23-7 shows only one, much smaller depth range that contains significant scattering attenua-

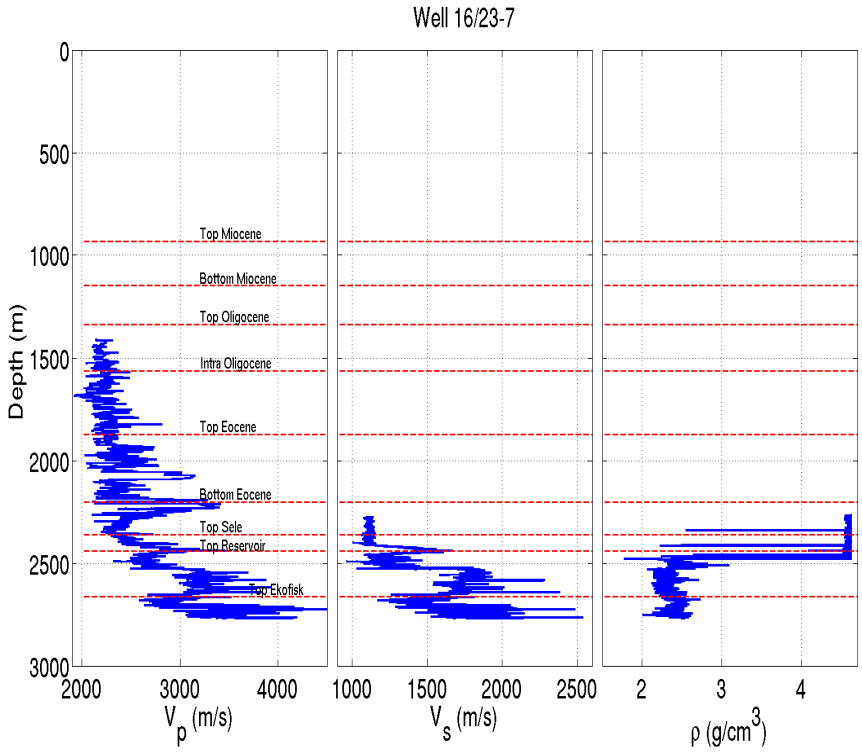

Figure 4.3: Compressional- and shear-wave sonic logs and density logs for wells 16/23-7.

tion, with peak scattering attenuation of $1/Q_{sc}$=0.013 (Q_{sc}=77) between depths of 2400m and 2500m. The peak scattering attenuation is lower in well 16/24A-1, with a peak $1/Q_{sc}$=0.0085 (Q_{sc}=118) but with several peak s of relatively high scattering $1/Q$ (peaks of Q_{sc} between 140 and 150) in the depth range 2150m to 2700m.

Although the mean and median scattering $1/Q_{sc}$ from table 4.2 suggest a small degree of scattering attenuation, with a maximum mean scattering attenuation of $1000/Q_{sc}$ of 1.2 (Q=833), the maximum scattering attenuation estimated from the entire well log would suggest a significant contribution to scattering attenuation, with a maximum scattering attenuation of $1000/Q_{sc}$=16 (Q=63).

An underlying assumption of the methods of Shapiro and Zien (1993) and Shapiro et al. (1994) is that the velocity and density logs can be described by a variation around a constant background value. However, if there is a change in lithology or acoustic properties with depth (by compaction for example), then the

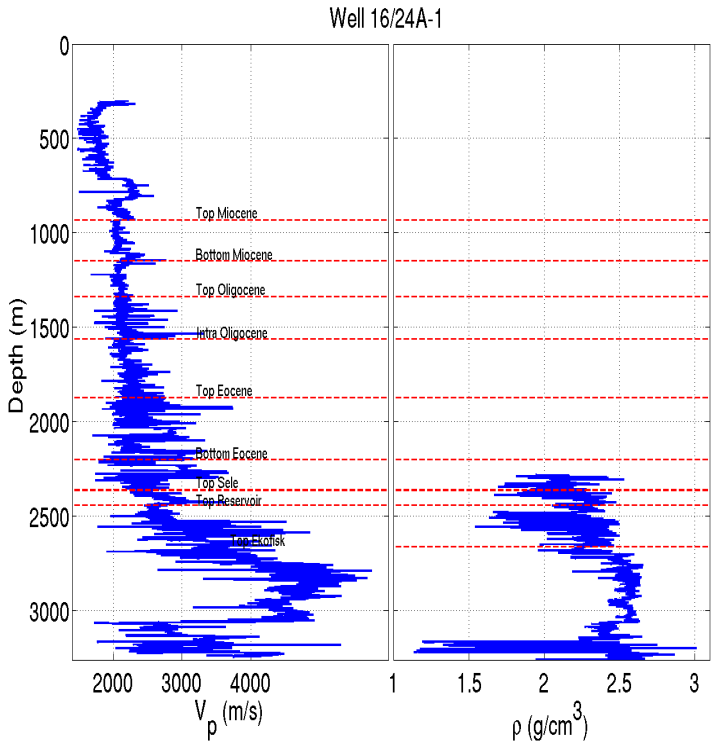

Figure 4.4: Compressional- and shear-wave sonic logs and density logs for wells 16/24A-1.

underlying assumption of a variation around a background trend is violated and the resultant estimates of scattering attenuation may be higher than expected. By using a shorter rolling window or by fitting a higher order polynomial to the velocity and density logs can mitigate this effect to some degree, but not entirely. If a log contains, for instance, multiple coal seems, or any abrupt changes in their characteristics, then it will not be possible to accurately fit a polynomial to the highly variant logs to recover the small variations in each different lithology. For this reason, the scattering attenuation values estimated from the entire well log interval (last column of table 4.2) will not be used.

Figure 4.9 shows the histograms of the estimated scale lengths from each well. All three histograms show a distinct peak around 1m and table 4.3 outlines the statistical properties of the histograms. Table 4.3 shows that all three histograms are strongly peaked (leptokurtic), given by a large, positive kurtosis excess and all three are left skewed distributions, denoted by a highly positive skewness

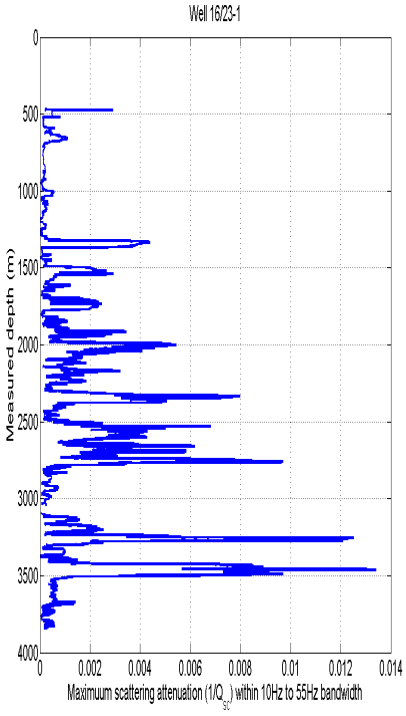

Figure 4.5: Scattering $1/Q$ profile from well 16/24A-1. Scattering attenuation is estimated from the method of Shapiro et al. (1994).

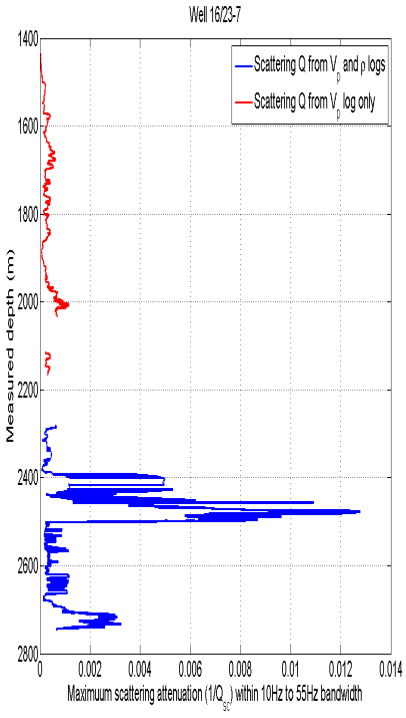

Figure 4.6: Scattering $1/Q$ profile from well 16/23-7. Scattering attenuation estimated from the method of Van Der Baan (2001) is given in red and scattering attenuation estimated from the method of Shapiro et al. (1994) is given in blue.

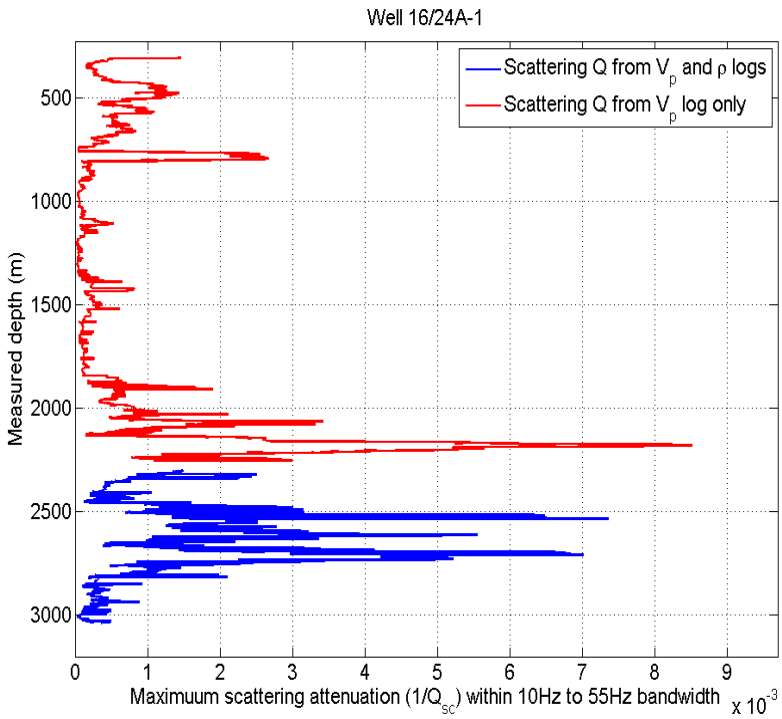

Figure 4.7: Scattering $1/Q$ profile from well 16/24A-1. Scattering attenuation estimated from the method of Van Der Baan (2001) is given in red and scattering attenuation estimated from the method of Shapiro et al. (1994) is given in blue.

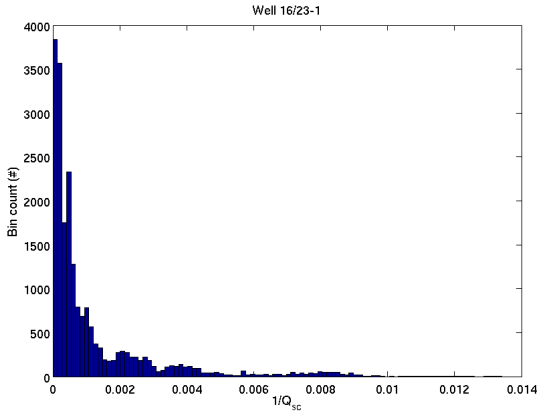

(a)

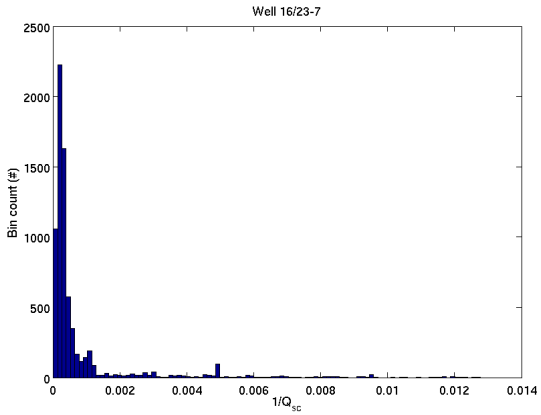

(b)

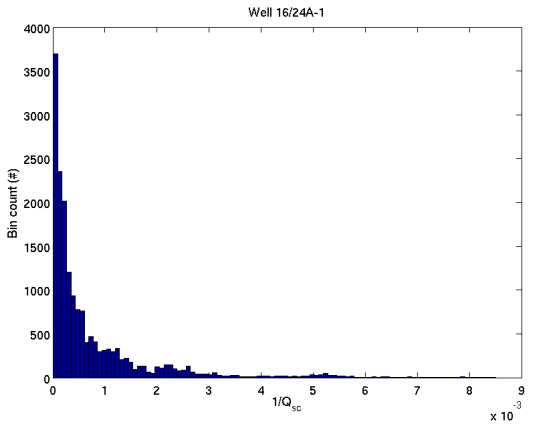

(c)

Figure 4.8: Histograms of the scattering attenuation ($1/Q_{sc}$) estimated for the three wells (from top to bottom) 16/23-1, 16/23-7 and 16/24A-1. The values given are the maximum scattering attenuation within the 10Hz to 55Hz rolling window which can be seen in figures 4.5 to 4.7.

Table 4.2: Statistical properties of the distribution of the maximum $1000/Q_{Sc}$ values estimated in wells 16/23-1, 16/23-7 and 16/24A-1 using a 45m rolling window over the bandwidth 10Hz to 55Hz. $1000/Q_{sc}$ is presented instead of $1/Q_{sc}$ due to the small values of the mean and median scattering attenuation. σ is the standard deviation and γ is the kurtosis excess.

well	mean $1000/Q_{sc}$	median $1000/Q_{sc}$	1000σ	skewness	γ	maximum $1000/Q_{sc}$ from entire log range
16/23-1	1.20	0.49	1.80	2.73	11.20	16.0
16/23-7	0.79	0.29	1.60	4.10	18.87	9.3
16/24A-1	0.77	0.31	1.20	2.97	10.57	5.1

value, although both of these properties can be clearly seen in the histograms themselves. The median scale length is between 0.91m and 1.22m and the mean scale length varies between 2.27m and 2.43m, similar to the values of 1.5m to 3m found in diverse geological environments by White et al. (1990).

Table 4.3: Statistical properties of the distribution of scale length values corresponding to scattering attenuation in wells 16/23-1, 16/23-7 and 16/24A-1. σ is the standard deviation and γ is the kurtosis excess.

well	mean a (m)	median a (m)	σ (m)	skewness	γ
16/23-1	2.43	0.91	4.52	4.00	18.57
16/23-7	2.29	1.22	4.48	4.76	25.93
16/24A-1	2.27	0.91	4.35	4.35	19.75

For some depth intervals, neither velocity or density logs exist. For these intervals, is it possible to gauge scattering attenuation from logs that do exist, such as gamma ray logs? To answer this question, we analyse the correlation between the normalised sum square residuals in the gamma ray log with the scattering attenuation in figures 4.5 to 4.7 over the same 45m rolling window. Table 4.4 shows the correlation coefficient, R^2, of the correlation between the variation in the gamma ray log and the scattering attenuation. It is clear that there is no correlation between the variation in the gamma ray log and the estimated scattering attenuation and thus the gamma ray log can not be used to estimate a pseudo-scattering attenuation value.

It is important to note that any scattering attenuation measured from well log data necessarily involves a 1D assumption. Any scattering attenuation due to

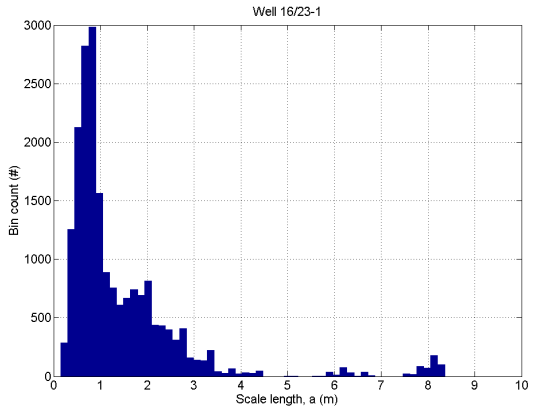

(a)

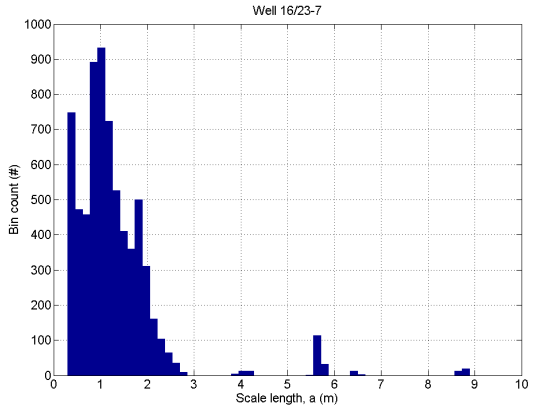

(b)

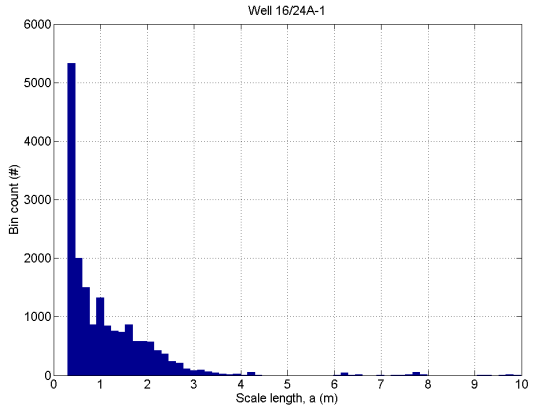

(c)

Figure 4.9: Histograms of the scale length, a, for the three wells (from top to bottom) 16/23-1, 16/23-7 and 16/24A-1.

Table 4.4: Correlation coefficient, R^2 between normalised variation in the gamma ray log and the estimated scattering attenuation in figures 4.5 to 4.7.

well	R^2
16/23-1	0.10
16/23-7	0.10
16/24A-1	0.06

lateral heterogeneities or structure within the subsurface, which will contribute to scattering attenuation at the well location if it is within the Fresnel zone, will not be included in any values presented here. This means that the presented values are likely an under-estimate of the true scattering attenuation within the subsurface. The scattering attenuation is also likely to be spatially variant and this variability will not be captured by any well log based method either, due to the typically sparse distribution of wells within a survey area.

4.5 Vertical seismic profile data

4.5.1 Data overview

A vertical seismic profile (VSP) is an ideal geometry for attenuation studies within the seismic bandwidth. In a vertical seismic profile survey the seismic waveform is recorded at set depth intervals as it propagates. In this manner, it is possible to see changes in the propagating waveform from one depth interval to another and thus quantify the attenuation within that depth interval. As noted by Blias (2012), this process is subject to certain assumptions, namely that the source spectra do not change from one shot to another, the geophone coupling is uniform at all depth intervals and no interference exists from reflected waves, mode converted waves, tube waves (interface waves which travel down the borehole wall) or any other form of coherent arrival.

The vertical seismic profile data used in this case study comes from the Kinnoull field (Padmos et al. (2010)). The survey comprises of a rig-source VSP acquired in well 16/23-7 (Figure 4.1). An 8-level VSI accelerometer array was used to acquire the data which was recorded with receiver spaced at 15.12m depth

intervals between measured depths of 104.1m and 2750.0m relative to the Kelly Bushing (RKB). The number of shots into each depth interval varies between 5 and 8. There was no overlap between shot points. The lateral deviation between the well head and the bottom of the well is 400m. The shot point had a 20m lateral offset form the well head.

The data at depths shallower than 285.3m is poor and was discarded. The data at depths between 1343.9m and 1495.1m is also poor due to washout at the base of the casing and is subsequently omitted from any further analysis. Figure 4.10 shows the stacked vertical and horizontal components of the VSP data, showing the poor data quality around the aforementioned depth intervals. The stacked data, as supplied, has been processed from the raw data. The supplied VSP data had already been preprocessed by way of a 2,5-120,130Hz filter, amplitude recovery equal to the arrival time to the power of 1.6 ($t^{1.6}$) and stacking of traces at the same receiver depth.

4.5.2 Data preprocessing

The VSP data consist of 3-components, X, Y and Z, in cartesian coordinates. However, for any well that is not completely vertical, and in which the source is not located directly above the well, the ray paths from source to receiver will not be in alignment with the gimballed receivers. To correct for this, the X-, Y- and Z-component of the data are vector rotated using equations 4.3 and 4.4 such that the output is now a component which lies along the propagation direction of the wave and two components which are perpendicular to the direction of propagation of the wave.

By applying the rotation matrices given in equation 4.3 and 4.4 the energy in the Y component is minimized with respect to the X component and subsequently the energy in the X' component is minimized with respect to the Z component.

$$\begin{pmatrix} X' \\ Y' \\ Z' \end{pmatrix} = \begin{pmatrix} \cos(\theta_1) & \sin(\theta_1) & 0 \\ -\sin(\theta_1) & \cos(\theta_1) & 0 \\ 0 & 0 & 1 \end{pmatrix} \begin{pmatrix} X \\ Y \\ Z \end{pmatrix} \tag{4.3}$$

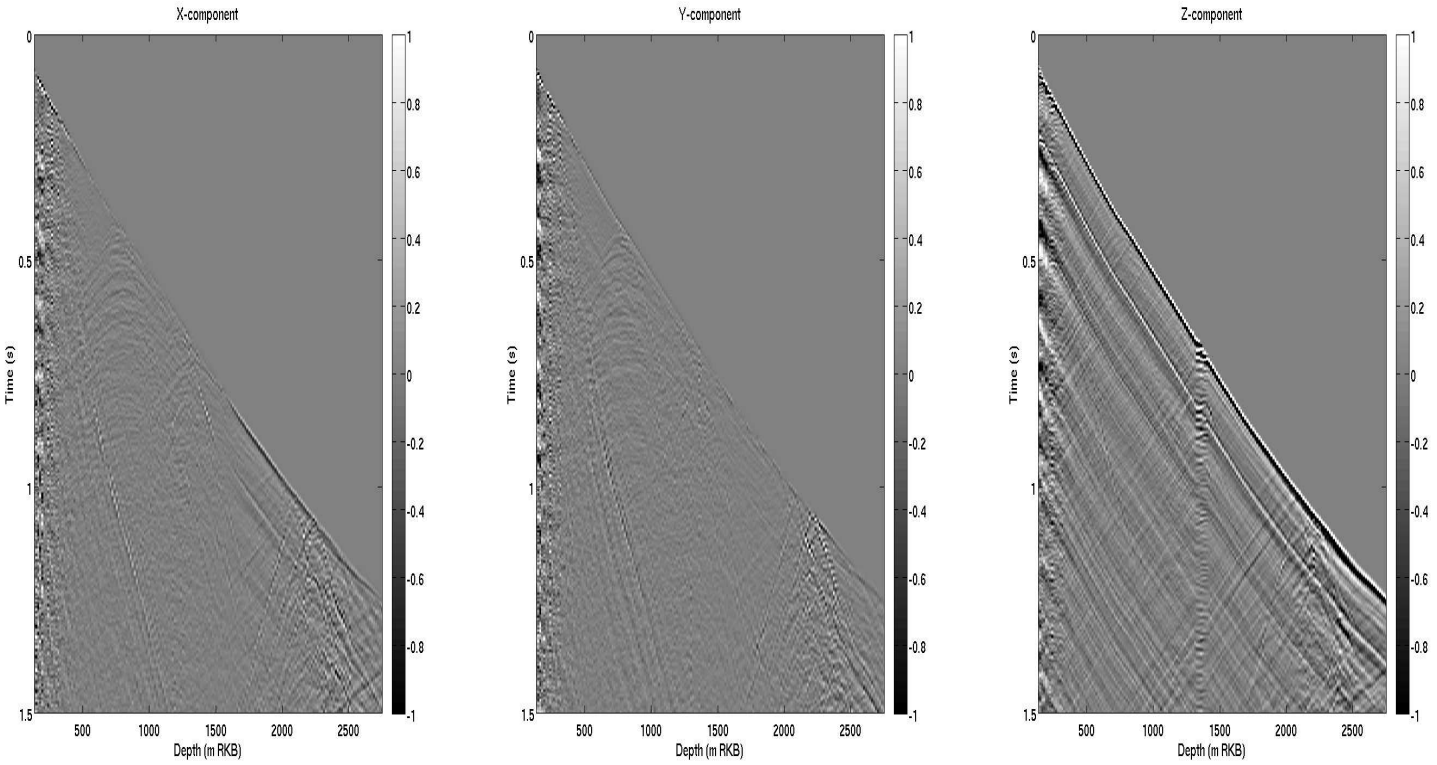

(a) (b) (c)

Figure 4.10: Stacked VSP data from the Kinnoull field, well 16_23-7. From left to right the data corresponds to the first (X) and second (Y) horizontal components and the vertical (Z) component of the seismic wave.

$$\begin{pmatrix} X'' \\ Y'' \\ Z'' \end{pmatrix} = \begin{pmatrix} \cos(\theta_2) & 0 & \sin(\theta_2) \\ 0 & 1 & 0 \\ -\sin(\theta_2) & 0 & \cos(\theta_2) \end{pmatrix} \begin{pmatrix} X' \\ Y' \\ Z' \end{pmatrix} \tag{4.4}$$

Here X, Y and Z correspond to the X-, Y- and Z-component of the VSP dataset, the Z-component being vertical and the X- and Y-components being two orthogonal lateral components. The angle θ_1 is estimated from fitting a line to the hodogram (figure 4.11) of the X- and Y-component data at each depth trace, the arc tangent of the slope of which gives the angle θ_1. In a similar manner, the angle θ_2 is estimated from hodogram analysis of the X'-component and the Z-component.

X' is the horizontal component containing the highest energy but energy still exists in the second horizontal component. An arrival with the velocity of the shear wave exists on the Z'' component due to high levels fo mode conversion at certain depths, such as 2250m measured depth. These depths can be seen in the X- and Y-components where relatively strong down-going shear arrivals branch from the down-going direct compressional arrival.

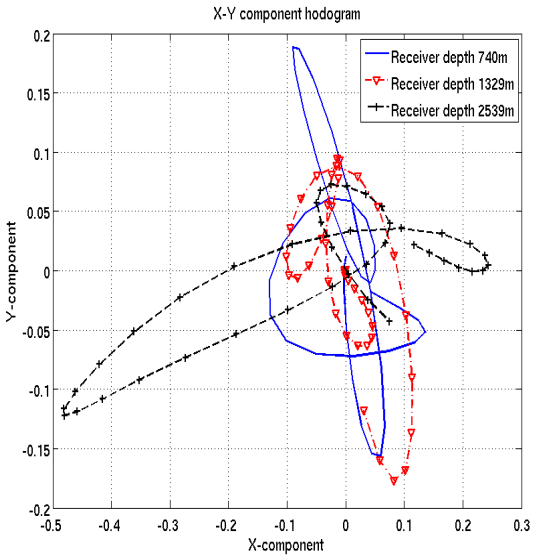

Figure 4.11: Hodogram of X- and Y-component of VSP dataset for 3 receiver depths.

Figure 4.12 show the new Z''- component of the VSP data and Figure 4.13

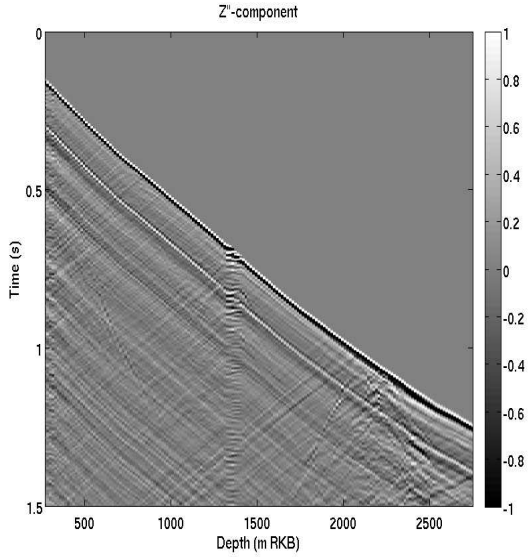

Figure 4.12: Component of VSP parallel to propagation direction of downgoing wave (Z'' in equation 4.4).

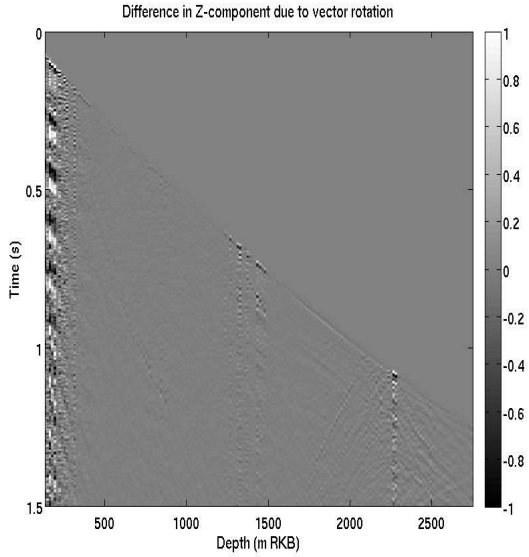

Figure 4.13: Difference between Z'' component and Z-component of VSP data, i.e the energy removed (or added) due to vector rotation to the vertical component (Z) to form the along wave propagation component (Z'').

shows the difference between the Z- and Z''-component of the data. The majority

of the energy in the difference plot, barring the first few noisy traces, exists in arrivals which correspond to the velocity of the shear-wave. There is little difference between the Z component and the Z'' component, as would be expected due to the small deviation of the well from vertical. The comparison is provided as the following analysis of the VSP data could be carried out on the Z-component with similar results, due to the similarity in the Z and Z'' components.

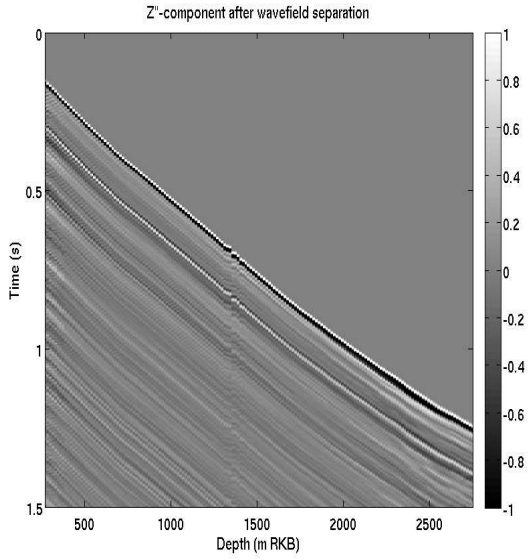

Figure 4.14: Component of VSP parallel to propagation direction of downgoing wave (Z'' in equation 4.4) after wavefield separation.

The last step of preprocessing involves separating the upgoing from the downgoing energy via wavefield separation. The wavefield separation can be accomplished by many methods that include, but are not limited to, filtering the data in the frequency-wavenumber (FK) domain, as upgoing events have opposite dip to downgoing events, or by applying of a median filter to the data after alignment of the direct wave. For this dataset, a median filtering approach was applied to the data with a 7 sample window. A window length of 7 samples was determined to be optimal by qualitatively analysing the wave-separated VSP data. Figure 4.14 shows the Z''-component after application of the median filter and removing the direct wave alignment.

The direct wave is identified as the first arrival in time at each depth interval.

To help identify the arrival time of the peak energy, the analytic amplitude of the signal is formed using the Hilbert transform. The Hilbert transform is used to form the quadrature trace to the recorded signal from which the analytic signal can be formed:

$$z(t) = u(t) + iv(t) \tag{4.5}$$

Here, $z(t)$ is the complex trace which is formed from the real trace, $u(t)$, and the quadrature trace, $v(t)$. In some literature the Hilbert transform of a signal may refer to z, the complex trace, rather than just the process which forms the quadrature trace. Note that the absolute value of the complex trace and analytic signal are generally taken to be interchangeable terms. In a similar manner, trace-envelope, analytic amplitude and instantaneous amplitude are referring to the same property:

$$a(t) = \sqrt{u(t)^2 + v(t)^2} \tag{4.6}$$

Here, $a(t)$ is the analytic amplitude.

The arrival time of the peak energy of the direct wave at each depth interval is then defined as the maximum analytic amplitude. Figure 4.15 shows the instantaneous amplitude of the stacked, vertical component of the VSP data. The peak of the instantaneous amplitude of each of the usable depth intervals corresponding to the down-going direct compressional wave is also marked. Some editing of this automation is necessary if high energy is present later in the depth trace. This editing was carried on the first few traces for instance, in which high energy tubes waves are present. The washout at the base of the 13 5/8ins casing at depths 1330m to 1400m is present as a constant energy in these depth traces. The arrivals which do not travel at the same speed as the direct wave at around 2200m to 2500m do not correspond to any casing shoe but exist between the base of the lower Eocene sand (2200m TVDSS) and the oil-water contact (2495m TVDSS).

For this attenuation study, the spectral ratio method (Bath (1974), Tonn (1991)) is used to carry out attenuation analysis. The spectra at each depth interval, used in the spectral ratio method, are extracted from integration over the

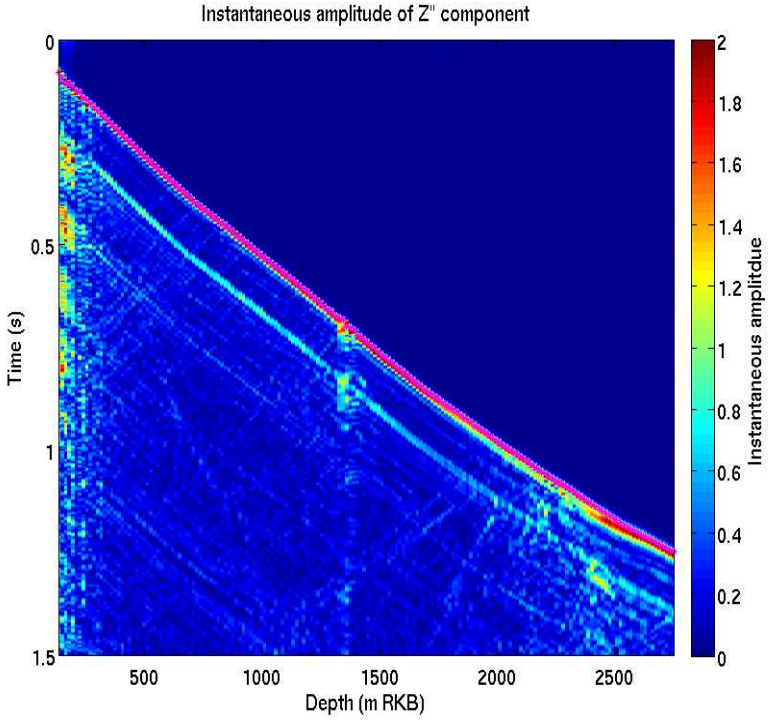

Figure 4.15: Instantaneous amplitude of the vertical component of the stacked VSP data with the peak of the instantaneous amplitude of the direct wave in the depth intervals of interest marked as magenta stars.

time-frequency distributions of each trace formed via the Wigner-Ville Distribution (WVD, Ville (1958)) in a window encompassing the direct wave. The times of the maximum analytic amplitude of the direct wave at each depth interval are used as the time instants on which these windows are to be centred. The spectral ratio of every pair of spectra are formed and an effective $1/Q$ estimated for each pair of receiver depths.

4.5.3 Estimating Q

Attenuation in the form in $1/Q$ is estimated from equation 4.1. The two amplitude spectra that are used in the equation are that of the direct wave recorded at two different depths. A trade-off exists between resolution of measured attenuation in depth and accuracy of the estimated attenuation values.

Spencer et al. (1982) suggest using a receiver separation as small as 200ft only in specific circumstances and highlight that no one particular receiver separation can universally be the optimal value as the ability to accurately estimate Q on a fine scale is dependent upon the level of attenuation itself. For a highly attenuative medium, the effect of attenuation of the spectral ratio is large and relatively easy to measure, however, for low attenuation, the effect on the spectral ratio is small and can be dominated by interference effects, necessitating a larger receiver separation, as attenuation is cumulative.

The receiver separation is determined by analysing the estimated $1/Q$ values for a large range of receiver separations and qualitatively analysing the resultant $1/Q$ profiles. The receiver separation to be used is the smallest which provides a stable $1/Q$ profile, the metric of stable is determined qualitatively.

To estimate the bandwidth over which the regression of the spectral ratio is carried out, the standard deviation of the spectral ratio slopes at all frequencies are analyzed. To avoid an increase in standard deviation due to amplitude differences, each spectral ratio is normalized to be equal to 1 at 10Hz. The effect of attenuation on the spectral ratio values at all depths should vary little at low frequencies with an increase in the variation of the spectral ratio values with increasing frequency. At a certain frequency, dependent upon the level of attenuation, signal bandwidth and, signal-to-noise ratio, the spectral ratio will correspond more to noise than the attenuation and the standard deviation should increase.

Standard deviation of the log spectral ratio curves in figure 4.17 formed from the spectra in figure 4.16 that are 8 receiver separations (≈120m) apart. This amalgamation of $1/Q$ values for different receiver separations is analyzed to determine the optimal the receiver separation to use in forming the spectral ratios from which the effective $1/Q$ will be taken.

Figure 4.17 shows the standard deviation of the spectral ratio slopes as a function of frequency. The standard deviation of the low frequency range (<4Hz, see figure 4.16), where the spectral ratio is dominated by noise, is 55±10. This value is reached again at 130Hz, which puts a limit to the extent of useful frequencies in the shallowest depths, however, as attenuation preferentially cuts out higher frequencies, the spectral ratio curves corresponding to intervals deeper in the section

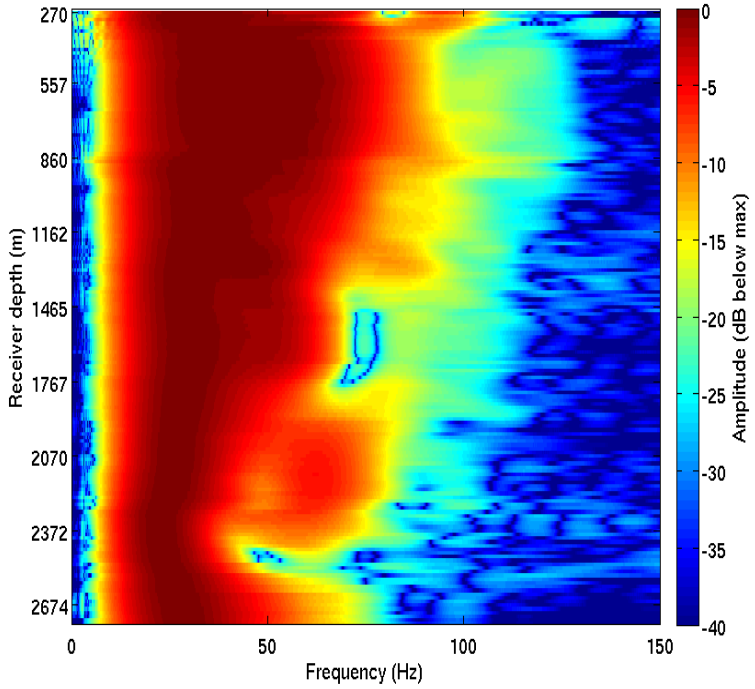

Figure 4.16: Frequency content of the direct, downgoing compressional wave as a function of depth in the VSP survey.

will not have energy at these frequencies. The standard deviation values begin to be erratic at 70Hz and correspond to the limit of useful frequency content in the spectral ratio curves in the deepest part of the VSP data. Therefore the usable frequency content in the downgoing direct wave is between approximately 5Hz and 70Hz, although, to be cautious, only frequency content between 10Hz and 60Hz are used to form the spectral ratio curves from which $1/Q$ values are to be estimated.

This can also be determined from the $F - Z$ spectrum of the Z''-component of the VSP data in figure 4.16. Indeed, an upper limit of 70Hz is found for the 20dB down amplitude contour at 2550m depth in figure 4.20.

Figure 4.19a shows the estimated effective $1/Q$ profile from the spectral ratio method between depths of 500m and 2500m (RKB). Figure 4.19b shows the estimated effective $1/Q$ profile from the spectral ratio method as well the centroid frequency shift method of Quan and Harris (1997) and a smoothed centroid fre-

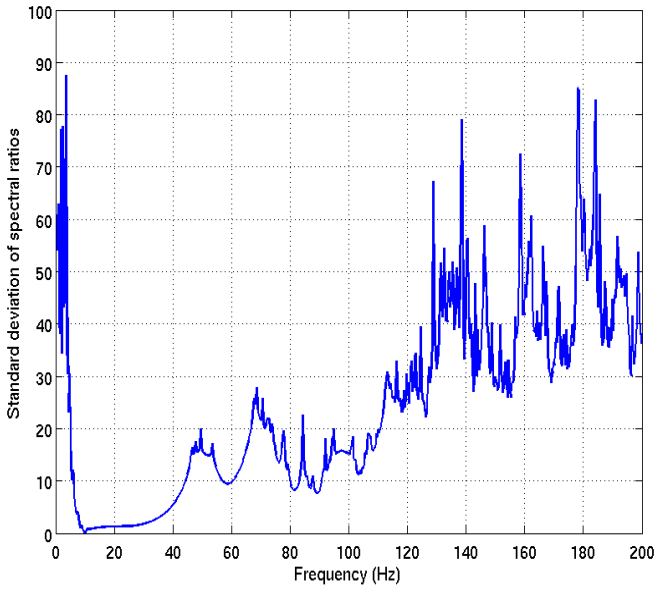

Figure 4.17: Standard deviation of the log spectral ratio curves formed from the spectra in figure 4.16 that are 8 receiver separations (120m) apart.

quency shift $1/Q$ estimation method. It is clear that the centroid frequency shift method is much less stable than either the spectral ratio method or the smoothed centroid frequency method.

Figure 4.18a shows a scatter plot of the attenuation $(1/Q)$ estimated for every possible receiver separations for the 16/23-7 VSP data, the colour corresponds to the error on each estimate. Figure 4.18b shows the same estimated $1/Q$ values in a "tartan triangle" plot where values further from the diagonal correspond to estimates from larger receiver separations.

The smoothed centroid frequency method was developed to counteract the variability in the $1/Q$ values estimated from the centroid frequency shift. The smoothed centroid frequency shift method extracts the maximum and minimum frequency which attain decibel levels of between 0.25dB below peak amplitude in 0.25 dB increments to 25dB below peak (figure 4.20a) in the FZ representation of the direct wave (figure 4.16). These contour envelopes are then fitted by an 11th order polynomial (figure 4.20b). The polynomial fits to the contours are then used to calculate centroid frequency and hence $1/Q$ in the usual manner. An

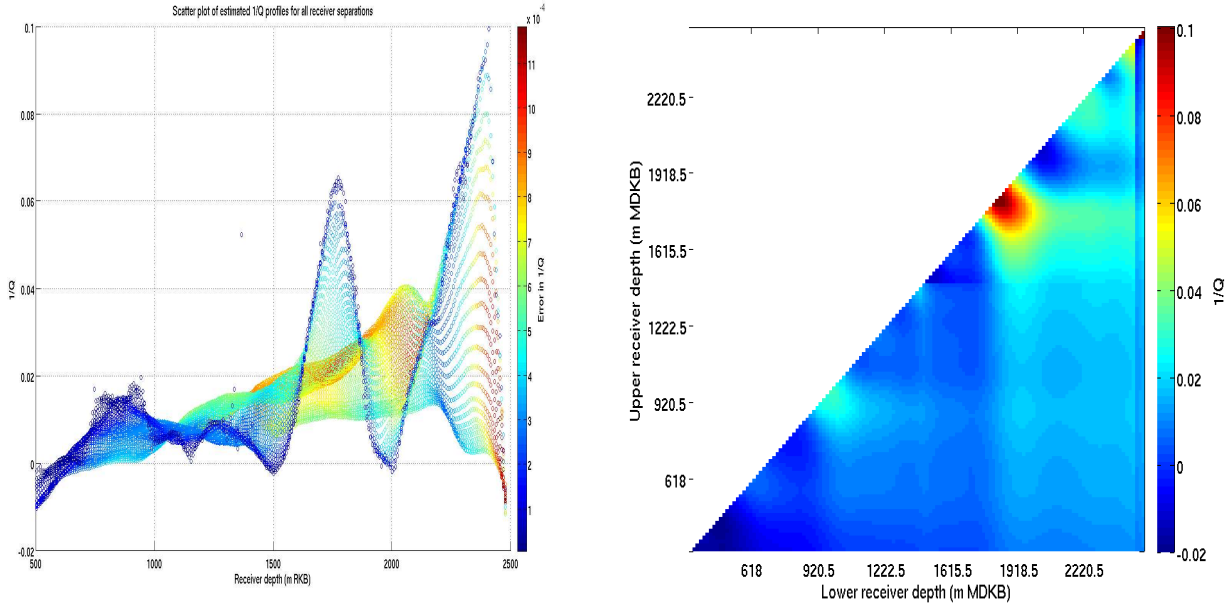

(a) (b)

Figure 4.18: $1/Q$ profiles estimated for every possible receiver separation with colour denoting error on $1/Q$ estimate (a) and a "tartan triangle" plot showing the $1/Q$ estimated at each possible receiver separation (b). The closer to the diagonal in the tartan triangle plot the small the receiver separation used to estimate the $1/Q$ value.

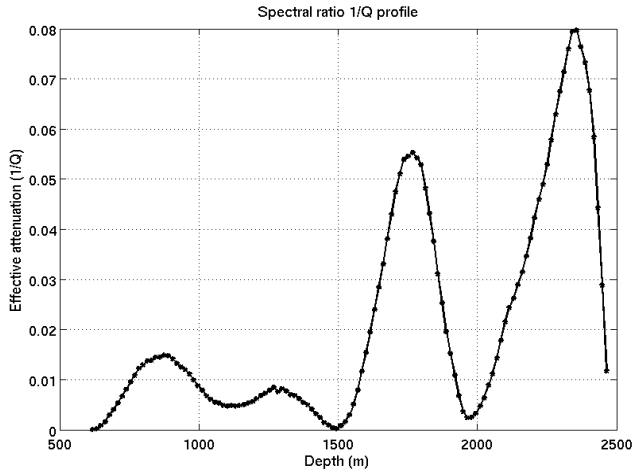

(a)

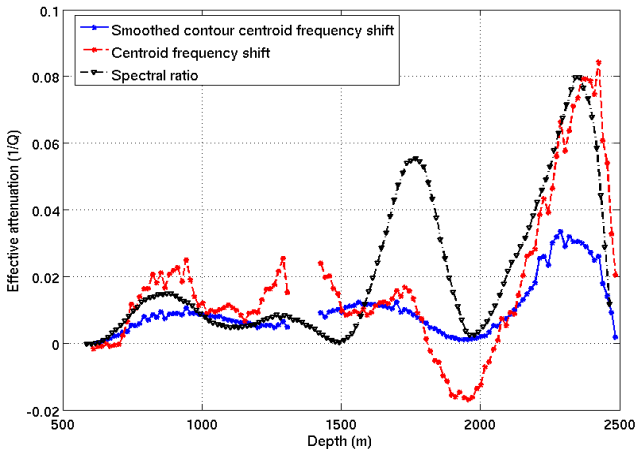

(b)

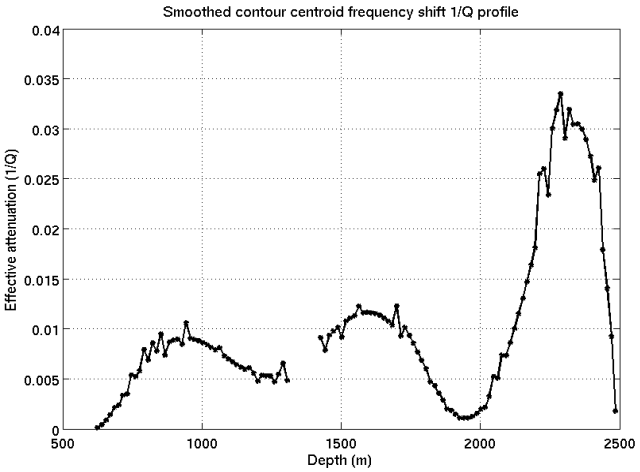

(c)

Figure 4.19: a.) Initial effective $1/Q$ profile estimated via the spectral ratio method. b.) Effective $1/Q$ profile estimated by the spectral ratio, centroid frequency and smoothed centroid frequency methods. c.) Effective $1/Q$ profile estimated from the smoothed centroid frequency method.

11th order polynomial was chosen as it allows for greater spatial variability than a lower order polynomial whilst still allowing the removal of localized changes in the frequency contours not associated with attenuation, because attenuation is a cumulative affect, so sharp changes in frequency content is not to be expected from attenuation alone. An 11th order polynomial was found, through testing various orders of polynomials, to be the lowest order of polynomial which could faithfully represent the frequency contours whilst removing local variations in them. A lower limit of 25dB below peak amplitude was chosen as the noise floor in the FZ data lies at -28dB below peak, so, to be cautious, 25dB below peak was chosen.

All three attenuation profiles show the same trend, a peak in attenuation between 800m and 1000m depth (RKB) with values of $1/Q$=0.01 (Q=100) and $1/Q$=0.015 (Q=67) for the smoothed centroid frequency and spectral ratio methods respectively.

Figure 4.21 shows the $1/Q$ profile estimated via the spectral ratio method in figure 4.19 along with the scattering $1/Q$ profile from figure 4.6 and the subsequent intrinsic $1/Q$ subtracting the scattering attenuation from the effective attenuation estimated in the VSP dataset.

The largest peak in attenuation, situated at 2350m depth and corresponding to $1/Q$=0.0325 (Q=31) and $1/Q$=0.08 (Q=12.5) for the smoothed centroid frequency and spectral ratio methods respectively may not be due to attenuation, but be an artificial peak created by interference. Figure 4.16 shows that there is a very clear interference pattern seen between 2350m and 2550m depth which is lowering the amplitudes of high frequencies and bringing about an artificially high attenuation peak in the $1/Q$ profiles in figures 4.19a-c. The interfering wave can also be seen in the trace envelope of the VSP component parallel to the propagation direction of the direct wave (figure 4.15).

4.5.4 Interference in VSP data

The region 2350m to 2550m depth is interpreted to be an example of a tuning curve. This interference is cause by an arrival separate to the direct wave but close enough to interfere with the waveform of the direct wave. Notch theory (Liner

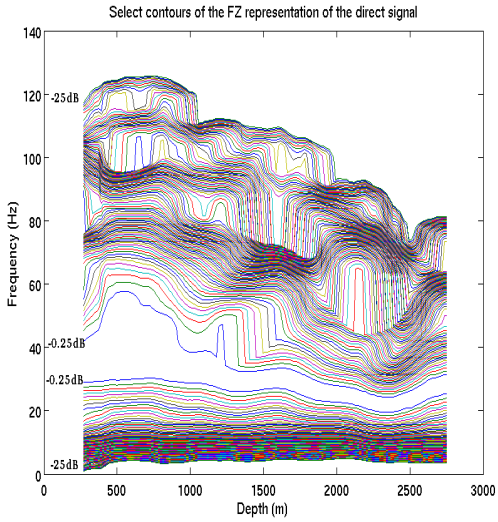

(a)

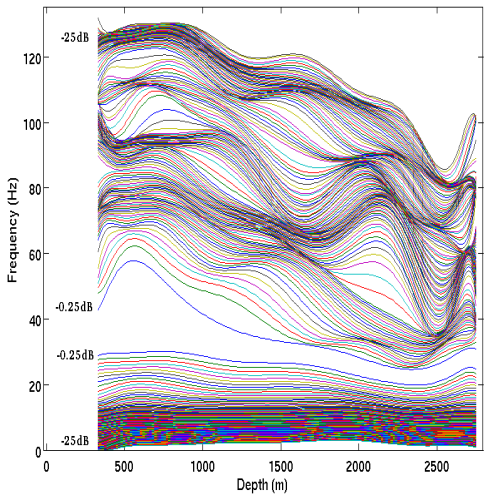

(b)

Figure 4.20: a.) Maximum and minimum frequency content to attain discrete amplitudes of 0.25dB below peak amplitude in 0.25dB increments to 25dB below peak amplitude. b.) 11th order polynomial fits to the contour envelopes seen in (a).

(2012)) is used to characterise this interference phenomenon. In notch theory, the frequency at which a notch occurs is directly related to the time difference between the peak energy of the two interfering waves.

Figure 4.22a shows a zoom of the Z-component of the VSP data around the downgoing direct P-wave arrival showing a change in waveform between approx-

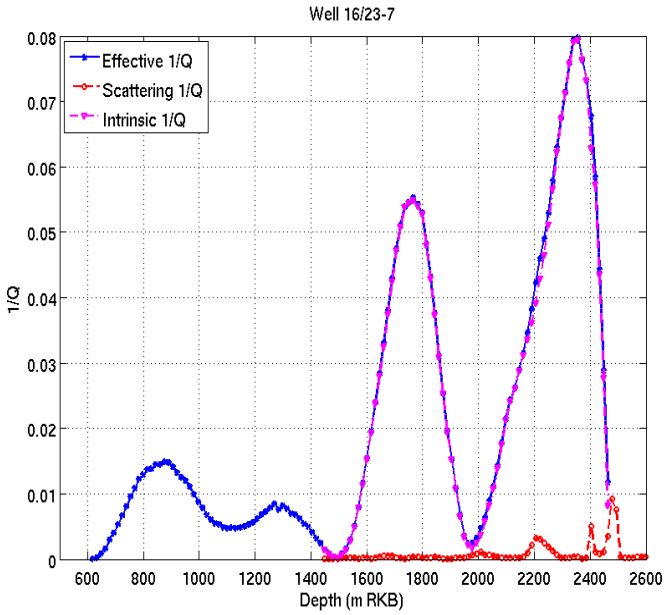

Figure 4.21: Effective attenuation estimated from VSP (blue) data along with the scattering attenuation estimated from well log data (red) and the intrinsic attenuation which results from subtracting the scattering attenuation from the effective attenuation (magenta).

imately 2000m and 2400m depth. Figure 4.22b is an overlay of three traces of the Z-component of the VSP data at depths of 1994m, 2296m and, 2599m depth were the traces at 2296m and 2599m depth have been shifted such that the maximum envelope of the signal aligns with that of the trace at 1994m depth. The change in the waveform between 1994m and 2599m depth is a broadening of the direct wave due to the effect of attenuation but the difference between the trace at 2296m depth and both the trace at 1994m and 2599m depth is significant with two distinct troughs in the main waveform.

$$\begin{aligned} f_s &= \tfrac{n_s}{\Delta t} \\ n_s &= 1, 2, 3, ... \\ f_d &= \tfrac{1+n_d}{2\Delta t} \\ n_d &= 0, 1, 2, .. \end{aligned} \tag{4.7}$$

Here the form of the equation depends upon whether the polarity of the two

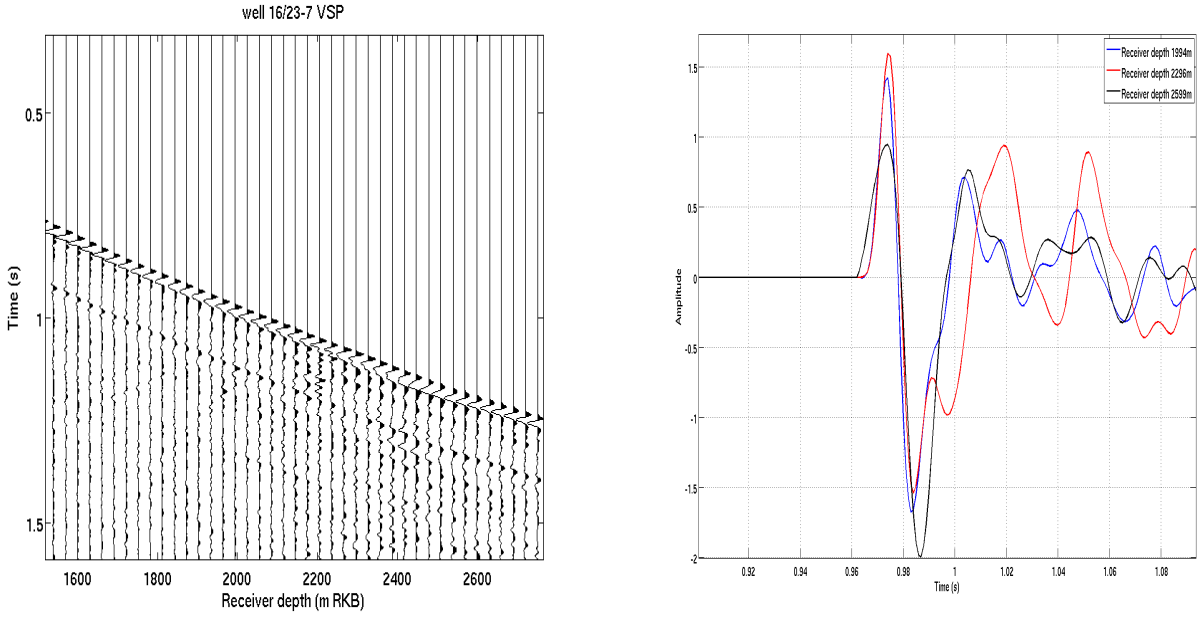

(a) (b)

Figure 4.22: Zoom in to the region in the Z-component of the VSP data which is undergoing interference from an unknown arrival (a) and an overlay of the traces at depths of 1994m, 2296m and, 2599m depth where the latter two traces have been shifted such that their maximum envelope aligns with that of the trace at 1994m depth.

waves is the same (f_s) or different (f_d) and Δt is the time difference between the two waves.

By selecting the minimum spectral amplitudes corresponding with the notch within the depth range 2350m to 2550m it is possible to isolate the tuning curve. By transforming the frequencies at which notches occur back to time differences using equation 4.7 and the timing of the direct wave, it is possible to find the arrival time of the interfering wave as a function of depth.

Figure 4.23 shows the arrival time of the wave causing interference with the direct wave. The wave is travelling downwards but is also travelling faster than the direct wave. As this unknown wave is travelling faster than the direct wave, it is reasonable to assume that it is not propagating along the same direction as the direct wave but at a more oblique angle to the well, hence why the recorded apparent velocity would be higher than the direct wave. Assuming that the wave is propagating at some angle to the well, θ, then simple trigonometry gives the value of θ as 28^o with respect to the direct wave.

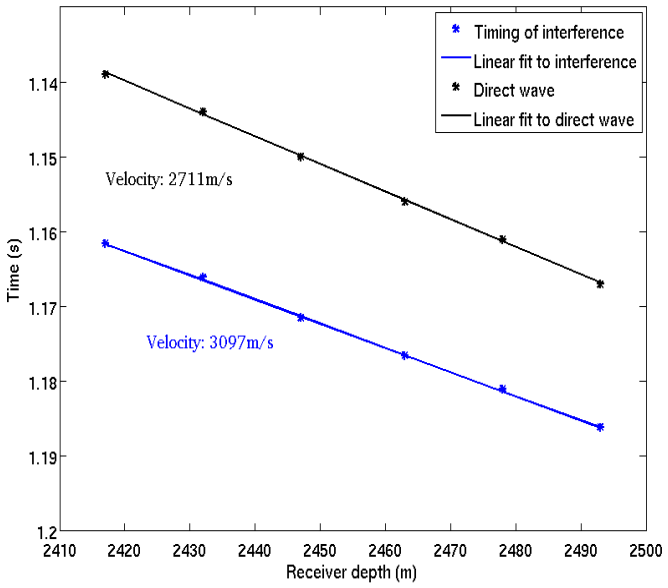

Figure 4.23: Traveltime function of interfering wave in the depth range 2400m to 2550m depth (blue line) compared to the direct wave (black line). A least squares linear trend is fitted, showing that the velocity of the interfering wave is greater than that of the direct wave.

A vespagram is created to ascertain whether or not the interfering waveform is separable from the direct wave, and hence removable from the VSP data. If the unknown arrival can be removed from the VSP data then this should also remove the tuning wedge which is affecting the estimation of attenuation in the region of 2400m to 2500m depth. If the unknown arrival appears to have a different velocity along the well path then its waveform will plot in a different location of the vespagram.

Figure 4.24 shows the vespagram for the component of the VSP data parallel to the propagation of the direct wave (figure 4.10) along with the location of the direct wave at each depth interval (black circles) and the location of the unknown wave (magenta cross). Although the unknown wave between 2400m and 2500m depth has a higher wave speed along the well path compared to the direct wave in the same interval (2400m to 2500m depth), it is not faster than the direct wave deeper in the well and also shares a similar time intercept. Therefore it is not possible to remove the waveform of the interfering wave from that of the direct wave in this domain.

A ray tracing exercise was performed with a 1D velocity model to investigate the direct wave and possibly shed some light on the origins of the interfering wave. Figure 4.25 shows the ray path of the direct wave to each receiver depth in the VSP data (note the horizontal axes have been exaggerated for clarity). Figure 4.26a shows the estimated arrival time of the direct wave from ray tracing which is in agreement with the values of arrival time estimated from the maximum envelope of the complex signal (figure 4.15), when the time difference between onset of direct wave and maximum energy is taken into account. Figure 4.26b shows a zoom of the Z'' component of the VSP data around the direct wave to show more clearly the fit between the ray traced arrival times and the seismic data. However, this does not shed any light on the cause of the interfering wave.

The cause of the interfering wave is currently unclear, however it is interesting to note that the interference coincides with a sharp increase in scattering attenuation within the well (figure 4.6). The rise in scattering attenuation denotes a large variation on a mean background velocity and density, which could be due to changes in pore fluid fill or pressure which can cause significant attenuation.

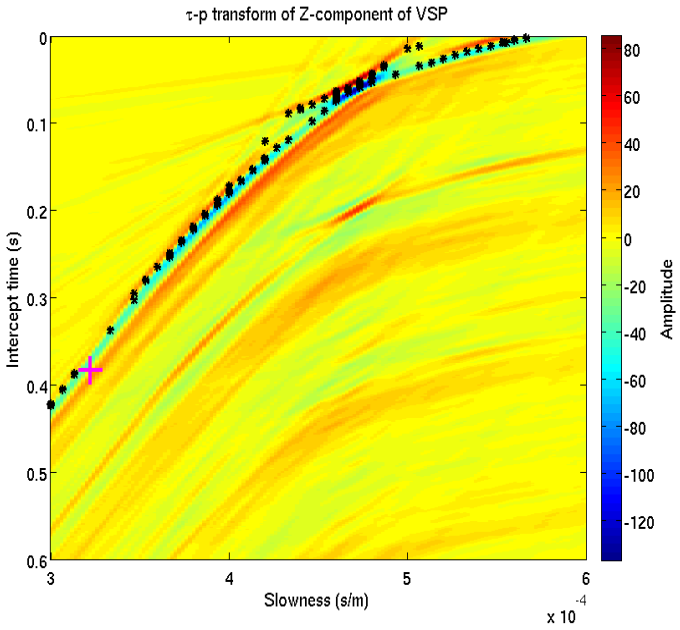

Figure 4.24: Vespagram of the component of the stacked VSP data parallel to the propagation direction of the direct wave showing the location of the direct wave at each depth interval (black circles) and the location of the interfering wave (magenta cross).

4.6 Stacked data

Attenuation is estimated from the stacked seismic data via the spectral ratio method (equation 4.1 where Δt_{ij} is a constant). The spectral ratio method is implemented in two different ways. First, the spectrum of the seismic data within two rolling windows at a set separation in two-way-time (TWT) from one another are estimated and used in the spectral ratio scheme. Second, available seismic horizon data is utilized by taking the spectrum of the seismic data in a small window around each seismic horizon and used to estimate seismic attenuation in the interval between each possible successive pair of seismic horizons. In both cases, the estimated spectra are averaged over a spatial window of 5 inlines by 5 crosslines in order to suppress any incoherent noise which would cause notching in the spectra, this is well within the first Fresnel zone which is 370m at the depth of the reservoir.

By having rolling windows in time in within which the spectra are estimated,

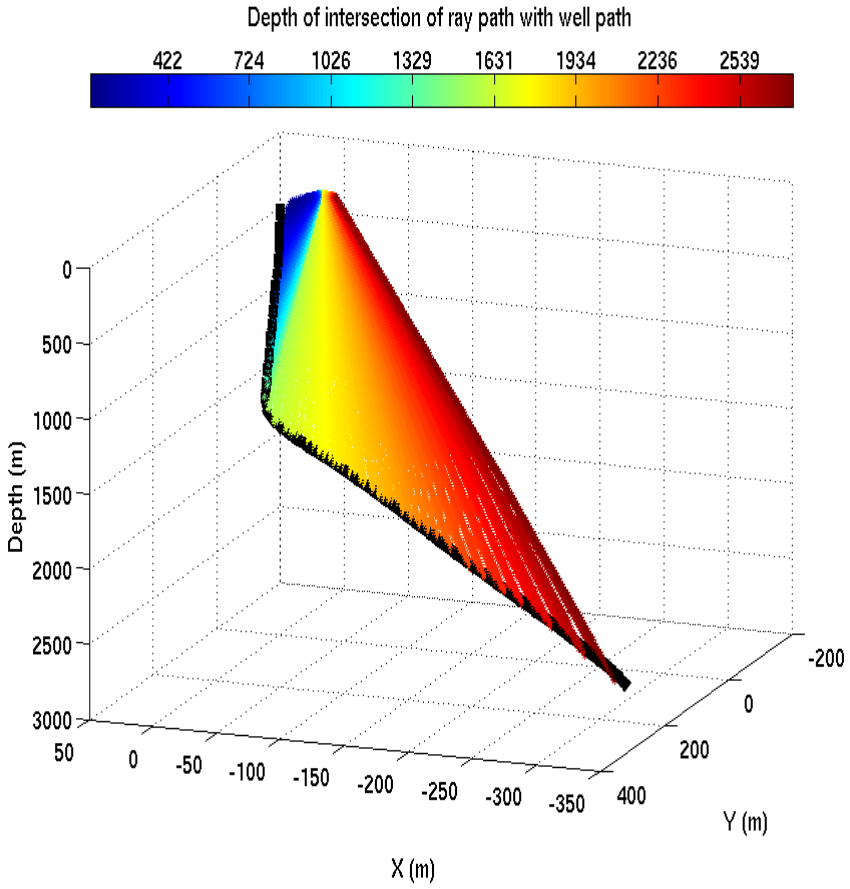

Figure 4.25: Ray paths for direct wave to each receiver depth (black stars) in the VSP dataset. The horizontal axes have been exaggerated for clarity and have been translated such that the origin is defined as the x/y co-ordinate of the first receiver depth.

and subsequently attenuation estimated, it is possible to derive an attenuation volume in which estimated attenuation is placed at the centre of the two windows used to calculate the spectral ratio. Figure 4.27 is an example of an inline, crossline and time slice extracted from this volume and displayed in a 3D view.

The spatial sampling in these volumes can be as small as that of the original seismic data but the sampling in the time domain (two-way-time) is subject to a trade-off between estimating accurate seismic attenuation values and temporal resolution. Attenuation is a cumulative affect, hence the larger the time difference between the windows then the greater the difference between the spectra of the

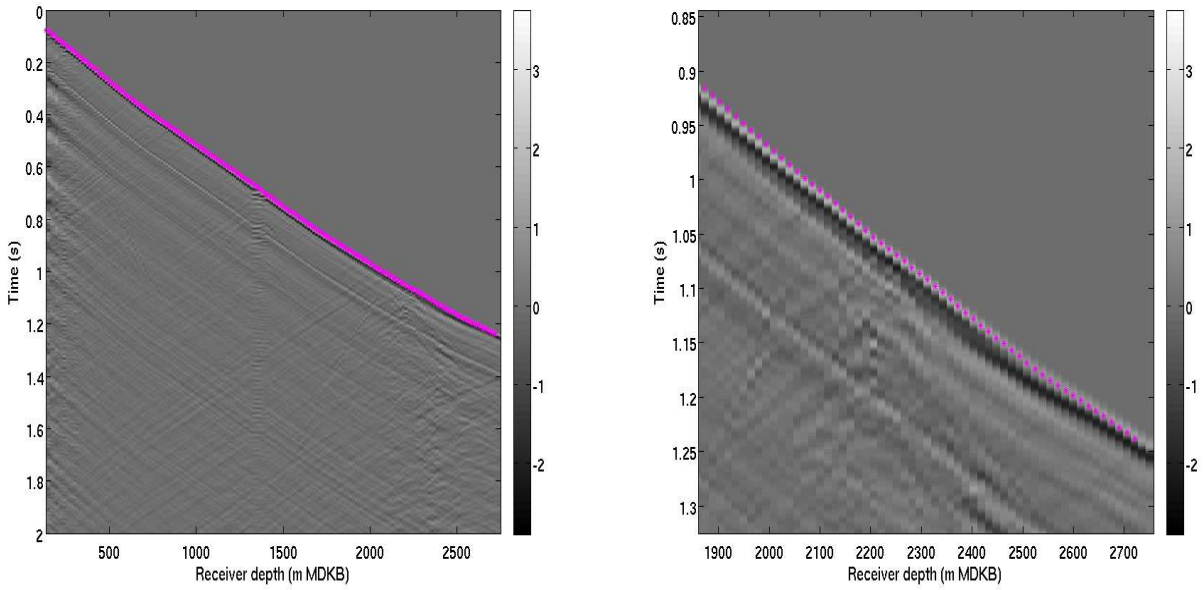

(a) (b)

Figure 4.26: Z'' component of the VSP data with the arrival time of the direct wave (magenta stars) estimated from ray tracing plotted, c.f. figure 4.15 (a) and a zoom of the Z'' component of the VSP data showing more clearly the fit of the ray traced arrivals times to the seismic data (b).

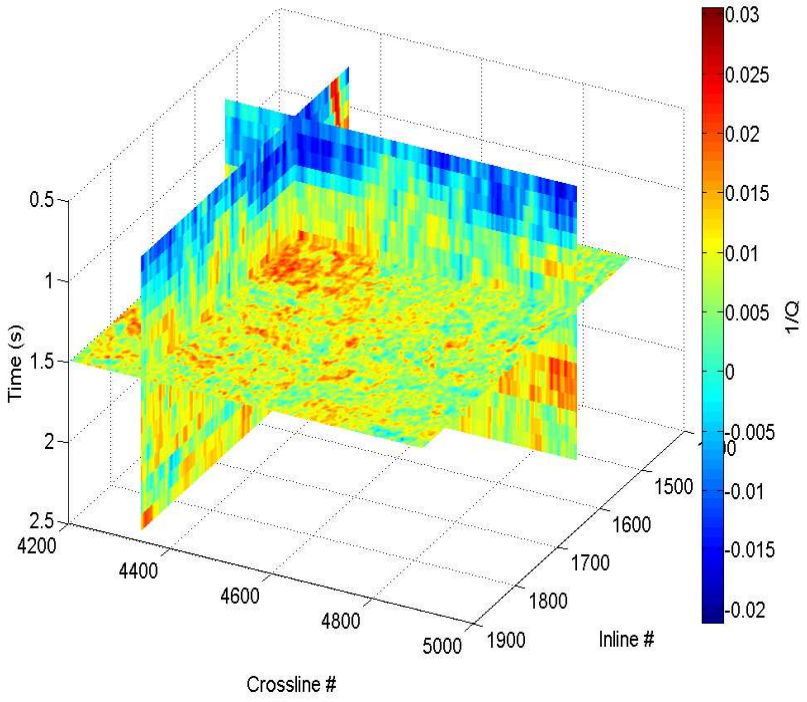

Figure 4.27: Inline 1510, crossline 4350 and a time slice at 1500ms TWT extracted from the seismic attenuation volume estimated form the stacked data.

data falling within these windows. A larger time separation for the windows means a lower temporal resolution. A smaller time difference between the centre of the windows leads to a higher temporal resolution but the difference in the spectra of the seismic data falling within these windows will be less due to the reduced travel time difference between the window centres (Δt_{ij} in equation 4.1). In all instances, the amplitude spectrum of the data is estimated by integrating the time-frequency distribution, estimated via the SDD method, of the seismic trace over a 125ms window whose centre is then rolled along by 100ms. The frequency range over which a linear trend is fit is 20Hz to 75Hz in all cases.

With a 125ms window and a 100ms window overlap, the temporal sampling is too low to make inlines and crosslines of the seismic attenuation volume of much use in interpreting the characteristics of the seismic data (see figure 4.27). However, there is a visible change in the overall characteristics of the seismic attenuation with two-way-time; a negative attenuation feature at approximately

0.75s TWT, inlines 1500-1600, crosslines 4400-4500; and a positive attenuation anomaly at approximately 1.5s TWT. The negative attenuation anomaly followed by a positive attenuation anomaly is systematic of, and coincides with, a temporary drop in centroid frequency (figure 4.28).

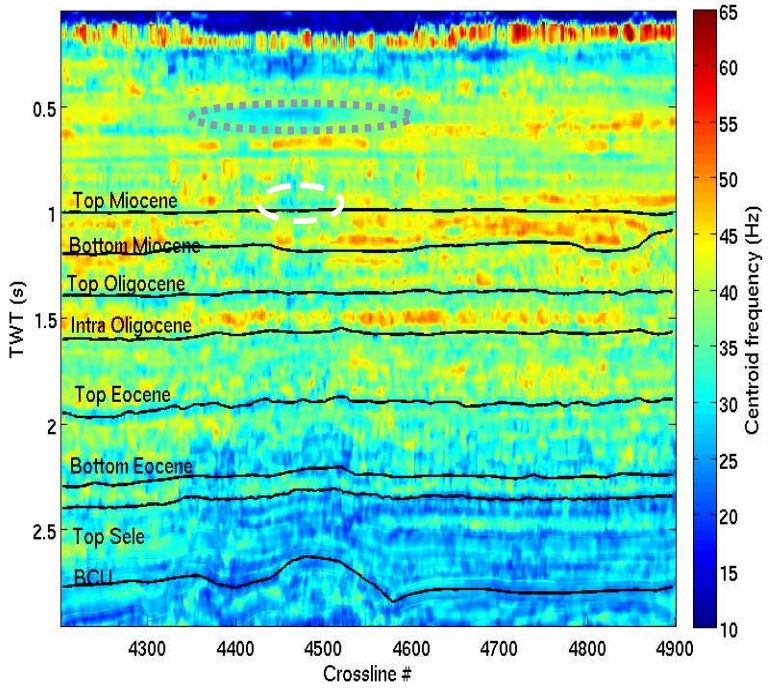

Figure 4.28: Centroid frequency section estimated via a short-time-Fourier-transform (STFT). White dashed and gray dotted ellipses correspond to low frequency shadows under amplitude anomalies.

The spatial resolution of the attenuation volume is the same as the underlying seismic data, although spectra are smoothed over a 5x5 grid of inlines and crosslines. This means that time slices through the attenuation volume may be much more informative in terms of analysing the characteristics of the seismic data than that of the inlines/crosslines of the attenuation volume. Of course, the smoothing over 5 by 5 bins causes some loss in spatial resolution but this is more than made up for in the improved estimates of attenuation due to the greater signal-to-noise ratio. Figure 4.29 shows 3 isochrons of the seismic attenuation volume at times as close to 2.336s TWT as possible (2.325s for 0.25s window

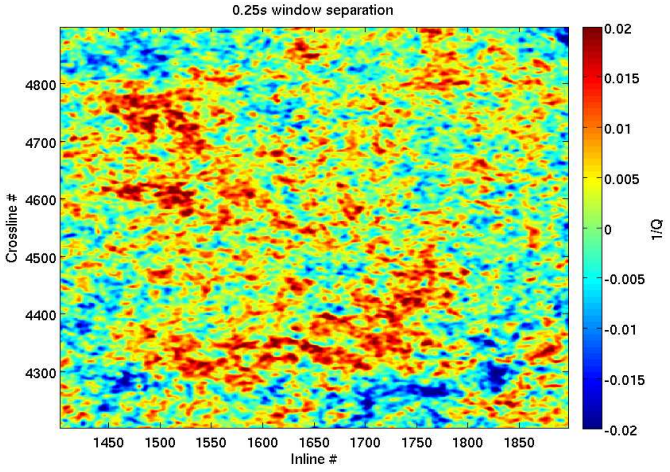

(a)

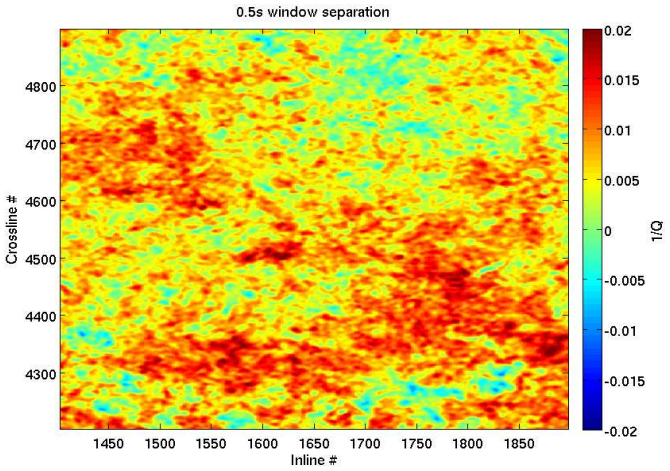

(b)

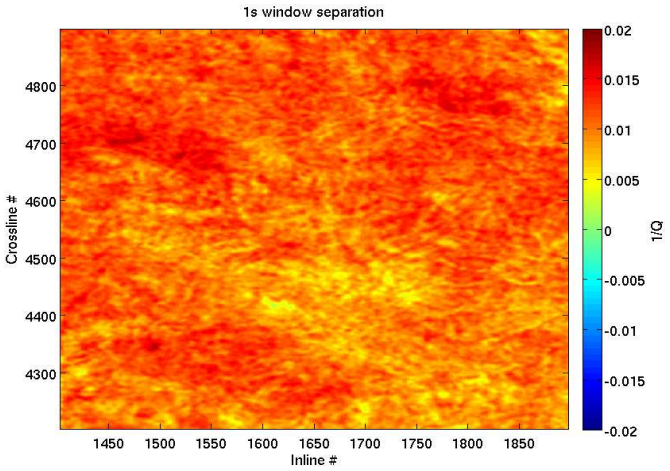

(c)

Figure 4.29: Isochron surfaces extracted from the seismic attenuation volume estimated via the spectral ratio method applied to rolling time windows with a separation of 0.25s (a), 0.5s (b) and 1s (c).

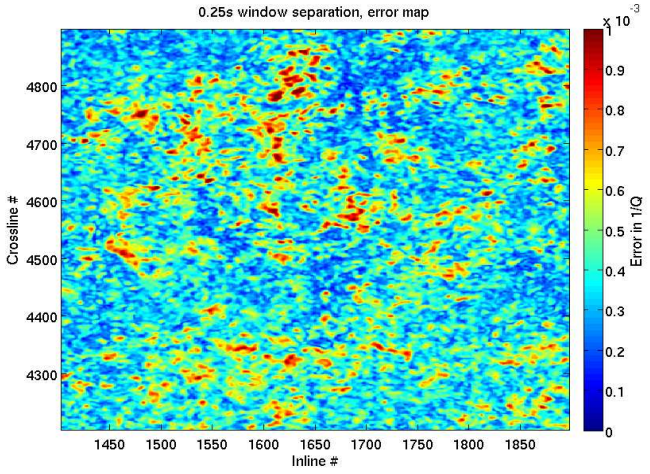

(a)

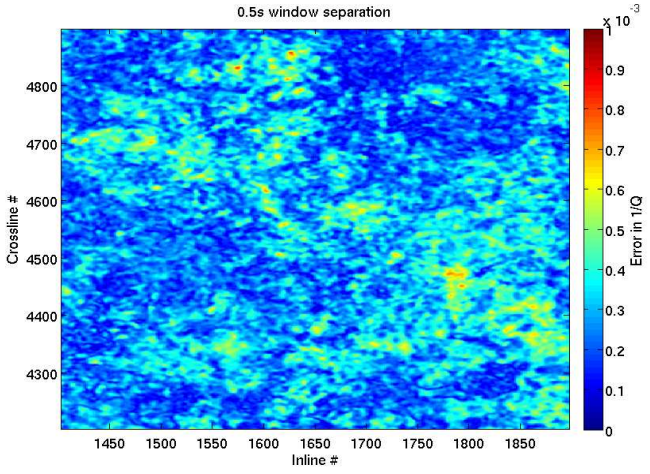

(b)

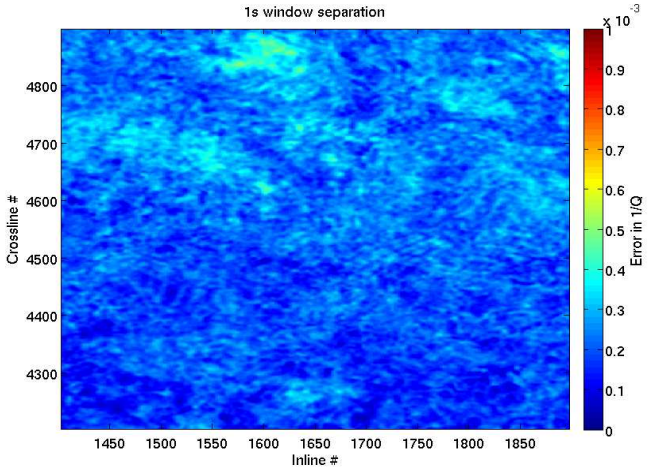

(c)

Figure 4.30: Errors in the estimated $1/Q$ values in figure 4.29.

separation, 2.35s for 0.5 window separation and 2.2s for 1s window separation).

The main difference in the isochrons (figure 4.29) are the degree and coherency of spatial variations in estimated seismic attenuation values. The isochron extracted from the attenuation volume estimated with windows 1s apart shows little variation over the surface, with $1/Q$ values from 0.005 to 0.015, compared to that of the isochron from the 0.5s window separation attenuation volume, which shows a variation of $1/Q$ from 0 to 0.02. The isochron from the 0.25s window separation attenuation volume shows the largest variation but also contains highly negative ($1/Q$<-0.02) attenuation values which are unrealistic and due to the noise on the spectral ratio slope swamping the slope induced by attenuation. Figure 4.30 shows the error in the estimated $1/Q$ values in figure 4.29 and shows support for this claim as the average error increases with decreasing time separation of the window centres. However, the high attenuation values estimated for the 0.25s window separation isochron shows some correlation with the high attenuation values seen in the 0.5s window separation isochron, although much the attenuation anomaly is much less coherent in the 0.25s window separation isochron. This suggest that the 0.25s window separation is too short, due to the presence of highly negative attenuation values and that a 1s window separation is too large, due to the small variation in attenuation values and the lack of correlation of any high attenuation features with the other isochrons.

Figure 4.31 shows the histograms of the attenuation volumes estimated for window separation of 0.25s, 0.5s and 1s. The aforementioned reduction in variation of values is visible as a narrowing of the distribution with increasing window separation. Figure 4.32 shows a plot of the natural logarithm of the standard deviation of the histograms in figure 4.31 versus the natural logarithm of the time separation of the windows. If the estimated attenuation values were both random and normally distributed then the plot in figure 4.32 would show a straight line with a slope equal to -1. The slope of the trend in figure 4.32 is approximately -0.72 (although only three data points, corresponding to three different window separations, are used) and hence, although the estimated attenuation values are not normally distributed random values, a decline in standard deviation would be expected with increased time separation between windows, as the affect of attenuation is being averaged over a larger distance (in two-way-time).

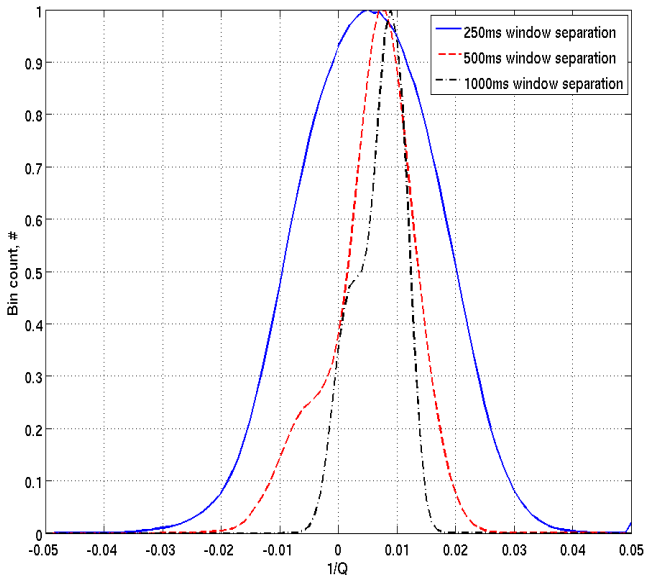

Figure 4.31: Histograms of the attenuation volumes estimated from stacked seismic data via the spectral ratio method with time separation between windows of seismic data of 0.25s, 0.5s and 1s.

Figure 4.33 shows maps of seismic attenuation for four intervals between mapped seismic horizons. These are estimated by using the spectral ratio method with spectra formed via integration of a 125ms window around each seismic horizon at each crossline/inline location. The spectra are smoothed via applying a mean filter with length 5 crosslines by 5 inlines prior to forming the spectral ratio curve.

The top Miocene to top Tor interval (Figure 4.33a) shows a distribution of attenuation values centered around an average $1/Q$ of 0.01 (Q=100) with lower attenuation in the south (low y co-ordinate) and a linear, relatively high attenuation anomaly running east-west from y=8000m, x=0m to x=2000m (2km long) with a $1/Q$ value of 0.014 ($Q \approx$70). The top Miocene to top Tor interval is thick, with an average two-way travel time difference of 1.5s, and encompasses several other seismic horizons. To be able to separate out the causes of the lower and higher attenuation anomalies from the background trend it is necessary to look into thinner intervals. As before, there is a trade-off between temporal res-

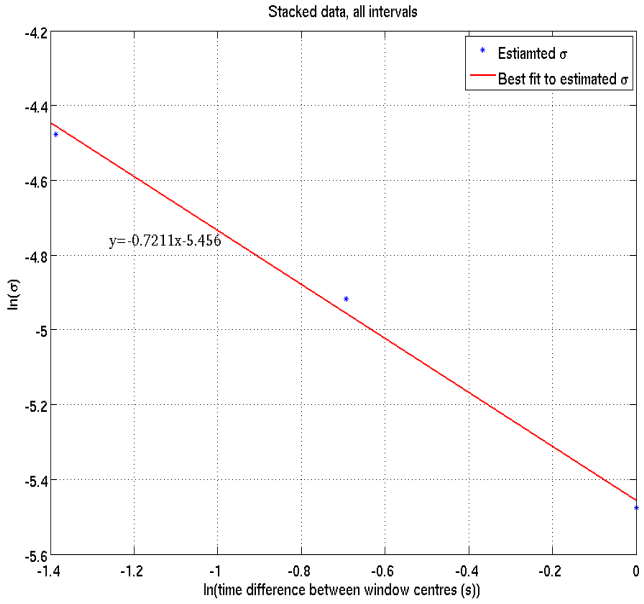

Figure 4.32: Natural logarithm of the standard deviations of the histograms seen in figure 4.31 as a function of the natural logarithm of the time separation between window centres.

olution and estimating accurate attenuation values, thus some smaller intervals may contain unreasonable attenuation values due to the effect of notching in the spectra of seismic horizons, caused by local interference, being greater than the attenuation signal that is to be measured.

The top Miocene to bottom Eocence interval map (figure 4.33b) shows an a more bimodal distribution of attenuation with a higher attenuation anomaly in the north-east and a generally lower attenuation value in the south-west. This can possibly explain the lower attenuation values seen in the top Miocene to top Tor interval, where a generally lower attenuation is observed in the south of the attenuation map and the generally larger attenuation values seen in the north-east of the top Miocene to top Tor attenuation map. There is no large, linear east-west trending, high attenuation feature in the top Miocene to bottom Eocene map similar to that seen in the top Miocene to top Tor attenuation map. This leads to the conclusion that this must be caused by some attenuation anomaly in the interval between the bottom Eocene and the top Tor.

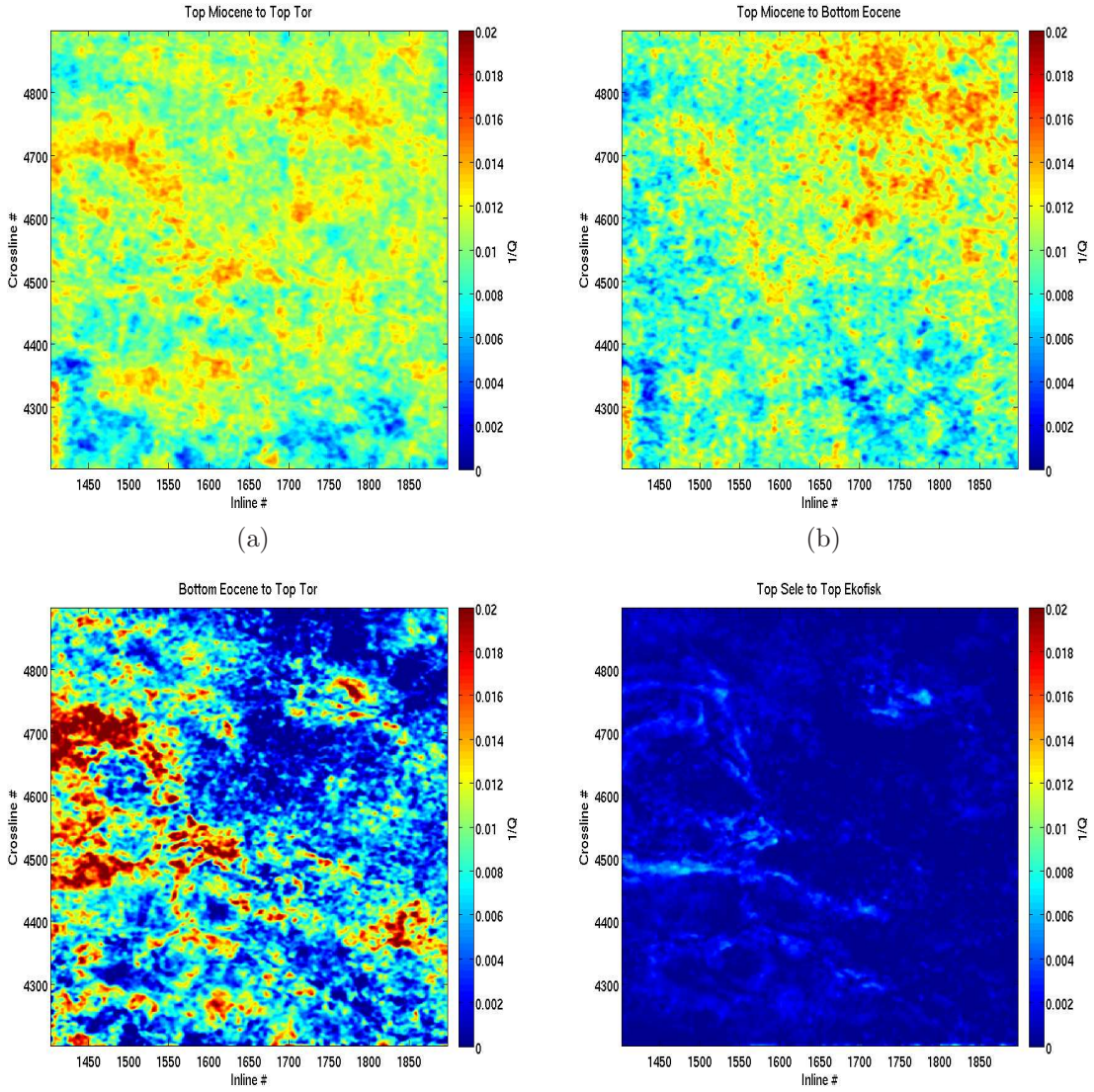

Figure 4.33: Maps of attenuation for the intervals top Miocene to top Tor (a), top Miocene to bottom Eocene (b), bottom Eocene to top Tor (c) and top Sele to top Tor (d) as estimated from spectra extracted around the aforementioned seismic horizons in the stacked seismic data. All plots are scaled to the same colour scale.

Figure 4.33c gives the attenuation map for the bottom Eocene to top Tor interval and shows a background attenuation (Q <0.008) that is much lower than that seen in the shallower interval of the top Miocene to bottom Eocene and lower than that of the thick interval between the top Miocene and top Tor. The

bottom Eocene to top Tor interval is thinner than that of the top Miocene to bottom Eocene interval, a two-way travel time difference of 0.3s as opposed to 1.2s for the top Miocene to bottom Eocene. A strong quasi-linear attenuation anomaly at approximately y=8000m, stretching from x=0m to x=2000m (2km long) can be seen in the attenuation map for the bottom Eocene to top Tor interval, explaining the presence of the linear feature in the top Miocene to top Tor interval attenuation map.

The top Sele to top Ekofisk interval, the deepest interval shown (figure 4.33d), shows a very low average attenuation with an average $1/Q$ of much less than 0.005 (Q=200). Attenuation anomalies, in terms of trends which stand out from the background, are present in this interval, but the magnitudes of these anomalies are still low with $1/Q$ being less than 0.008 (Q=125) when compared to other intervals (figure 4.33a-c). The lack of any large attenuation anomaly in the top Sele to top Ekofisk interval would suggest that the large, linear, east-west trending attenuation anomaly in the bottom Eocene to top Tor interval (figure 4.33c) is due to properties of the subsurface within this interval, as the top Ekofisk to top Tor interval is approximately 0.01s thick (in two-way-time) and thus could not contribute to such a large attenuation anomaly over a 0.3s second interval without containing an unrealistically high $1/Q$ (low Q) values.

4.7 Pre-stack data

4.7.1 Preprocessing and Q estimation parameters

The pre-stack data used in this study is limited to the same spatial extent as the stacked seismic section. Although the pre-stack data covers a larger areal extent. The available velocity and anisotropy parameter models are also limited to the spatial extent of the stacked seismic data. The pre-stack data is limited in spatial extent because without an accurate velocity model it will not be possible to accurately determine the correct moveout for the seismic horizons in the $\tau - p$ domain and hence the estimated spectra, and eventually attenuation values, will be negatively affected.

The supplied pre-stack data is preprocessed to improve the quality of the $\tau - p$

gathers derived from a linear Radon transform. Figure 4.34 shows a comparison of a pre-stack common midpoint (CMP) gather in the time-offset (t-x) domain before and after the application of preprocessing as well as the resultant $\tau - p$ gathers. The preprocessing involved application of a top mute to cut out signal energy prior to the shallowest reflection of interest (top Miocene); trace weighting of the nearest offset 5 traces (in split spread shots) with a 0.75, 0.5, 0.25, 0.5, 0.75 weighting, where 0.25 is multiplied by the amplitude of the nearest offset trace, to remove some linear artefacts in the $\tau - p$ transform; and $f - x$ trace interpolation to increase the sampling in the offset direction to limit aliasing in the $\tau - p$ domain.

The $\tau - p$ transform in figure 4.34d shows fewer linear transform artefacts and the reflections of interest have a higher coherency and are stronger. Figure 4.35 shows the $\tau - p$ gather seen in figure 4.34d with the seismic horizons of interest overlain.

The $\tau - p$ gathers are formed from preprocessed supergathers. The supergathers are formed from varying inline/crossline smash extents. For the purposes of testing, supergathers are formed from a 5 inline by 5 crossline summation of CMP gathers, and also from a 20 crossline by 20 inline summation. The X/Y co-ordinates of the supergather are defined as the mean of the X/Y co-ordinates of the component CMP gathers. Estimated $1/Q$ values from variable supergather sizes are compared to estimated $1/Q$ values from individual CMP gathers over a limited spatial extent. The supergathers do not overlap and thus are independent from one another, although this limits spatial resolution of the estimated $1/Q$ values.

The Q estimation method employed here is the pre-stack-Q-inversion (PSQI) method Reine et al. (2012a). The PSQI method is a modified spectral ratio attenuation estimation method which works in the τ-p domain. By transforming the pre-stack data into the $\tau - p$ domain it is possible to match ray paths in the overburden and mitigate angle dependent effects in the overburden on the estimated $1/Q$ values.

To estimate the spectra at each horizontal slowness, the signal-dependent-distribution (SDD), a time-frequency distribution, is formed for each slowness trace and a 120ms window centred at the two-way time of the relevant seismic

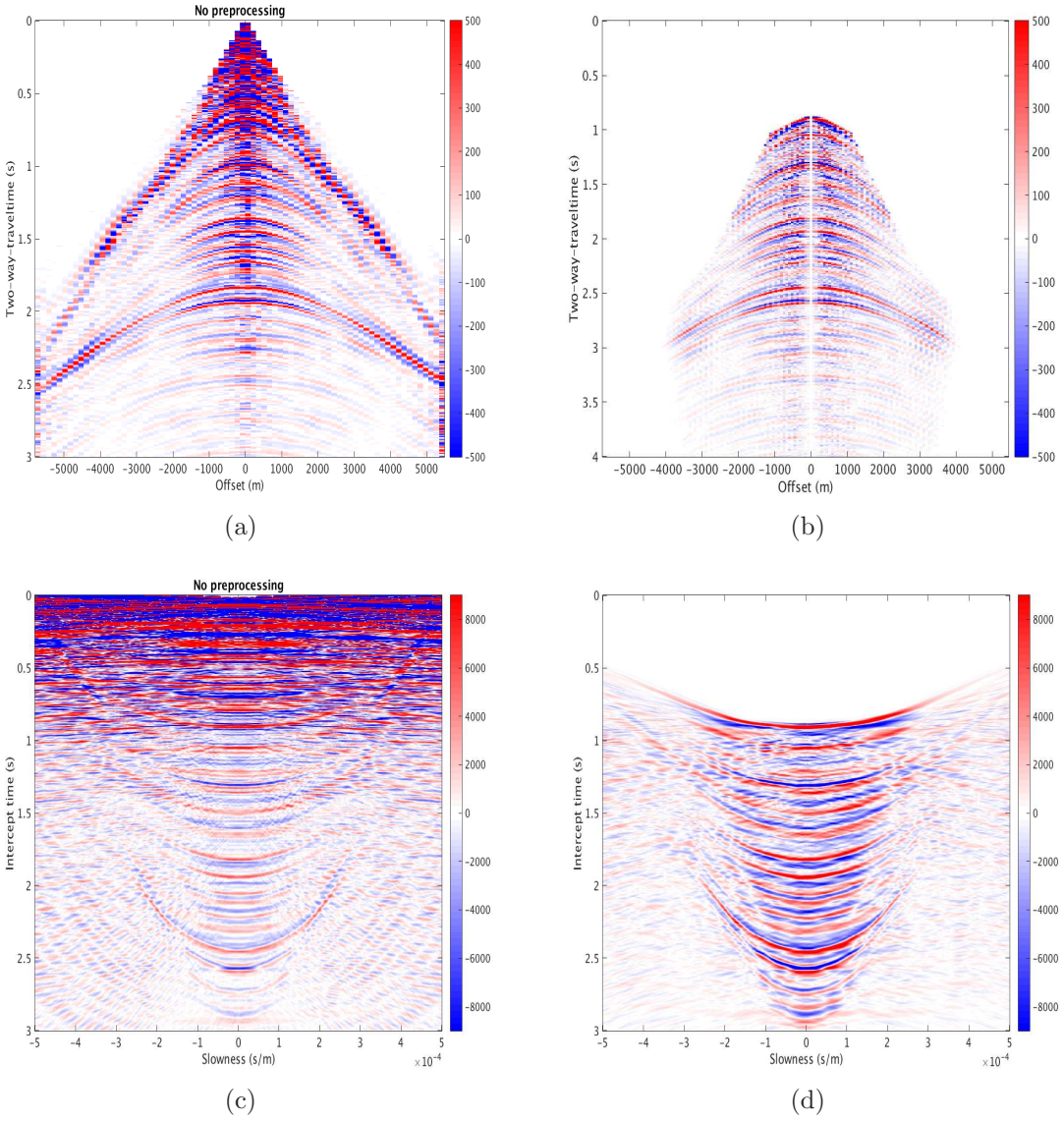

Figure 4.34: Pre-stack CMP gathers before (a) and after (b) preprocessing and the resulting $\tau - p$ gathers formed via linear Radon transform (c,d respectively).

horizon at the current horizontal slowness is integrated to form the spectra of that seismic horizon at that horizontal slowness. To avoid bias in the spectral ratio surfaces from high slowness traces, which are more susceptible to transform artefacts and interference from neighboring reflections, the maximum absolute slowness analyzed is limited to 0.1ms/m. The parameters used in estimating $1/Q$

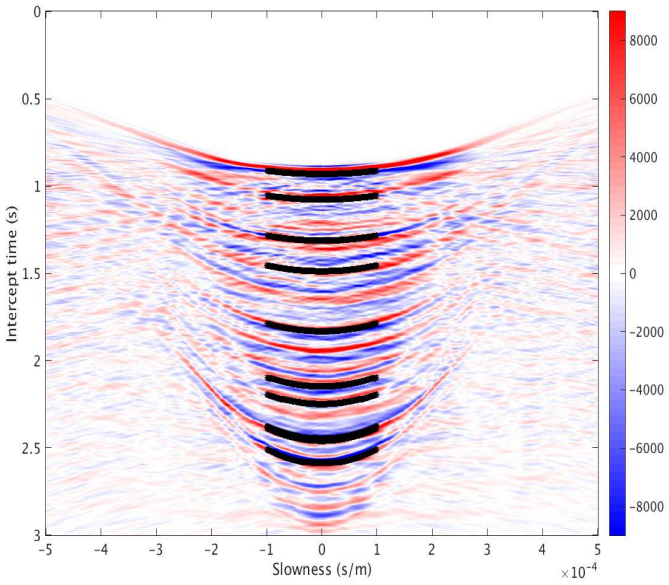

Figure 4.35: $\tau - p$ gather as seen in figure 4.34d with the moveout of the seismic reflections of interest overlain.

values from the $\tau - p$ gathers are summarized in table 4.5.

The spectral estimation method is also tested by forming the spectra used in the PSQI method via the short-time-Fourier-transform (STFT) and Stockwell transform.

Table 4.5: Parameters used in estimating $1/Q$ values from $\tau - p$ gathers via the PSQI method. f_{low} and f_{end} is the start and end of the bandwidth of the spectral ratio surface used to estimate $1/Q$, t_{int} is the length of the integration window in the time-frequency domain, t_{STFT} is the length of the window used in the STFT transform.

Parameter	Value
f_{low}	15
f_{high}	55
t_{int}	0.12s
t_{STFT}	0.06s

4.7.2 Estimated 1/Q results

Figure 4.36 shows the attenuation ($1/Q$) maps estimated via the PSQI method applied to the 5 inline by 5 crossline supergather data for the top Miocene to top Tor, top Miocene to bottom Eocene, bottom Eocene to top Tor and top Sele to top Ekofisk intervals.

One obvious feature of the top Miocene to top Tor and top Miocene to bottom Eocene intervals is the presence of strong linear features running North/South (Y direction, figures 4.36a and 4.36b).The lack of these features in deeper intervals (figures 4.36c and 4.36d) suggest that is a feature present only in the shallower section. Given the linearity of these features, it is unlikely that they are due to the underlying geometry and more likely an imprint of the acquisition geometry. This could be due to small bins between sail lines not including the near offset traces which would have a horizontal slowness of less than 0.1ms/m. This would mean that the subsequent spectral ratio of these regions would be dominated by noise and transform artefacts from the τ-p domain. Figure 4.37 lends credence to this as the bin size is much larger, 20x20 as opposed to 5x5 in figure 4.36, and the strong linear features running North/South are no longer present.

The variability in attenuation values in the attenuation maps in figure 4.36 shows that for thinner intervals such as the top Sele to top Ekofisk (figure 4.36d), which is approximately 0.2s thick, the variability in estimated attenuation values is greater than for that of larger intervals such as the top Miocene to top Tor interval, which is approximately 1.5s thick. The background attenuation in the attenuation map for the bottom Eocene to top Tor interval is low, with an average value of less than 0.004 (Q=250), whereas the background for the interval from the top reflection of interest to the bottom reflection of interest (top Miocene to top Tor) is approximately 0.006 (Q=167). The top Miocene to bottom Eocene interval shows the greatest background attenuation with a an average background attenuation of approximately 0.0075 (Q=133). These results suggest that, broadly speaking, the shallower section of the seismic data (above bottom Eocene) is more attenuative than the deeper part of the region (below bottom Eocene).

Figure 4.37 shows the estimated $1/Q$ maps for the same four intervals observed

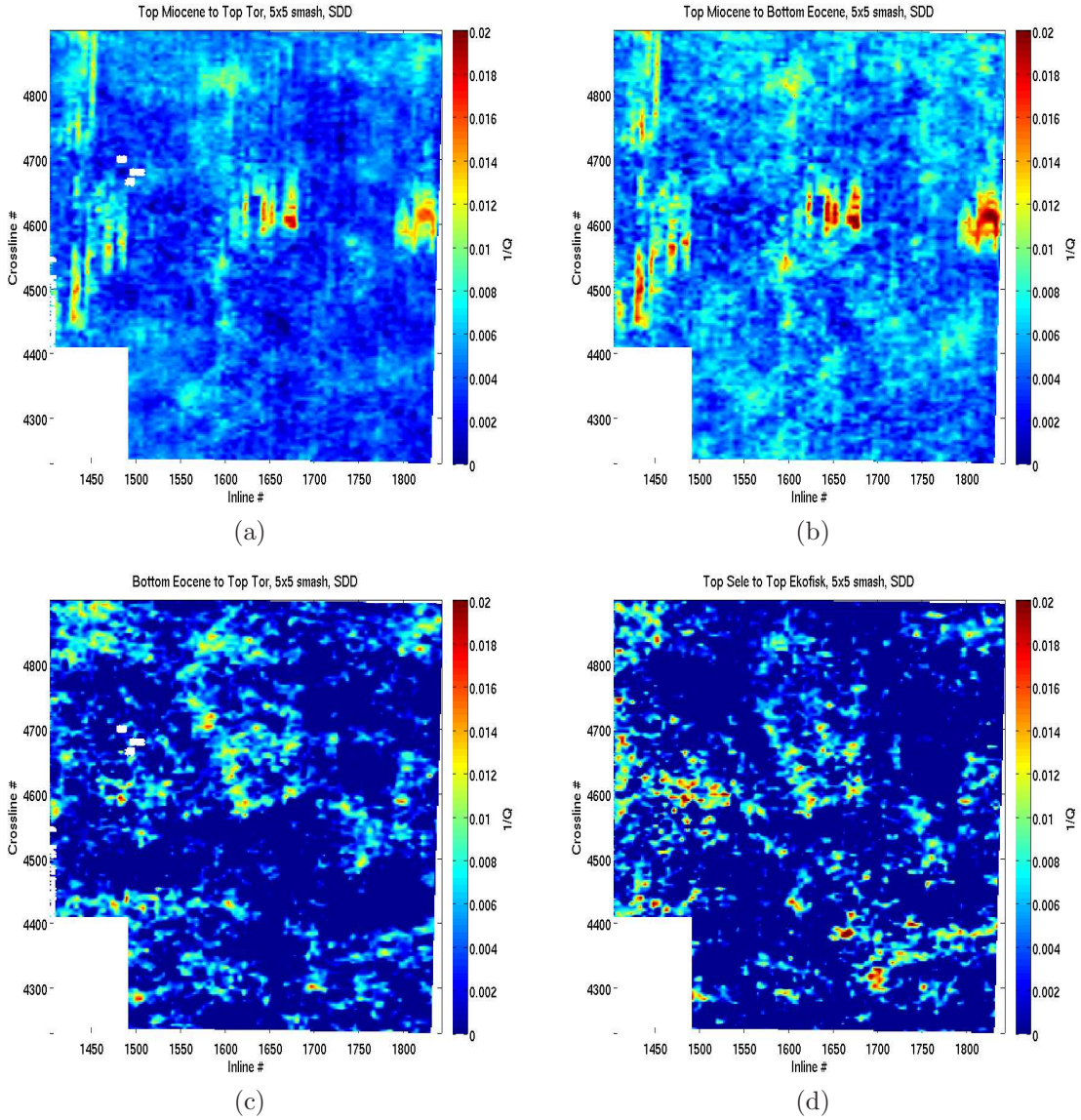

Figure 4.36: Maps of attenuation for the intervals top Miocene to top Tor (a), top Miocene to bottom Eocene (b), bottom Eocene to top Tor (c) and top Sele to top Tor as estimated from the PSQI method applied to the aforementioned seismic horizons in the prestack seismic supergathers created via a 5 inline by 5 crossline smash.

in figure 4.36 for 20 inline by 20 crossline supergather data. The strong linear features seen in the top Miocene to top Tor and top Miocene to bottom Eocene maps (figures 4.36a and 4.36b) for the 5 inline by 5 crossline supergathers can no longer be seen in the 20 inline by 20 crossline maps. Nevertheless, the 20

inline by 20 crossline results are useful in qualitatively analyzing the background attenuation value at a glance.

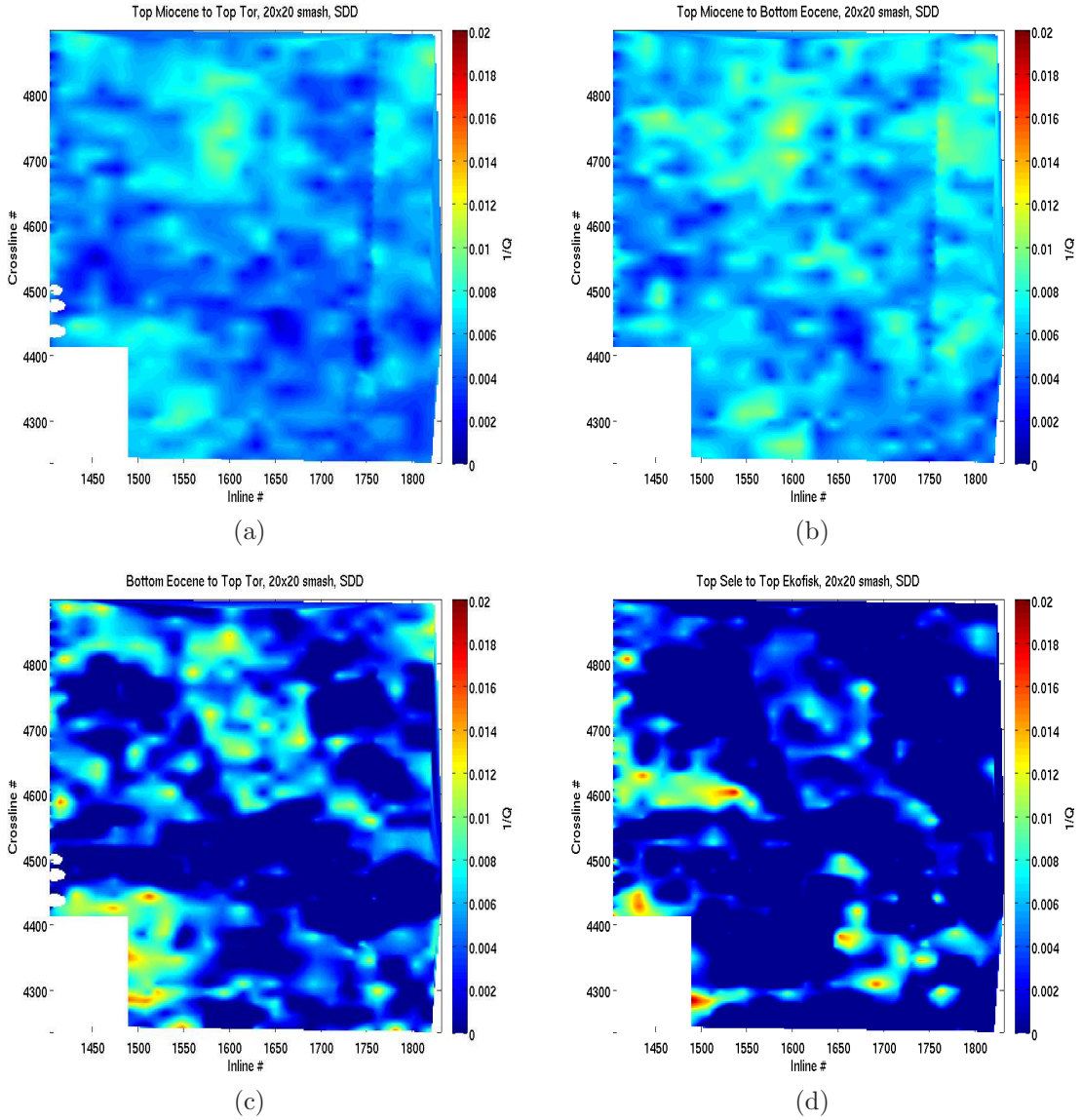

Figure 4.37: Maps of attenuation for the intervals top Miocene to top Tor (a), top Miocene to bottom Eocene (b), bottom Eocene to top Tor (c) and top Sele to top Tor as estimated from the PSQI method applied to the aforementioned seismic horizons in the prestack seismic supergathers created via a 20 inline by 20 crossline smash and interpreted to the same spatial density as the maps in figure 4.36.

Figure 4.38 shows an attenuation map estimated via the PSQI method from

individual CMP gathers for the top Miocene to top Tor interval over the inline range 1420 to 1600, as opposed to 1400 to 1850 shown in figures 4.36 and 4.37. The imprint of the acquisition geometry is clearer in figure 4.38 than in figure 4.36. Although coherent regions of higher than average attenuation ($1/Q \approx 0.01$) are present at inline 1460-1520, crossline 4300, the interpretability of the attenuation map is severely reduced by the imprint of the acquisition geometry. This imprint occurs because CMP locations far from sail lines do not contain near offsets, this lack of near offsets means that it is not possibly to accurately construct low slowness traces in the $\tau - p$ transform and only spectra from slowness traces up to 0.1ms/m are taken to form the spectral ratio surface from which $1/Q$ is estimated.

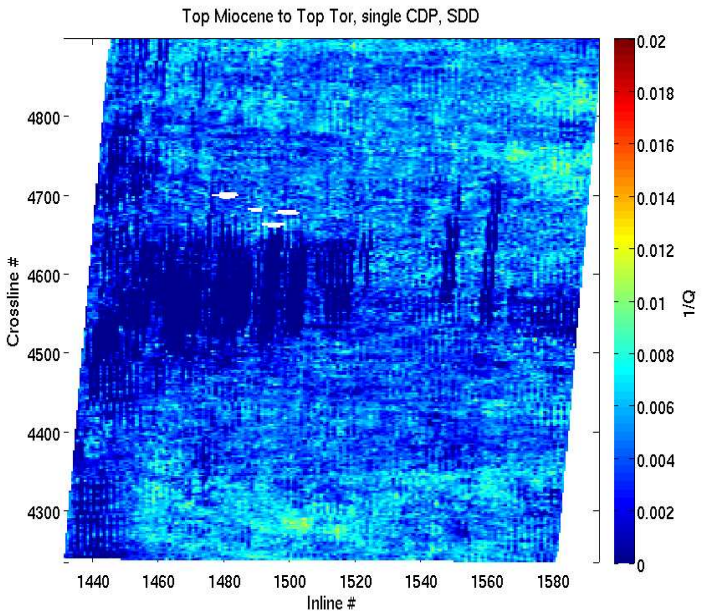

Figure 4.38: Attenuation map for the top Miocene to top Tor interval estimated via the PSQI method for individual CMP gathers. Note that the horizontal scale is exaggerated compared to figures 4.36 and 4.37.

Figure 4.39a-b shows the estimated $1/Q$ maps for the top Miocene to top Tor interval estimated via PSQI whilst using the STFT and Stockwell transform respectively. Similarly, figure 4.39c-d shows the $1/Q$ maps for the top Sele to top Ekofisk interval. The general structure of the attenuation maps estimated whilst

utilizing a Stockwell transform or a STFT (figure 4.39) are very similar to those derived using the SDD (figure 4.36) but the range in estimated $1/Q$ values from the STFT and Stockwell transform are greater. Figure 4.40 shows a comparison of the distribution of estimated $1/Q$ values for all three time-frequency transform methods. Although the attenuation maps for all three methods are similar, the distribution of values is different, especially for the SDD method. It can be argued that the distribution of values for the STFT and Stockwell transforms more closely resemble the distribution of $1/Q$ values from the stacked seismic data (figure 4.41). However, although the median values may be closer than the median of the SDD derived population, the standard deviation is much larger and the maps of attenuation values given in figure 4.39 show little correlation with those estimated from the stacked seismic data seen in figure 4.33.

The blank zones in figures 4.39a and 4.39b correspond to points which have unrealistically negative ($1/Q$>-0.1) points, the interpolation of the results to form the images seen cannot accurately fit these points and has failed, causing a blank in the attenuation map.

4.8 Comparison of attenuation results

Attenuation maps estimated from the stacked data (figure 4.33) are much more interpretable than those estimated from the prestack data (figures 4.36, 4.37 and, 4.38) in terms of showing more coherent structure, and it is assumed that any attenuation anomaly in the subsurface would be spatially coherent. Statistically, the distributions of the stacked and prestack values do not belong to the same underlying distribution. Due to the large sample size of each population, >18,000, the difference between the mean values of each distribution would have to be very small to imply a statistical similarity based on the t-test, as they are very well defined by the standard error. Table 4.6 summarizes the statistics of the $1/Q$ values estimated from the 20 crossline by 20 inline supergather prestack seismic data and the stacked seismic data at the well location.

The stacked and pre-stack seismic data at the well location has a much reduced sample size which means that the T-statistic for these two data sets is 0.81, which means that the $1000/Q$ values estimated at the well location from the stacked

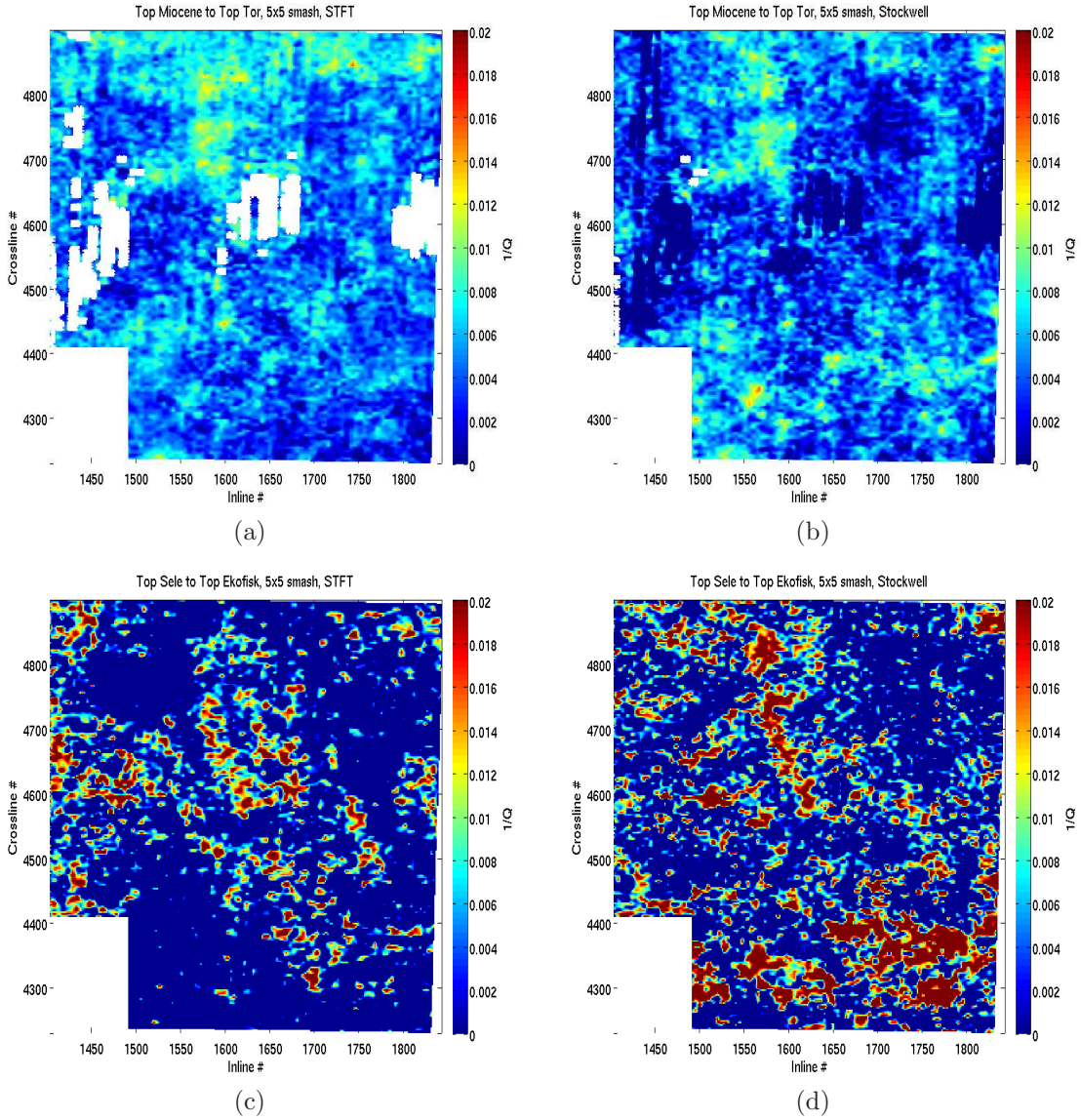

Figure 4.39: Maps of attenuation for the intervals top Miocene to top Tor estimated via PSQI whilst utilizing a STFT (a) and Stockwell transform (b) as well as maps of attenuation over the top Sele to top Ekofisk interval estimated via PSQI whilst utilizing a STFT (c) and Stockwell transform (d).

and pre-stack data belong to a distribution with the same underlying mean at the 95% confidence level. However, neither are statistically similar to the $1000/Q$ estimated from the VSP data, with T-values of 7.4 and 8.3 respectively. A T-value of 1.645 is needed for the distribution to be statistically similar for datasets

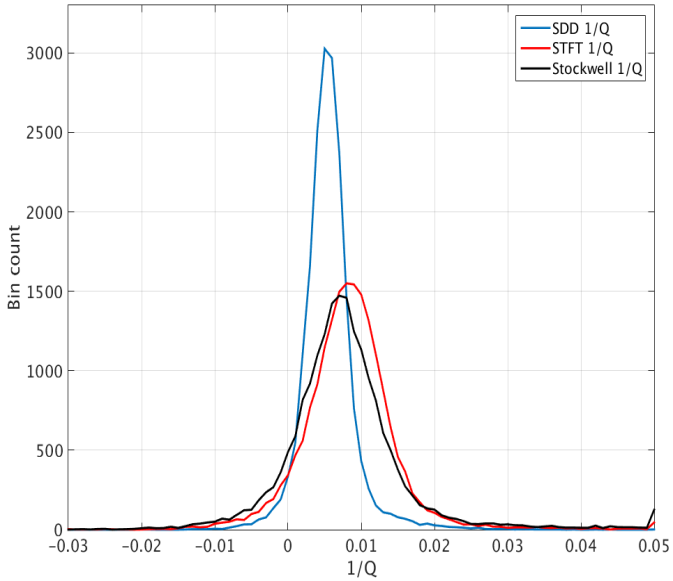

Figure 4.40: Distribution of $1/Q$ values estimated for the prestack data via PSQI whilst utilizing a SDD, STFT and Stockwell transform to form the spectra.

Table 4.6: Statistical properties of the distribution of $1/Q$ values estimated from stacked and prestack seismic data close to the location of well 16/23-7. $\bar{\sigma}$ is a standard deviation, σ is the standard error and γ is the kurtosis excess.

	mean	median	$\bar{\sigma}$	σ	skewness	γ
Prestack	0.0039	0.0045	0.0077	0.0011	3.2	54
Stacked	0.0053	0.0092	0.0055	0.0013	-7.0	71

of these sizes.

Table 4.7: Comments and properties of the attenuation maps for the Top Miocene to Top Tor interval for the VSP data, stacked and, prestack seismic data (PS). σ is the standard deviation of the $1000/Q$ values.

Data source	Comments	mean $1000/Q$	median $1000/Q$	σ
Stacked (figure 4.33a)	High $1/Q$ (≈ 0.016) curved feature starts at inline 1400, crossline 4700	10.5	10.6	1.8
VSP (figure 4.41b)[1]	-	23.5±2.0	11.4	23.0
PS 20x20 (figure4.37a)	Low spatial resolution	5.5±0.1	5.4	1.9
PS 5x5 (figure 4.36a)	N/S trending high $1/Q$ lines	4.7±0.1	4.3	2.6
PS 1x1 (figure 4.38)	High $1/Q$ zone at inline 1850, corssline 4600 acquisition imprint	3.7±0.1	4.2	3.3
PS 20x20 STFT (figure 4.39a)	Blank zones due to $1/Q$<-0.1	5.3±0.1	5.2	2.6
PS 20x20 Stockwell (figure 4.39b)	Highly negative $1/Q$ zones coincident with those in STFT map	2.0±0.1	4.1	12.7

Table 4.8: Comments and properties of the attenuation maps for the Top Sele to Top Ekofisk interval for the VSP data, stacked and, prestack seismic data (PS). σ is the standard deviation of the $1000/Q$ values.

Data source	Comments	mean $1000/Q$	median $1000/Q$	σ
Stacked (figure 4.33d)	Higher $1/Q$ ($\approx$0.006) trending E/W at inlines 1400-1550, crossline 4500	0.7	0.5	0.9
VSP (figure 4.41b)[1]	Strong peak of $1/Q\approx$0.08	55.1$\pm$9.0	63.1	24.6
PS 20x20 (figure4.37d)		0.7$\pm$0.3	0.6	7.8
PS 5x5 (figure 4.36d)	Higher $1/Q$ ($\approx$0.016) at inlines 1400-1525, crossline 4600	0.2$\pm$0.1	0.2	8
PS 20x20 STFT (figure 4.39c)	Low spatial coherency	-3.1$\pm$0.1	-2.4	17.4
PS 20x20 Stockwell (figure 4.39d)	N/S trending high $1/Q$ (>0.02) at inline 1600, crosslines 4550-4750. Low spatial coherency	1.5$\pm$0.1	1.3	17.2

[1]The usable range of attenuation values for the VSP data set extends to 2463m MD which is which the Sele formation. Quoted VSP values are to the bottom of the usable range and not the necessarily the given formation top.

Table 4.9: Comments and properties of the attenuation maps for the Top Miocene to Bottom Eocene interval for the VSP data, stacked and, prestack seismic data (PS). σ is the standard deviation of the $1000/Q$ values.

Data source	Comments	mean $1000/Q$	median $1000/Q$	σ
Stacked (figure 4.33b)	High $1/Q$ ($\approx$0.016) at inlines 1650-1900, crosslines 4600-4900	10.1	10.1	2.3
VSP (figure 4.41b)	-	16.4$\pm$2	8.0	16.2
PS 20x20 (figure4.37b)	Low spatial resolution	6.3$\pm$ 0.1	6.2	2.2
PS 5x5 (figure 4.36b)	N/S trending high $1/Q$ lines High $1/Q$ zone at inline 1850, crossline 4600	5.8$\pm$0.1	5.3	3.1

Table 4.10: Comments and properties of the attenuation maps for the Bottom Eocene to Top Tor interval for the VSP data, stacked and, prestack seismic data (PS). σ is the standard deviation of the $1000/Q$ values.

Data source	Comments	mean $1000/Q$	median $1000/Q$	σ
Stacked (figure 4.33c)	High $1/Q$ (>0.02) lines trending E/W across inlines 1400-1525 at crosslines 4475 and 4700	7.0	6.5	5.1
VSP (figure 4.41b)[1]	-	58.1±4	60.7	18.6
PS 20x20 (figure4.37c)	lower $1/Q$ (≈0) at inlines 1400-1850 between crosslines 4450 and 4550	2.7±0.2	3.2	6.1
PS 5x5 (figure 4.36c)	Low spatial coherency	0.8±0.1	1.1	5.9

[1]The usable range of attenuation values for the VSP data set extends to 2463m MD which is which the Sele formation. Quoted VSP values are to the bottom of the usable range and not the necessarily the given formation top

Tables 4.7 to 4.10 give an overview of the statistics, for various intervals, of the estimated $1000/Q$ values from the stacked, pre-stack and VSP data. Statistically, only the $1000/Q$ values estimated from the stacked data and the pre-stack 20x20 CMP smash data for the top Sele to top Ekofisk interval belong to distributions with the same mean (estimated via a t-test), this is due to the fact that the mean of the two data sets is equal.

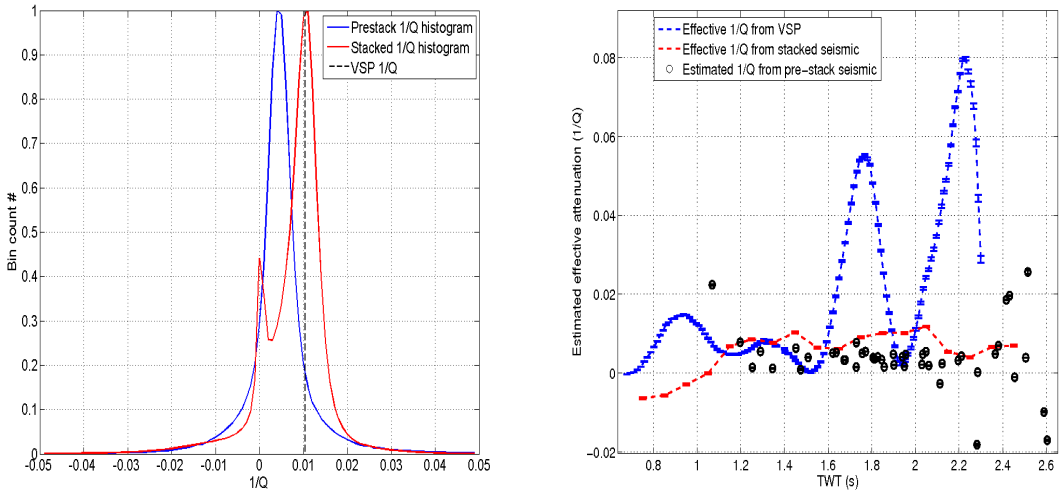

(a) (b)

Figure 4.41: Distribution of $1/Q$ values estimated from stacked and prestack seismic data (a). The attenuation value estimated over the entire VSP interval is also shown as a dashed black line. b.) The estimated effective $1/Q$ values from the VSP data set along wih the effective $1/Q$ estimated from the pre-stack and stacked seismic datasets in the region of well 16/23-7.

Figure 4.41a shows that the median of all the stacked $1/Q$ volume lies close to that of the median of the VSP data. However, they are not from the same distribution owing to the large number of data points in the stacked seismic volume meaning that differences in the mean value would have to be negligible for the distributions to be statistically similar. The median pre-stack $1/Q$ value does not correspond with that of either the stacked $1/Q$ distribution nor the median VSP $1/Q$ values. This combined with the lack of interpretability of the pre-stack attenuation maps in figure 4.36 implies that the values estimated from the stacked seismic data are more reliable and realistic than those from the pre-

stack seismic data.

Figure 4.41b shows a comparison of the estimated effective $1/Q$ at the closest data point to the location of well 16/23-7. The VSP results show much higher attenuation anomalies than the stacked and pre-stack surface seismic derived $1/Q$ values. The pre-stack surface seismic results show an overall lower average attenuation than those estimated from surface seismic data and the VSP data. The effective $1/Q$ measured from the stacked surface seismic data also has a median value similar to that given for the entire survey in table 4.6. Although the attenuation anomalies seen in the effective $1/Q$ results from the VSP data are large ($1/Q$>0.04) and cover a range of approximately 200ms but these may be quite deceptive.

The distance between receivers used to form the spectral ratio curves from which $1/Q$ is estimated is set to be 121m, which corresponds to a TWT of approximately 0.115s at 2km depth. This will have the effect of broadening and reducing the magnitude of any attenuation anomaly in the $1/Q$ values measured from the borehole seismic, indicating that although relatively high attenuation is measured in the borehole seismic, peaking at $1/Q$=0.08 (Q=12.5), the true value may be even higher attenuation in a more compact region. However, these proposed high attenuation regions do not similarly affect the seismic waves in the surface seismic data as no attenuation peaks can be seen. Thus either the regions are not expressed in the results of the surface seismic or the attenuation peaks are due to interference in the VSP data, similar to what has been previously mentioned (section 4.5.4).

A counter argument would be that if the attenuation regions are thin then the effect upon the spectra may not be detectable in surface seismic data due to the lower signal-to-noise ratio in the surface seismic compared to the borehole seismic.

The statistics in table 4.6 show that the distributions of both the $1/Q$ values estimated via the prestack and stacked seismic data are leptokurtic (strongly peaked), given by the high kurtosis excess values, but whereas the $1/Q$ values estimated from the prestack data are only slightly right skewed, the $1/Q$ values estimated from the stacked seismic data are strongly left skewed. The median $1/Q$ value from the stacked seismic data is also in agreement with the $1/Q$ value

estimated from the VSP data for the entire interval covered by the VSP data.

The estimated values of $1/Q$ so far have assumed that $1/Q$ is independent of frequency. However, most models for attenuation mechanisms, such as squirt-flow, predict that $1/Q$ would be frequency-dependent. In Chapter 3 frequency-dependent $1/Q$ was estimated for synthetic datasets, and for the Kinnoull dataset analysed here, via fitting power-law curves to the spectral ratio surface utilised by the PSQI algorithm. The power-law curves is defined by; a coefficient which gives the frequency-independent $1/Q$ at 1Hz and; an exponent which describes the frequency-dependence of $1/Q$.

Figure 4.42 shows a comparison of the inverse coefficient and exponent of frequency-dependent attenuation, assuming a power-law frequency dependence of Q of the form $1/Q = f^{-b}/a$, from the VSP data of well 16/23-7 and the pre-stack seismic data. The inverse coefficient $(1/a)$ estimated from the borehole seismic is larger than that estimated from the pre-stack surface seismic data but this is to be expected given the difference in estimated frequency-independent $1/Q$ from both borehole and surface seismic given in figure 4.41b. The frequency exponent estimated from the borehole seismic survey varies typically between -0.6 and 0.2 with a median value of -0.2. Some large exponent values can be a source of information for quality control of the estimated frequency-independent $1/Q$ values, for instance the constant frequency exponent values of 1 between 1.45s and 1.55s TWT are co-located with an area of low signal-to-noise due to wash-out at the bottom of a casing. Although the pre-stack surface seismic exponent results show a very small exponent value, ignoring the two values at 1 which are due to poor fitting of the spectral ratio surface, the borehole seismic derived frequency exponent values have average values between -0.3 and 0, with an exception at 2.25s TWT which may be due to the noise present and described above in the VSP section.

The $1/Q$ maps estimated from the stacked and prestack seismic data are compared to average centroid frequency maps and average instantaneous amplitude maps over the same intervals in order to gain an understanding as to how some of the attenuation features may have formed. Figure 4.43 shows the average centroid frequency maps over the same intervals as seen in figures 4.33 and 4.36 whilst figure 4.44 shows the average instantaneous amplitude (estimated via a

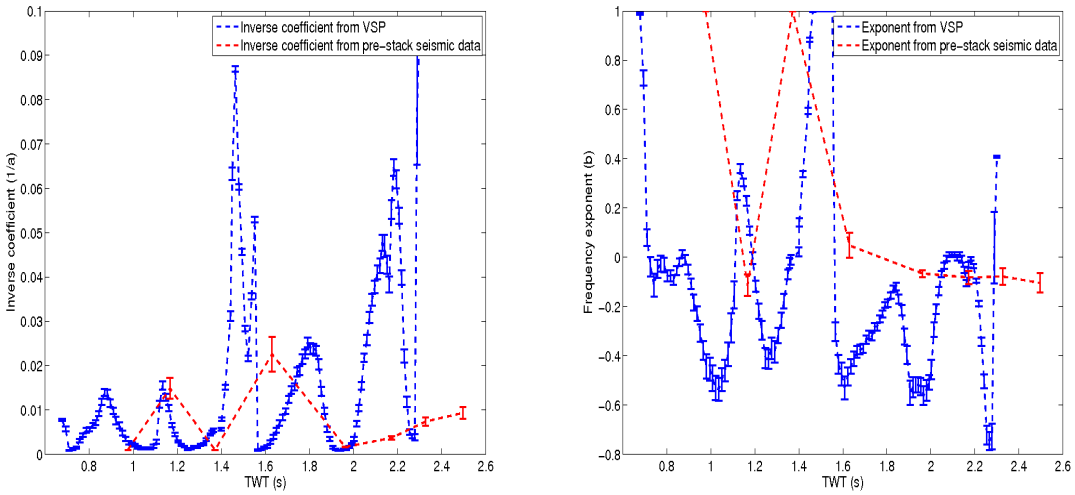

(a) (b)

Figure 4.42: Estimated inverse coefficient of frequency-dependence of Q from the pre-stack surface seismic and the VSP data set (a) and the frequency exponent from the prestack surface and borehole seismic datasets (b).

Hilbert transform) over the same intervals. The centroid frequency volume was estimated via a short-time-Fourier-transform (STFT).

Figure 4.43c shows a high average centroid frequency over the bottom Eocene to top Tor interval between inline 1400 and 1900 and crossline 4200 to 4500, which coincides with lower attenuation in figure 4.33c, which is to be expected as lower attenuation will mean that the centroid frequency is not lowered as much with traveltime of the wave.

This is not always the case though. For instance, the top Miocene to bottom Eocene interval there is no correlation between centroid frequency and attenuation. However, there is a correlation between instantaneous amplitude (figure 4.44b) and attenuation, in which higher attenuation zones at high crossline and inline numbers are coincident with higher average instantaneous amplitude within the interval.

Given these results, it appears that the mapped attenuation does not correlate with either averaged centroid frequency or averaged instantaneous amplitude within an interval in a way which is consistent across all intervals. It should also be noted that no correlation between the attenuation maps estimated from the

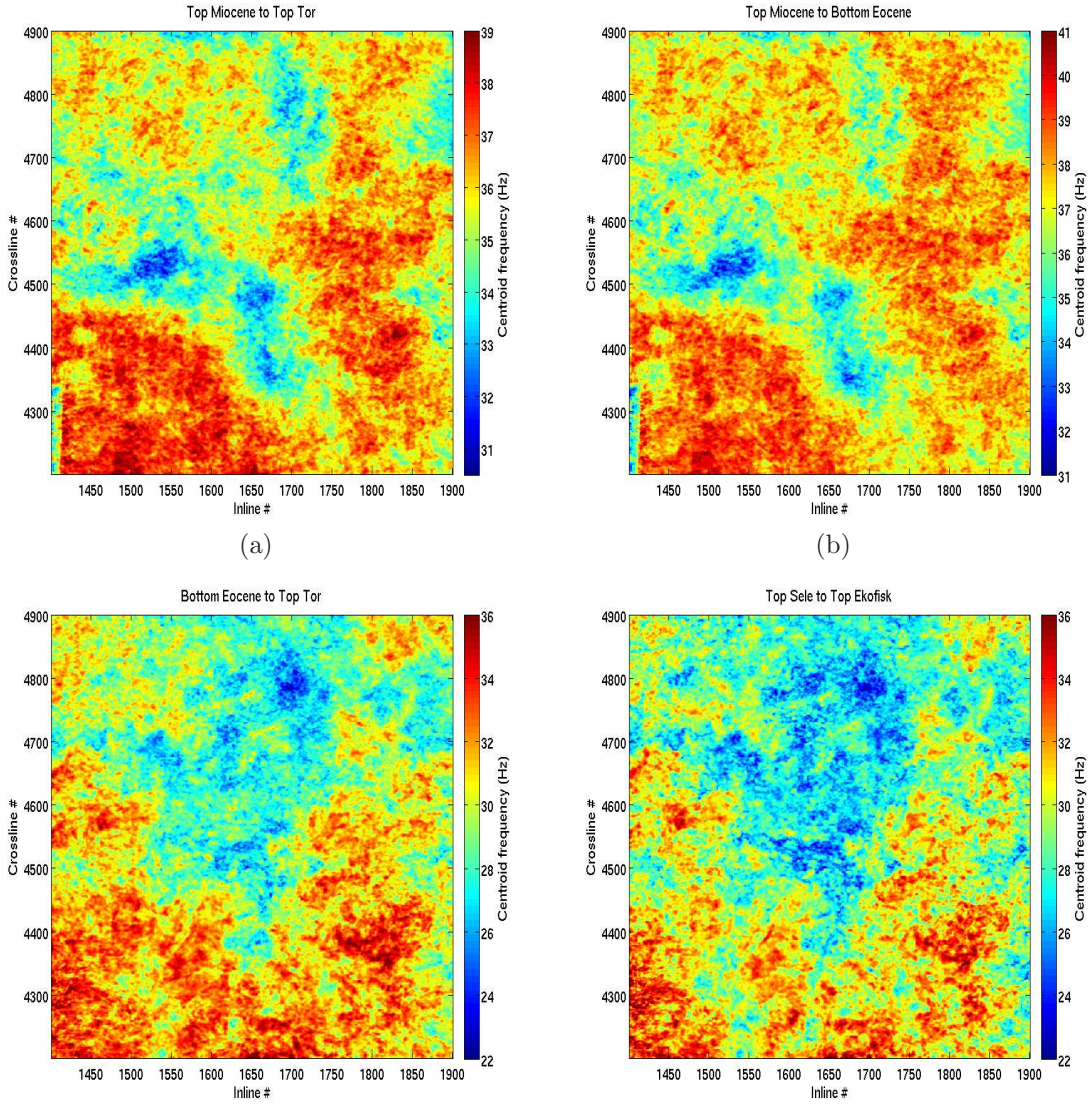

Figure 4.43: Maps of average centroid frequency over the intervals top Miocene to top Tor (a), top Miocene to bottom Eocene (b), bottom Eocene to top Tor (c) and top Sele to top Tor.

prestack data and either the averaged centroid frequency or averaged instantaneous amplitude can be observed for any interval.

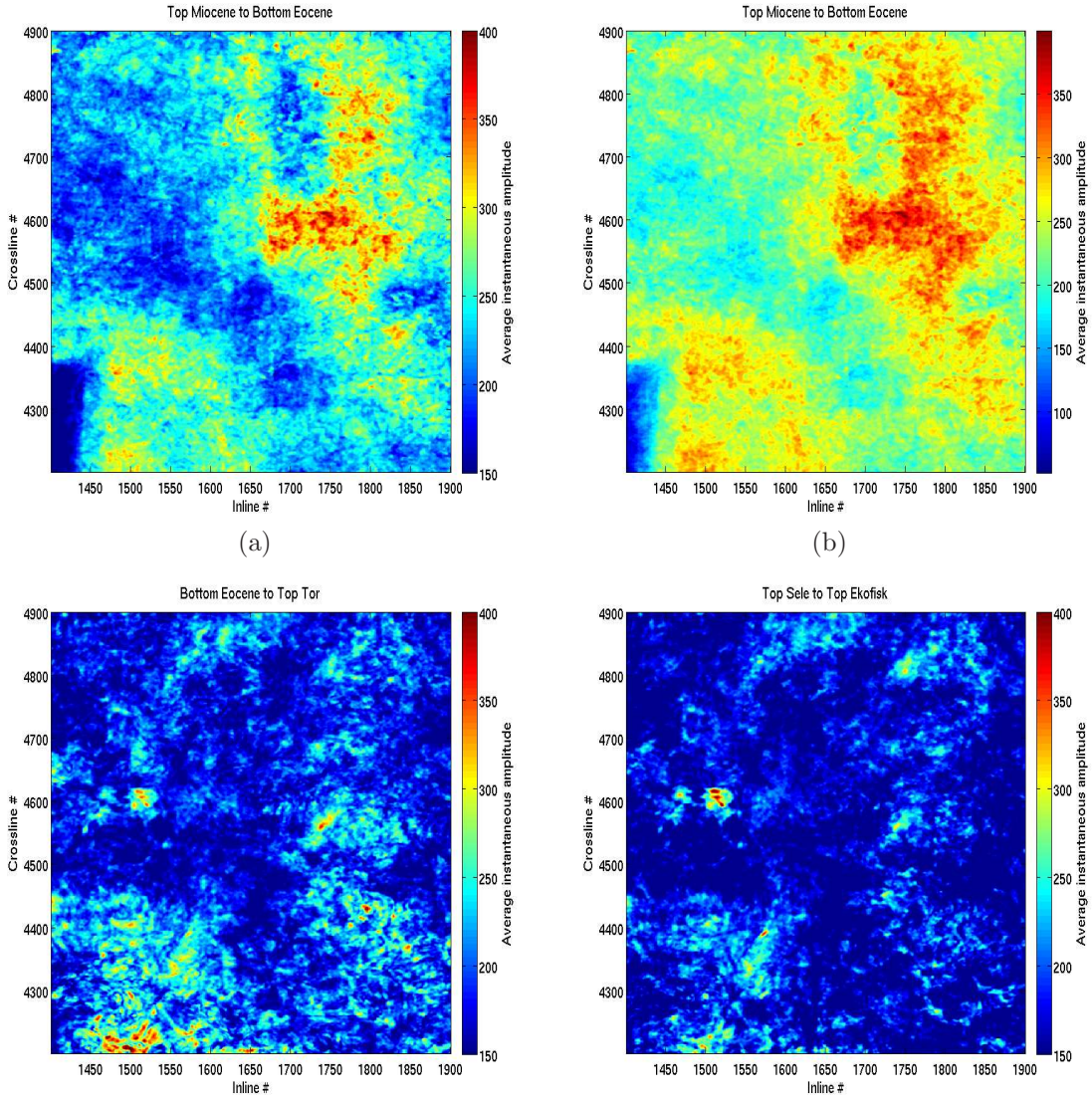

Figure 4.44: Maps of average instantaneous amplitude for the intervals top Miocene to top Tor (a), top Miocene to bottom Eocene (b), bottom Eocene to top Tor (c) and top Sele to top Tor.

4.9 Discussion

One reason for using pre-stack data to estimate attenuation, as opposed to stacked seismic data, is that stacking of seismic data involves a summation of the wave across different offsets, in which the wave will have travelled through the subsur-

face at different angles and thus traveled through the overburden and interval of interest a different amount of time. This leads to a reflection at different offsets having undergone different amounts of attenuation and having a different spectrum. The stacking process then sums the reflection over a large offsets range which then smears the different spectrum at each offset. By working in the pre-stack domain, it is possible to utilize the different ray paths to add information into the inversion for attenuation (Reine et al. (2012a)).

Figure 4.45a shows the result of ray tracing through the velocity model of the Kinnoull data around the 16/23-7 well location for the reflection from the top of the Miocene and the top of the Oligocene. Assuming an input wavelet of a 50Hz zero-phase Ricker wavelet and a constant attenuation of Q=50, the resultant wavelet when stacking all offsets is given in figure 4.45b. It is important to note that although the traveltimes for the reflections are shown, the wavelet at each offset was formed at a constant time, the traveltime of the reflection at different offsets was used to form $t*$ (traveltime/Q) which was used to attenuate the wavelet. The spectrum of the top Miocene reflection as a function of TWT is given in figure 4.46.

Using the spectral ratio method to estimate the attenuation from the stacked wavelets (figure 4.45b) results in a value of Q=50.7$\pm$1, which is, within errors, equal to the input attenuation of Q=50. The spectral ratio method was also applied to the near and far offset wavelets for the top Miocene reflection and the seismic attenuation factor was found to be Q=49$\pm$2, also equal to the input of Q=50, within errors. This result indicates that the summation of different ray paths, which have undergone different levels of attenuation, is not significant in terms of estimating attenuation. This tests was also performed between the top Miocene and top Tor (1.5s deeper than the top Miocene) with similar results. It is important to note that this test does not include the effects of common processing techniques on the spectrum of the wavelet and does not include the possible effects of NMO correction, which is known to cause a stretching of the wavelet with offset which could negatively impact upon the summed wavelet.

The difference between the attenuation estimated from the stacked data and the attenuation estimated from the pre-stack seismic data is then due to the processing sequence, namely the NMO correction and stacking process, and the

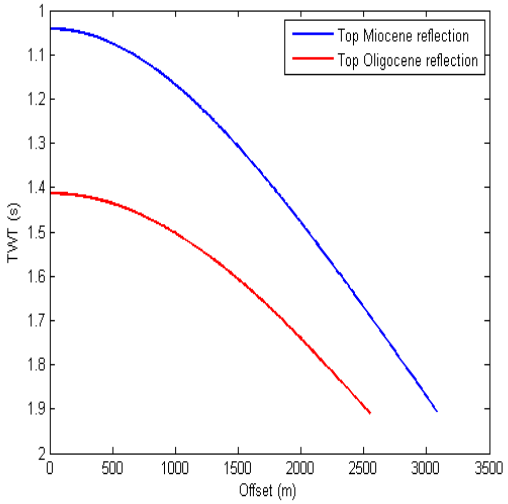

(a)

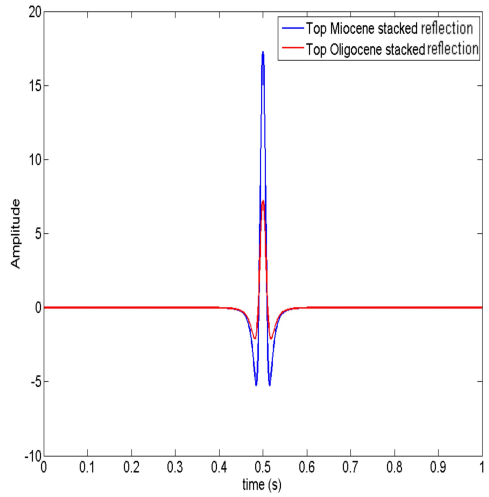

(b)

Figure 4.45: Ray traced traveltime for a reflection from the top of the Miocene and the top of the Oligocene (a) and the stacked spectrum assuming an input wavelet of a 50Hz Ricker wavelet and a constant attenuation of Q=50.

increased signal-to-noise in the stacked data. The VSP data has a higher resolution than the either the stacked or pre-stack data. The attenuation estimated on the stacked and pre-stack data are based on horizons, with 10 horizons spanning almost 2 seconds TWT (varying over the survey area) whereas the VSP data is estimated with receivers separated by 151m (varying between 90ms and 168ms

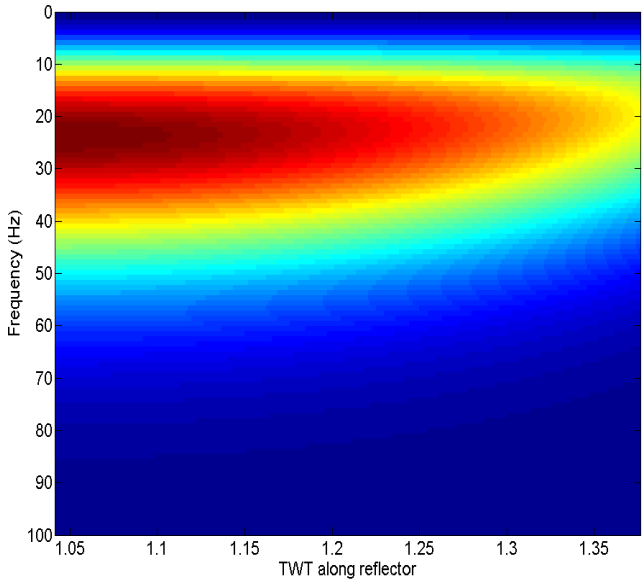

Figure 4.46: Spectrum of the top Miocene reflection as a function of TWT along the reflection.

TWT separation). This is to provide optimal resolution in the attenuation profile. To compare with the stacked and pre-stack seismic data it is necessary to lower this resolution to at least a 220ms TWT average.

Using a receiver separation of 17 gives a TWT difference between receivers of between 162ms and 284ms. Figure 4.47 shows the VSP results for a larger receiver separation, showing that the attenuation peaks are slightly reduced in comparison to figure 4.21. In terms of statistics, the median is increased from $1000/Q$ of 10.4 to $1000/Q$ of 11.0 whilst the mean is reduced from $1000/Q$ of 23.5±2.0 to $1000/Q$ of 19.4±1.7, as the increased receiver separation pushes the estimated values towards a background average $1/Q$ for the entire VSP interval. If the attenuation peak between at 2350m depth is then assumed to be due to interference and removed for the statistics then the mean, median and standard deviation of the estimated $1000/Q$ values are 14.2±1.1, 10.4 and 11.8 respectively. Although the median for the larger separation with interference omitted is the same as for the $1/Q$ estimated with a receiver separation of 8 samples, the mean has been reduced from 20.0±2.0 to 14.2±1.1. The $1/Q$ values estimated from the

VSP data are still not statistically from the same distribution as the stacked and pre-stack estimated $1/Q$ values at the 95% confidence interval.

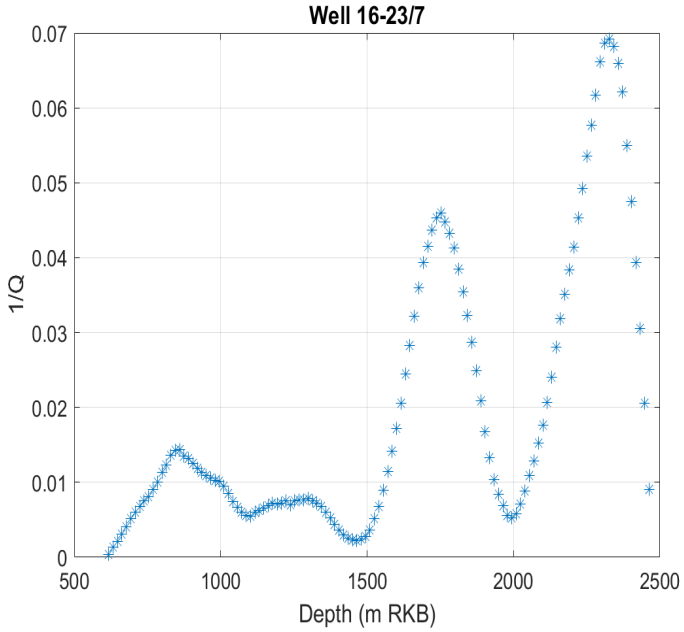

Figure 4.47: Estimated attenuation profile from the VSP data of well 16/23-7 using a receiver separation of 16, which gives an average TWT separation of receivers similar to the average TWT difference between horizons in the surface seismic data.

4.10 Conclusions

Through analysis of well log, vertical seismic profile, stacked seismic and pre-stack seismic data, attenuation has been investigated in the region of the Kinnoull field in central North Sea.

The compressional wave velocity, shear wave velocity and density logs from 3 wells, 16/23-1, 16/23-7 and 16/24A-1 have been used to estimate scattering attenuation over the Kinnoull field. It is found that scattering attenuation across the three wells has an average $1000/Q_{sc}$ value of 0.36, roughly 4% of the average frequency-independent $1000/Q$ value estimated from the stacked seismic data and VSP data. The median characteristic scale length of attenuation was calculated to be 1.01m, with a mean of 2.33m, similar to previously derived results. The

degree of variation in the velocity and density logs controls the magnitude of attenuation and the lack of any significant prolonged variations in the well logs collected from the three wells leads to a low estimate of scattering attenuation in the vicinity of the well logs. The correlation between the scattering attenuation and the gamma ray log is not statistically significant and thus the gamma ray log cannot be used as a proxy for scattering attenuation in the absence of velocity log information.

It is important to note that methods used to estimate scattering attenuation involves a 1D assumption and that any spatial variation in scattering attenuation or contribution to scattering attenuation at the well location due to structural and spatial variability within the subsurface will not be captured.

Attenuation from vertical seismic profile data, recorded at well 16/23-7, was estimated through a spectral ratio of shallower and deeper recordings of the downgoing direct wave. Although the VSP setup is theoretically ideal for estimating attenuation, it was found that spurious downgoing noise, traveling faster than the direct wave, caused problems in estimating $1000/Q$ values below a depth of 2300m MD accurately. A large attenuation peak corresponding to the interval between the intra-Oligocene reflection and the top of the Eocene reflection is present in the attenuation profile estimated from the seismic data. An estimate of attenuation over the whole interval covered by the VSP data gives $1000/Q$=10.4±2, in close agreement with the median value estimated from the stacked seismic data of $1000/Q$=9.2.

Analysis of the attenuation characteristics of the stacked seismic data is carried out using a spectral ratio method centered on spectra extracted around strong reflections. Although for certain intervals the estimated attenuation can be qualitatively correlated well with either average centroid frequency within the same interval or the average energy with the interval for each spatial location, the correlations do not hold for every interval. Thus the estimated attenuation does not correlate with centroid frequency or energy of the seismic data in a consistent manner. The median of the distribution of all $1000/Q$ values estimated from the stacked seismic data is 9.2, which is in agreement with the value estimated from the VSP data but not in agreement with the median attenuation estimated form the pre-stack seismic data.

The estimated attenuation from the pre-stack seismic data shows no correlation with centroid frequency or energy of the seismic data for any interval. Furthermore, the median value of the distribution of estimated $1000/Q$ values, 4.5, does not agree with the stacked seismic data or VSP data. The main interpretable feature in the maps of attenuation estimated from the pre-stack seismic data is the imprint of the acquisition geometry for shallower intervals. This combined with the similar mean attenuation between the stacked and VSP $1/Q$ values leads to the conclusion that attenuation values estimated from stacked data are more reliable than those estimated from pre-stack data.

References

Bath, M., 1974, Spectral analysis in geophysics: Elsevier Scientific Publishing Company, Amsterdam, volume **7** *of* Developments in Solid Earth Geophysic. 113, 133

Behura, J., and I. Tsvankin, 2009, Estimation of interval anisotropic attenuation from reflection data: Geophysics, **74**, A69–A74. 114

Blias, E., 2012, Accurate interval q-factor estimation from vsp data: Geophysics, **77**, WA149–WA156. 127

Chapman, M., S. V. Zatsepin, and S. Crampin, 2002, Derivation of a microstructural poroelastic model: Geophysical Journal International, **151**, 427–451. 112

Dasgupta, R., and R. Clark, 1998, Estimation of q from surface seismic reflection data: Geophysics, **63**, 2120–2128. 114

Egan, M., K. G. ElKasseh, and N. Moldoveanu, 2007, *in* Full deghosting of OBC data with over/under source acquisition: 31–35. 115

Galvin, R., T. Muller, R. Pevzner, and B. Gurevich, 2013, Estimation of scattering attenuation from zero-offset vsp data: Co2crc otway project case study: Presented at the EAGE workshop on seismic attenuation 2013. 117

Liner, C. L., 2012, Elements of seismic dispersion: A somewhat practical guide to frequency-dependent phenomena: Society of Exploration Geophysicists. 140

Mangriotis, M.-D., J. W. RectorIII, E. F. Herkenhoff, and J. C. Neu, 2013, Scattering versus intrinsic attenuation in the vadose zone: A vsp experiment: Geophysics, **78**, B49–B63. 113, 116

Mavko, G., T. Mukerji, and J. Dvorkin, 2009, The rock physics handbook. tools for seismic analysis of porous media: Cambridge University Press. 112

Mller, T. M., and B. Gurevich, 2005, Wave-induced fluid flow in random porous media: Attenuation and dispersion of elastic waves: The Journal of the Acoustical Society of America, **117**, 2732–2741. 112

Mller, T. M., B. Gurevich, and M. Lebedev, 2010, Seismic wave attenuation and dispersion resulting from wave-induced flow in porous rocks, a review: Geophysics, **75**, 75A147–75A164. 112

Odoherty, R., and N. Anstey, 2006, Reflections on amplitudes: Geophysical Prospecting, **19**, 430–458. 113

Padmos, L., D. Davies, M. Davies, and J. McGarrity, 2010, Using high-density obc seismic data to optimize the andrew satellites development.: First Break, **28**, 61–67. 25, 115, 116, 117, 127

Pevzner, R., B. Gurevich, K. Tertyshnikov, A. Bona, and S. Vlasov, 2016, Scattering attenuation from the coal seams (cooper basin, australia): Presented at the EAGE Technical Program Extended Abstracts 2016. 113

Pride, S. R., J. G. Berryman, and J. M. Harris, 2004, Seismic attenuation due to wave-induced flow: Journal of Geophysical Research: Solid Earth, **109**, n/a–n/a. (B01201). 112

Quan, Y., and J. M. Harris, 1997, Seismic attenuation tomography using the frequency shift method: Geophysics, **62**, 895–905. 113, 136

Reine, C., R. Clark, and M. van der Baan, 2012a, Robust prestack Q-determination using surface seismic data: Part 1-Method and synthetic examples: Geophysics, **77**, R45–R56. 158, 178

———, 2012b, Robust prestack q-determination using surface seismic data: Part 2 - 3d case study: GEOPHYSICS, **77**, B1–B10. 114

Shapiro, S. A., and H. Zien, 1993, The o'doherty-anstey formula and localization of seismic waves: Geophysics, **58**, 736–740. 116, 119

Shapiro, S. A., H. Zien, and P. Hubral, 1994, A generalized o'doherty-anstey formula for waves in finely layered media: Geophysics, **59**, 1750–1762. 16, 113, 116, 117, 118, 119, 121, 122, 123

Singleton, S., 2008, The use of seismic attenuation to aid simultaneous impedance inversion in geophysical reservoir characterization: The Leading Edge, **27**, 398–407. 114

Spencer, T. W., J. R. Sonnad, and T. M. Butler, 1982, Seismic q-stratigraphy or dissipation: Geophysics, **47**, 16–24. 134

Tonn, R., 1991, The determination of the seismic quality factor q from vsp data: A comparison of different computational methods.: Geophysical Prospecting, **39**, 1–27. 113, 133

Van Der Baan, M., 2001, Acoustic wave propagation in one dimensional random media: the wave localization approach: Geophysical Journal International, **145**, 631–646. 16, 113, 116, 117, 118, 122, 123

Ville, J., 1958, Theory and application of the notion of complex signal: Technical

report, DTIC Document. 134

Wang, Y., 2008, Seismic inverse q filtering: Wiley-Blackwell. 112

White, B., P. Sheng, and B. Nair, 1990, Localization and backscattering spectrum of seismic waves in stratified lithology: Geophysics, **55**, 1158–1165. 117, 125

Ziolkowski, A., J. Underhill, and R. Johnston, 1998, Wavelets, well ties, and the search for subtle stratigraphic traps: Geophysics, **63**, 297–313. 112

Chapter 5

Attenuation in the Barents Sea

5.1 Abstract

Coincident vertical seismic profiles and well log data have been used to estimate seismic attenuation quality factors, and its frequency-dependence, from six wells in the Norwegian Barents Sea license blocks 7120-7122. Scattering attenuation is estimated from well log data using a wave localisation method and then subtracted from the effective attenuation, estimated from vertical seismic profile data, to estimate intrinsic attenuation. The intrinsic attenuation is then averaged over each formation encountered in each well, and then over all wells to form an average attenuation profile.

The formation averaged intrinsic attenuation shows a generally higher level of attenuation within the Nordmela to Snadd formations, with lower attenuation in the Torsk to Støformations. The seismic attenuation quality factor, Q, is assumed to have a powerlaw frequency-dependence described by a coefficient, a, and an exponent, b. The formation averaged exponent of frequency-dependence, b, is low throughout all formations, falling within the range -0.1$< b <$0.2 and with a median value of 0.02.

Squirt flow modelling of the measured frequency-dependence of attenuation leads to estimated crack aspect ratios of between 10^{-3} and 6x10^{-3}, similar to the range of crack aspect ratios expected to mainly contribute to squirt flow attenuation. For the Snadd formation, the characteristic peak frequency of attenuation

of 10^{-5}Hz and the estimated crack aspect ratio of 10^{-6} indicate that the observed frequency-dependent attenuation is not dominated by squirt flow.

Bulk, shear, Young's and compressional wave modulus as well as Lamé's parameter, Poisson's ratio, brittleness index, porosity and sand percentage are all calculated from well logs and compared to the estimated intrinsic attenuation. Bulk modulus, shear modulus, Young's modulus and Poisson's ratio showed statistical significant correlation with the estimated intrinsic attenuation at the 95% confidence level. The correlation of intrinsic attenuation with Poisson's ratio is negative whereas the correlation with bulk, shear and Young's modulus are positive. An empirical relationship based on a linear dependence of attenuation on these four elastic parameters has been created but attenuation values reconstructed from this relationship could not accurately reproduce the estimated intrinsic attenuation, with a median error of 44%, although they reconstructed values do show a statistically significant correlation.

The lack of sample data points, 22 for the four elastic parameters which show a statistically significant correlation, has contributed to a lack of knowledge on the relationship between elastic parameters and the intrinsic attenuation, a linear relationship between the elastic parameters and attenuation is assumed but more data can help to refine this relationship.

5.2 Introduction

A consequence of seismic attenuation is the loss of energy per cycle of propagation through the subsurface. This leads to a preferential loss of the high frequency content of a seismic wave as it propagates through the subsurface. Seismic attenuation is often defined by a unitless variable, Q, whereby $1/Q$ is proportional to the fractional loss of energy per cycle of a wave. The loss of high frequency content leads to a reduced bandwidth and hence a loss of resolving power with depth, which can be corrected for via inverse-Q filtering (Wang (2008)), given an estimate of Q either known or estimated from the data. It is therefore desirable to estimate an accurate Q model from the seismic data.

Malinowski et al. (2011) use a trial and error method of matching real and synthetic AVO responses to find the best fit starting Q-model for their visco-

acoustic full waveform inversion (FWI), but an initial model of Q with depth could also be used as a starting model for visco-acoustic FWI.

The seismic wave can lose energy through intrinsic attenuation due to fluid flow induced by the propagating wave (Chapman et al. (2002), Mller and Gurevich (2005)). The energy of seismic wave can also be redistributed by scattering due to layering of lithology in the subsurface (Mangriotis et al. (2013), Van Der Baan (2001) and Odoherty and Anstey (2006)), which can act as a low-pass filter and mimic the response of attenuation. When estimating seismic attenuation from seismic surveys (such as surface seismic surveys and vertical seismic profiles (VSPs)), it may not be possible to separate the effects of intrinsic and scattering attenuation. However, with the help of coincident well log data, the scattering attenuation may be estimated assuming a 1D homogeneous medium and removed from the measured effective attenuation to leave only intrinsic attenuation.

As attenuation preferentially cuts out high frequencies and lowers the bandwidth, altering the shape of the wavelet, it is possible to estimate Q from a variety of methods which focus on either the changing spectrum of the signal or the changing pulse shape of the signal with propagation distance (Tonn (1991), Quan and Harris (1997)). A popular method by which to estimate Q is the spectral ratio method (Bath (1974)) where the frequency content of a wavelet is compared at two points along a co-linear path, and the loss of amplitude with frequency is measured. The spectral ratio method can be summarised by the equation

$$ln\left(\frac{A_i(f)}{A_j(f)}\right) = ln(C) - \frac{\pi f \Delta t_{ij}}{Q_{ij}} \tag{5.1}$$

Here A_i is the amplitude spectrum of the wavelet after a propagation time t_i and A_j is the amplitude spectrum of the wavelet after a propagation time t_j, where $t_j < t_i$. C accounts for the ratio of transmission coefficients experienced by the wave and at the top and bottom of the interval of interest, similar but not equivalent to the energy partitioning term in the PSQI method (Reine et al. (2012)) and geometric spreading is corrected for prior to attenuation estimation. Δt_{ij} is the time difference between t_i and t_j and Q_{ij} is the attenuation in the interval between i and j. The spectrum of the source wavelet (A_0), if known, can

be set to be A_j and a cumulative attenuation estimated with propagation time, which can then be converted to an interval attenuation by the equation

$$\frac{1}{Q_{ij}} = \frac{1}{\Delta t_{ij}} \left(\frac{t_j}{Q_{0j}} - \frac{t_i}{Q_{0i}} \right) \tag{5.2}$$

Here Q_{0j} is the cumulative attenuation between the source wavelet and the wavelet at a propagation time of t_j.

The relationship between seismic quality factor and petrophysical parameters has been investigated in laboratory experiments at high frequencies (typically between 0.3MHz and 1.5MHz). Results are varied as Klimentos and McCann (1990) present data which shows a correlation between attenuation rate, α, and porosity and clay content where as Shatilo et al. (1998) present data which shows no evidence of a relationship between attenuation rate and clay content, however they do find a correlation between attenuation rate and both porosity and permeability. Best et al. (1994) present data which suggest only a weak correlation between the compressional-wave seismic quality factor, Q_p, and both compressional-wave velocity and porosity: however, they do find a strong correlation between Q_p and both the shear-wave seismic quality factor, Q_s and the volume percentage of intra-pore minerals.

Koesoemadinata and McMechan (2001) combine petrophysical data from 18 published studies on sandstones and fit an empirical relationship to find the dependence of the compressional seismic quality factor, Q_p, on porosity, clay content, permeability, water saturation, effective pressure and frequency. They find that compressional wave attenuation, for clay contents >0.29, is dependent upon all of the fitted parameters, although less so for effective pressure at low frequencies. The data included are mainly from laboratory measurements at high frequencies. However, petrophysical values derived from 2 offshore wells in Indonesia were also included.

Although many studies have been carried out to investigate the link between attenuation and petrophysical properties in laboratory experiments, fewer have attempted the same using in situ measurements. Hauge (1981) establish a correlation between attenuation and sand percentage using five detailed VSP datasets and coincident well logs from Texas and Louisiana, finding that porous sands

have a greater attenuation than neighboring shales. Zhang et al. (2013) attempt to estimate an empirical relationship between compressional wave quality factor, Q_p, and porosity, shale volume, compressional-wave modulus and the ratio of compressional- to shear-wave velocity (V_p/V_s), in a similar manner to Koesoemadinata and McMechan (2001). They find that the attenuation decreases as shale volume increases, in agreement with Hauge (1981), and also find that attenuation also decreases with increasing porosity.

Pride et al. (2003) and Pride and Berryman (2003) discuss and show evidence for a relationship between the frequency dependence of the seismic quality factor, Q, and permeability. If permeability is to be estimated from seismic data, whether that be surface seismic surveys or vertical seismic profiles, it is necessary to estimate the frequency dependence of the seismic attenuation.

Sams et al. (1997) measure the frequency-dependence of attenuation over 5 orders of magnitude of frequency with VSP, crosshole, sonic and core data. They also model the observed attenuation with a squirt-flow model using the methods of Jones (1986) and Mavko and Jizba (1991).

In this paper we will first review the data and processes used for the estimation of petrophysical parameters, effective $1/Q$ values and scattering $1/Q$ values. Second, we will present and discuss the estimated parameters and then conclude with a discussion of any perceived relation between the estimated petrophysical parameters and intrinsic $1/Q$ values (derived from the effective $1/Q$ and scattering $1/Q$ values).

5.3 Data overview

The data used in this study consists of 6 sets of coincident VSP and well log datasets from license blocks 7120-7122 of the Norwegian Barents Sea (figure 5.1).

The lithologies encountered are of middle Triassic age and younger and are dominated by clastic deposition. An overview of the geology of the Barents Sea is given in Dor (1995). The youngest formation analysed is the Torsk formation and the oldest formation analysed is the Kobbe formation. Note that not every formation is encountered in every well. The depth to the top of the formations encountered in each well is given in table 5.1.

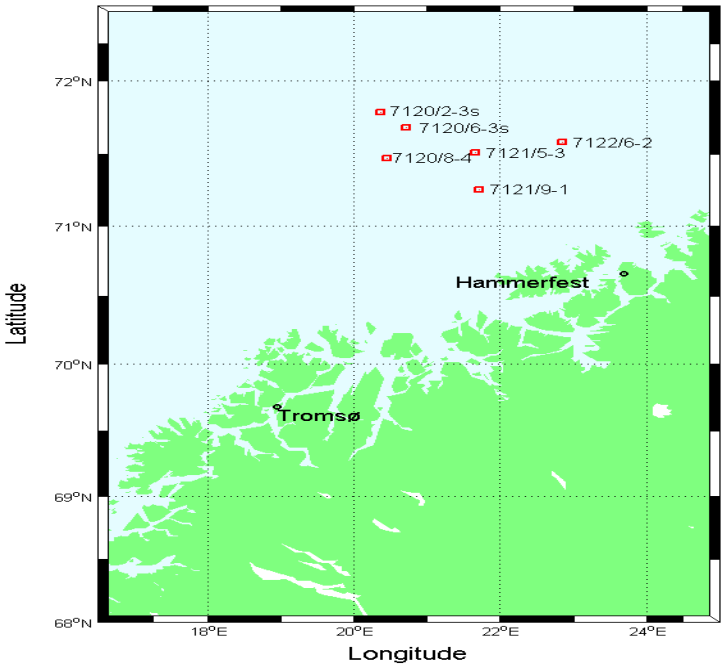

Figure 5.1: Map of the location of the wells used in this study (red squares) in relation to the North coast of Norway.

5.4 Estimating attenuation

After applying edits to the raw VSP data to remove noisy traces, the traces recorded at each specific depth locations are stacked and vector rotated via hodogram analysis. In all surveys four shots were taken with the receivers at each depth location, thus for each depth location at most four traces were stacked, this number may be less if noisy traces have been removed at that depth location prior to stacking. Figures 5.2 to 5.6 show the stacked component of the VSP data parallel to the direction of propagation of the downgoing direct wave for each of the six wells analysed in this study.

The VSP data in figure 5.2 to 5.6 are then synchronized to the direct wave and wavefield separation applied via use of a spatial median filter, and the alignment then removed. The Wigner-Ville distribution of each trace is taken to form its time-frequency representation and summed in time along a window centered on

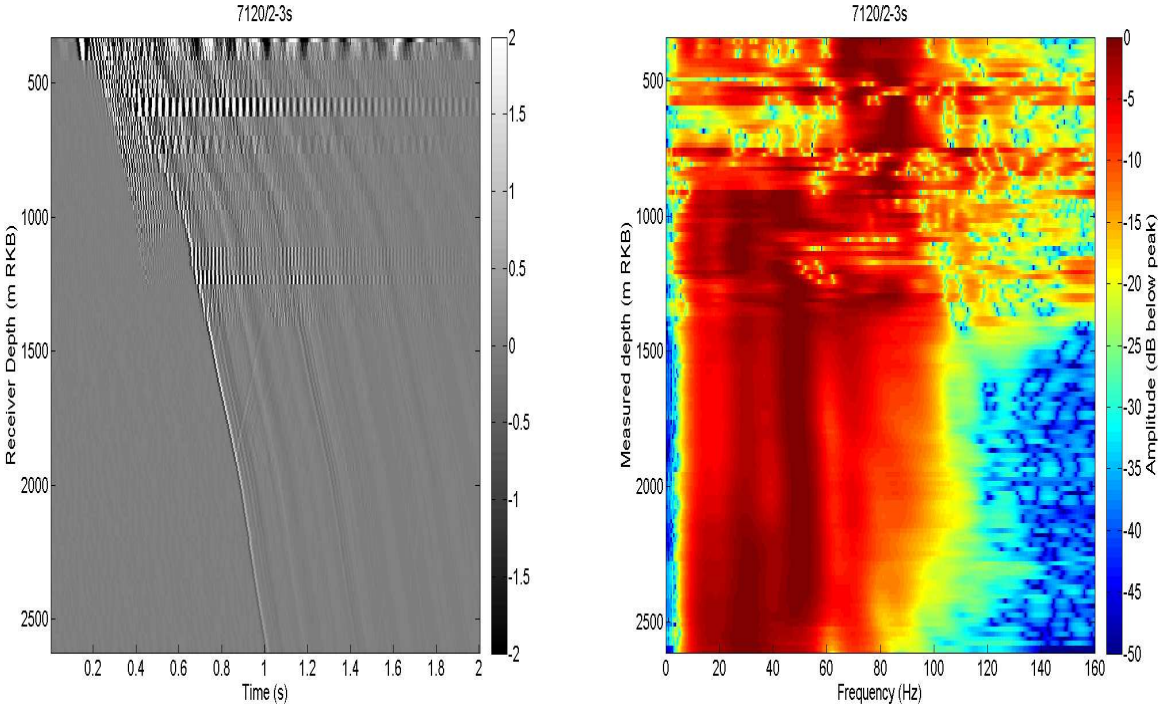

(a) (b)

Figure 5.2: Stacked component of VSP wavefield parallel to the direction of propagation of the down-going direct wave for well 7120/2-3s (a) along with the frequency content of the down-going direct wave at each depth trace (b).

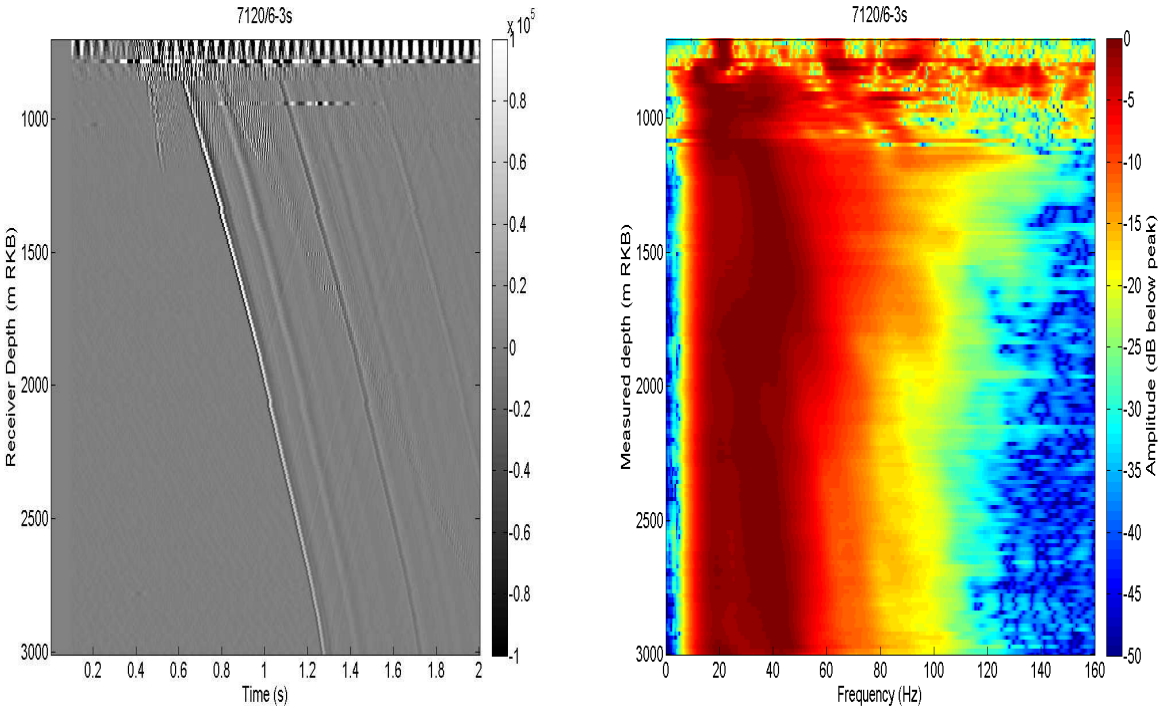

(a) (b)

Figure 5.3: Stacked component of VSP wavefield parallel to the direction of propagation of the down-going direct wave for well 7120/6-3 (a) along with the frequency content of the down-going direct wave at each depth trace (b).

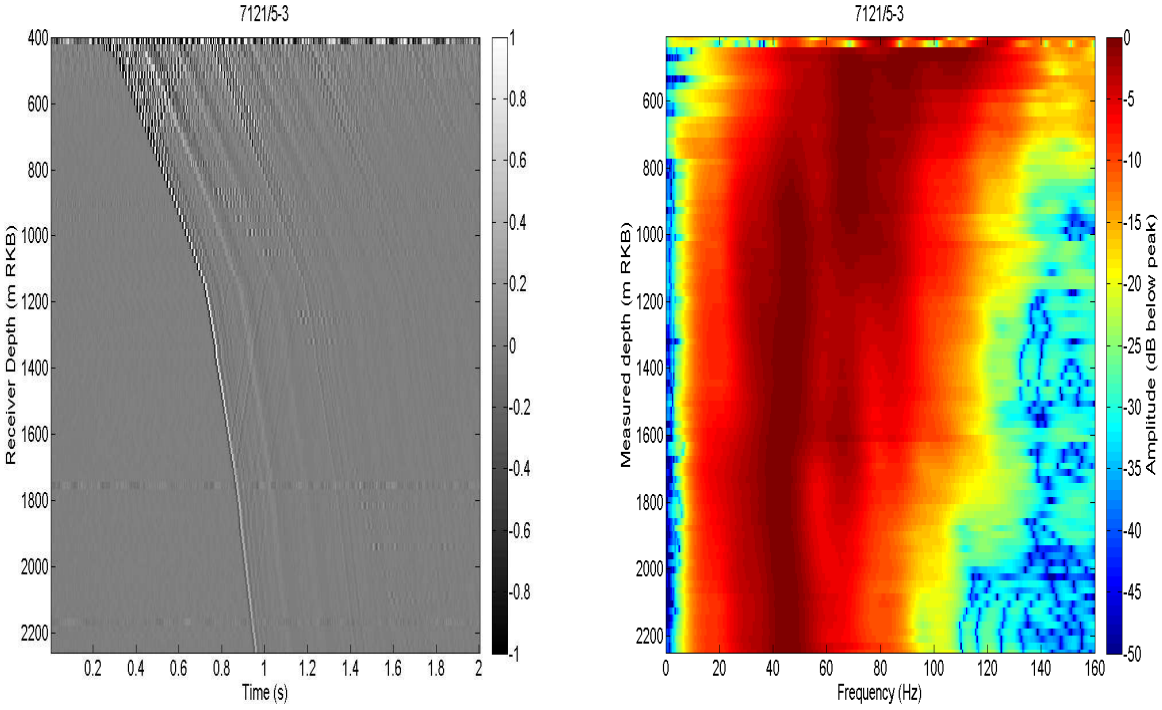

(a) (b)

Figure 5.4: Stacked component of VSP wavefield parallel to the direction of propagation of the down-going direct wave for well 7121/5-3 (a) along with the frequency content of the down-going direct wave at each depth trace (b).

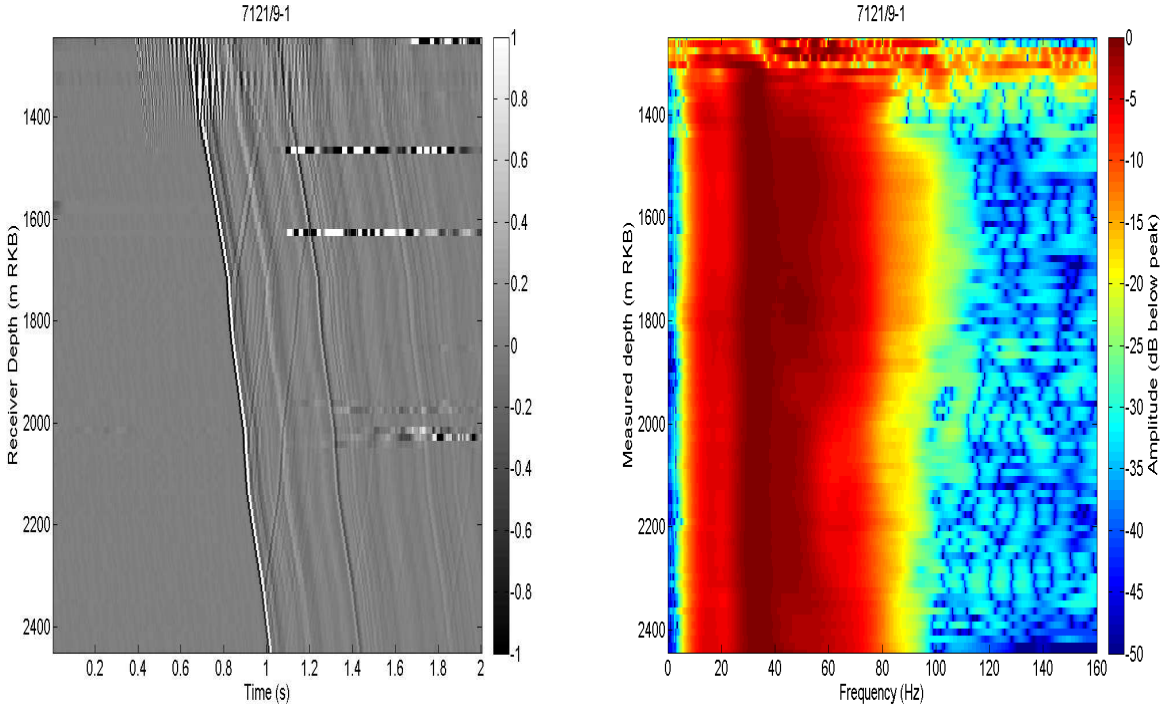

(a) (b)

Figure 5.5: Stacked component of VSP wavefield parallel to the direction of propagation of the down-going direct wave for well 7121/9-1 (a) along with the frequency content of the down-going direct wave at each depth trace (b).

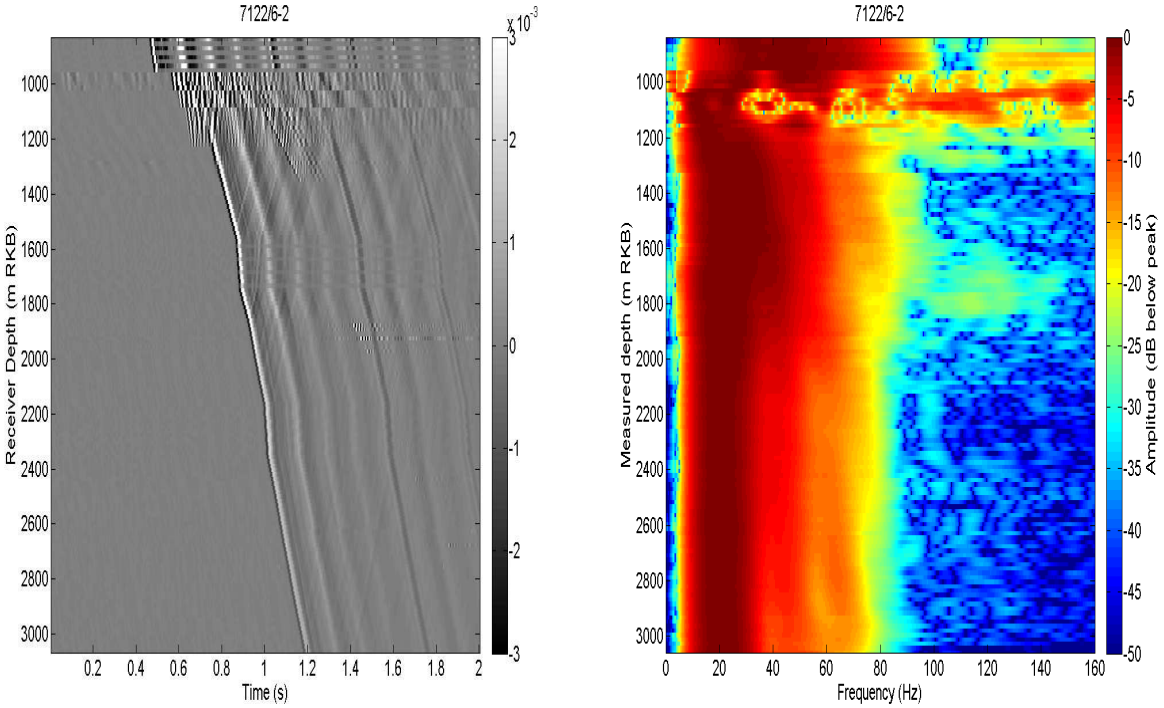

(a) (b)

Figure 5.6: Stacked component of VSP wavefield parallel to the direction of propagation of the down-going direct wave for well 7122/6-2 (a) along with the frequency content of the down-going direct wave at each depth trace (b).

Table 5.1: Depth (m) to the top of formations encountered in each well. Note that some smaller formations, such as the Fuglen formation encountered in well 7120/8-4 which has a thickness of 14m, has been omitted from further analysis and formations which are penetrated by the well but for which a good estimate of attenuation could not be contained are also omitted.

formation	7120/2-3s	7120/6-3s	7120/8-4	7121/5-3	7121/9-1	7122/6-2
Torsk	375	370	376	412	421	–
Kveite	–	1256	–	–	–	791
Kviting	–	–	1186	844	900	–
Kolmule	1441	1289	1279	865	910	852
Kolje	1702	1996	1798	1625	1545	1623
Knurr	1932	2665	2142	1790	1809	1875
Hekkingen	2000	2811	2179	1832	2081	1936
Stø	2071	2893	2264	1880	–	2048
Nordmela	2221	2979	2360	1928	–	2088
Tubåen	2299	–	2496	1984	–	2104
Fruholmen	2363	–	2643	2034	–	2113
Snadd	2563	–	–	2223	–	2202
Kobbe	–	–	–	–	–	3006

the maximum envelope of the direct wave, to form the spectrum at that particular depth. The latter can be represented in an frequency vs depth (FZ) image, which is shown next to the corresponding VSP data in figures 5.2 to 5.6. The spectra at a set receiver sample separation are then used to form a spectral ratio curve (equation 5.3) from which attenuation is estimated.

$$\ln\left(\frac{A_j(f)}{A_i(f)}\right) = \ln(C) - \frac{\pi f \Delta t}{Q_{ij}} \tag{5.3}$$

Here, A_i is the spectrum of the downgoing direct wave at depth level i, C is a constant to account for reflection/transmission losses between depth intervals i and j, Δt is the one-way time difference between depth intervals i and j for the downgoing direct wave and Q_{ij} is the seismic attenuation quality factor in the depth interval between levels i and j. Geometric spreading is not included in this equation as it simple to correct for given knowledge fo the receiver depths and has been corrected for prior to attenuation estimation. Table 5.2 shows the processing parameters used in estimating attenuation from the VSP data.

Table 5.2: Processing parameters used to preprocess the VSP data in figures 5.2 to 5.6 and estimate attenuation. Note that changes in attenuation may necessitate the use of different processing parameters, for instance a high value of attenuation causes a readily observable different in frequency content or a relatively small spatial scale whereas a low value of attenuation does not. Here f_{low} and f_{high} represent the low and high ends of the frequency band used for the regression analysis of the spectral ratio slopes.

Well	f_{low}	f_{high}	Integration window length (ms)	Receiver separation for spectral ratio
7120/2-3s	14	120	30	10
7120/6-3s	5	120	40	40
7120/8-4 (500m-1100m)	10	120	20	8
7120/8-4 (1600m-2500m)	10	120	20	30
7121/5-3	10	100	30	8
7121/9-1 (1600m-2020m)	7	95	30	7
7121/9-1 (2070m-2210m)	7	95	30	35
7122/6-2	8	85	30	25

For wells 7120/8-4 and 7121/9-1 different processing parameters have been used for different depth ranges within the data. For well 7121/9-1, the attenuation in the depth range 2070m to 2210m is low (average Q over 300) so the preferential loss of high frequency content is less noticeable, and so to accurately estimate a value for Q, which is not due to noise in the data, a longer receiver separation is needed as attenuation is a cumulative effect; the longer the analysis interval the larger the difference in frequency content between the top and bottom of that window. As attenuation is a cumulative effect but noise should be similar between two depth locations regardless of separation, then the effect of attenuation as compared to noise will increase with increasing separation of the traces used to estimate Q.

This is also the case for all of well 7120/6-3s, where no large attenuation peaks are present. The receiver separation may also need to be large if the signal to noise level in the data is poor, or interference on the direct wave causes excessive notching, as is the case for well 7120/8-4 in the depth range (1600m-2500m) and for most of well 7122/6-2. In all wells, the receiver separation in metres can be obtained by multiplying the receiver separation in samples (given in table 5.2) by 15.12m.

Scattering attenuation is estimated from the compressional velocity and density logs using the method of Mangriotis et al. (2013) and Shapiro et al. (1994), but from the wave localisation method of Van Der Baan (2001) where only the compressional wave speed log is available. Both methods rely on using the relative variability in the logs to estimate a characteristic scale length which determines the frequency at which scattering attenuation peaks. The degree of relative variation in the well logs around their respective background trends is the dominant control on the magnitude of scattering attenuation.

5.4.1 Estimating frequency-dependent attenuation

To estimate frequency-dependent attenuation, we assume a powerlaw form of frequency-dependence of the seismic attenuation quality factor (equation 5.4). Here, the exponent b controls the level of frequency-dependence and the coefficient $1/a$ is the frequency-independent attenuation factor, which is equivalent to

the inverse seismic attenuation quality factor, $1/Q$, at 1Hz.

$$\frac{1}{Q_{ij}} = \frac{1}{a_{ij} f^{b_{ij}}} \tag{5.4}$$

When the powerlaw frequency-dependent form of Q given in equation 5.4 is substituted into equation 5.3 the resultant is the following form of the spectral ratio equation

$$\ln\left(\frac{A_j(f)}{A_i(f)}\right) = \ln(C) - \frac{\pi f^{1-b_{ij}} \Delta t}{a_{ij}} \tag{5.5}$$

All symbols have the same meanings as are defined for equations 5.4 and 5.3.

Equation 5.3 can be solved by linear least squares inversion for Q_{ij} given that the frequency vector, f, and time difference are known. However, Equation 5.5 is non-linear with respect to the model parameters 1/a and b. Available methods of solving this equation include, but are not limited to, non-linear inversion, forward modelling, Monte-Carlo and directed Monte-Carlo methods. The method utilized in this study is the forward modelling method. The forward modelling, or grid search, method samples a regular grid of the parameter space of 1/a and b to form a theoretical spectral ratio curve, given that C is already known, and compares the theoretical curve to the data. The best fit set of model parameters is then chosen as the one which has the least absolute difference between modeled and data spectral ratio curves (an L1-norm).

In practice, this was previously found, in chapter 4, to be one of the least efficient methods of estimating the required parameters but is also one of the most robust. On synthetic data, the forward modelling method gave the correct result more often than a non-linear inversion or genetic algorithm approach but was approximately 12 times slower, although an added benfit is the creation of a residual map within the search range. Given the limited amount of data available in a VSP survey, even an inefficient method such as the forward modelling method will take up minimal resources.

5.5 Analysis of attenuation results

The estimated attenuation profiles for each of the wells are given in figure 5.7.

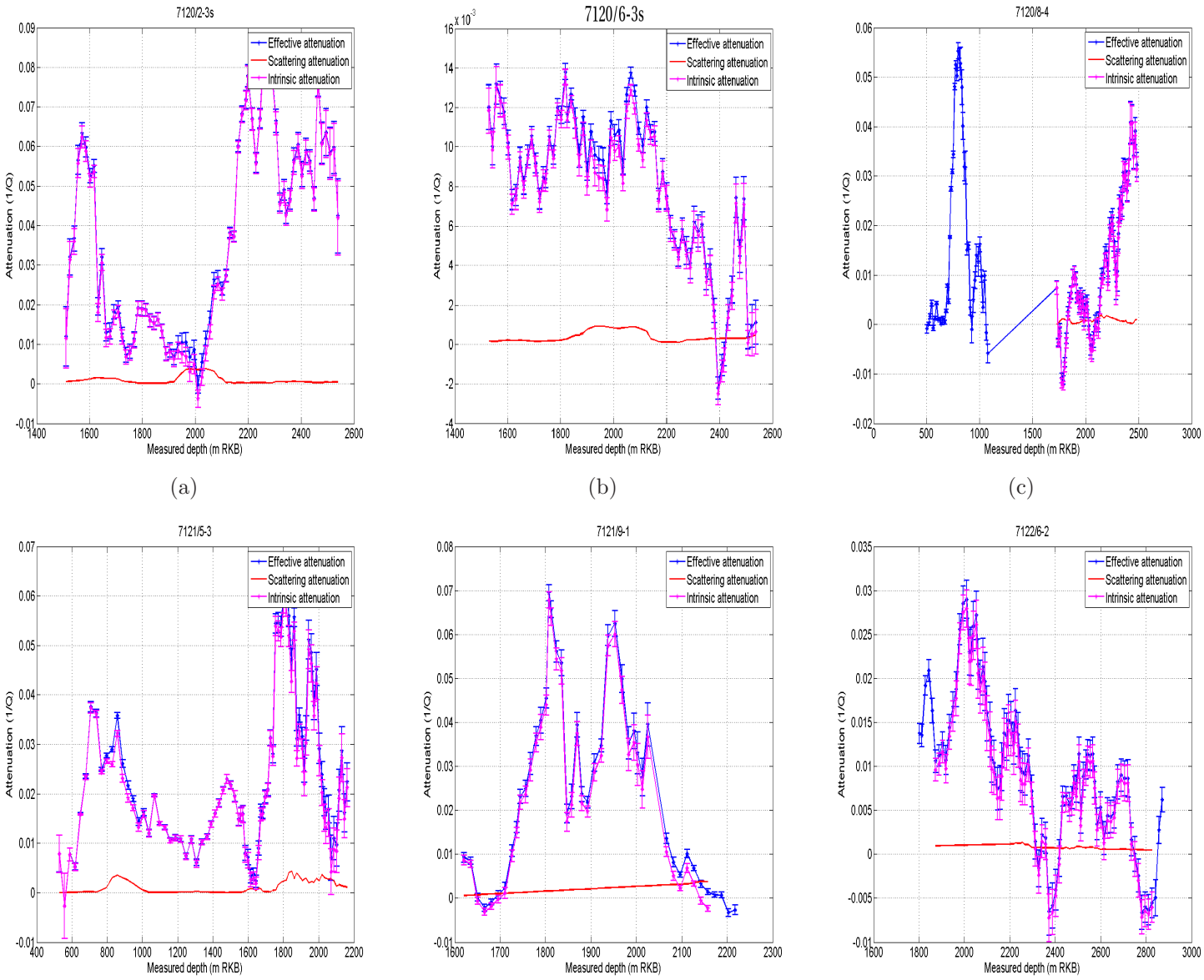

Figure 5.7: Profiles of effective, scattering and intrinsic $1/Q$ value as a function of depth for all 6 wells. The intrinsic $1/Q$ values are estimated by subtracting the scattering $1/Q$ values from the effective $1/Q$ values.

The range of estimated attenuation quality factor values varies from negative values, of the order of $1/Q$=-0.01 (Q=-100), to positive quality factor values of $1/Q$=0.09 (Q=10). The measured attenuation in every well varies and the attenuation profile shows several distinct peaks. Individual peaks can be correlated with other well information, for instance the peak in attenuation seen between 1530m and 1630m depth in well 7120/2-3s is well correlated with a gas column in the Kolmule formation described in the well log history. However, a deeper gas column in the Støformation, between 2071m and 2100m, also in well 7120/2-3s, does not show a distinct peak in attenuation. This implies that the presence of gas alone does not constitute high, or low, attenuation values.

The attenuation profiles show that intrinsic attenuation dominates over scattering attenuation for the vast majority of all wells studied.

In order to derive a background attenuation profile for the Barents Sea license area 7120-7122 (figure 5.1), the intrinsic attenuation profiles (measured $1/Q$ from the VSP data minus the scattering $1/Q$ from the corresponding well logs) are transformed into $t*$ values ($t* = \Delta t/Q$) and averaged over each formation, then transformed back into attenuation quality factor values. This results in a traveltime-weighted average $1/Q$ value. The formation attenuation values are then averaged across all wells, with error in the mean given by the standard error. Figure 5.8 shows the average inverse quality factor value over each formation.

The mean attenuation within each formation is positive and greater attenuation exists in formations between the Nordmela and Snadd. Only one well had attenuation data within the Kobbe formation, and therefore its error bar is taken as the mean error in the attenuation values estimated within the Kobbe formation in well 7122/6-2 (the only well in which the Kobbe formation was penetrated). Only the Kviting formation average attenuation value has an error larger than the value itself. Only two wells provided information on attenuation from the Kviting formation, wells 7120/8-4 and 7121/5-1, both of which had significantly different attenuation values, and hence the error on the average is large. Although the Kveite formation is penetrated by both wells 7120/6-3s and well 7122/6-2, no reliable measure of attenuation could be estimated in these regions and thus the Kveite formation average attenuation is not present in figure 5.8.

Although the standard error on the mean is used as a measure of error in

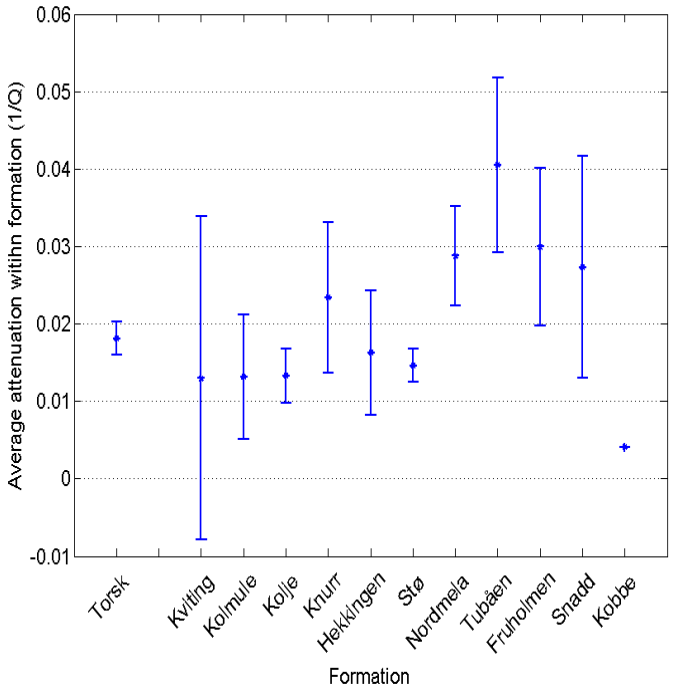

Figure 5.8: Average attenuation as a function of formation for the six wells studied in this survey. Error bars are given by the standard error on the mean.

the formation average inverse quality factors values, the errors themselves should be treated with scepticism. Due to the low number of values available for each formation, between 0 and a maximum of 6, there is not a statistically significant amount of data available for any individual formation and thus any statistical inferences should be taken with caution.

Figure 5.9 shows the formation averaged frequency-dependence of attenuation across all six wells used in this study. The frequency formation averaged frequency exponent, b, lies in the range -0.1<b<0.2 for all formations, thus no formation shows a high level of frequency dependence on the seismic attenuation quality factor. The level of frequency dependence present would, however, lead to a change in the seismic attenuation quality factor over the seismic bandwidth used in each VSP (table 5.2) albeit a modest one. For example, given a frequency-dependent coefficient, a, of 100 and a frequency exponent of 0.052 (the mean of the formation averaged frequency exponent values, table 5.3) then the seismic

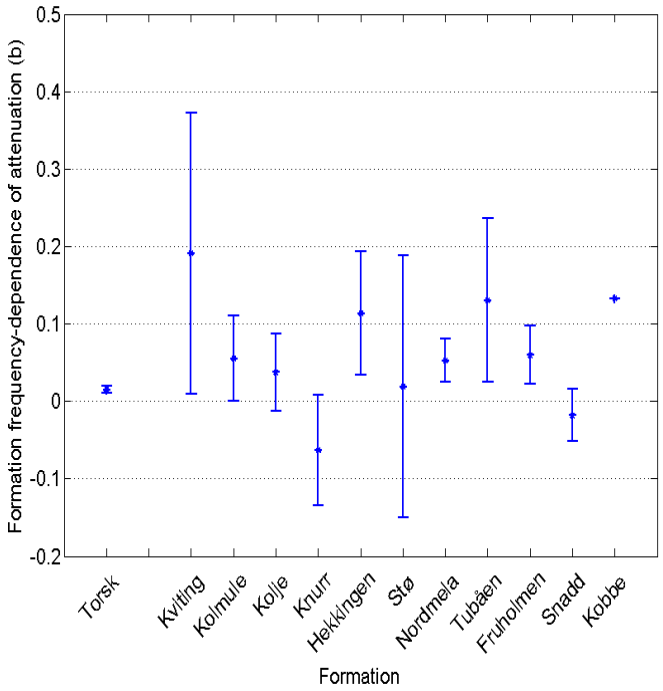

Figure 5.9: Formation averaged frequency-dependence of attenuation as a function of formation for the six wells studied in this survey. Error bars are given by the standard error on the mean.

quality factor, Q, would change from 89 at 10Hz to 79 at 100Hz. For the Tubåen formation with $1/a$=0.0494 and b=0.12 the range of $1/Q$ between 10Hz and 100Hz is 0.0375 (Q=26.7) to 0.0284 (Q=35.2).

Table 5.3 shows that the formation averaged frequency-dependence of seismic attenuation is low, with a median value of 0.02. The lower the level of frequency dependence, the harder the frequency-dependence is to estimate accurately due to a smaller effect on the spectral ratio curve. Previous results of Carey et al. (2008) and Jeng et al. (1999) have suggested higher levels of frequency-dependence of the seismic attenuation quality factor, with Carey et al. (2008) estimating a frequency exponent of between 0.6 and 0.87. However, these studies were also carried out on near surface and water bottom regions where the unconsolidated rocks make for a much different geomechanical context than the more consolidated rocks in this study at a depth of between 300m and 2500m below the sea floor.

Table 5.3: Statistics of the formation averaged frequency-dependence of seismic attenuation as estimated from all six wells. σ is the standard deviation, $\bar{\sigma}$ is the standard error and γ is the kurtosis excess (kurtosis-3).

Statistic	value
Mean	0.052
Median	0.020
σ	0.14
$\bar{\sigma}$	0.022
Skewness	0.21
γ	0.10

5.6 Estimation of petrophysical parameters

The coincident well log data for the wells studied so far have different logs run within them but some logs are universally present. These include; gamma ray log, deep, medium and micro resistivity, compressional wave transit time (which can be converted to compressional velocity), neutron porosity, density porosity, caliper and photoelectric factor. Additionally, only well 7121/5-3 does not contain a shear wave transit time log.

The first step of the well log interpretation is to separate the well into zone which reflect changes in the well log characteristics. The well logs are then analysed to estimate sand percentage and then porosity. Most wells used in this study show little hydrocarbon saturation.

The determination of shale volume is carried out via analysis of both the gamma ray log and the neutron porosity/density crossplot. In estimating shale/sand percentage from a gamma ray log, first a clean shale and a clean sand gamma ray reading is determined from a priori knowledge of the geology, from previous studies and drilling reports for example, and the gamma ray log itself. The sand percentage is then the percentage of the distance between the clean sand line and clean shale line that corresponds to the gamma ray log value. Care must be taken here as organic matter in shales can increase the gamma ray reading by a factor of 2-4 and if radioactive minerals are present in sand intervals then these could be falsely interpreted as shale intervals using the gamma ray alone. Spectral gamma ray tools can be helpful in avoiding the latter scenario (Rider (2011)).

Sand volume can also be estimated from a neutron porosity/density crossplot. In this method, a clean sand line and a shale point (or clay point, assuming that most shales contain 50% to 80% shale) are defined. The distance of the neutron porosity/density point from the clean sand line, following the trend of the line perpendicular to the clean sand line which passes through the shale/clay point, gives an estimate of the sand percentage. Figure 5.10 shows an example of a neutron-density crossplot for well 7120/6-3s in which a clean sand line and a shale point has been picked.

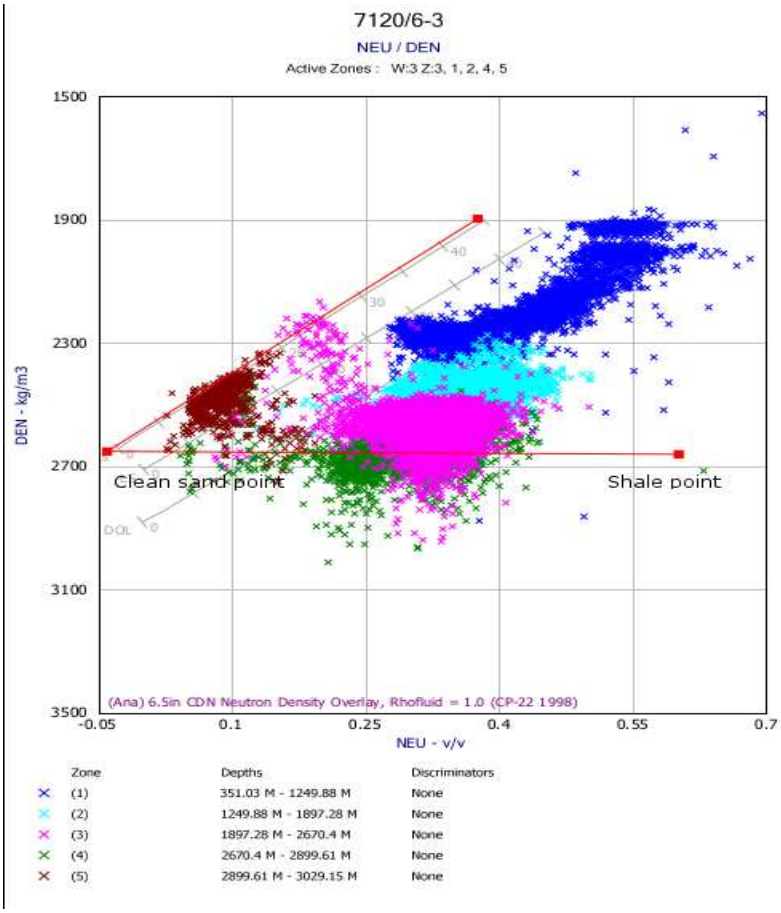

Figure 5.10: Neutron porosity/density crossplot for well 7120/6-3s used in the estimation of sand percentage. The well is split into 5 working zones, plotted as different colours, which are characterized by changes in gamma ray log response. A clean sand point and shale point is annotated in the crossplot.

In the absence of neutron porosity and density logs, usually in shallow forma-

tions, the method of estimating porosity from sonic travel time of Magara (1978) is used. The method is based on empirical data from Cretaceous shales in the western Canada basin, assuming a matrix density of shale of 2720 kg/cm^3 and a water density of 1020 kg/m^3. Some care should be taken when interpreting the porosity and sand percentage of the shallow formations as the method may not directly translatable to Cretaceous shales in the Barents Sea.

In a similar manner to estimating sand percentage form a neutron-density crossplot, porosity can also be estimated. In the case of sand percentage, the distance from the clean sand line was a determination of the sand percentage, but in terms of estimating the porosity, the key parameter is where along the clean sand line the projection along the perpendicular to the shale point lies. For instance, the clean sand line exists between a complete, zero porosity quartz to pure water, i.e. complete porosity, and thus the line itself can be gradated into measurements of porosity from zero (quartz matrix) to 100% (pure formation fluid).

5.6.1 Estimation of elastic moduli

Useful elastic moduli can be defined which can be used to help specify the stress-strain relationship (Mavko et al. (2009)). The elastic moduli considered here are the bulk modulus, K, shear modulus, μ, Lamé's parameter, λ, compressional wave modulus, M and Young's modulus, E. Poisson's ratio , ν, and the brittleness index, BI, (Heath-Clark et al. (2016), Rickman et al. (2008)) are also considered but are dimensionless ratios and as such are not moduli. This is a relatively exhaustive list and indeed some moduli can be formed by combinations of others, as in equation 5.7. Along with sand percentage (or conversely shale volume) and porosity this is a fair number of parameters to compare with attenuation. Ideally permeability would also be available to compare with attenuation as Koesoemadinata and McMechan (2001), Pride et al. (2003) and Pride and Berryman (2003) all found a relationship between attenuation and permeability but unfortunately it is not.

The bulk, shear and compressional wave moduli are defined by equation 5.6.

$$\begin{aligned} \mu &= \rho V_s^2 \\ M &= \rho V_p^2 \\ K &= \rho \left(V_p^2 - \frac{4}{3} V_s^2 \right) \end{aligned} \tag{5.6}$$

Given that bulk, shear and compressional wave moduli are estimated from equation 5.6 then all other moduli, Poisson's ratio and the brittleness can be calculated from these moduli via the equations 5.7.

$$\begin{aligned} \lambda &= K - \frac{2}{3}\mu \\ \nu &= \frac{3K - 2\mu}{2(3K + \mu)} \\ E &= \frac{9K\mu}{3K + \mu} \\ BI &= 0.5 \left(\frac{E - E_{min}}{E_{max} - E_{min}} + \frac{\nu - \nu_{min}}{\nu_{max} - \nu_{min}} \right) \end{aligned} \tag{5.7}$$

Here, E_{max} and E_{min} refer to the maximum and minimum Young's modulus within the interval to be analysed, similarly for Poisson's ratio.

Well 7121/5-1 does not contain a shear transit time log and thus shear wave speed can not be estimated directly from the well logs for this well. A shear wave speed could be created by assuming a relationship between compressional wave speed and shear wave speed in conjunction with the compressional wave speed log, but this would introduce an artificial correlation between the compressional and shear wave speed logs.

5.7 Comparison of attenuation and petrophysical parameters

The petrophysical parameters, elastic moduli and intrinsic attenuation are averaged over each formation for each well (table 5.1) prior to comparison. Figures 5.11 and 5.12 show the relationship between average formation attenuation and

Table 5.4: Table of correlation coefficients between several petrophysical parameters and estimated intrinsic attenuation. The probability to achieve the given correlation coefficient by chance, estimated via a student t-statistic (equation 5.8), is also given.

Parameter	Correlation coefficient (R)	Probability to achieve correlation by chance (%)
Sand percentage	0.037	82
Porosity	-0.15	37
Bulk modulus	0.49	2
P-wave modulus	0.34	7
Shear modulus	0.62	0.2
Poisson's ratio	-0.52	1
Young's modulus	0.62	0.2
Lamé's parameter	0.12	61
Brittleness index	0.28	22

the average formation elastic moduli. The relationship between sand percentage and attenuation as well as porosity and attenuation is given in figure 5.13. Table 5.4 gives the Pearson correlation coefficient of each of the plots in figures 5.11 and 5.12 as well as the probability of encountering this correlation by chance given a random distribution. The probability is derived via transforming the correlation coefficient to a t-statistics via equation 5.8 and using a t-test for statistical significance.

$$t = \sqrt{\frac{1 - R^2}{n - 2}} \tag{5.8}$$

In equation 5.8, n is the number of data samples and R is the Pearson correlation coefficient. For the correlations of elastic moduli with attenuation n=22, for the correlation of attenuation with porosity n=37 and for the correlation of attenuation with sand percentage n=41. The method of transforming the correlation coefficient to a t-statistic assumes that the data are normally distributed, which is difficult to tell with the small population of data points present, however it has been shown in other study areas that at least the shear and Young's moduli follow a Gaussian distribution (Karacan (2009)).

Table 5.4 shows that, at the 95% confidence interval, the hypothesis that the there is no significant correlation between bulk modulus, shear modulus,

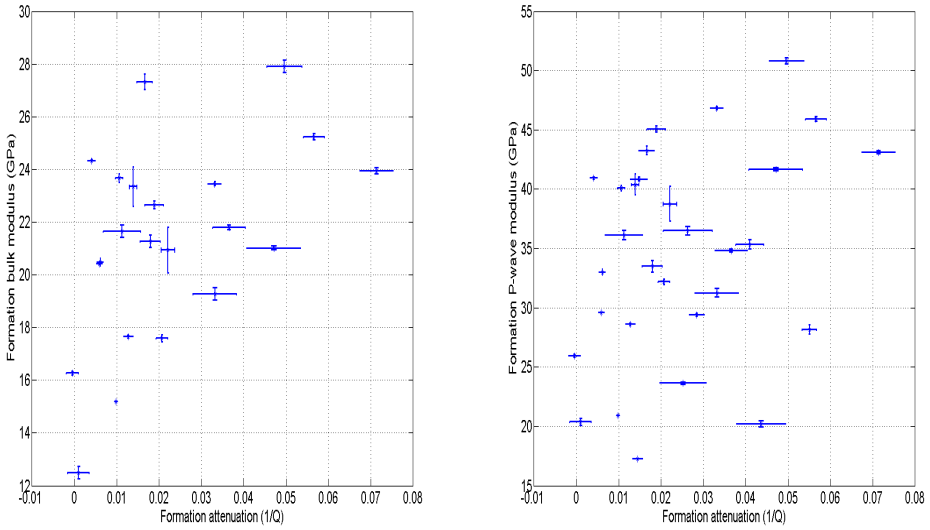

(a) (b)

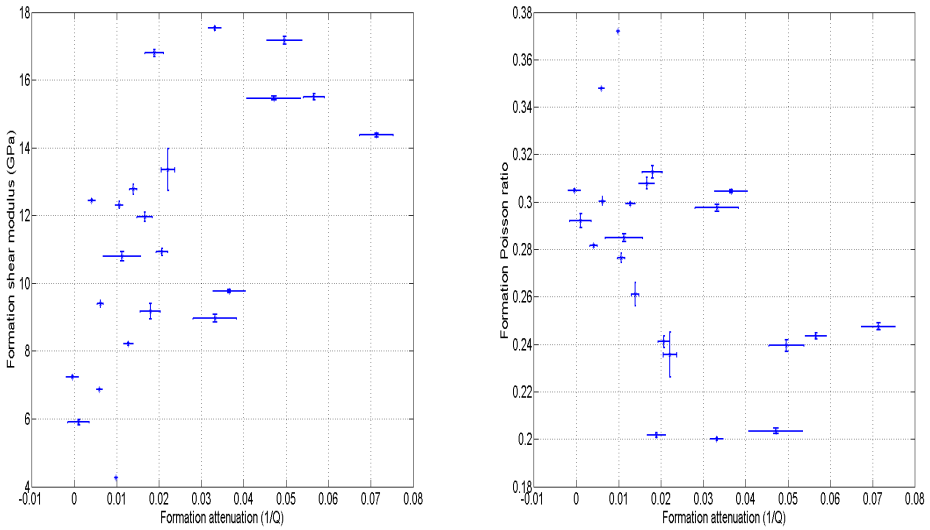

(c) (d)

Figure 5.11: Average formation attenuation (given as $1/Q$) as a function of bulk modulus (a), P-wave modulus (b), shear wave modulus (c) and Poisson's ratio (d) for all six wells in the study.

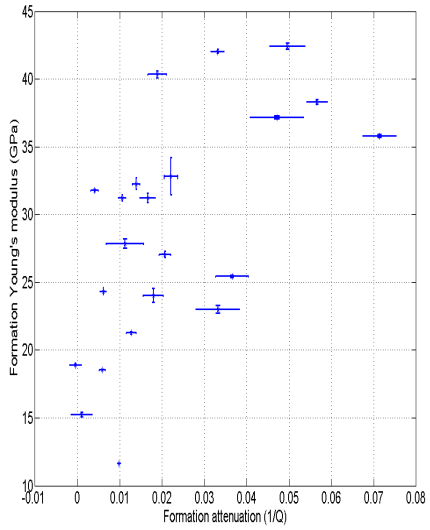

(a)

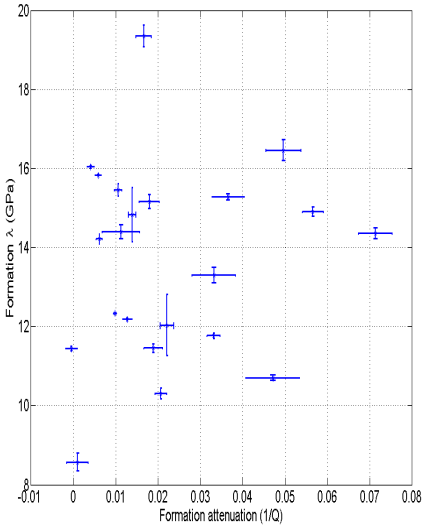

(b)

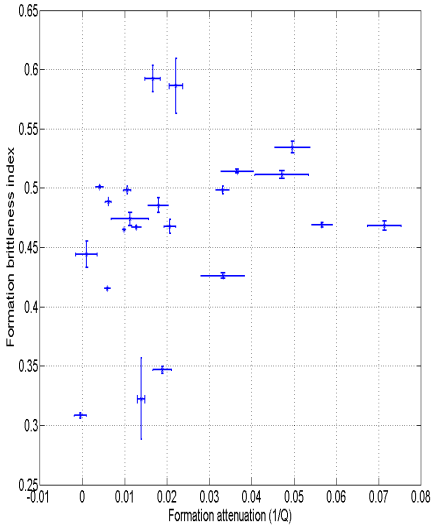

(c)

Figure 5.12: Average formation attenuation (given as $1/Q$) as a function of Young's modulus (a), Lamé's parameter (b) and brittleness index (c) for all six wells in the study.

Table 5.5: Table of correlation coefficients between several petrophysical parameters and estimated frequency-dependence of seismic attenuation, b. The probability of achieving the given correlation coefficient by chance, estimated via a t statistic (equation 5.8), is also given.

Parameter	Correlation coefficient (R)	Probability to achieve correlation by chance (%)
Sand percentage	-0.084	60
Porosity	0.24	15
Bulk modulus	0.079	73
P-wave modulus	0.12	53
Shear modulus	0.15	51
Poisson's ratio	-0.14	53
Young's modulus	0.14	54
Lamé's parameter	-0.027	90
Brittleness index	-0.28	21

Poisson's ratio or Young's modulus and attenuation is rejected. This means that there *is* a statistically significant correlation between these four elastic parameters and attenuation. Also, compressional wave modulus (P-wave modulus) shows statistically significant correlation at the 93% confidence interval. For Lamé's parameter, brittleness index, sand percentage and porosity their is no significant correlation with estimated intrinsic attenuation. Of the significant correlations, only Poisson's ratio has a negative correlation with attenuation, Poisson's ratio decreasing as attenuation increases.

The relationship between the formation averaged frequency-dependence of seismic attenuation (b, equation 5.4) and elastic moduli as well as porosity and sand percentage is given in figures 5.14 to 5.16 and the correlations of the relationships are given in table 5.5.

Table 5.5 shows that there is no statistically significant correlation between the frequency-dependence of the seismic attenuation quality factor, b, and any of the elastic moduli, porosity or sand percentage. The probability of achieving the given correlation coefficients by chance is greater than 15% in all cases. However, this is assuming a linear correlation between the frequency-dependence of the seismic attenuation quality factor and any of these elastic moduli or petrophysical parameters. A non-linear relationship, or a more complex relationship in which

Table 5.6: Table of correlation coefficients between several petrophysical parameters and P-wave attenuation given by Best et al. (1994). The probability to achieve the given correlation coefficient by chance, estimated via a t statistic (equation 5.8), is also given.

Parameter	Correlation coefficient (R)	Probability to achieve correlation by chance (%)
Bulk modulus	-0.59	0.2
P-wave modulus	-0.67	0.02
Shear modulus	-0.69	0.01
Poisson's ratio	0.49	1
Young's modulus	-0.68	0.01
Lamé's parameter	-0.27	18

the frequency-dependence of attenuation is non-linearly related to the product of several parameters is also a possibility that cannot be ruled out given the data presented.

Best et al. (1994) give values for several of the elastic moduli given in table 5.4 for 29 water saturated shale and sandstone samples as well as measuring attenuation at ultrasonic frequencies of between 0.54MHz and 0.88MHz (given in their tables 1 and 2). Figure 5.17 shows the data for P-wave attenuation as a function of bulk, shear, Young's modulus as well as Poisson's ratio. All correlations between attenuation quality factor and the elastic parameters for the data of Best et al. (1994) are the opposite of that given in table 5.4, essentially all correlations are negative with the exception of the correlation between Poisson's ratio and seismic P-wave attenuation quality factor, which is negative. The correlation coefficients for the data of Best et al. (1994) are given table 5.6.

Although there are important differences in the correlations between attenuation and elastic parameters between the data presented here and that of Best et al. (1994), some information is consistent. Namely that there is a statistically significant correlation between P-wave attenuation and bulk, shear and Young's modulus as well as Poisson's ratio and that there is not a statistically significant correlation with Lameé's parameter. The differences observed between the correlations of Best et al. (1994) and that presented here could be due to different geology; note that the Poisson's ratio of all samples of Best et al. (1994) are below

0.2 whereas the all formation averaged Poisson ratio values in this study are over 0.2. A more important distinction is that, in this study, the P-wave attenuation quality factor values are estimated within the seismic bandwidth (table 5.2) whereas the values of Best et al. (1994) are estimated at ultrasonic frequencies. If different attenuation mechanisms are dominant at different frequencies (Mller et al. (2010)) then it would not be surprising that the correlation of attenuation to petrophysical and elastic parameters would also change.

There is not enough data to assess whether or not there are non-linear relationships between any of the elastic or petrophysical parameters and the seismic attenuation quality factor, Q. If however, we assume a linear relationship between Q and those parameters given in table 5.4 which show a statistically significant correlation with Q at the 95% confidence interval then an empirical relationship between Q and these parameters can be determined as per equation 5.9.

$$\frac{1}{Q_{intrinsic}} = C_1 K + C_2 \mu + C_3 \nu + C_4 E \tag{5.9}$$

The coefficients C_1 to C_4 are determined through a least squares inversion of the intrinsic attenuation $(1/Q)$ and the formation averaged bulk, shear and Young's modulus (in GPa) as well as the Poisson's ratio. The coefficients are determined as; $C_1 = 0.028 \pm 0.007$, $C_2 = -0.014 \pm 0.001$, $C_3 = 0.034 \pm 0.003$ and $C_4 = 0.0013 \pm 0.0004$. To test the validity of this empirical relationship, the intrinsic formation attenuation estimated so far is reproduced using the elastic moduli and Poisson's ratio (figure 5.18). The trend line in figure 5.18 shows the ideal reconstruction line, i.e. a line of $y = x$. The reconstructed data do not fall on this line, with reconstructed attenuation being over estimated for less attenuative formations and under estimated for highly attenuative formations. The median deviation of the reconstructed values from the estimated intrinsic values is 44%. The empirical relationship may therefore be used to distinguish between low and high attenuation media but care must be taken given the high level of inaccuracy in the reconstructed values presented.

Although correlations between attenuation and elastic moduli are present, there is not an empirical relationship that linearly relates these elastic moduli to the estimated attenuation. This may be an example of correlation not being equal

to causation. The correlations therefore may be due to a number of reasons. The relationship between attenuation and these elastic moduli may be complex and non-linear, hence the breakdown of the empirical relationship. The relationship may be due to other petrophysical parameters not considered in this study, such as permeability which is proposed to affect attenuation (Pride et al. (2003)). The correlations may be a coincidence, which is not out of the question given the small dataset present.

The results presented here do not show a conclusive empirical relationship that can be applied to well data from the Barents Sea, but the method of analysing the data introduced here shows promise in that statistically significant correlations between intrinsic attenuation and 4 elastic parameters exists. To better understand the relationship between each parameter analysed and attenuation, it is necessary to include more data. With more information it will be possible to better constrain the relationship between attenuation and the petrophysical/elastic parameters and subsequently refine the form of the empirical relationship given in equation 5.9.

5.8 Modelling of frequency-dependence of attenuation

Although the frequency-dependence measured here is only over the frequency band of roughly 10Hz to 100Hz (specific frequency ranges for each well are given in table 5.2), a modelling approach similar to that of Sams et al. (1997) can be performed.

The modelling equations used are given in Jones (1986) and equation 5.10 and requires 3 parameters to be optimised to fit the observed data.

$$
\begin{aligned}
&M_{re}(\omega) = M_u + \tfrac{1}{2}(M_r - M_u)\left[1 - \frac{\sinh(1-\beta)x}{\cosh(1-\beta)x + \sin(\beta\pi/2)}\right] \\
&M_{im}(\omega) = \frac{\frac{1}{2}(M_u - M_r)\cos(\beta\pi/2)}{\cosh(1-\beta)\xi + \sin(\beta\pi/2)} \\
&\frac{1}{Q(\omega)} = \frac{M_{im}(\omega)}{M_{re}(\omega)} \\
&x = \ln(\omega\tau) \\
&\tau = 1/2\pi f_0
\end{aligned}
\tag{5.10}
$$

Here M_u and M_r are the unrelaxed and relaxed moduli, in this instance we use bulk modulus and the unrelaxed and relaxed bulk modulus are given estimated by using the p-wave velocity at high and low frequencies. The velocity at low frequency given by the log measurements. The high frequency velocity is a parameter to be optimised. β controls the width of the frequency-dependent $1/Q$ distribution with high β values giving a flatter less frequency-dependent distribution of attenuation with frequency and is also to be optimised. The last variable which is to be optimised is the peak frequency of the distribution given by f_0.

A simple grid search method is performed to find the value of the three variables, f_0, β and, the high frequency velocity, which define a distribution of $1/Q$ which most closely matches that given by the estimated frequency-dependence of $1/Q$ from the VSP data.

The central frequency, f_0, and the average bulk modulus are used along with the viscosity of water at room temperature (1 mPa s) in equation 5.11 to estimate the aspect ratios of the cracks causing squirt flow, following Sams et al. (1997) with the exception that they estimate the average bulk modulus through the mineralogy which they estimated via x-ray diffraction. It is not possible to estimate the bulk modulus via the mineralogy estimated from x-ray diffraction due to a lack of core samples. In this instance the average bulk modulus is estimated from the compressional-wave and density well logs.

$$f_0 = \frac{K_{av}}{\nu} a^3 \tag{5.11}$$

Here ν is the viscosity of water, a is the aspect ratio of cracks and K_{av} is the average bulk modulus.

Figures 5.19 to 5.21 gives the estimated β, peak frequency (f_0) and, the aspect ratio of the cracks causing squirt flow.

The β values in figure 5.19 are higher than those in Sams et al. (1997) and show that the frequency-dependent attenuation curves are relatively flat, which is to be expected given the low frequency dependence estimated from the VSP data and given in figure 5.9.

The range of peak frequencies, f_0, in figure 5.20 cover almost 10 orders of magnitude in frequency from approximately 10kHz down to 20Hz in the Fruholmen

formation. An exceptionally low peak frequency of 10^{-5}Hz exists in the Snadd formation and leads to a low value for the aspect ratio of cracks in figure 5.21.

The aspect ratio of cracks given in figure 5.21 are between 10^{-3} and $6\text{x}10^{-3}$, roughly in agreement with the range of 10^{-4} to 10^{-3} that is likely to cause squirt flow attenuation (Jones (1986)). The crack aspect ratio in the Snadd formation is orders of magnitude lower and could either be due to a dominant attenuation mechanism other than squirt flow in the Snadd formation or an inaccurate estimate of the frequency-dependence of attenuation within the formation from the VSP data.

5.9 Conclusions

This study investigated the average formation attenuation, as well as the frequency-dependence of the seismic attenuation quality factor, in the 7120-7122 license blocks of the Norwegian Barents Sea and to investigate possible relationships between petrophysical or elastic parameters and the measured intrinsic attenuation. To this end, six wells with coincident VSP and well log data have been analysed in order to obtain these goals. The well log information pertains to formations ranging form the Torsk formation (Paleocene to Oligocene in age) to the Kobbe formation (Middle Triassic in age). All but one well contained the density, compressional transit time and shear transit time logs necessary to estimate the elastic parameters used in the study.

The intrinsic attenuation, estimated from the difference in inverse estimated effective attenuation quality factor ($1/Q_{eff}$) and inverse scattering attenuation quality factor ($1/Q_{sc}$), has been averaged across each formation and then across each well. The resulting attenuation profile with formation age (youngest to oldest) shows a generally higher level of attenuation within the Nordmela to Snadd formations with lower attenuation in the Torsk to Støformations. The attenuation estimated in the Kviting formation has an error of greater than 100% due to the value being an average of two average formation attenuation values present in two wells with vastly different attenuation values. The median error in the intrinsic formation attenuation results is 31%, as given by the standard error.

If the seismic attenuation quality factor is assumed to be dependent upon

frequency in a powerlaw form over the seismic bandwidth then the results show that the frequency-dependence of Q across all six wells studied and across all formations is relatively low. The frequency-dependent exponent, b, which describes the powerlaw dependence of the seismic attenuation quality factor is within the range -0.1< b <0.2 when averaged over each formation in each well. The intrinsic attenuation was found to correlate well with bulk modulus, shear modulus, Young's modulus and Poisson's ratio, with the hypothesis that the correlation is by chance rejected at the 95% confidence interval. No statistically significant correlation was found between intrinsic attenuation and Lamé's parameter, brittleness index, porosity or sand percentage. With the exception of Poisson's ratio, all correlations were positive. The frequency-dependent attenuation exponent, b, does not correlate with any of the elastic moduli or petrophysical parameters in any statistically significant way.

A squirt flow model is fit to the frequency-dependence of the attenuation estimated from the VSP data via a simple grid search for the peak frequency of attenuation, β value which controls the width of the distribution and, the high-frequency velocity. Results of this fitting procedure show that the peak frequency of attenuation is highly variable, with values between 20Hz and 10kHz with an outlying value of 10^{-5}Hz, although the distribution are relatively flat, denoted by β values close to 1. The aspect ratio of cracks causing the squirt flow attenuation is estimated to be between 10^{-3} and 6x10^{-3}, similar to the range proposed expected range given by Jones (1986). The outlying data value is likely due to inaccurate frequency-dependence of attenuation measured from the VSP data or a dominant attenuation mechanism other than squirt flow within the Snadd formation.

An empirical relationship between intrinsic attenuation and bulk modulus, shear modulus, Young's modulus and Poisson's ratio has been calculated through linear least squares regression. The empirical relationship was constructed as a linear summation of the relevant elastic parameters multiplied by a coefficient, determined through linear least squares regression. The intrinsic attenuation values reconstructed form the empirical relationship were, on average, 44% in error, showing that the empirical relationship could not accurately reproduce the estimated intrinsic attenuation.

The breakdown of the empirical relationship may be due to several factors; The elastic parameters may not have a linear relationship with attenuation although this is difficult to distinguish given the lack of data points. The correlation may be dependent upon others parameters not included in the analysis, such as permeability. Any anomalous points may skew the empirical relationship given the lack of data points. There may also not be an empirical relationship between these elastic parameters and attenuation, however to consolidate this idea more data points, and hence data, is required.

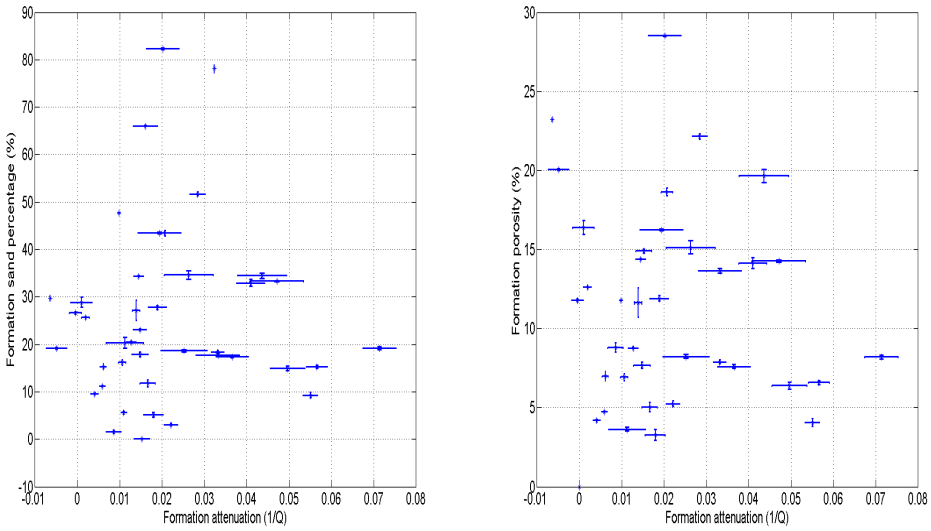

(a) (b)

Figure 5.13: Average formation attenuation (given as $1/Q$) as a function of average formation sand percentage (a) and average formation porosity (b) for all six wells in the study.

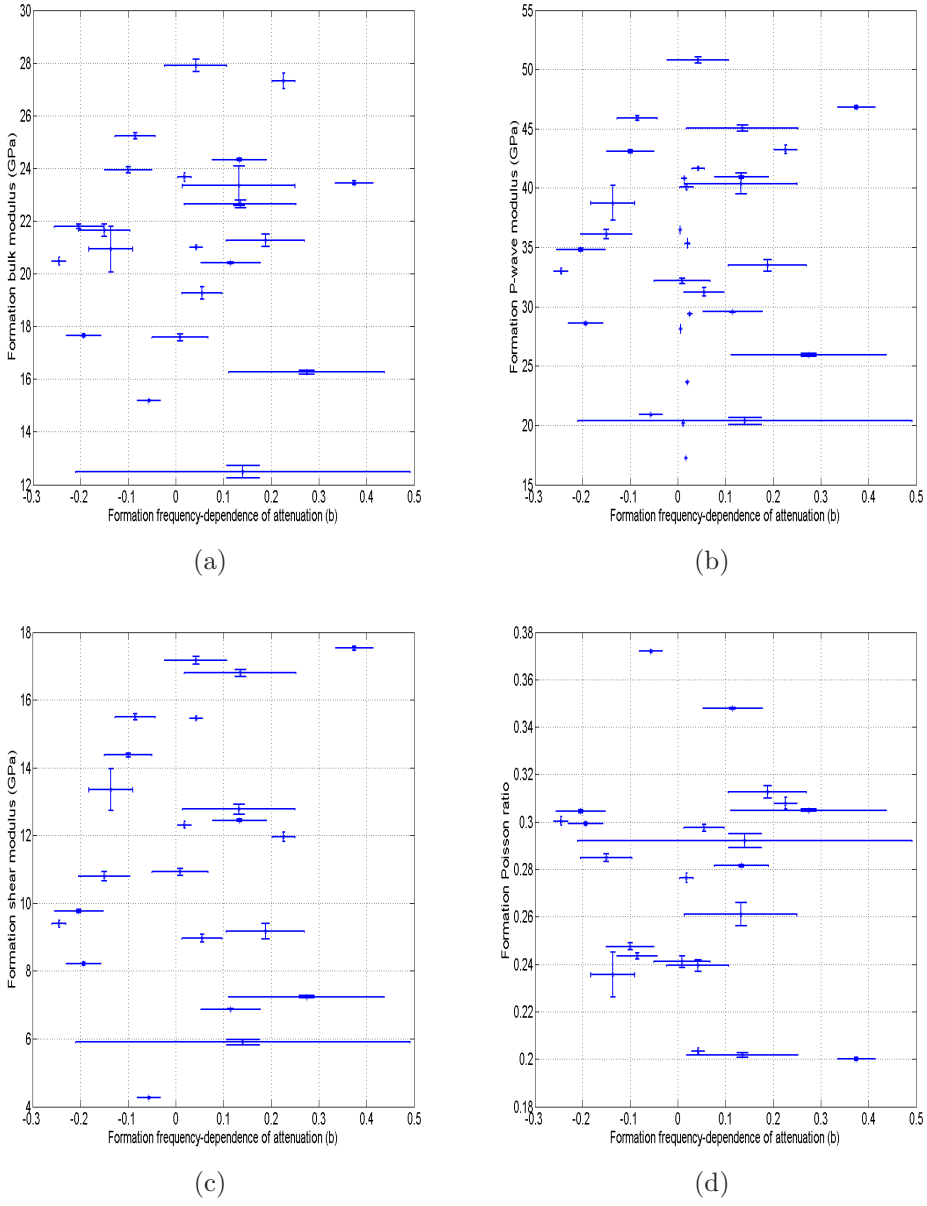

Figure 5.14: Average formation frequency-dependence of attenuation (b) as a function of bulk modulus (a), P-wave modulus (b), shear wave modulus (c) and Poisson's ratio (d) for all six wells in the study.

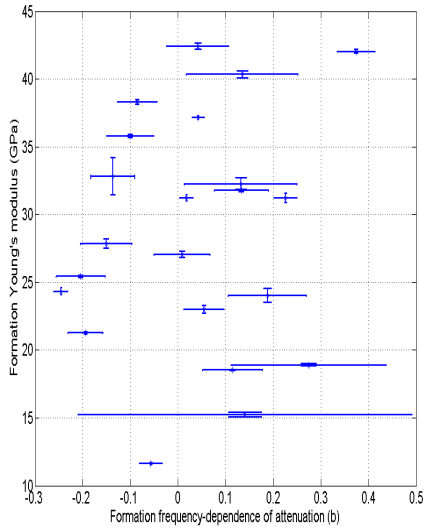

(a)

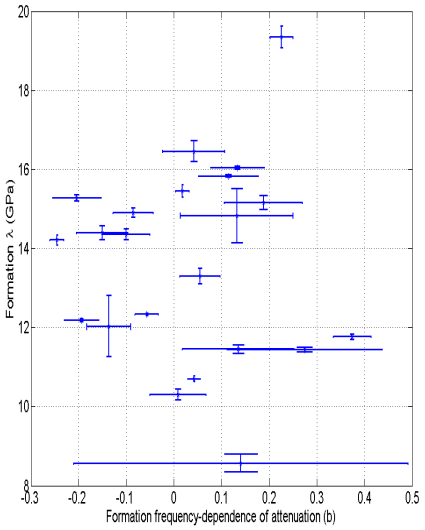

(b)

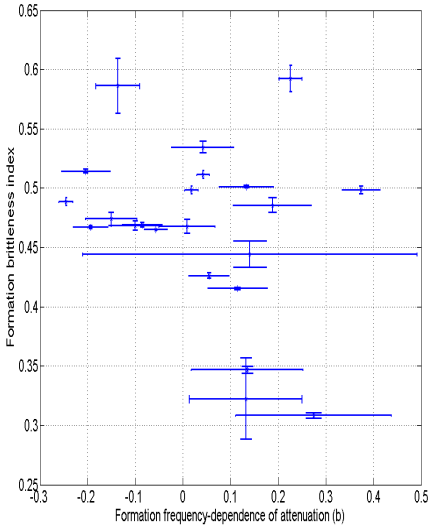

(c)

Figure 5.15: Average formation frequency-dependence of attenuation (b) as a function of Young's modulus (a), Lamé's parameter (b) and brittleness index (c) for all six wells in the study.

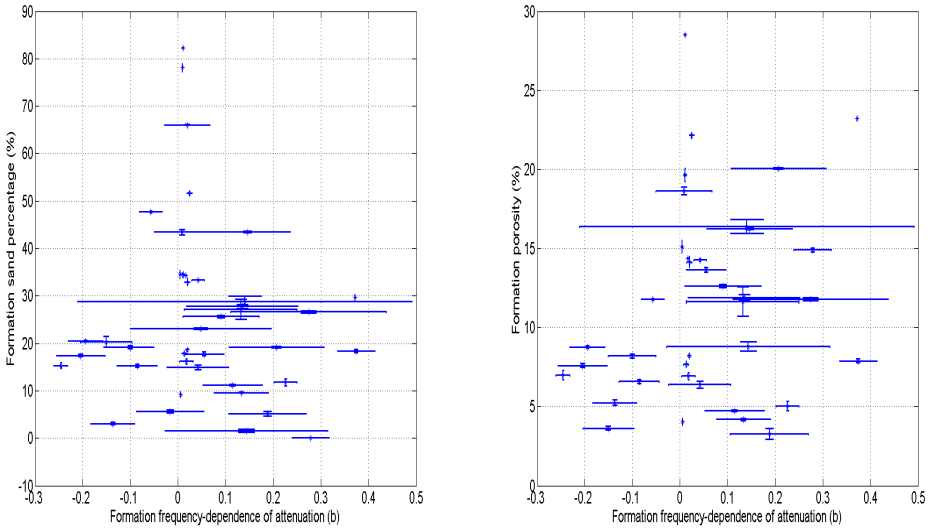

(a) (b)

Figure 5.16: Average formation frequency-dependence of attenuation (b) as a function of average formation sand percentage (a) and average formation porosity (b) for all six wells in the study.

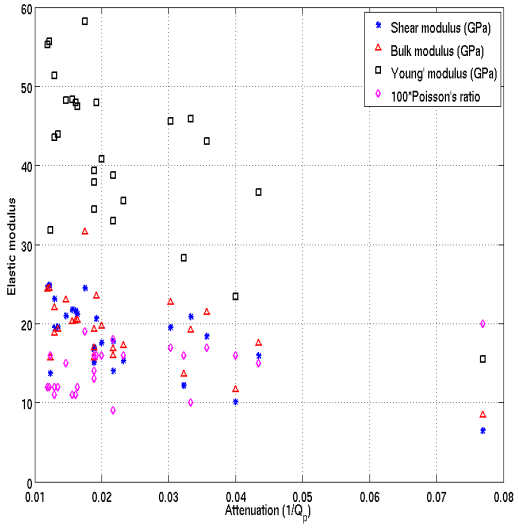

Figure 5.17: Bulk, shear and Young's modulus as well as Poisson's ratio as a function of P-wave attenuation as measured at ultrasonic frequencies by Best et al. (1994).

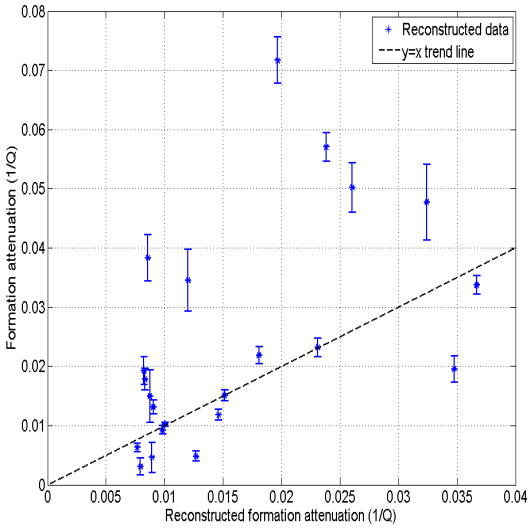

Figure 5.18: Reconstructed attenuation as a function of estimated intrinsic attenuation. The dashed red line represents the ideal $y = x$ reconstruction trend.

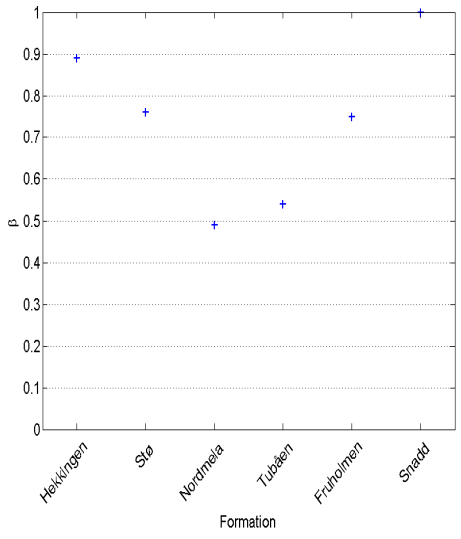

Figure 5.19: β values estimated via fitting of a squirt flow model to the frequency-dependence of attenuation estimated from VSP data.

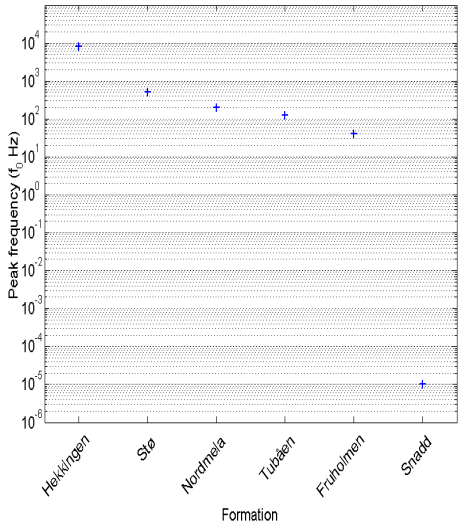

Figure 5.20: Peak frequency of attenuation estimated via fitting of a squirt flow model to the frequency-dependence of attenuation estimated from VSP data.

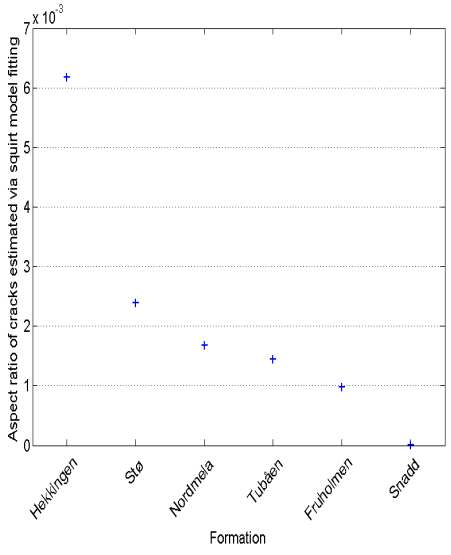

Figure 5.21: Aspect ratio of cracks estimated from the peak frequency given in figure 5.20 and the average bulk modulus via equation 5.11.

References

Bath, M., 1974, Spectral analysis in geophysics: Elsevier Scientific Publishing Company, Amsterdam, volume **7** *of* Developments in Solid Earth Geophysic. 189

Best, A., C. McCann, and J. Sothcott, 1994, The relationships between the velocities, attenuations and petrophysical properties of reservoir sedimentary rocks1: Geophysical Prospecting, **42**, 151–178. 22, 27, 190, 214, 215, 224

Carey, W. M., A. D. Pierce, R. E. Evans, and J. D. Holmes, 2008, On the exponent in the power law for the attenuation at low frequencies in sandy sediments: The Journal of the Acoustical Society of America, **124**, EL271–EL277. 205

Chapman, M., S. V. Zatsepin, and S. Crampin, 2002, Derivation of a microstructural poroelastic model: Geophysical Journal International, **151**, 427–451. 189

Dor, A., 1995, Barents sea geology, petroleum resources and commercial potential: ARCTIC, **48**, 207–221. 191

Hauge, P. S., 1981, Measurements of attenuation from vertical seismic profiles: Geophysics, **46**, 1548–1558. 190, 191

Heath-Clark, M., k. Taylor, D. Harrison, A. Fogg, F. Hughes, M. Harrhoff, and A. Mortimer, 2016, The characterization of unconventional reservoirs in the bowland sequence using onshore 3d seismic data, cleveland basin, uk: First Break, **34**, 45–52. 208

Jeng, Y., J.-Y. Tsai, and S.-H. Chen, 1999, An improved method of determining near-surface q: Geophysics, **64**, 1608–1617. 205

Jones, T. D., 1986, Pore fluids and frequency-dependent wave propagation in rocks: Geophysics, **51**, 1939–1953. 191, 216, 218, 219

Karacan, C. Ö., 2009, Elastic and shear moduli of coal measure rocks derived from basic well logs using fractal statistics and radial basis functions: International Journal of Rock Mechanics and Mining Sciences, **46**, 1281–1295. 210

Klimentos, T., and C. McCann, 1990, Relationships among compressional wave attenuation, porosity, clay content, and permeability in sandstones: Geophysics, **55**, 998–1014. 190

Koesoemadinata, A. P., and G. A. McMechan, 2001, Empirical estimation of viscoelastic seismic parameters from petrophysical properties of sandstone: Geo-

physics, **66**, 1457–1470. 190, 191, 208

Magara, K., 1978, Compaction and fluid migration: Elsevier. 208

Malinowski, M., S. Operto, and A. Ribodetti, 2011, High-resolution seismic attenuation imaging from wide-aperture onshore data by visco-acoustic frequency-domain full-waveform inversion: Geophysical Journal International, **186**, 1179–1204. 188

Mangriotis, M.-D., J. W. RectorIII, E. F. Herkenhoff, and J. C. Neu, 2013, Scattering versus intrinsic attenuation in the vadose zone: A vsp experiment: Geophysics, **78**, B49–B63. 189, 200

Mavko, G., and D. Jizba, 1991, Estimating grain-scale fluid effects on velocity dispersion in rocks: Geophysics, **56**, 1940–1949. 191

Mavko, G., T. Mukerji, and J. Dvorkin, 2009, The rock physics handbook. tools for seismic analysis of porous media: Cambridge University Press. 208

Mller, T. M., and B. Gurevich, 2005, Wave-induced fluid flow in random porous media: Attenuation and dispersion of elastic waves: The Journal of the Acoustical Society of America, **117**, 2732–2741. 189

Mller, T. M., B. Gurevich, and M. Lebedev, 2010, Seismic wave attenuation and dispersion resulting from wave-induced flow in porous rocks, a review: Geophysics, **75**, 75A147–75A164. 215

Odoherty, R., and N. Anstey, 2006, Reflections on amplitudes: Geophysical Prospecting, **19**, 430–458. 189

Pride, S. R., and J. G. Berryman, 2003, Linear dynamics of double-porosity dual-permeability materials. i. governing equations and acoustic attenuation: Phys. Rev. E, **68**, no. 3, 036603. 191, 208

Pride, S. R., J. M. Harris, D. L. Johnson, A. Mateeva, K. T. Nihel, R. L. Nowack, J. W. Rector, H. Spetzler, R. Wu, T. Yamomoto, J. G. Berryman, and M. Fehler, 2003, Permeability dependence of seismic amplitudes: The Leading Edge, **22**, 518–525. 191, 208, 216

Quan, Y., and J. M. Harris, 1997, Seismic attenuation tomography using the frequency shift method: Geophysics, **62**, 895–905. 189

Reine, C., R. Clark, and M. van der Baan, 2012, Robust prestack Q-determination using surface seismic data: Part 1-Method and synthetic examples: Geophysics, **77**, R45–R56. 189

Rickman, R., M. J. Mullen, J. E. Petre, W. V. Grieser, and D. Kundert, 2008, A practical use of shale petrophysics for stimulation design optimization: All shale plays are not clones of the barnett shale.q: Presented at the SPE Annual Technical Conference and Exhibition, Expanded Abstracts. 208

Rider, M., 2011, The geological interpretation of well logs: Rider-French. 206

Sams, M., J. Neep, M. Worthington, and M. King, 1997, The measurement of velocity dispersion and frequency-dependent intrinsic attenuation in sedimentary rocks: Geophysics, **62**, 1456–1464. 191, 216, 217

Shapiro, S. A., H. Zien, and P. Hubral, 1994, A generalized o'doherty-anstey formula for waves in finely layered media: Geophysics, **59**, 1750–1762. 200

Shatilo, A. P., C. Sondergeld, and C. S. Rai, 1998, Ultrasonic attenuation in glenn pool rocks, northeastern oklahoma: Geophysics, **63**, 465–478. 190

Tonn, R., 1991, The determination of the seismic quality factor q from vsp data: A comparison of different computational methods.: Geophysical Prospecting, **39**, 1–27. 189

Van Der Baan, M., 2001, Acoustic wave propagation in one dimensional random media: the wave localization approach: Geophysical Journal International, **145**, 631–646. 189, 200

Wang, Y., 2008, Seismic inverse q filtering: Wiley-Blackwell. 188

Zhang, Z., R. Stewart, and D. Lawton, 2013, Measurements of attenuation from vertical seismic profilesestimating seimsic attenuation (qp & qs) from rock porperties: Canadian Journal of Exploration Geophysics, **38**, 1–3. 191

Chapter 6

Discussion and Conclusions

6.1 Discussion

In chapter 2, I introduced the signal dependent time-frequency distribution (SDD), a quadratic time-frequency distribution, which is not limited by the Gabor uncertainty relationship but which is subject to a trade off between joint time-frequency resolution and suppression of transform artefacts. The SDD allows the user to design a window function, in the Doppler-frequency/time-lag domain, which can optimize this trade-off.

The SDD, as well as the short-time-Fourier transform (STFT), Stockwell transform and the Fourier transform have been analyzed for their ability to estimate the spectrum of a known wavelet used in a tuning wedge model and, to estimate spectra from a zero-offset synthetic seismogram, based on well log data, for use in attenuation estimation. In each test the SDD out-performed the fixed- and variable-window transforms, with the exception that the attenuation estimated from the wedge model, expected to be zero, was, on average, closer to zero for the STFT.

All three time-frequency transforms were used in a pre-stack attenuation estimation method (the PSQI algorithm) applied to a pre-stack gather from a surface seismic survey carried out over the Kinnoull discovery in the central North Sea. In this case the SDD produced spectra more consistent with the constant-Q model of attenuation. Integration over time-limited windows of the SDD to form spectra

was then used as the go-to method of estimating spectra for attenuation analysis.

Without a window function the SDD is more commonly referred to as the Wigner-Ville distribution (WVD). The advantage of the WVD over the SDD is that no parameters are needed to complete the transform, unlike most time-frequency distributions. The WVD will have higher time-frequency resolution than the SDD but will also contain all transform artefacts. The SDD is more computationally expensive than the WVD, STFT and Stockwell transform due to the forward and inverse transformation to the ambiguity plane. Parametrizing the SDD requires the selection of a window function, as opposed to a few singular valued parameters for the STFT and Stockwell transform, which, although relatively simple, can change from trace to trace.

Further work to develop the SDD could include further analysis of the effects of the designed window function on the estimated attenuation values. The selection of the window function may also be automated to select coherent energy around the origin of the ambiguity plane, although this would require further testing. Although presented here in terms of estimating spectra for attenuation studies, the SDD method can replace the more common fixed- and variable-window time-frequency transforms used in other applications, such as spectral decomposition. Due to the SDD being a quadratic time-frequency transform, a time-phase representation of an input signal is not readily available but further research may reveal a method of collecting this information from the SDD method. Further research could also include an analysis of the time-frequency resolution of the SDD method with a generic window function in order to quantify the trade-off between time-frequency resolution and suppression of transform artefacts for any choice of window.

The transform artefacts inherent in the WVD are at times halfway between events, so the first arrival in a time series is unaffected by them. This means the WVD is ideal for estimating the spectra of the downgoing direct compressional wave in a vertical seismic profile (VSP) dataset. The method of integration of a small window of the WVD to estimate a spectrum is used to estimate the spectra of the downgoing direct wave in a VSP dataset over the Kinnoull field and 6 VSP datasets in the Norwegian Barents Sea.

Effective attenuation is estimated from the VSP datasets and scattering at-

tenuation is measured from coincident well log data using the wave localisation method of Mangriotis et al. (2013). From these two values, the intrinsic attenuation can be estimated.

The intrinsic attenuation estimated for the Kinnoull dataset shows high attenuation peaks of $1/Q \approx 0.08$ ($Q \approx 12.5$). However, this high attenuation peak occurs at a depth in which the downgoing direct wave is undergoing interference, visibly present as a typically tuning wedge notch in the frequency-depth plot, and this peak is likely due to the interference.

The median $1000/Q$ estimated from stacked seismic data, 9.2, is in agreement with that estimated from the vertical seismic profile data ($1000/Q = 10.4 \pm 2$) however the median $1000/Q$ of 4.5 ± 1 from the pre-stack data does not agree with the VSP data (figure 6.1). Individual profiles of attenuation taken at or near well 16/23-7 from the VSP, stacked and pre-stack seismic data shows little correlation between the VSP attenuation values and those estimated from either the stacked or pre-stack data, but the stacked and pre-stack attenuation values are statistically from a distribution with the same mean. Either the high attenuation anomalies seen in the VSP data are in regions that are spatially small and mainly avoided by the surface seismic or the attenuation peaks are due to interference in the VSP data, which has been shown to present and significant below 2300m MD, or the effect of these small, high attenuation regions is not large enough to have a detectable impact upon the spectra estimated from surface seismic data due to the lower signal-to-noise ratio in the surface seismic compared to the borehole seismic.

Maps of attenuation as a function of inline and crossline coordinates are found to not correlate with average centroid frequency or average energy within the same interval on a consistent basis, although for some individual intervals the attenuation may correlate with either the average centroid frequency *or* the average energy.

Attenuation estimated from pre-stack supergather data shows an imprint of the acquisition geometry for shallower intervals and no correlation with average centroid frequency or average energy for any intervals analyzed. When estimating attenuation on individual CMP gathers, the imprint of the acquisition geometry is significant for every interval.

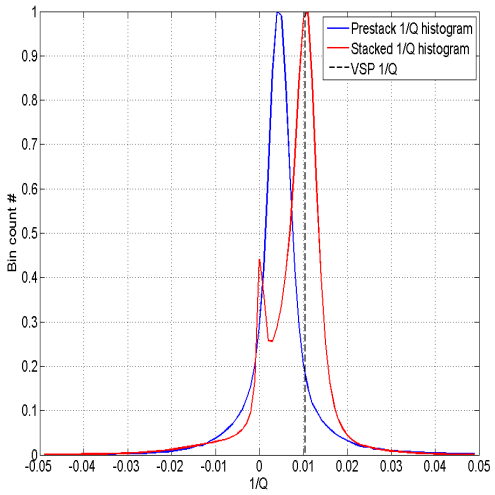

Figure 6.1: Distribution of 1/Q values estimated from VSP, stacked and prestack seismic data in the region of well 16/23-7.

Further work could incorporate an analysis of the possible correlation between the estimated attenuation values from the stacked and pre-stack seismic data with other seismic attributes, such as AVO intercept, AVO gradient and acoustic impedance. Further processing of the VSP data could make estimation of shear-wave attenuation possible, and thus give an estimation of the ratio of compressional- to shear-wave attenuation.

The scattering attenuation for the Kinnoull VSP dataset was found to be minimal throughout the depth range of the well VSP data, rising to approximately 1/Q of 0.01 (Q=100) at the bottom of the VSP depth range. This may however be a shortcoming of the wave localization method. The method assumes that scattering attenuation occurs from variations in the compressional- and shear-wave velocity logs and, density logs around a background trend. This variation around a background trend is then correlated to find a scale length of variation and a degree of variation. However, their is not necessarily a single background density or velocity values, different lithologies are likely to have different densities and velocities, fitting a polynomial function will not remove this varying background trend as the variations are likely to be piece-wise, i.e sharp changes in a constant background, rather than slowly varying, although this may be the case

for changes in the background density and velocity due to compaction.

Further analysis of the well log data for scattering attenuation could include using the original Odoherty and Anstey (2006) method of taking the Fourier transform of the reflectivity series and seeing how this compares with the method of Mangriotis et al. (2013).

For the 6 Barents Sea VSP datasets, the estimated attenuation is averaged over formations and wells to produce a formation dependent average 1/Q for the region of the licence block 7120-7122 which contains the 6 wells. The formation averaged intrinsic attenuation shows a generally higher level of attenuation within the Nordmela to Snadd formations, with lower attenuation in the Torsk to Støformations (figure 6.2). However, it is possible that attenuation could varying dramatically with spatial location within a given formation due to changes in petrophysical properties such as pore fluid fill, permeability, porosity.

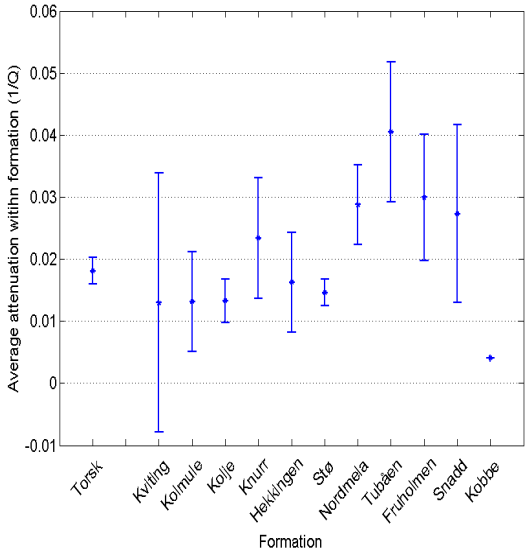

Figure 6.2: Average attenuation as a function of formation for the six wells studied in this survey. Error bars are given by the standard error on the mean.

In addition to estimating scattering attenuation from the well log data, several moduli and petrophysical properties were also calculated. Bulk modulus, shear modulus, Young's modulus and Poisson's ratio showed statistically significant correlation with the estimated intrinsic attenuation at the 95% confidence level.

The correlation of intrinsic attenuation with Poisson's ratio is negative whereas the correlation with bulk, shear and Young's modulus are positive. An empirical relationship based on a linear dependence of attenuation on these four elastic parameters has been created but attenuation values reconstructed from this relationship could not accurately reproduce the estimated intrinsic attenuation, with a median error of 53%. The linear relationship between these four elastic parameters and attenuation is not valid but this is not to say a more complex relationship does not exist. The lack of sample data points, 22 for the four elastic parameters which show a statistically significant correlation, has contributed to a lack of knowledge on the relationship between the elastic parameters and the intrinsic attenuation, hence a linear relationship between the elastic parameters and attenuation is assumed but more data can help to refine this relationship.

Incorporation of more VSP surveys located within the Norwegian Barents Sea may be able to further constrain the statistically significant correlations between attenuation and elastic moduli and may reveal that some correlations are non-linear.

The seismic quality factor estimated from VSP data and surface seismic data so far has been assumed to be frequency-independent. However, the intrinsic seismic quality factor, Q, is known, from poro-elastic rock physics theory, to be frequency-dependent, even within typical bandwidths of individual surface- and borehole-based surveys - where measurement methods usually deliver frequency-*independent* Q. Thus, measuring frequency-dependent Q instead offers better characterization of seismic properties and moreover a potential step towards estimating permeability directly from seismic data. Therefore, I introduced a method to measure frequency-dependent Q from pairs of reflections in pre-stack τ-p domain surface seismic data - a data type that, unlike a VSP, offers useful areal coverage. This adaptation was also applied to the spectral ratio method for estimating attenuation from VSP data.

The pre-stack Kinnoull seismic dataset and VSP acquired within well 16/23-7 over the Kinnoull field as well as the 6 Barents Sea VSP data sets are analysed through an adaptation of the PSQI algorithm and spectral ratio method respectively to allow for estimation of a frequency-dependent attenuation.

Whilst, in principle, any analytic form with a manageable number of pa-

rameters could be prescribed, frequency-dependence of Q has been modelled as a power-law, $Q(f)=af^b$. The power-law model of frequency dependent attenuation is one which has been used in attenuation studies previously (Gurevich and Pevzner (2015), Jeng et al. (1999), Carey et al. (2008)) and fits the squirt flow model given by Sams et al. (1997) which was used to fit the attenuation estimated from various experiments which covered several orders of magnitude from a few hundreds of Hertz to several MHz.

Inversion is done with a simple grid-search over coefficient (1/a) and exponent b, seeking a minimum L1-residual: we show, using a numerical experiment and a synthetic dataset, that it is robust, and also accurate down to a signal-to-noise ratio of approximately 0.65.

A key feature of the grid-search method is the ability to produce a residual map to see how the estimated inverse coefficient and exponent of frequency-dependence trade-off against one another. However, this is also a downside of the approach, as the grid-search method can be slow and for models of frequency-dependent attenuation characterised by more than two variables the grid search method may be prohibitively slow and the residual cube harder to interpret. In this instance a well-regularised non-linear inversion may be the most appropriate method to use.

Q is estimated for some 955 250mx250m superbins of the 3D pre-stack OBC dataset over the Kinnoull Field. All combinations of 8 prominent reflections between Top Miocene and Base Cretaceous were treated together, to give some 21,000 frequency-dependent results. The median coefficient (1/a) and exponent b are 0.0074 and 0.06 respectively, with sharply-peaked distributions (excess kurtosis >10). Figure 6.3 is a 2D histogram of the estimated inverse coefficient and exponent values. Outlier, strongly frequency-dependent, results, given by $|b| > 0.2$, coincide with low-frequency 'shadows' under amplitude anomalies, adversely affecting the spectra of reflections. Low-frequency shadows are interpreted as a temporary drop in centroid frequency.

Although the estimated frequency exponent in the Kinnoull dataset suggests that the assumption of frequency-independent attenuation quality factor is valid, this is only valid in the seismic bandwidth and for the relatively consolidated lithologies represented between the top of the Miocene and the Base Cretaceous.

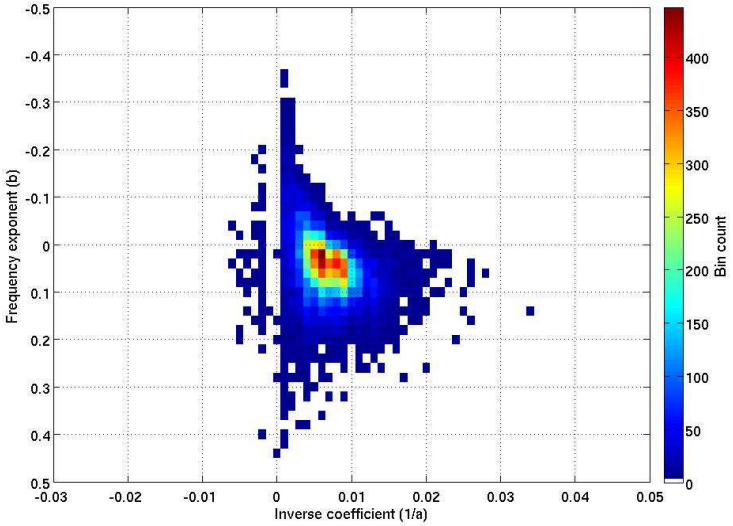

Figure 6.3: 2D histogram of the estimated coefficient/exponent pairs from the North Sea survey. Reproduced from Chapter 4.

Application of this frequency-dependent Q estimation method to a land or shallow marine dataset containing relatively unconsolidated sediments may reveal larger frequency dependencies, as suggested by Carey et al. (2008) and Jeng et al. (1999). Further investigation into estimating frequency-dependent attenuation through constrained non-linear inversion or directed Monte-Carlo simulations with a priori information may also result in a more efficient frequency-dependent Q estimation method.

For the 6 Barents Sea VSP datasets, the formation averaged exponent of frequency-dependence, b, is low throughout all formations, falling within the range -0.1<b<0.2 and with a median value of 0.02 (Figure 6.4).

A squirt flow model is fit to the formation averaged frequency-dependence of the attenuation estimated from the 6 Barents Sea VSP data sets via a simple grid search for the peak frequency of attenuation, β value which controls the width of the distribution and, the high-frequency velocity. Results of this fitting procedure show that the peak frequency of attenuation is highly variable, with values between 20Hz and 10kHz with an outlying value of 10^{-5}Hz, although the distribution are relatively flat, denoted by β values close to 1. The aspect ratio

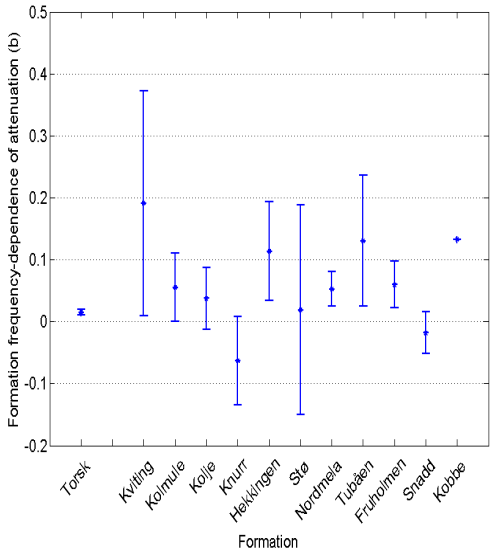

Figure 6.4: Formation averaged frequency-dependence of attenuation as a function of formation for the six wells studied in this survey. Error bars are given by the standard error on the mean.

of cracks causing the squirt flow attenuation is estimated to be between 10^{-3} and $6\text{x}10^{-3}$, similar to the proposed expected range given by Jones (1986).

The outlying data value is likely due to inaccurate frequency-dependence of attenuation measured from the VSP data or a dominant attenuation mechanism other than squirt flow within the Snadd formation. The large range of peak frequency values and the β values close to 1, denoting flat distributions of attenuation with frequency, are likely due to the small range of frequencies over which the frequency-dependence of attenuation is estimated. As the range of energy in the VSP data only exists from ≈10Hz to ≈100Hz, which is far from the several tens of kHz reported by Sams et al. (1997).

6.2 Conclusions

In this thesis I have introduced a new method to estimate the time-frequency distribution of a seismic trace, the signal-dependent-distribution (SDD). The SDD is proven to out perform the STFT and Stockwell transforms in synthetic examples

including a wedge model and a synthetic zero-offset reflection experiment. The SDD also produced spectral ratio ratios from a pre-stack data set which more closely matched what would be expected by theory.

The SDD is then applied to stacked and pre-stack seismic data over the Kinnoull discovery, central North Sea, in order to estimate spectra for use in the spectral ratio and PSQI method respectively. The estimated attenuation values from the stacked and pre-stack data are compared to VSP data and seismic attributes. The median attenuation estimated from the stacked surface seismic data agrees with the median values estimated from the VSP data but they do not agree with the value estimated from pre-stack surface seismic data. The estimated attenuation from stacked and prestack seismic data does not correlate with maps of average energy or average centroid frequency within any interval.

The frequency-dependence of attenuation in the pre-stack surface seismic and VSP data over the Kinnoull discovery has then been estimated by adaptation of the PSQI method and spectral ratio method respectively. The same frequency-dependent Q estimation method is applied to VSP data in the Barents Sea also. In all cases the median exponent of the powerlaw frequency-dependent attenuation model is small, with median values of 0.0074, -0.2 and 0.052 for the Kinnoull pre-stack seismic data, Kinnoull VSP data and Barents Sea VSP data respectively.

The attenuation values estimated from the Barents Sea VSP data, utilising the SDD method for estimating spectra, are compared to petrophysical parameters and elastic moduli estimated from coincident well log data. Statistically significant correlations were found between attenuation and Bulk modulus, shear modulus, Young's modulus and Poisson's ratio. Fitted squirt flow models predict peak frequencies of between 20Hz and 10kHz with crack aspect ratios of between 10^{-3} and $6\text{x}10^{-3}$.

The results from squirt flow modelling of the frequency-dependent attenuation seen in the Barents Sea point to the squirt flow model being a valid mechanism causing intrinsic attenuation within the subsurface due to realistic crack aspect ratios estimated. Modelling of other attenuation mechanisms such as the Biot flow and combined Biot/squirt flow (BISQ) model was not carried out and thus cannot be commented on but could be an avenue for further research.

6.3 Summary of suggestions for future work

1. Analysis of the effects of the designed window function in the SDD on the estimated attenuation values from synthetic seismic data.

2. Development of a method to estimate a time-phase representation of the signal from the SDD.

3. Development of a method to quantify the time-frequency resolution of SDD with a generic window function.

4. Comparison of attenuation estimated over the Kinnoull discovery to other seismic attributes, such as AVO intercept, AVO gradient and acoustic impedance.

5. Estimation of shear-wave attenuation from the VSP data in well 16/23-7, located over the Kinnoull discovery, to estimate the ratio between compressional- and shear-wave attenuation.

6. Application of the frequency-dependent Q estimation method to different seismic surveys, specifically shallow marine or shallow land data which contain unconsolidated lithologies.

7. Incorporation of more VSP datasets from the Barents Sea into those already used in this study, in order to further constrain relationships between attenuation and elastic moduli or petrophysical parameters.

8. Incorporation of laboratory measurements at ultrasonic frequencies to consolidate the squirt flow modelling of estimated frequency-dependent attenuation.

9. Analysis of attenuation at different frequencies for the Barents Sea wells to estimate the frequency dependence of attenuation over different orders of magnitude in frequency.

References

Carey, W. M., A. D. Pierce, R. E. Evans, and J. D. Holmes, 2008, On the exponent in the power law for the attenuation at low frequencies in sandy sediments: The Journal of the Acoustical Society of America, **124**, EL271–EL277. 236, 237

Gurevich, B., and R. Pevzner, 2015, How frequency dependency of q affects spectral ratio estimates: Geophysics, **80**, A39–A44. 236

Jeng, Y., J.-Y. Tsai, and S.-H. Chen, 1999, An improved method of determining near-surface q: Geophysics, **64**, 1608–1617. 236, 237

Jones, T. D., 1986, Pore fluids and frequency-dependent wave propagation in rocks: Geophysics, **51**, 1939–1953. 238

Mangriotis, M.-D., J. W. RectorIII, E. F. Herkenhoff, and J. C. Neu, 2013, Scattering versus intrinsic attenuation in the vadose zone: A vsp experiment: Geophysics, **78**, B49–B63. 232, 234

Odoherty, R., and N. Anstey, 2006, Reflections on amplitudes: Geophysical Prospecting, **19**, 430–458. 234

Sams, M., J. Neep, M. Worthington, and M. King, 1997, The measurement of velocity dispersion and frequency-dependent intrinsic attenuation in sedimentary rocks: Geophysics, **62**, 1456–1464. 236, 238